BRNO UNIVERSITY OF TECHNOLOGY

VYSOKÉ UČENÍ TECHNICKÉ V BRNĚ

CENTRAL EUROPEAN INSTITUTE OF TECHNOLOGY BUT

STŘEDOEVROPSKÝ TECHNOLOGICKÝ INSTITUT VUT

SPECIAL PROBLEMS OF FRACTURE MECHANICS OF SINGULAR STRESS CONCENTRATORS IN COMPOSITE MATERIALS

SPECIÁLNÍ PROBLÉMY LOMOVÉ MECHANIKY SINGULÁRNÍCH KONCENTRÁTORŮ NAPĚTÍ V KOMPOZITNÍCH MATERIÁLECH

DOCTORAL THESIS
DIZERTAČNÍ PRÁCE

AUTHOR — **Ing. Ondřej Krepl**
AUTOR PRÁCE

SUPERVISOR — **doc. Ing. Jan Klusák, Ph.D.**
ŠKOLITEL

BRNO 2018

Abstract

The presented dissertation deals with general singular stress concentrators (GSSC) namely with a sharp notch also known as a V-notch, a sharp bi-material notch and a sharp material inclusion. The review section briefly outlines the Kolosov-Muskhelishvili complex potential theory of the plane elasticity applied on fracture mechanics problems. Next, the linear elastic fracture mechanics of cracks, V-notches, bi-material notches and bi-material junctions is discussed. The review also includes the crack initiation direction and the stability criteria of the maximum tangential stress, the strain energy density factor and the coupled stress-energy criterion. In the following text, limits of the single parameter and advantages of the multi-parameter fracture mechanics are presented. The next section introduces methods to determine the necessary parameters to describe the stress and displacement field near the GSSCs. The parameters include the eigenvalue λ_k and the generalized stress intensity factor H_k. The λ_k is determined as an eigenvalue problem, while the methods to calculate the H_k are the Ψ-integral and the overdeterministic method. Both the methods are applied on the studied GSSCs and mutually compared. Finally the criteria for crack initiation in the GSSCs are proposed in the multi-parameter form. The crack initiation direction and the stability conditions are predicted for particular problems in numerical examples. The failure forces for a V-notch are predicted by above mentioned criteria and compared with experimental data found in literature. In following section methods to analyze multi-material problem are shown. The final section summarizes with means of the crack initiation and propagation near the sharp material inclusion.

Keywords

Fracture mechanics, general singular stress concentrator, bi-material notch, sharp material inclusion, composite material

Abstrakt

Předkládaná disertace se zabývá obecnými singulárními koncentrátory napětí a to zejména ostrým vrubem neboli V-vrubem, ostrým bi-materiálovým vrubem a ostrou materiálovou inkluzí. V první části práce je stručně nastíněna Kolosovova-Muschelišviliho teorie komplexních potenciálů rovinné pružnosti aplikovaná na problémy lomové mechaniky. Dále je diskutována lineární elastická lomová mechanika trhlin, V-vrubů, bi-materiálových vrubů a bi-materiálových spojů. V rešerši jsou dále zahrnuta kritéria směru iniciace trhliny i její stability a to kritérium maximálního tečného napětí, faktor hustoty deformační energie a sdružené napěťově-energetické kritérium. Následují text uvádí omezení jednoparametrové lomové mechaniky a výhody její multiparametrové formy. Další část představuje metody pro určení nezbytných parametrů pro popsání pole napětí a posuvů v blízkosti obecného singulárního koncentrátoru napětí. Tyto parametry zahrnují vlastní číslo λ_k a zobecněný faktor intenzity napětí H_k. Vlastní číslo λ_k je určeno jako řešení problému vlastních hodnot zatímco metody pro určení H_k tvoří Ψ-integrál a metoda přeurčitosti. Obě zmiňované metody jsou aplikovány na zde studované obecné singulární koncentrátory napětí a vzájemně porovnány. Kritéria pro vznik trhliny v obecném singulárním koncentrátoru napětí jsou navržena. V rámci numerických příkladů jsou předpovězeny směry iniciace trhliny a podmínky stability pro konkrétní problémy. Kritické síly pro V-vrub jsou předpovězeny pomocí výše zmíněných kritérií a srovnány s experimentálními daty v literatuře. V následující části jsou ukázány metody analýzy multi-materiálového problému. V závěru práce jsou shrnuty způsoby iniciace a šíření trhliny v blízkosti ostré materiálové inkluze.

Klíčová slova

Lomová mechanika, obecný singulární koncentrátor napětí, bi-materiálový vrub, ostrá materiálová inkluze, kompozitní materiál

Bibliographic citation

KREPL, O. *Special problems of fracture mechanics of singular stress concentrators in composite materials.* Brno: Brno University of Technology, Central European Institute of Technology, 2018. 115 p. Dissertation supervisor: doc. Ing. Jan Klusák, Ph.D.

Bibliografická citace

KREPL, O. *Special problems of fracture mechanics of singular stress concentrators in composite materials.* Brno: Vysoké učení technické v Brně, Středoevropský technologický institut VUT, 2018. 115 s. Vedoucí dizertační práce doc. Ing. Jan Klusák, Ph.D.

Sworn statement

I state that I am the only author of this work, which I elaborated based on the discussions with my supervisor doc. Ing. Jan Klusák, Ph.D. and by the use of the referenced literature.

Čestné prohlášení

Prohlašuji, že jsem tuto disertační práci zpracoval samostatně na základě konzultací se svým školitelem doc. Ing. Janem Klusákem, Ph.D. a s použitím uvedené literatury.

Ondřej Krepl

Preface

The dissertation "Special problems of fracture mechanics of singular stress concentrators in composite materials" is the culmination of my doctoral studies and research in the fracture mechanics. Its creation started during my research internship in Paris in the autumn of 2016 and ended in the beggining of 2018, although much of the theoretical work was developed earlier at the time of my doctoral study, which initiated in 2013.

It would have been very difficult or even impossible without the support and advice of some great people. First of all, I would like to thank my supervisor doc. Ing. Jan Klusák, Ph.D. for his excellent guidance the whole time of my PhD study. I am very grateful to him for everything he has taught me, the inspiration he provided and I truly appreciate his support. I would also like to thank Prof. Dominique Leguillon for his professional guidance during the research internship in France. Last but not least, I would like to thank doc. Ing. Tomáš Profant, Ph.D. who introduced me about eight years ago in the fascinating field of the fracture mechanics.

The author would like to thank the Czech Science Foundation for financial support through the Grant 16/18702S. The research within this dissertation has been financially supported by the Ministry of Education, Youth and Sports of the Czech Republic under the project CEITEC 2020 [LQ1601].

CEITEC IPM, Institute of Physics of Materials AS CR

Žižkova 22, Brno 616 62, Czech Republic

krepl@ipm.cz

Contents

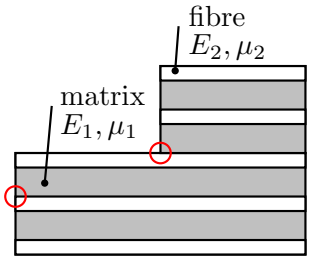

Figure 1: Locations in a composite material where a singular stress concentration is expected.

1. Introduction

Fracture mechanics has been developed following the fact that the majority of components and structures in engineering application contain cracks or crack-like flaws [1]. Linear elastic fracture mechanics (LEFM) uses methods of the linear elastic stress analysis of a cracked part to determine the conditions under which a crack, or crack-like flaw will extend. The linear elastic analysis of a body with a crack shows that the stresses around the crack tip vary according to $r^{-1/2}$ where r is the distance from the crack tip. It is obvious that the elastic stresses become unbounded as r approaches the crack tip [2, 3].

As a result of the near tip stress field character of a crack, it is among so called singular stress concentrators. A crack can be conceived as a special case of a sharp V-notch with an opening angle equal to zero. It has been found that the stress field in the vicinity of a sharp V-notch tip (with a non-zero opening angle) also has the singular character, nonetheless different from the case of a crack [8]. The singular stress concentrators discussed above originate from a discontinuity in geometry. However, singular stress character in a body different from a crack can also arise from a material properties discontinuity. This may be the case of a bi-material junction which is a model for a sharp polygon-like inclusion embodied in a parent material. An ultimate case of a singular stress concentrator a sharp bi-material notch is the case combining both geometrical and material discontinuities.

Nowadays we encounter a rising number of components and structures made out of composite materials. The composite materials (or composites) consist of two or more combined constituents that are combined at a macroscopic level [6]. One constituent is called the *reinforcing phase* and the one in which the reinforcement is embedded is called the *matrix* as shown in Figure 1. The reinforcing phase material may be in the form of fibers, particles, or flakes. One of the reasons to choose composites is that for example monolithic metals and their alloys cannot always meet the demands of today's advanced technologies. Only by combining several materials can the performance requirements be met as we can see in the aerospace industry where a combination of supreme structural characteristics and low weight is critical. On the other hand, the very nature of composites (the material properties mismatch) brings higher complexity of their description in terms of fracture mechanics.

Advanced studies of the linear elastic fracture mechanics of cracks show an influence of particular singular and non-singular stress series terms on the fracture behavior of solids with a crack. It is shown in literature that the first non-singular (constant) term of Williams' stress series [9] called T-stress plays an important role within crack behavior assessment both in the case of brittle fracture and in the case of fatigue crack propagation [11, 12, 13, 14]. Similarly, the effects of the T-stress on interfacial cracks in isotropic bi-materials were studied [15].

Contrary to this, the approaches that will be able to assess the influence of the non-singular stress terms on a fracture initiation in the general singular stress concentrators are in the focal point to be developed. The following stress concentrators are considered: the sharp V-notch in isotropic material, the sharp bi-material notch composed of two isotropic materials, and the bi-material junction composed of two isotropic materials. In the case of the general stress concentrators, the influence of the non-singular terms has not been studied sufficiently, but it is expected as well. The stress concentrators mentioned above can model a number of typical dangerous points of components usually responsible for their failure.

Depending on loading conditions and geometry of a component with the stress concentrator, a generalized constraint can have a positive or negative influence. It can counteract crack initiation or it can stimulate it. Thus assessment not covering the influence of the constraint provides overestimated or underestimated results. In the first case the new approaches can save a certain volume of material, while in the second case the new stability assessment can prevent a fatal damage. Thus the results of the future research can raise the credibility and extend the application possibilities of the fracture mechanics.

As mentioned above, the general singular stress concentrators (GSSCs) exhibit a stress distribution at their tip

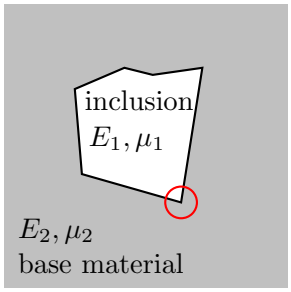

Figure 2: Sharp material inclusion tip where a singular stress concentration is expected.

similar to a crack in linear elastic fracture mechanics. Within the description of the stress distribution in the form of an infinite series the stress singularity exponents differ from ½. Similarly, the higher order terms appearing in the stress distribution of the general stress concentrators have their generalized form (e.g. the exponent of the first non-singular term differs from 0).

Some of crack initiation criteria of generalized stress concentrators require establishing a specific distance from the tip of the concentrator, which depends on material characteristics (the strength and fracture toughness of the material [23] or the size of material grain, [18, 19]). In fact, these distances are in some cases much larger than the characteristic dimension of the domain of prevailing singular stress terms [16, 17, 21, 22]. Consequently, the influence of the non-singular stress terms could be significant and emphasizing the necessity of their study is due to good understanding of fracture processes at the sharp bi-material notch or the sharp material inclusion tip, Figure 2, studied within the dissertation.

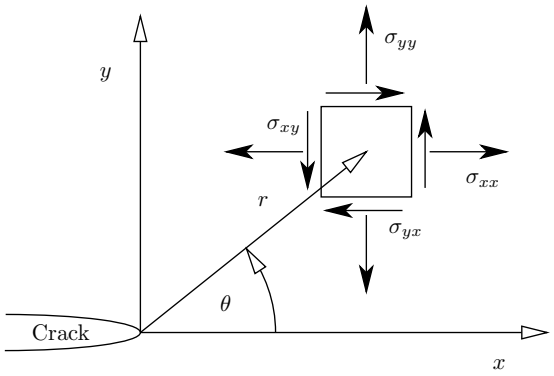

Figure 3: A coordinate system located at the crack tip and the Cartesian stress field components.

2. Review

2.1. Methods of the Kolosov-Muskhelishvili complex potential theory for plane elasticity

Among various mathematical methods in plane elasticity, the complex potential function method developed by Kolosov and Muskhelishvili is one of the most powerful and convenient methods to treat two-dimensional problems [3, 4, 5]. In the complex potential method the displacement and stresses are expressed in terms of analytical functions of complex variables. The basic equations of elasticity consist of equilibrium equations of stresses without presence of body forces in the form of:

$$\begin{aligned} \frac{\partial \sigma_{xx}}{\partial x} + \frac{\partial \sigma_{xy}}{\partial y} &= 0, \\ \frac{\partial \sigma_{xy}}{\partial x} + \frac{\partial \sigma_{yy}}{\partial y} &= 0, \end{aligned} \tag{1}$$

where the individual stress components together with the coordinate system located at the crack tip are depicted in Figure 3. The relations between strains and displacements are:

$$\varepsilon_{xx} = \frac{\partial u_x}{\partial x}, \quad \varepsilon_{yy} = \frac{\partial u_y}{\partial y}, \quad \varepsilon_{xy} = \frac{1}{2}\left(\frac{\partial u_x}{\partial y} + \frac{\partial u_y}{\partial x}\right), \tag{2}$$

and finally the stress-strain relations are:

$$\begin{aligned} \sigma_{xx} &= \lambda^*(\varepsilon_{xx} + \varepsilon_{yy}) + 2\mu\varepsilon_{xx}, \\ \sigma_{yy} &= \lambda^*(\varepsilon_{xx} + \varepsilon_{yy}) + 2\mu\varepsilon_{yy}, \\ \sigma_{xy} &= 2\mu\varepsilon_{xy}. \end{aligned} \tag{3}$$

The symbol μ stands for the shear modulus and λ^* is given by:

$$\lambda^* = \frac{(3-\kappa)}{(\kappa-1)}\mu,$$

where κ is Kolosov's constant defined as:

$$\kappa = \begin{cases} 3-4\nu & \text{plane strain} \\ \frac{3-\nu}{1+\nu} & \text{palne stress} \end{cases}.$$

In the expression above υ is Poisson's ratio. It is common also to use the equation (3) in inverted form, which is:

$$\begin{aligned} \varepsilon_{xx} &= \frac{1}{E}\left[\sigma_{xx} - \nu\left(\sigma_{yy} + \sigma_{zz}\right)\right], \quad \varepsilon_{xy} = \frac{1}{2\mu}\sigma_{xy}, \\ \varepsilon_{yy} &= \frac{1}{E}\left[\sigma_{yy} - \nu\left(\sigma_{xx} + \sigma_{zz}\right)\right], \quad \varepsilon_{yz} = \frac{1}{2\mu}\sigma_{yz}, \\ \varepsilon_{zz} &= \frac{1}{E}\left[\sigma_{zz} - \nu\left(\sigma_{xx} + \sigma_{yy}\right)\right], \quad \varepsilon_{zx} = \frac{1}{2\mu}\sigma_{zx} \end{aligned} \tag{4}$$

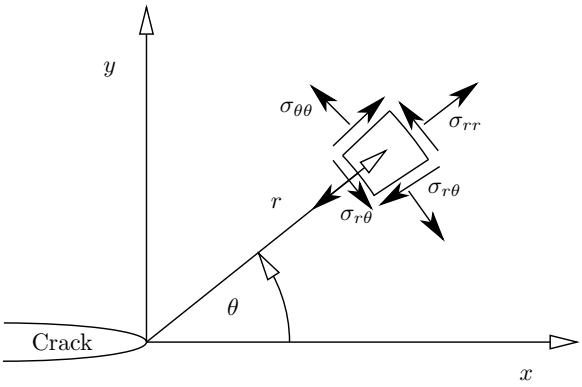

Figure 4: A coordinate system located at the crack tip and the polar stress field components.

Throughout presented dissertation, materials are always represented by linear elastic material model. The compatibility equations of strains can be obtained from equation (2) by eliminating displacements as follows:

$$\frac{\partial^2 \varepsilon_{xx}}{\partial y^2} + \frac{\partial^2 \varepsilon_{yy}}{\partial x^2} = \frac{2\partial^2 \varepsilon_{xy}}{\partial x \partial y}. \tag{5}$$

By using the stress-strain relations (4) and the equilibrium conditions (1) the compatibility condition (5) above can be expressed in terms of stresses as:

$$\nabla^2(\sigma_{xx} + \sigma_{yy}) = 0,$$

where ∇^2 is the Laplace operator given by:

$$\frac{\partial^2}{\partial x^2} + \frac{\partial^2}{\partial y^2} = 0.$$

The Airy's stress function Φ is defined as:

$$\sigma_{xx} = \frac{\partial^2 \Phi}{\partial x^2}, \quad \sigma_{yy} = \frac{\partial^2 \Phi}{\partial y^2}, \quad \sigma_{xy} = \frac{\partial^2 \Phi}{\partial x \partial y}$$

Using the relations above, the equilibrium equations (1) are automatically satisfied and the compatibility equation (5) becomes:

$$\nabla^4 \Phi = 0. \tag{6}$$

Any function which satisfies the equation above is called a bi-harmonic function. Once the Airy's stress function is known, the stresses, strains and displacements are expressed through equations (3) and (2) respectively. The solution for the stress field has to satisfy both the equation (6) above and the boundary conditions. The main difficulty may arise in finding the stress function which satisfies the boundary conditions of interest [1]. The problem can be approached in reverse order, that is we can first postulate the function $\Phi(z)$ and then examine what boundary conditions are satisfied. Finally, the complex potential representation of the Airy's stress function [3, 4, 5] is given by:

$$\begin{aligned} \Phi &= \Re\left\{\bar{z}\Omega(z) + \chi(z)\right\}, \\ 2\Phi &= \bar{z}\Omega(z) + z\bar{\Omega}(z) + \chi(z) + \bar{\chi}(z), \end{aligned}$$

where $\Omega(z)$ and $\chi(z)$ are analytic functions (also known in literature as complex potentials). Complex variable is $z = x + iy$ for Cartesian coordinate system and $z = r(\cos\theta + i\sin\theta) = re^{i\theta}$ for polar coordinate system as shown in Figure 4. The line over the symbols stands for the complex conjugate and the symbol $\Re\{z\}$ represents the real part of the complex number z. Considering $\omega(z) = \chi'(z)$, where the symbol $'$ denotes the derivative by variable z, the Kolosov-Muskhelishvili formulas for general plane problems are:

$$\begin{aligned} \sigma_{xx} + \sigma_{yy} &= 4\Re\left\{\Omega'(z)\right\}, \\ \sigma_{xx} - \sigma_{yy} + i\sigma_{xy} &= 2\left\{\bar{z}\Omega''(z) + \omega'(z)\right\}, \\ 2\mu(u_x + iu_y) &= \kappa\Omega(z) - z\bar{\Omega}'(z) - \bar{\omega}(z). \end{aligned} \tag{7}$$

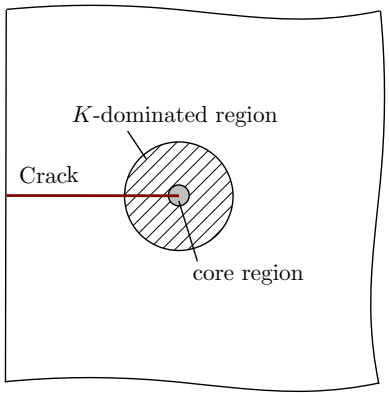

Figure 5: Zones surrounding the crack tip.

By simple algebraic operations and the choice of polar coordinate system the set of equations (7) can be rewritten into a form used through the dissertation [43]:

$$\begin{aligned} \sigma_{rr} + i\sigma_{r\theta} &= \Omega'(z) + \bar{\Omega}'(z) - z\bar{\Omega}''(z) - \bar{\omega}'(z), \\ \sigma_{\theta\theta} - i\sigma_{r\theta} &= \Omega'(z) + \bar{\Omega}'(z) + z\bar{\Omega}''(z) + \bar{\omega}'(z), \\ u_r + iu_\theta &= \frac{1}{2\mu} e^{-i\theta} \left[\kappa\Omega(z) - z\bar{\Omega}'(z) - \bar{\omega}(z)\right]. \end{aligned} \tag{8}$$

By adding the complex conjugate of first equation of (8) to the first equation of (8) we obtain the expression for the radial stress component. Similarly we can obtain any individual stress or displacement component. The resulting equations are as follows:

$$\begin{aligned} \sigma_{rr} &= \Omega'(z) + \bar{\Omega}'(z) - \frac{\bar{z}}{2}\Omega''(z) - \frac{z}{2}\bar{\Omega}''(z) - \frac{1}{2}\omega'(z) - \frac{1}{2}\bar{\omega}'(z), \\ \sigma_{\theta\theta} &= \Omega'(z) + \bar{\Omega}'(z) + \frac{\bar{z}}{2}\Omega''(z) + \frac{z}{2}\bar{\Omega}''(z) + \frac{1}{2}\omega'(z) + \frac{1}{2}\bar{\omega}'(z), \\ \sigma_{r\theta} &= \frac{\bar{z}}{2i}\Omega''(z) - \frac{z}{2i}\bar{\Omega}''(z) + \frac{1}{2i}\omega'(z) - \frac{1}{2i}\bar{\omega}'(z), \\ u_r &= \frac{1}{4\mu}\left\{e^{-i\theta}\left[\kappa\Omega(z) - z\bar{\Omega}(z) - \bar{\omega}(z)\right] + e^{i\theta}\left[\kappa\bar{\Omega}(z) - \bar{z}\Omega(z) - \omega(z)\right]\right\}, \\ u_\theta &= \frac{1}{4i\mu}\left\{e^{-i\theta}\left[\kappa\Omega(z) - z\bar{\Omega}(z) - \bar{\omega}(z)\right] - e^{i\theta}\left[\kappa\bar{\Omega}(z) - \bar{z}\Omega(z) - \omega(z)\right]\right\}. \end{aligned} \tag{9}$$

2.2. Fracture mechanics of a crack in homogeneous media

Linear elastic analysis of a cracked body shows that for the stresses σ_{ij} near the crack tip it follows that:

$$\sigma_{ij} \propto \frac{1}{\sqrt{r}},$$

where r is the distance from the crack tip as shown in Figure 3 or Figure 4. It is obvious that $\sigma_{ij} \to \infty$ as r approaches the crack tip [1, 2, 3]. A fundamental concept of fracture mechanics is to accept the theoretical stress singularity at the crack tip but not to use stress directly to determine failure or crack extension. This is based on the fact that the stress in the vicinity of the crack tip has a limit which is the yield stress or the cohesive stress between atoms. The singular stress field is a convenient representation of the actual finite stress field if the actual discrepancy between the two lies in a small area near the crack tip, in a so called core region as shown in Figure 5. This concept is known as *small-scale yielding*. Thus the validity of Hooke's law in all areas of the body except the core region is the basic assumption of Linear Elastic Fracture Mechanics (LEFM). When a load is applied to a cracked body, the crack surfaces move relative to each other and there are three possible modes of crack surface displacement as shown in Figure 6. These are:

- Mode I, the opening mode when the opposing crack surfaces move directly apart, Figure 6a.

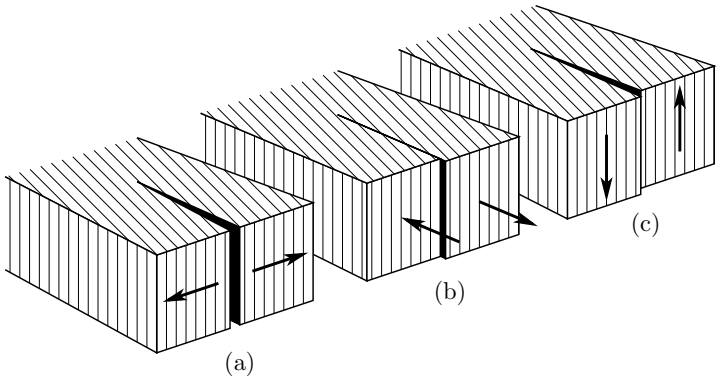

Figure 6: Basic fracture modes, (a) Mode I, opening (b) Mode II, in-plane shear (c) Mode III, out-plane shear

- Mode II, the in-plane shear when the crack surfaces move over each other perpendicular to the crack front, Figure 6b.
- Mode III, the out-plane shear when the crack surfaces move over each other parallel to the crack front, Figure 6c.

A general case of crack tip surface displacement can be described by superimposing the three modes. In practice, most cracks tend to grow in Mode I, [1]. In order to describe the stress field in a cracked body a suitable Airy's stress function has to be found as discussed in sub-section 2.1. Consider an infinite plate with a crack along the x-axis as shown in Figure 7. The solution proposed by Westergaard begins by defining the stress function $Z(z)$ in the following form:

$$Z(z) \quad = \quad 2\Phi'(z)$$

If both the loading and geometry are symmetrical about the x-axis, then $\sigma_{xy} = 0$ along $y = 0$ and it follows that:

$$\begin{aligned} \sigma_{xx} &= \Re\{Z(z)\} - y\Im\{Z'(z)\} - A, \\ \sigma_{yy} &= \Re\{Z(z)\} - y\Im\{Z'(z)\} + A, \\ \sigma_{xy} &= -y\Re\{Z'(z)\}, \end{aligned}$$

where A is a real constant. The symbol $\Im\{z\}$ denotes the imaginary part of the complex number z. The suitable function for given geometry and boundary conditions is:

$$\Phi(z) \quad = \quad \sigma_\infty[z - a^2(z^2 - a^2)^{-1/2})].$$

Then the near-tip solution for the stress components is given by:

$$\begin{aligned} \sigma_{xx} &= \frac{K_\mathrm{I}}{\sqrt{2\pi r}} \cos\frac{\theta}{2}\left(1 - \sin\frac{\theta}{2}\sin\frac{3\theta}{2}\right), \\ \sigma_{yy} &= \frac{K_\mathrm{I}}{\sqrt{2\pi r}} \cos\frac{\theta}{2}\left(1 + \sin\frac{\theta}{2}\sin\frac{3\theta}{2}\right), \\ \sigma_{xy} &= \frac{K_\mathrm{I}}{\sqrt{2\pi r}} \cos\frac{\theta}{2}\sin\frac{\theta}{2}\cos\frac{3\theta}{2}. \end{aligned}$$

The detailed determination of equations above can be found in [1, 3]. The near-tip displacements are obtained similarly, therefore:

$$\begin{aligned} u_x &= \frac{K_\mathrm{I}}{8\mu\pi}\left[(2\kappa - 1)\cos\frac{\theta}{2} - \cos\frac{3\theta}{2}\right], \\ u_y &= \frac{K_\mathrm{I}}{8\mu\pi}\left[(2\kappa + 1)\sin\frac{\theta}{2} - \sin\frac{3\theta}{2}\right]. \end{aligned}$$

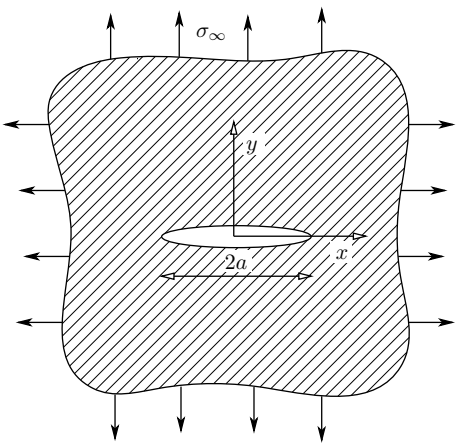

Figure 7: Central crack in an infinite sheet under uniform biaxial tension.

Thus the formal definition of mode I Stress Intensity Factor (SIF) is:

$$K_{\mathrm{I}} = \lim_{r\to 0} \sqrt{2\pi r}\sigma_{yy}\left(\theta = 0\right).$$

Simple analysis reveals that the unit of SIF is $[K_i] = \mathrm{MPa}\cdot \mathrm{m}^{\frac{1}{2}}$. The Williams's stress function [8, 9] is a generalized form of the Westergaard's stress function [1], stresses are expanded into a series. The Airy's stress function has the following form:

$$\Phi = \sum_{k=0}^{\infty} r^{\lambda_k+1} F_k\left(\theta\right),$$

where λ_k is eigenvalue and $F_k\left(\theta\right)$ is corresponding eigenfunction. The solution of the bi-harmonic equation (6) is given by:

$$F_k(\theta) = A_k \sin(\lambda_k+1)\theta + B_k\cos(\lambda_k+1)\theta + C_k\sin(\lambda_k-1)\theta + D_k\cos(\lambda_k-1)\theta.$$

For Mode I crack problems, the constants A_k and C_k are zero. It can be shown [3] that for the nontrivial solution of the remaining constants B_k and D_k the characteristic equation of the eigenvalue λ_k is:

$$\sin\left(2\lambda_k\pi\right) = 0.$$

Thus the roots[1] of this equation are $\lambda_k = \frac{k}{2}$, $k = 1, 2, \ldots$ Finally the Williams's stress series can be written as [2]:

$$\sigma_{ij} = \frac{K_{\mathrm{I}}}{\sqrt{2\pi r}} f_{ij}\left(\theta\right) + \sum_{k=0}^{\infty} k_k r^{\frac{k}{2}} g_{ijk}\left(\theta\right),$$

where the $f_{ij}\left(\theta\right)$ and $g_{ijk}(\theta)$ are eigenfunctions. Analysis of stress term behavior when $r \to 0$ indicates that the first singular term becomes unbounded, the term of stress intensity factor k_k with $k = 0$ is constant and the other higher terms ($k > 0$) disappear. Nevertheless, as for Westergaard's solution, the stress field in the vicinity of a crack tip is dominated by the leading term of the Williams's stress function.

Determination of the stress intensity factors

In general there are two methods how to determine SIFs by finite element analysis of a homogeneous body with a crack. In the first case the mid-side nodes of a special triangular plane element are moved to the 1/4 points as shown in Figure 8. Such a modification results in a $1/\sqrt{r}$ strain singularity, which enhances the numerical accuracy of the solution. Then the numerical determination of the stress intensity factor by fitting into the analytical relations is usually a built-in part of an FE system postprocessor. The second widely used option of SIF calculation without a need for special elements is its determination by the contour integral. The path integration sufficiently far from the singular point mitigates incorrect results of FEM in the closest vicinity of the singular stress concentrator.

[1] Only the positive values of λ_k are considered. The negative values would lead to infinite displacements at the crack tip and $\lambda_k = 0$ leads to unbounded strain energy [3].

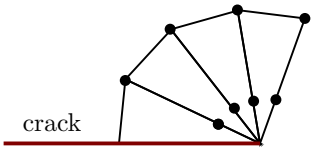

Figure 8: Special triangular elements with shifted mid-side nodes.

Criteria of crack propagation direction

Maximum tangential stress criterion. The path of a crack in homogeneous material is sometimes curved. Generally we can say that a crack tends to propagate in Mode I of loading [1, 2]. Thus for the case of a crack subjected to a combined loading mode, the crack deflects towards the direction corresponding to a normal loading mode. The criterion of the maximum tangential stress used for determination of crack propagation direction is based on the assumption that a crack will propagate in the direction where the stress opening the crack will reach its maximum [26]. The angle θ_0 of further crack propagation must meet the following conditions:

$$\left(\frac{\partial \sigma_{\theta\theta}}{\partial \theta}\right)_{\theta=\theta_0} = 0,$$

$$\left(\frac{\partial^2 \sigma_{\theta\theta}}{\partial \theta^2}\right)_{\theta=\theta_0} < 0.$$

Strain energy density factor. Another method to predict crack propagation direction is to use Sih's Strain energy density factor (SEDF), it states that the crack will propagate in the direction of minimal value of SEDF [57]:

$$\left(\frac{\partial \Sigma}{\partial \theta}\right)_{\theta=\theta_0} = 0,$$

$$\left(\frac{\partial^2 \Sigma}{\partial \theta^2}\right)_{\theta=\theta_0} > 0,$$

where the SEDF can be calculated using stress components as:

$$\Sigma = r\left[2\sigma_{\theta\theta}\sigma_{rr}(k-1) + (\sigma_{\theta\theta}^2 + \sigma_{rr}^2)(k+1) + 4\sigma_{r\theta}^2\right]\frac{1}{8\mu} \tag{10}$$

and k is constant defined:

$$k = \begin{cases} 1-2\nu & \text{plane strain} \\ \frac{1-\nu}{1+\nu} & \text{palne stress} \end{cases}. \tag{11}$$

Stability criteria

Critical value of stress intensity factor. A crack does not propagate if the value of the stress intensity factor K_{I} is below its critical value K_{Icrit}. The critical value K_{Icrit} can be represented by the fracture toughness K_{IC} for cases of brittle fracture or by the threshold value K_{Ith} for fatigue crack propagation[2]. Then the stability criterion is:

$$K_{\mathrm{I}} < K_{\mathrm{Icrit}}. \tag{12}$$

[2]In the case of fatigue crack propagation, the stability condition is written $\Delta K_I < K_{Ith}$, where the ΔK_I is the stress intensity factor range. The condition is valid for stress ratio $R = 0$.

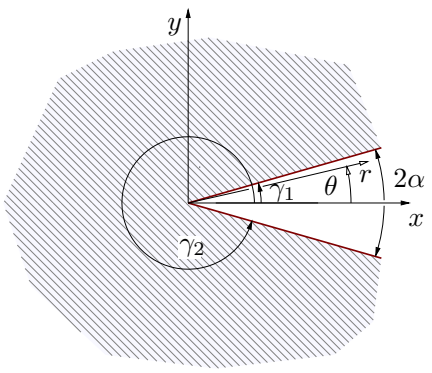

Figure 9: The sharp homogeneous notch with a Cartesian and polar coordinate system at its tip.

Critical value of strain energy density factor. The Sih's stability criterion states, that the crack will propagate when the SEDF Σ reaches its critical value Σ_{crit}:

$$\Sigma \quad < \quad \Sigma_{\text{crit}}.$$

The critical value of SEDF Σ_{crit} is material parameter, which can be determined in relation to the critical value of K_{Icrit} for given material:

$$\Sigma_{\text{crit}} \quad = \quad \frac{kK_{\text{Icrit}}^2}{4\pi\mu}. \tag{13}$$

2.3. Fracture mechanics of V-notch and bi-material notch

In the following we consider the geometrical and material configuration of a sharp homogeneous notch or sharp bi-material notch as shown in Figure 9 and Figure 10 respectively. In following text we will intentionally omit the word sharp, however both the homogeneous and bi-material notch are always considered sharp, i.e. with a zero notch radius throughout this dissertation. Please note that the sharp homogeneous notch is often referred in the literature by simplistic V-notch which will be also used in this text. The geometry of a V-notch is characterized by the angles γ_1 and γ_2 and complementary opening angle 2α. The case of a bi-material notch has three geometric parameters γ_1, γ_2 and γ_3 and complementary opening angle 2α. The material properties are given by the elastic constants of Young's moduli and Poisson's ratios. The solution mostly presupposes the approximation of plane strain or plane stress. For the case of a bi-material notch a perfect bonding (displacement and traction continuity) is assumed at the interface. The material characteristics, therefore, change by step at the interface. Furthermore, the notch surfaces are traction-free. Stress distribution in the case of a V-notch or bi-material notch [17, 27] is given by:

$$\sigma_{ij} \quad = \quad \sum_{k=1}^{n} \frac{H_k}{\sqrt{2\pi}} r^{-p_k} f_{ijk}\left(\theta\right) \tag{14}$$

where the indices $(i,j) \equiv (r,\theta)$ are polar coordinates. The symbol H_k stands for the Generalized Stress Intensity Factor (GSIF) with the unit of $[H_k] = \text{MPa}\,.\,\text{m}^{p_k}$. The $f_{ijk}\left(\theta\right)$ is the angular eigenfunction, which is dimensionless. The stress singularity exponents are given by:

$$p_k \quad = \quad 1 - \lambda_k$$

where λ_k is the kth eigenvalue of the problem, which is real or complex number. In most of the geometrical and material configurations of V-notches and bi-material notches there are two real stress singularity exponents p_1 and p_2 in the interval $(0,1)$ corresponding to the singular terms of the series [28]. Higher order eigenvalues can be either real or complex numbers. Since its real part is greater than one, these eigenvalues correspond to the non-singular higher order terms. The Figure 23 on p. 35 shows the dependence of real and imaginary part of the eigenvalues λ_k on the notch opening angle 2α for the V-notch. Similarly in Figure 24 on p. 36, the resulting eigenvalues for the bi-material notch are depicted.

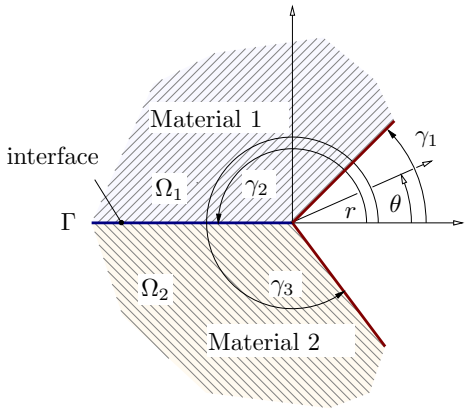

Figure 10: The sharp bi-material notch with a Cartesian coordinate system at its tip.

Determination of the stress terms order

As mentioned above we consider that notch surfaces are traction-free and the interface between the materials is perfectly bonded (ideal adhesion). The eigenvalues of V-notches or bi-material notches are gained from a numerical solution of so the called characteristic equation depending on the geometry and material properties of the notch [29, 30, 31]. An effective tool to describe problems of isotropic plane elasticity is the Muskhelishvili's complex potential theory [4, 5, 7]. Another advantage of the stress-displacement field description by the complex potentials is the effortless handling of the complex eigenvalues and the corresponding complex stress singular and non-singular exponents. For the case of a bi-material notch the characteristic equation originates from equations enforcing zero stress at the ith notch free surfaces, traction (both $\sigma_{\theta\theta}$ and $\sigma_{r\theta}$) and displacement continuity at the interface. In the above-mentioned (and other) publications the exponents corresponding to the singular stress terms are described. The stress exponents of higher order (non-singular) terms will be determined within the dissertation from a set of the boundary conditions corresponding to a particular problem [32]. The determination is shown in detail in sub-chapter 4.2 on p. 27.

Determination of the stress intensity factors of particular stress terms

Methods for determination of the stress intensity factors of cracks are generally available in FEM commercial systems. However, in the case of GSSCs, no simple method incorporated in FEM systems exists, and the amplitudes of the stress terms must be determined via direct or integral methods e.g. [33, 36, 37, 38] . Both direct and integral methods are combination of FEM and analytical approaches. For the case of determination of non-singular terms the direct methods must be further modified. The direct method called the overdeterministic method (ODM) is based on the solution of overdetermined system of linear equations by least-squares method [36]. The ODM has been chosen for the study especially because of its minimal requirements for the FE software (there is no need to use any special crack finite elements like the one depicted in Figure 8). The system of linear equations can be written:

$$\mathbf{F}_{[2m\times n]}\mathbf{H}_{[n]} \quad = \quad \mathbf{u}_{[2m]},$$

where $\mathbf{F}_{[2m\times n]}$ is the matrix composed of the analytically determined eigenfunctions for displacements in radial and tangential direction. $\mathbf{H}_{[n]}$ is the unknown vector of GSIFs. On the right hand side stands the vector $\mathbf{u}_{[2m]}$ of radial and tangential displacements calculated by means of FEM[3]. Since $2m > n$ the system is overdetermined as stated above and the unknown vector $\mathbf{H}_{[n]}$ is calculated as a least square solution. In principal, the GSIFs can be determined by taking both displacements and stresses from FEA. In such cases the matrix $\mathbf{F}_{[2m\times n]}$ has to contain the eigenfunctions for both displacements and stresses. However, the displacement results from displacement based FE system should be more accurate than stress results, which are in that case derived from displacement results. Therefore the ODM based on displacement results only is sometimes preferred. See p. 44.

An alternative method of choice to determine GSIFs is the two state path independent integral, also called Ψ-integral. The successful application of the Ψ-integral is conditioned by the knowledge of the so-called regular and auxiliary solutions of the above-mentioned eigenvalue problem, [39], following from the stress analysis of the notch

[3]Index m does not represent material number m, it is used due to lack of useful indices.

tip. By means of the Ψ-integral kth GSIF can be calculated as:

$$H_k = \frac{\Psi(u^{\mathrm{FE}}, r^{-\lambda_k} f^{-}_{ijk}(\theta))}{\Psi(r^{\lambda_k} f_{ijk}(\theta), r^{-\lambda_k} f^{-}_{ijk}(\theta))},$$

where u^{FE} is the FEM solution, $f_{ijk}(\theta)$ is the eigenfunction by ordinary analytical solution and $f^{-}_{ijk}(\theta)$ is the one given by auxiliary analytical solution. Both analytical solutions will be described via Muskhelishvili's formalism. If U and V are two elastic solutions, the Ψ-integral is defined as:

$$\Psi(U,V) = \frac{1}{2}\int_{\Gamma}(\sigma(U)nV - \sigma(V)nU)\mathrm{d}s,$$

where n is a normal pointing towards the origin [23]. Calculations of GSIFs based on the Ψ-integral method require extracting the FEM results along the path sufficiently far from the notch tip, where the FEM results are rather accurate (which is also the region where not only the singular terms of the stress expansion are dominant). See p. 38.

Criteria of crack initiation direction and stability criteria

A V-notch, bi-material notch and a crack in homogeneous material are all the singular stress concentrators. Thus we suppose that the mechanism of crack initiation in a V-notch or bi-material notch is the same as the mechanism of crack propagation in single material. The criteria of the direction of crack initiation at a V-notch or bi-material notch tip and the criteria of the stability of a V-notch or bi-material notch are derived in analogy to the approaches of a crack in homogeneous material. The criteria of the direction of crack initiation in these cases will be described in detail in sub-chapter 4.2 on p. 55. Note that the definition of the stability of notches means determination of conditions under which a crack initiates from the notch tip. Contrary to the case of a crack, in the case of a V-notch or bi-material notch, the stress singularity exponent changes as a step function during crack initiation. The stress singularity exponent of the initiated crack differs from the original exponent of a V-notch or bi-material notch. Moreover, in the case of a bi-material notch, each stress term in (14) represents an inherently combined loading mode (the function $f_{ijk}(\theta)$ contains both odd and even terms). Note that the dimension of generalized stress intensity factors is $[H_k] = \mathrm{MPa}\,\mathrm{m}^{p_k}$ and depends on p_k. All these facts lead to the conclusion that it is not possible to describe the behavior of a V-notch or bi-material notch by applying the standard (classic) approaches of the (crack) fracture mechanics. The general principle of stability assessment of a GSSC was introduced in [41]. The classic fracture mechanics approach of comparison of the stress intensity factor K_{I} with its critical value K_{Icrit} (12) is generalized to the following relation:

$$H_1(\sigma_{\mathrm{appl}}) < H_{1,\mathrm{crit}}(K_{\mathrm{Icrit}}). \tag{15}$$

The stability condition can be understood in the following way. A crack is not initiated at the notch tip if the value H_1 is lower than its critical value $H_{1,\mathrm{crit}}$. The value $H_1(\sigma_{\mathrm{appl}})$ follows from a numerical solution and depends mainly on the level of external loading and on the global geometry. Its critical value $H_{1,\mathrm{crit}}$ depends on the critical material characteristic K_{IC} or K_{Ith} and has to be deduced with the help of the controlling variable L, see [41]. The controlling variable L needs to have a clear and identical physical meaning in the case of assessing both a crack in homogeneous material and a V-notch or bi-material notch. With respect to particularities of a V-notch or bi-material notch following controlling variables L were chosen: (i) the mean value of the stress component $\sigma_{\theta\theta}$ and (ii) the mean value of the strain energy density factor Σ. These two have been found suitable controlling quantities to derive generalized multi-parameter fracture mechanics (see below) of V-notches or bi-material notches in the dissertation. The alternative approach is to use (iii) coupled stress-energy criterion by Leguillon [23], which states that both the energy and stress criteria are necessary conditions for fracture but neither one nor the other are sufficient. The fracture occurs when the two criteria are fulfilled simultaneously, together they form a sufficient one. With consideration of single real governing term of the stress series, the Leguillon criterion can be written[4]:

$$H_1 < \left(\frac{G_{\mathrm{C}}}{A(2\alpha,\theta_0)}\right)^{1-\lambda}\left(\frac{\sigma_{\mathrm{C}}}{f_{\theta\theta}(\theta_0)}\right)^{2\lambda-1},$$

where G_{C} is material toughness and σ_{C} is material strength. The coefficient $A(2\alpha,\theta_0)$ is a scaling term dependent on local geometry (2α) and the direction of crack initiation θ_0. Its determination is further commented in sub-chapter 4.2 on p. 59.

[4]Single real governing singularity term is assumed, which occurs for instance in the case for a symmetric loading [23].

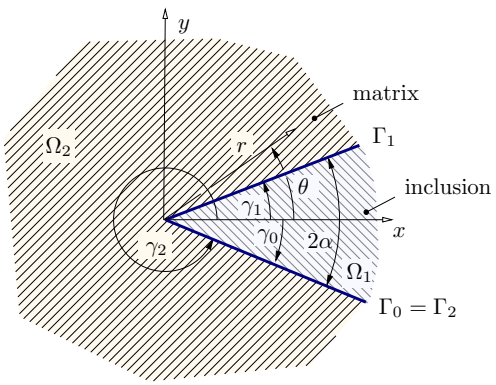

Figure 11: Bi-material junction as a model for a sharp material inclusion.

2.4. Fracture mechanics of sharp material inclusion

The literature review of the sharp material inclusion fracture mechanics revealed that only limited research had been focused on this field of interest. In the studies found, attention is mostly paid to the order of singularity determination of a sharp material inclusion model, a bi-material junction, which is the special case of a multi-material junction [42, 43]. Even fewer studies regarding stress series terms calculation have been found [44] and none that would describe crack initiation direction or a stability condition formulation. Establishing these will be in the main focus of the dissertation. The geometry of a bi-material junction as shown in Figure 11 is characterized by angles γ_0, γ_1 and γ_2. Analogically to the case of the sharp notch, complementary opening angle 2α is defined. The joint has two interfaces and no free surface. The material is considered as linear elastic and fully described by Young's moduli and Poisson's ratios in terms of elasticity. Perfect bonding is assumed at the interfaces. The material characteristics change by step at each interface. Displacements and tractions are assumed to be continuous. The solution mostly presupposes the approximation of plane strain or plane stress. In this dissertation, the bi-material junction tip is always presumed to be sharp. The stress distribution in the case of a bi-material junction is given by the asymptotic expansion [42]:

$$\sigma_{ij} = \frac{H_1}{\sqrt{2\pi}} r^{\lambda_1 - 1} f_{ij1}(\theta) + \frac{H_2}{\sqrt{2\pi}} r^{\lambda_2 - 1} f_{ij2}(\theta) + \frac{H_3}{\sqrt{2\pi}} r^{\lambda_3 - 1} f_{ij3}(\theta) + \ldots, \tag{16}$$

where the indices $(i, j) \equiv (r, \theta)$ are polar coordinates. The symbol H_k again stands for the GSIF. Please note that this expansion is identical to the one for a bi-material notch, just the exponents of the singularity are not denoted by symbol $p_k = 1 - \lambda_k$ anymore. Generally, the eigenvalue λ_k is a complex number. For λ_k satisfying $0 < \Re(\lambda_k) < 1$, the corresponding stress term is considered singular. For λ_k where $1 < \Re(\lambda_k)$ the corresponding stress term is considered non-singular. The dependence of the eigenvalues for the bi-material junction of given bi-material combination on opening angle 2α has been calculated for one particular bi-material configuration in Numerical example A. It is shown in a Figure 63 shows on p. 63.

Determination of the stress terms order

We consider that the interface between materials is perfectly bonded (ideal adhesion). The eigenvalues are gained from a numerical solution to the characteristic equation depending on the geometry and material properties of a bi-material junction [42, 43, 44]. Similar to the case of a V-notch or bi-material notch, an effective tool to describe problems of isotropic plane elasticity is the Muskhelishvili's complex potential theory [5, 43]. The characteristic equation originates from equations enforcing stress and displacement continuity at the ith interface Γ_i. The stress exponents of singular and higher order (non-singular) terms will be determined within the dissertation from a set of the boundary conditions corresponding to a particular problem as shown in detail in sub-section 4.3 on p. 70.

Determination of the stress intensity factors of particular stress terms

As in the case of a V-notch and bi-material notch the overdeterministic method [36] is an appropriate method to be used for stress terms determination. An alternative method of stress terms determination for the case of a V-notch or bi-material notch, the path independent Ψ-integral can also be applied to the case of a bi-material junction. We previously assumed that this integral method cannot be applied, because of the non existing free

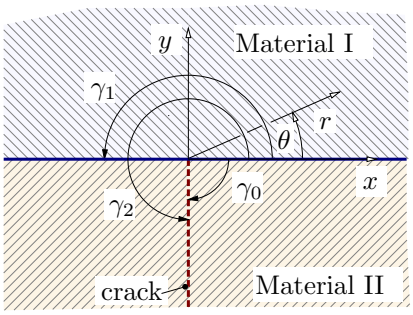

Figure 12: Crack terminating at the inclusion/matrix interface.

surfaces. However by prof. Leguillon it has been shown that it can indeed be applied as it will be explained later in the text. Nevertheless, to author's best knowledge, these two methods for GSIFs determination has been applied to V-notches or bi-material notches only. Its application to multi-material junctions will be a subject of the dissertation. A method of stress intensity factor determination based on the quantity of Π was proposed in [44], but this method does not give reliable results when all of the eigenvalues are small. See details on p. 75 for the Ψ-integral and p. 82 for the ODM.

Criteria of crack initiation direction and stability criteria

A sharp material inclusion is regarded as a singular stress concentrator, which is represented by a model of a bi-material junction. As in the case of a V-notch or bi-material notch the criteria of the direction of crack initiation near the bi-material junction tip and the criteria of the stability of bi-material junctions are derived in analogy to the approaches of a crack in homogeneous material. Again, the mechanism of crack initiation from the bi-material junction tip is presumed to be identical to the mechanism of crack propagation in single homogeneous material. The stability condition of a bi-material junction suggests the condition when the crack is initiated from the bi-material junction tip. Analogical to the case of a V-notch or bi-material notch, the stress singularity exponent changes as the step function during crack initiation. The stress singularity exponent of the initiated crack differs from the original exponent of a bi-material junction. Since an inherently combined loading mode is observed in majority of cases it is generally speaking not possible to separate the modes from each other (possible only in e.g. the symmetrically loaded symmetrical bi-material junction). Moreover, the dimension of generalized stress intensity factors is $[H_k] = \text{MPa} \cdot \text{m}^{\lambda_k - 1}$and depends on $\lambda_k - 1$. The discussion above indicates that the classic approaches of LEFM cannot be applied directly and have to be modified. The stability assessment of a GSSC as it is defined in (15) for notches can be utilized for the case of a bi-material junction. Then the controlling quantity L regarding the identical physical meaning for a crack in homogeneous material and a bi-material junction has to be chosen, approaches (i) or (ii). Similarly as in the case of a V-notch and bi-material notch, coupled stress-energy criterion can be used to assess the stability of a bi-material junction, (iii). Note that this model will contribute to a complete description of fracture behavior near the sharp material inclusion (see Figures 83-86 on p. 96). The following four models can be utilized:

- interfacial crack
- crack with its tip at a bi-material interface (see Figure 12)
- bi-material notch
- bi-material junction

The former two are described in literature, while the latter two are not described sufficiently and will be a part of the dissertation. See also the chapter 4: Methods on p. 24.

2.5. Limitations of single-parameter fracture mechanics

The area near the crack in which the stress field is precisely described only by a singular term is known as the K-dominated region (in the case of fracture mechanics of cracks). A similar region can be found near the notch tip or the bi-material junction tip, and it is again a region where the singular stress terms dominate as illustrated in

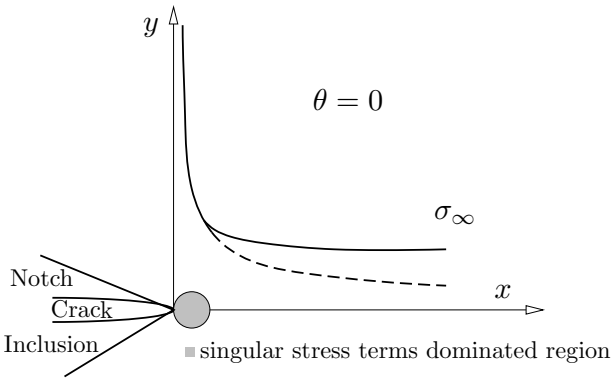

Figure 13: Region of domination of singular terms ahead of a crack and a notch or an inclusion, where stress is precisely described by singular terms only. Dashed line describes the singular terms solution.

Figure 13. This region with dominating singular terms is one of the building blocks of classic fracture mechanics. However, some criteria based on the parameter of a specific distance from the singular stress concentrator tip require sufficiently precise knowledge of stresses further away from the notch tip. In fact, this means that a description only by a singular term may not be sufficient to describe stresses precisely enough and therefore to assess reliably the stability of a dangerous point. Single-parameter fracture mechanics is not sufficient in the case of assessment of crack initiation and propagation in silicate-based composites. In these quasi-brittle materials a fracture process zone ahead of a crack has a larger size (in the order of millimeters) than a plastic zone occurring in the case of metallic materials (typically from micrometers to 1 mm). For this reason, stress distribution must be described reliably in a larger area ahead of the stress concentrator by singular and non-singular terms.

Another question arises in the case of a free-edge singularity, which can be modeled as the bi-material notch with the opening angle $2\alpha = 180°$ and as illustrated in Figure 14. This geometrical configuration leads to the existence of one singular term. When considering only singular stress terms, the crack initiation direction θ_0 resulting from generalized fracture mechanics assessment depends on the ratio H_2/H_1, see [32]. Thus for the existence of only one singular term, the crack initiation angle is independent of the direction of external loading. This fact should not correspond to reality. Further (non-singular) terms are a promising tool to cover the influence of the direction of external loading in this case.

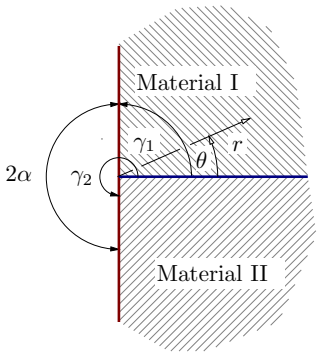

Figure 14: Free edge singularity, where $2\alpha = 180°$. The angles $\gamma_1 = 90°$ and $\gamma_2 = 180°$.

2.6. Multi-parameter fracture mechanics

Multi-parameter fracture mechanics of a crack (T-stress)

In 1952 Williams described the stress field around the notch tip for linear elastic materials as a set of infinite series expansions [8]. If the notch angle becomes zero, i.e. $2\alpha = 0°$, the notch turns into a sharp crack as shown in Figure 15. The Cartesian coordinate system form of the equations for a crack in mode I loading is given by:

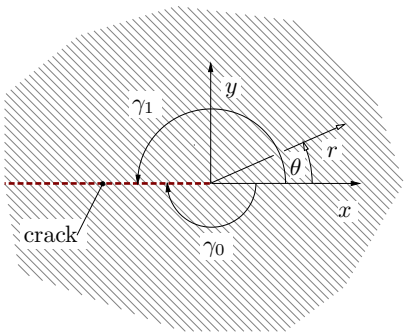

Figure 15: Crack in homogeneous material.

$$\begin{aligned}
\sigma_{xx} &= \frac{K_{\mathrm{I}}}{\sqrt{2\pi r}} \cos\frac{\theta}{2}\left(1 - \sin\frac{\theta}{2}\sin\frac{3\theta}{2}\right) + T + O\left(r^{1/2}\right) + \ldots, \\
\sigma_{yy} &= \frac{K_{\mathrm{I}}}{\sqrt{2\pi r}} \cos\frac{\theta}{2}\left(1 + \sin\frac{\theta}{2}\sin\frac{3\theta}{2}\right) + O\left(r^{1/2}\right) + \ldots, \\
\sigma_{xy} &= \frac{K_{\mathrm{I}}}{\sqrt{2\pi r}} \cos\frac{\theta}{2}\sin\frac{\theta}{2}\cos\frac{3\theta}{2} + O\left(r^{1/2}\right) + \ldots.
\end{aligned}$$

The first term in each stress component expansion for which $n = 1$, is singular while the higher order terms are non-singular. The second term of Williams's solution for which $n = 2$, often called T-stress, is a constant term independent of the distance from the crack tip. The previous studies on the fracture assessment of cracked bodies have shown that in addition to the singular term, T-stress may significantly affect the process of crack growth. For example, Larsson and Carlsson in [45] investigated the effect of T-stress on the size and shape of the plastic zone in Mode I loading. Similarly, Bétegon and Hancock in [46]. Ayatollahi et al. in [47] also showed T-stress could influence the initiation of brittle fracture. Furthermore, it has been shown that in loading Mode I T-stress is an important parameter for the stability analysis of the fracture trajectory (Cotterell and Rice, [48]). They suggested that for positive values of T-stress, the fracture trajectory gradually deviates from the line of the initial crack. In contrast, specimens with negative T-stress exhibit a stable fracture path. Calculations of non-singular terms were performed using various methods [49, 50, 51].

Multi-parameter fracture mechanics of V-notches and bi-material notches

The effects of non-singular terms on the behavior of cracks have been assessed by many researchers. Despite this, almost no results have been reported concerning the role of non-singular terms in the stress distribution description around GSSCs such as V-notches or bi-material notches. The only notable works are related to Kim et al. and Ayatollahi et al. In [52] Kim et al. studied the effect of the first non-singular term of Mode I on the size and shape of the plastic zone around a V-notch. Ayatollahi et al. [27, 53] studied the influence of the presence of generalized T-stress (so called I-stress) on stress distribution in the case of a V-notch. In [54] Ayatollahi used the photoelasticity method to determine the higher order stress terms in bi-material notches. Further, they used the overdeterministic method for calculating the generalized stress intensity factors and the coefficients of the higher order terms for structures containing V-notches [36] and presented the first studies of evaluation of the eigenvalues of the first non-singular term for bi-material notches [55].

Multi-parameter fracture mechanics of a sharp material inclusion

Multi-parameter fracture mechanics of a bi-material junction is not available in literature (according to our knowledge). However, methods describing the behavior of GSSCs near the sharp material inclusion are required for a reliable description of their fracture behavior. Multi-parameter fracture mechanics is indispensable in the case of assessment of crack initiation and propagation in silicate-based composites. In this case the fracture process zone ahead of a crack has a larger size than a plastic zone occurring in the case of metallic materials. For this reason, stress distribution must be described reliably in a larger area ahead of the stress concentrator. Multi-parameter approaches provide a simple way to ensure this.

Summary of the state of the art

This review briefly describes current trends in extension of the classic linear elastic fracture mechanics to general singular stress concentrators. Possible approaches of stress term order determination are discussed with the main attention focused on the Muskhelishvili's complex variable function methods and all of its benefits. In terms of the non-singular terms in the case of a V-notch and bi-material notch this short literature review seems to be rather complete. The above-mentioned papers deal with initial studies of this field of problems, but they cover only a small group of geometrical and material configurations of the concentrators. However, for the case of a bi-material junction in comparison to bi-material notches a noticeably smaller amount of research has been performed. A very limited number of studies has been concerned with the singular stress terms determination and none has been published regarding the effect of the first non-singular term on the fracture behavior of a bi-material junction. Further, there is no study dealing with the stability criteria or the criteria of crack initiation direction or dealing with it comprehensively both from the theoretical and numerical point of view. Finally, there are no studies or papers (as far as we know) concerning the effect of higher order terms on the fracture behavior of bi-material junctions (or sharp polygon-like inclusions in general). The works [27, 36, 52, 53, 54, 55] published in 2009-2011 prove the topicality of the problem. Further it demonstrates that additional research of the problem will lead to innovative and up-to-date results contributing to higher credibility of fracture mechanics of general singular stress concentrators.

3. Aims of the thesis

On the basis of the literature survey, the aims of the research conducted within the PhD study were proposed as:

(i) formulation of multi-parameter fracture mechanics approaches for a V-notch or bi-material notch

a. determination and study of stress exponents of singular and non-singular terms

b. modification of methods for calculation of stress terms factors

c. derivation of multi-parameter criteria for crack initiation direction

d. derivation of multi-parameter criteria of stability

(ii) formulation of multi-parameter fracture mechanics approaches to a bi-material junction

a. determination and study of stress exponents of singular and non-singular terms

b. modification of methods for calculation of stress terms factors

c. derivation of multi-parameter criteria for crack initiation direction

d. derivation of multi-parameter criteria of stability

(iii) developing a complete description of crack initiation and propagation near a sharp inclusion

The generalized stability criteria determining the crack initiation conditions will contribute to overall assessment of V-notches, bi-material notches and bi-material junctions. The influence of the subsumption of the non-singular terms in analytical-numerical assessment will be described both qualitatively and quantitatively. The research is motivated by the attempt to enhance the safety of constructions or parts made of composite materials. The application of the results of the research in structural design will lead to better utilization of material volume and thus e.g. to weight reduction of components.

4. Methods and results

4.1. Fundamental equations to describe general singular stress concentrators

In general, there are three different methods to analyze stress singularities in terms of the asymptotic analysis, namely the eigenvalue expansion method, the Mellin transform technique and the complex function representation. The application of the eigenvalue expansion method was studied by Williams on reentrant corners in plates in extension [8] and on crack problems in [9]. Mellin transform technique was applied on some problems by Hein and Erdogan in [10] and by Pageau et al. in [42]. All three approaches were clearly summarized by Paggi and Carpinteri in [43]. This dissertation deals from now on with the complex function representation method. Please recall the Kolosov-Muskhelishvili's equations (8) for plane elasticity on p. 11. We assume functions $\Omega_{km}(z)$ and $\omega_{km}(z)$ of complex variable z in the form of:

$$\begin{aligned} \Omega_{km}(z) &= I_{km} z^{\lambda_k} + L_{km} z^{\bar{\lambda}_k}, \\ \omega_{km}(z) &= M_{km} z^{\lambda_k} + N_{km} z^{\bar{\lambda}_k}. \end{aligned} \tag{17}$$

where the I_{km}, L_{km}, M_{km} and N_{km} are unknown complex constants. The subscript k denotes that the particular constant that belongs to kth eigenvalue λ_k. The m defines quantities referred to the material sector m. These complex functions (17) are substituted into the Kolosov-Muskhelishvili equations for particular stress and displacement component, Eq. (9) on p. 11. The first and second derivative of the functions (17) and their complex conjugates are found in Appendix A.1 on p. 105 as well as the detailed derivation of following expressions for stress (18) and displacement components (19) written below:

$$\begin{aligned} \sigma_{rrkm}(r,\theta) &= \frac{1}{2}\{r^{\lambda_k-1}\left[-I_{km}\lambda_k(\lambda_k-3)e^{i\theta(\lambda_k-1)} - \bar{L}_{km}\lambda_k(\lambda_k-3)e^{-i\theta(\lambda_k-1)} - M_{km}\lambda_k e^{i\theta(\lambda_k+1)} - \bar{N}_{km}\lambda_k e^{-i\theta(\lambda_k+1)}\right] + \\ &+ r^{\bar{\lambda}_k-1}\left[-\bar{I}_{km}\bar{\lambda}_k\left(\bar{\lambda}_k-3\right)e^{-i\theta\left(\bar{\lambda}_k-1\right)} - L_{km}\bar{\lambda}_k\left(\bar{\lambda}_k-3\right)e^{i\theta\left(\bar{\lambda}_k-1\right)} - \bar{M}_{km}\bar{\lambda}_k e^{-i\theta\left(\bar{\lambda}_k+1\right)} - N_{km}\bar{\lambda}_k e^{i\theta(\lambda_k+1)}\right]\}, \end{aligned} \tag{18}$$

$$\begin{aligned} \sigma_{r\theta km}(r,\theta) &= \frac{1}{2i}\{r^{\lambda_k-1}\left[I_{km}\lambda_k(\lambda_k-1)e^{i\theta(\lambda_k-1)} - \bar{L}_{km}\lambda_k(\lambda_k-1)e^{-i\theta(\lambda_k-1)} + M_{km}\lambda_k e^{i\theta(\lambda_k+1)} - \bar{N}_{km}\lambda_k e^{-i\theta(\lambda_k+1)}\right] + \\ &+ r^{\bar{\lambda}_k-1}\left[-\bar{I}_{km}\bar{\lambda}_k\left(\bar{\lambda}_k-1\right)e^{-i\theta\left(\bar{\lambda}_k-1\right)} + L_{km}\bar{\lambda}_k\left(\bar{\lambda}_k-1\right)e^{i\theta\left(\bar{\lambda}_k-1\right)} - \bar{M}_{km}\bar{\lambda}_k e^{-i\theta\left(\bar{\lambda}_k+1\right)} + N_{km}\bar{\lambda}_k e^{i\theta\left(\bar{\lambda}_k+1\right)}\right]\}, \end{aligned}$$

$$\begin{aligned} \sigma_{\theta\theta km}(r,\theta) &= \frac{1}{2}\{r^{\lambda_k-1}\left[I_{km}\lambda_k(\lambda_k+1)e^{i\theta(\lambda_k-1)} + \bar{L}_{km}\lambda_k(\lambda_k+1)e^{-i\theta(\lambda_k-1)} + M_{km}\lambda_k e^{i\theta(\lambda_k+1)} + \bar{N}_{km}\lambda_k e^{-i\theta(\lambda_k+1)}\right] + \\ &+ r^{\bar{\lambda}_k-1}\left[\bar{I}_{km}\bar{\lambda}_k\left(\bar{\lambda}_k+1\right)e^{-i\theta\left(\bar{\lambda}_k-1\right)} + L_{km}\bar{\lambda}_k\left(\bar{\lambda}_k+1\right)e^{i\theta\left(\bar{\lambda}_k-1\right)} + \bar{M}_{km}\bar{\lambda}_k e^{-i\theta\left(\bar{\lambda}_k+1\right)} + N_{km}\bar{\lambda}_k e^{i\theta(\lambda_k+1)}\right]\}, \end{aligned}$$

$$\begin{aligned} u_{rkm}(r,\theta) &= \frac{1}{4\mu_m}\{r^{\lambda_k}\left[I_{km}(\kappa_m-\lambda_k)e^{i\theta(\lambda_k-1)} + \bar{L}_{km}(\kappa_m-\lambda_k)e^{-i\theta(\lambda_k-1)} - M_{km}e^{i\theta(\lambda_k+1)} - \bar{N}_{km}e^{-i\theta(\lambda_k+1)}\right] + \\ &+ r^{\bar{\lambda}_k}\left[\bar{I}_{km}\left(\kappa_m-\bar{\lambda}_k\right)e^{-i\theta\left(\bar{\lambda}_k-1\right)} + L_{km}(\kappa_m-\lambda_k)e^{i\theta(\lambda_k-1)} - \bar{M}_{km}e^{-i\theta(\lambda_k+1)} - N_{km}e^{i\theta(\lambda_k+1)}\right]\}, \end{aligned} \tag{19}$$

$$\begin{aligned} u_{\theta km}(r,\theta) &= \frac{1}{4i\mu_m}\{r^{\lambda_k}\left[I_{km}(\kappa_m+\lambda_k)e^{i\theta(\lambda_k-1)} - \bar{L}_{km}(\kappa_m+\lambda_k)e^{-i\theta(\lambda_k-1)} + M_{km}e^{i\theta(\lambda_k+1)} - \bar{N}_{km}e^{-i\theta(\lambda_k+1)}\right] + \\ &+ r^{\bar{\lambda}_k}\left[-\bar{I}_{km}\left(\kappa_m+\bar{\lambda}_k\right)e^{-i\theta\left(\bar{\lambda}_k-1\right)} + L_{km}\left(\kappa_m+\bar{\lambda}_k\right)e^{i\theta\left(\bar{\lambda}_k-1\right)} - \bar{M}_{km}e^{-i\theta\left(\bar{\lambda}_k+1\right)} + N_{km}e^{i\theta\left(\bar{\lambda}_k+1\right)}\right]\} \end{aligned}$$

Let's write down the most general, complex form of Williams's expansion describing stresses near a GSSC:

$$\sigma_{ij}(r,\theta) = \sum_{k=1}^{\infty}\left\{H_k r^{\lambda_k-1} f_{ijk}(\theta) + \bar{H}_k r^{\bar{\lambda}_k-1}\bar{f}_{ijk}(\theta)\right\}. \tag{20}$$

By using the superposition principle we consider the equation which consists of kth quantities (18) as an individual kth contribution to the actual stress field near the concentrator. This contribution is represented as a kth term of

the stress series (which contains kth eigenvalue, eigenfunction and GSIF). A V-notch consists of one material only, therefore the index m is omitted. For the case of a bi-material notch or a bi-material junction $m = 1, 2$. Please note that in this series we intentionally do not factor out the constant $1/\sqrt{2\pi}$ in contrast to form of the series of a bi-material notch as written in Eq. (14) on p. 15 or the series of a bi-material junction Eq. (16) on p. 18. We found the upper form of the series more convenient to work with. The conversion of GSIFs calculated in this work to form used sometimes in literature (the terms with out-factored constant $1/\sqrt{2\pi}$) is easy. It just requires division of individual H_k by $\sqrt{2\pi}$. In the case of a bi-material notch we define the angular eigenfunction and its complex conjugate for stress expansion in terms of material regions as:

$$f_{ijk}(\theta) = \begin{cases} f_{ijk1}(\theta) & \gamma_1 < \theta < \gamma_2 \\ f_{ijk2}(\theta) & \gamma_2 < \theta < \gamma_3 \end{cases}, \tag{21}$$

$$\bar{f}_{ijk}(\theta) = \begin{cases} \bar{f}_{ijk1}(\theta) & \gamma_1 < \theta < \gamma_2 \\ \bar{f}_{ijk2}(\theta) & \gamma_2 < \theta < \gamma_3 \end{cases},$$

where the angles γ_1, γ_2 and γ_3 are described in Figure 10 on p. 16. The case of a bi-material junction, the eigenfunction and its complex conjugate are defined:

$$f_{ijk}(\theta) = \begin{cases} f_{ijk1}(\theta) & \gamma_0 < \theta < \gamma_1 \\ f_{ijk2}(\theta) & \gamma_1 < \theta < \gamma_2 \end{cases}, \tag{22}$$

$$\bar{f}_{ijk}(\theta) = \begin{cases} \bar{f}_{ijk1}(\theta) & \gamma_0 < \theta < \gamma_1 \\ \bar{f}_{ijk2}(\theta) & \gamma_1 < \theta < \gamma_2 \end{cases}$$

and the angles γ_0, γ_1 and γ_2 are described in Figure 11 on p. 18. By comparison of expansion (20) with equations (18) and (21) or (22) we define eigenfunctions $f_{ijkm}(\theta)$ and $\bar{f}_{ijkm}(\theta)$ in terms of complex constants I_{km}, L_{km}, M_{km} and N_{km} as:

$$\begin{aligned}
f_{rrkm}(\theta) &= \frac{1}{2}\left[-I_{km}\lambda_k(\lambda_k-3)e^{i\theta(\lambda_k-1)} - \bar{L}_{km}\lambda_k(\lambda_k-3)e^{-i\theta(\lambda_k-1)} - M_{km}\lambda_k e^{i\theta(\lambda_k+1)} - \bar{N}_{km}\lambda_k e^{-i\theta(\lambda_k+1)}\right] \\
\bar{f}_{rrkm}(\theta) &= \frac{1}{2}\left[-\bar{I}_{km}\bar{\lambda}_k\left(\bar{\lambda}_k-3\right)e^{-i\theta\left(\bar{\lambda}_k-1\right)} - L_{km}\bar{\lambda}_k\left(\bar{\lambda}_k-3\right)e^{i\theta\left(\bar{\lambda}_k-1\right)} - \bar{M}_{km}\bar{\lambda}_k e^{-i\theta\left(\bar{\lambda}_k+1\right)} - N_{km}\bar{\lambda}_k e^{i\theta\left(\bar{\lambda}_k+1\right)}\right], \\
f_{r\theta km}(\theta) &= \frac{1}{2i}\left[I_{km}\lambda_k(\lambda_k-1)e^{i\theta(\lambda_k-1)} - \bar{L}_{km}\lambda_k(\lambda_k-1)e^{-i\theta(\lambda_k-1)} + M_{km}\lambda_k e^{i\theta(\lambda_k+1)} - \bar{N}_{km}\lambda_k e^{-i\theta(\lambda_k+1)}\right], \\
\bar{f}_{r\theta km}(\theta) &= \frac{1}{2i}\left[-\bar{I}_{km}\bar{\lambda}_k\left(\bar{\lambda}_k-1\right)e^{-i\theta\left(\bar{\lambda}_k-1\right)} + L_{km}\bar{\lambda}_k\left(\bar{\lambda}_k-1\right)e^{i\theta\left(\bar{\lambda}_k-1\right)} - \bar{M}_{km}\bar{\lambda}_k e^{-i\theta\left(\bar{\lambda}_k+1\right)} + N_{km}\bar{\lambda}_k e^{i\theta\left(\bar{\lambda}_k+1\right)}\right], \\
f_{\theta\theta km}(\theta) &= \frac{1}{2}\left[I_{km}\lambda_k(\lambda_k+1)e^{i\theta(\lambda_k-1)} + \bar{L}_{km}\lambda_k(\lambda_k+1)e^{-i\theta(\lambda_k-1)} + M_{km}\lambda_k e^{i\theta(\lambda_k+1)} + \bar{N}_{km}\lambda_k e^{-i\theta(\lambda_k+1)}\right], \\
\bar{f}_{\theta\theta km}(\theta) &= \frac{1}{2}\left[\bar{I}_{km}\bar{\lambda}_k\left(\bar{\lambda}_k+1\right)e^{-i\theta\left(\bar{\lambda}_k-1\right)} + L_{km}\bar{\lambda}_k\left(\bar{\lambda}_k+1\right)e^{i\theta\left(\bar{\lambda}_k-1\right)} + \bar{M}_{km}\bar{\lambda}_k e^{-i\theta\left(\bar{\lambda}_k+1\right)} + N_{km}\bar{\lambda}_k e^{i\theta\left(\bar{\lambda}_k+1\right)}\right].
\end{aligned} \tag{23}$$

Similarly the most general complex form of expansion describing displacement field a GSSC is:

$$u_i(r,\theta) = \sum_{k=1}^{\infty}\left\{H_k r^{\lambda_k} f_{ik}(\theta) + \bar{H}_k r^{\bar{\lambda}_k}\bar{f}_{ik}(\theta)\right\}. \tag{24}$$

Again, a V-notch consists of one material only, therefore the index m is omitted, while for the case of a bi-material notch or a bi-material junction we have $m = 1, 2$. Thus for a bi-material notch we define the angular eigenfunction and its complex conjugate for displacement expansion in terms of material regions as:

$$f_{ik}(\theta) = \begin{cases} f_{ik1}(\theta) & \gamma_1 < \theta < \gamma_2 \\ f_{ik2}(\theta) & \gamma_2 < \theta < \gamma_3 \end{cases}, \tag{25}$$

$$\bar{f}_{ik}(\theta) = \begin{cases} \bar{f}_{ik1}(\theta) & \gamma_1 < \theta < \gamma_2 \\ \bar{f}_{ik2}(\theta) & \gamma_2 < \theta < \gamma_3 \end{cases},$$

where the distinct material regions are illustrated in Figure 10. For the case of a bi-material junction we write the eigenfunction and its complex conjugate as follows:

$$f_{ik}(\theta) = \begin{cases} f_{ik1}(\theta) & \gamma_0 < \theta < \gamma_1 \\ f_{ik2}(\theta) & \gamma_1 < \theta < \gamma_2 \end{cases}, \tag{26}$$

$$\bar{f}_{ik}(\theta) = \begin{cases} \bar{f}_{ik1}(\theta) & \gamma_0 < \theta < \gamma_1 \\ \bar{f}_{ik2}(\theta) & \gamma_1 < \theta < \gamma_2 \end{cases}.$$

For the description of angles γ_0, γ_1 and γ_2 see Figure 11. Finally by using the superposition principle and by comparison of expansion (24) with (19) and (25) or (26) we define the eigenfunction $f_{ikm}(\theta)$ and its complex conjugate $\bar{f}_{ikm}(\theta)$ in terms of complex constants as:

$$\begin{aligned}
f_{rkm}(\theta) &= \frac{1}{4\mu_m}\left[I_{km}(\kappa_m - \lambda_k)e^{i\theta(\lambda_k-1)} + \bar{L}_{km}(\kappa_m - \lambda_k)e^{-i\theta(\lambda_k-1)} - M_{km}e^{i\theta(\lambda_k+1)} - \bar{N}_{km}e^{-i\theta(\lambda_k+1)}\right], \quad (27)\\
\bar{f}_{rkm}(\theta) &= \frac{1}{4\mu_m}\left[\bar{I}_{km}\left(\kappa_m - \bar{\lambda}_k\right)e^{-i\theta\left(\bar{\lambda}_k-1\right)} + L_{km}\left(\kappa_m - \bar{\lambda}_k\right)e^{i\theta\left(\bar{\lambda}_k-1\right)} - \bar{M}_{km}e^{-i\theta\left(\bar{\lambda}_k+1\right)} - N_{km}e^{i\theta\left(\bar{\lambda}_k+1\right)}\right],\\
f_{\theta km}(\theta) &= \frac{1}{4i\mu_m}\left[I_{km}(\kappa_m + \lambda_k)e^{i\theta(\lambda_k-1)} - \bar{L}_{km}(\kappa_m + \lambda_k)e^{-i\theta(\lambda_k-1)} + M_{km}e^{i\theta(\lambda_k+1)} - \bar{N}_{km}e^{-i\theta(\lambda_k+1)}\right],\\
\bar{f}_{\theta km}(\theta) &= \frac{1}{4i\mu_m}\left[-\bar{I}_{km}\left(\kappa_m + \bar{\lambda}_k\right)e^{-i\theta\left(\bar{\lambda}_k-1\right)} + L_{km}\left(\kappa_m + \bar{\lambda}_k\right)e^{i\theta\left(\bar{\lambda}_k-1\right)} - \bar{M}_{km}e^{-i\theta\left(\bar{\lambda}_k+1\right)} + N_{km}e^{i\theta\left(\bar{\lambda}_k+1\right)}\right].
\end{aligned}$$

In sake of completeness, let's write down the real form of the stress series, i.e. for $\lambda_k \in \mathbb{R}$ and $H_k \in \mathbb{R}$:

$$\sigma_{ij} = \sum_{k=1}^{\infty} H_k r^{\lambda_k - 1} f^*_{ijk}(\theta), \tag{28}$$

where the stress eigenfunction $f^*_{ijk}(\theta)$ is for different material regions $m = 1, 2$ of a bi-material notch defined as:

$$f^*_{ijk}(\theta) = \begin{cases} f^*_{ijk1}(\theta) & \gamma_1 < \theta < \gamma_2 \\ f^*_{ijk2}(\theta) & \gamma_2 < \theta < \gamma_3 \end{cases},$$

while for the case of a bi-material junction we have:

$$f^*_{ijk}(\theta) = \begin{cases} f^*_{ijk1}(\theta) & \gamma_0 < \theta < \gamma_1 \\ f^*_{ijk2}(\theta) & \gamma_1 < \theta < \gamma_2 \end{cases}.$$

The stress eigenfunction $f^*_{ijkm}(\theta)$ is defined:

$$\begin{aligned}
f^*_{rrkm}(\theta) &= f_{rrkm}(\theta) + \bar{f}_{rrkm}(\theta), \quad (29)\\
f^*_{r\theta km}(\theta) &= f_{r\theta km}(\theta) + \bar{f}_{r\theta km}(\theta),\\
f^*_{\theta\theta km}(\theta) &= f_{\theta\theta km}(\theta) + \bar{f}_{\theta\theta km}(\theta),
\end{aligned}$$

where eigenfunction $f_{ijkm}(\theta)$ and its complex conjugate $\bar{f}_{ijkm}(\theta)$ are found in set of equations (23). For a V-notch the same equations apply, only the index m is omitted. Similarly the real form of the displacement series, i.e. for $\lambda_k \in \mathbb{R}$ and $H_k \in \mathbb{R}$ is:

$$u_i = \sum_{k=1}^{\infty} H_k r^{\lambda_k} f^*_{ik}(\theta), \tag{30}$$

where again the displacement eigenfunction $f^*_{ik}(\theta)$ is for different material regions $m = 1, 2$ of a bi-material notch defined as:

$$f^*_{ik}(\theta) = \begin{cases} f^*_{ij1}(\theta) & \gamma_1 < \theta < \gamma_2 \\ f^*_{ij2}(\theta) & \gamma_2 < \theta < \gamma_3 \end{cases},$$

and similarly for the case of a bi-material junction we have:

$$f^*_{ik}(\theta) = \begin{cases} f^*_{ij1}(\theta) & \gamma_0 < \theta < \gamma_1 \\ f^*_{ij2}(\theta) & \gamma_1 < \theta < \gamma_2 \end{cases}.$$

Finally the displacement eigenfunctions $f^*_{ikm}(\theta)$ are defined:

$$\begin{aligned} f^*_{rkm}(\theta) &= f_{rkm}(\theta) + \bar{f}_{rkm}(\theta), \\ f^*_{\theta km}(\theta) &= f_{\theta km}(\theta) + \bar{f}_{\theta km}(\theta), \end{aligned}$$

where eigenfunction $f_{ikm}(\theta)$ and its complex conjugate $\bar{f}_{ikm}(\theta)$ are found in the set of equations (27).

4.2. Formulation of multi-parameter fracture mechanics approaches for V-notch and bi-material notch

It follows from the literature survey that the fracture mechanics behavior of V-notches and bi-material notches is well known considering singular stress terms. Non-singular terms are rarely considered, the mentioned publications [36, 52, 53, 54, 55] cover only a small group of geometrical and material configurations of the singular stress concentrators. Further, there is no study dealing with the stability criteria or the criteria of crack initiation direction or dealing with it comprehensively both from the theoretical and numerical point of view. Within the dissertation it is necessary to determine stress terms exponents, calculate factors of particular stress terms, derive the criteria for crack initiation direction and the criteria of stability.

Stress terms exponents determination and study

The exponents of series terms depend only on local boundary conditions, i.e. are independent of the applied loading and global geometry. The stress exponents of higher order (non-singular) terms will be determined within the dissertation from a set of the boundary conditions corresponding to a particular problem [32, 42, 43]. The boundary conditions of the V-notch are:

$$\begin{aligned} \sigma_{\theta\theta k}(r, \gamma_1) &= 0 \\ \sigma_{r\theta k}(r, \gamma_1) &= 0 \\ \sigma_{\theta\theta k}(r, \gamma_2) &= 0 \\ \sigma_{r\theta k}(r, \gamma_2) &= 0 \end{aligned} \tag{31}$$

for $\forall k$, where the angles γ_1 and γ_2 defines position of the notch faces and are depicted in Figure 9 on p. 15. Specifically the equations above enforce zero traction at both free surfaces of the notch. Similarly, the boundary conditions for the bi-material notch are:

$$\begin{aligned} \sigma_{\theta\theta k1}(r, \gamma_1) &= 0 \\ \sigma_{r\theta k1}(r, \gamma_1) &= 0 \\ u_{\theta k1}(r, \gamma_2) &= u_{\theta k2}(r, \gamma_2) \\ u_{rk1}(r, \gamma_2) &= u_{rk2}(r, \gamma_2) \\ \sigma_{\theta\theta k1}(r, \gamma_2) &= \sigma_{\theta\theta k2}(r, \gamma_2) \\ \sigma_{r\theta k1}(r, \gamma_2) &= \sigma_{r\theta k2}(r, \gamma_2) \\ \sigma_{\theta\theta k2}(r, \gamma_3) &= 0 \\ \sigma_{r\theta k2}(r, \gamma_3) &= 0 \end{aligned} \tag{32}$$

for $\forall k$, with the geometry described in Figure 10 on p. 16. The equations above enforce zero traction on the notch faces, i.e. locations $\theta = \gamma_1$ and $\theta = \gamma_3$. In addition, traction and displacement continuity is enforced at the interface Γ i.e. where $\theta = \gamma_2$. System of equations is formed based on the boundary conditions of the problem for the V-notch (31) or bi-material notch (32) by substituting Eq. (19) and (18) on p. 24. Such a system contains 4 equations for the V-notch problem and 8 equations for the bi-material notch. The complex constants M_{km}, $\bar{N}_{km}$, I_{km} and $\bar{L}_{km}$ are then factored out and the system of equations can be written in the matrix form. For the simpler case, the V-notch, the system is written as:

$$\begin{bmatrix} \frac{\lambda_k e^{i\gamma_1(\lambda_k+1)}}{2} & \frac{\lambda_k e^{-i\gamma_1(\lambda_k+1)}}{2} & \frac{\lambda_k(\lambda_k+1)e^{i\gamma_1(\lambda_k-1)}}{2} & \frac{\lambda_k(\lambda_k+1)e^{-i\gamma_1(\lambda_k-1)}}{2} \\ \frac{\lambda_k e^{i\gamma_1(\lambda_k+1)}}{2i} & -\frac{\lambda_k e^{-i\gamma_1(\lambda_k+1)}}{2i} & \frac{\lambda_k(\lambda_k-1)e^{i\gamma_1(\lambda_k-1)}}{2i} & -\frac{\lambda_k(\lambda_k-1)e^{-i\gamma_1(\lambda_k-1)}}{2i} \\ \frac{\lambda_k e^{i\gamma_2(\lambda_k+1)}}{2} & \frac{\lambda_k e^{-i\gamma_2(\lambda_k+1)}}{2} & \frac{\lambda_k(\lambda_k+1)e^{i\gamma_2(\lambda_k-1)}}{2} & \frac{\lambda_k(\lambda_k+1)e^{-i\gamma_2(\lambda_k-1)}}{2} \\ \frac{\lambda_k e^{i\gamma_2(\lambda_k+1)}}{2i} & -\frac{\lambda_k e^{-i\gamma_2(\lambda_k+1)}}{2i} & \frac{\lambda_k(\lambda_k-1)e^{i\gamma_2(\lambda_k-1)}}{2i} & -\frac{\lambda_k(\lambda_k-1)e^{-i\gamma_2(\lambda_k-1)}}{2i} \end{bmatrix} \begin{bmatrix} M_k \\ \bar{N}_k \\ I_k \\ \bar{L}_k \end{bmatrix} = \begin{bmatrix} 0 \\ 0 \\ 0 \\ 0 \end{bmatrix} \tag{33}$$

and v_k is the vector:

$$v_k^T = \begin{pmatrix} M_k & \bar{N}_k & I_k & \bar{L}_k \end{pmatrix}.$$

A V-notch consists only of one material, therefore the index m is intentionally omitted. The full matrix form of the equations for a bi-material notch is analogical, therefore it is not shown in the text. The main difference is that the matrix has 8 lines and the vector v_k is constructed for the first and second material region, i.e.:

$$v_k^T = \begin{pmatrix} M_{k1} & \bar{N}_{k1} & I_{k1} & \bar{L}_{k1} & M_{k2} & \bar{N}_{k2} & I_{k2} & \bar{L}_{k2} \end{pmatrix}. \tag{34}$$

Let's denote the matrix on the right-hand side of (33) as $\mathbf{A}(\lambda)$. The determination of eigenvalues and eigenvectors is virtually identical for the case of a V-notch or a bi-material notch. For the system:

$$\mathbf{A}(\lambda)\, v = \mathbf{0}, \tag{35}$$

there are 5 unknowns, i.e. eigenvalue λ_k and the complex coefficients M_k, $\bar{N}_k$, I_k and $\bar{L}_k$, and only 4 equations to be used (or 9 unknowns and 8 equations for the case of a bi-material notch). Therefore the system is undetermined. Following the basic principle of the linear algebra, the necessary condition for the non-trivial solution of (35) to exist is that:

$$\det(\mathbf{A}(\lambda)) = 0. \tag{36}$$

Expansion of this determinant leads to the so called characteristic equation, which roots are eigenvalues $\lambda_k \in \mathbb{C}$. A convenient way to study complex function $f(z) = \det(\mathbf{A}(\lambda))$, which is function $\mathbb{C} \to \mathbb{C}$, is to use domain coloring method (known also as HSV) [56]. Since the graph of complex function is an object in four real dimensions, this function is difficult to visualize in three-dimensional space. By domain coloring, the phase θ (also know as argument) of complex number $z = re^{i\theta}$ is represented as hue and the modulus $r = |z|$ is represented as intensity, see left-hand side of Figures 16-18 in the Numerical example A subsection on p. 30. The equation (36) is in general transcendental (does not have any closed form solution) and has to be solved numerically. Since the eigenvalues are complex numbers, the solution of equation is found as a vector $[\Re\{\lambda_k\}, \Im\{\lambda_k\}]$ by solving system of 2 real equations, i.e.:

$$\begin{aligned} \Re\{\det(\mathbf{A}(\Re\{\lambda_k\}))\} &= 0, \\ \Im\{\det(\mathbf{A}(\Im\{\lambda_k\}))\} &= 0. \end{aligned}$$

This is illustrated graphically on the right-hand side of Figure 16-18, where the blue and red curve stay for the loci where real and imaginary part of equation (36) respectively is equal to zero. In the graph the solution is represented as an intersection of the blue and red curve. When the system is solved, i.e. when the vector $[\Re\{\lambda_k\}, \Im\{\lambda_k\}]$ is found, the eigenvalue $\lambda_k \in \mathbb{C}$ is constructed as:

$$\lambda_k = \Re\{\lambda_k\} + i\Im\{\lambda_k\}.$$

For V-notches and bi-material notches where the opening angle $2\alpha < 180°$ we find one or two eigenvalues λ_k in the interval $\Re(0, 1)$ forming the singular terms exponents. There is also arbitrary number of eigenvalues λ_k to be found

in the interval $\Re(1,\infty)$ forming exponents of non-singular terms as shown in Figures 23 and 24 on p. 35 and 36. The characteristic equation (36) has a trivial root $\lambda_0^{\text{trans}} = 0$ which correspond to the term in displacement series responsible for rigid body translation and the term with $\lambda_k^{\text{rot}} = 1$ that stand for the rigid body rotation [36]. Since these terms do not contribute to the stress field, they are omitted, which is in accordance to approaches found in literature [23]. By substitution of particular kth eigenvalue λ_k back in the matrix $\mathbf{A}(\lambda)$ we can obtain eigenvector v_k, however since the system of equations (35) is a priori undetermined, value of one of the coefficients of vector v_k has to be chosen and only the ratios between coefficients of v_k can be determined. Practically, after the substitution of particular eigenvalue λ_k we take the matrix $\mathbf{A}(\lambda)$ and create reduced matrix $\mathbf{A}^{\text{red}}(\lambda)$ by removing its last line and taking its last column as a right side of the new reduced system of equations[5]. If we denote the right-hand side of the system as a^{red}, we write:

$$\mathbf{A}^{\text{red}}(\lambda)\, v_k^{\text{red}} = a^{\text{red}} \tag{37}$$

The dimension of $\mathbf{A}^{\text{red}}(\lambda)$ is 3×3. The unknown vector v_k^{red} and known vector a^{red} are both 1×3 (or in the case of a bi-material notch 7×7 for $\mathbf{A}^{\text{red}}(\lambda)$ and 1×7 for v_k^{red} and a^{red}). In other words the system is determined and ready to be solved. Since we removed the last line of the matrix $\mathbf{A}(\lambda)$, we choose the last coefficient of the vector v_k, the $\bar{L}_k$ equal to 1 (or $\bar{L}_{k2} = 1$ in the case of a bi-material notch). The eigenvector v_k is finally created by extending the vector v_k^{red}, which is the solution of reduced system of equations (37), by the unit coefficient ($\bar{L}_k$ or $\bar{L}_{k2}$). Since we have determined both the eigenvalue λ_k and the eigenvector v_k, it is trivial to take their complex conjugates and to construct the angular eigenfunctions $f_{ijk}(\theta)$ and $\bar{f}_{ijk}(\theta)$ for stress expansion (20) on p. 24 or $f_{ik}(\theta)$ and $\bar{f}_{ik}(\theta)$ for displacement expansion (24) on p. 25. Since the choice of unit coefficient in eigenvector v_k is arbitrary, the eigenfunctions may be further normalized, e.g.:

$$f_{\theta\theta k}(\theta_0) = 1, \tag{38}$$

for symmetric terms of the series, i.e. $k = 1,3,5\ldots$ where θ_0 is the crack initiation angle. For anti-symmetric terms of the series with $k = 2,4,6\ldots$:

$$f_{r\theta k}(\theta_0) = 1,$$

Alternative and common normalization for crack problems is [23]:

$$\begin{cases} f_{\theta\theta k}(\theta_0) = 1/\sqrt{2\pi} & k = 1,3,5\ldots \\ f_{r\theta k}(\theta_0) = 1/\sqrt{2\pi} & k = 2,4,6\ldots \end{cases}. \tag{39}$$

However, the choice of angle for eigenfunction normalization is arbitrary, therefore normalization by angles θ_0 different from crack initiation angle can be chosen. From the computational point of view, the normalization of eigenfunction is performed by its division by the function $f_{\theta\theta k}(\theta_0)$ or $f_{r\theta k}(\theta_0)$, so:

$$f_{ijk}^{\text{n}}(\theta) = \begin{cases} f_{ijk}(\theta)/f_{\theta\theta k}(\theta_0) & k = 1,3,5\ldots \\ f_{ijk}(\theta)/f_{r\theta k}(\theta_0) & k = 2,4,6\ldots \end{cases},$$

similarly the displacement eigenfunction is normalized:

$$f_{ik}^{\text{n}}(\theta) = \begin{cases} f_{ik}(\theta)/f_{\theta\theta k}(\theta_0) & k = 1,3,5\ldots \\ f_{ik}(\theta)/f_{r\theta k}(\theta_0) & k = 2,4,6\ldots \end{cases}.$$

The complex conjugates are normalized analogically. In the following text, eigenfunctions are always considered normalized and the superscript n is intentionally omitted. The above mentioned normalization is in general applicable only for the symmetrical V-notches and other symmetrical problems. The case of a bi-material notch is a non-symmetrical problem and each eigenfunction $f_{ijk}(\theta)$ consists of both odd and even functions. In other words, it is not true anymore that the eigenfunction with an odd k is odd function and the eigenfunction with even k is an even function. In case of non-symmetrical problems, the normalization should be performed on individual basis.

[5] The choice of line and column to be removed is arbitrary, the last line and column is seen by the author as the easiest choice.

Numerical example A: Eigenvalues, eigenvectors and eigenfunctions of V-notch. The V-notch with local geometry as shown in Figure 9 on p. 15 is considered. Let's study three geometrical configurations, i.e. (i) $2\alpha = 60°$, (ii) $2\alpha = 90°$, (iii) $2\alpha = 120°$, ($\gamma_1 = \alpha$, $\gamma_2 = 360° - \alpha$). The determination of eigenvalues λ_k and eigenvectors v_k from the mathematical point of view is described in the previous sub-section. From the computational point of view, the roots are found by a code written in Python programming language. The main part of the code, the eigenequation solver, contains command fsolve which is a part of Python library called scipy.optimize [60]. Numerical module fsolve is based on advanced MINPACK's hybrd and hybrj algorithms [61]. The roots can be found with arbitrary numerical precision by choice of the *xtol* factor, which is in calculation through the dissertation set to $xtol = 1e-7$. The calculation will terminate, if the relative error between two consecutive iterates is at most *xtol*. It is advised to check if the calculated value truly represents a root. This can be done by inserting a root back into the characteristic equation (36). Only the inputs which result in a close to zero value of the characteristic function are true roots. Another option is to compare the calculated value with the characteristic function plotted in a graph as it will be shown later. All the graphs are created by Python library called Mathplotlib [62]. In Tables 1, 2 and 3 we see first four resulting eigenvalues λ_k for the V-notches with opening angles 2α of 60°, 90° and 120° respectively. For the sake of completeness, the values of complex coefficients M_k, $\bar{N}_k$, I_k and $\bar{L}_k$ are listed in Tables 1-3 as well.

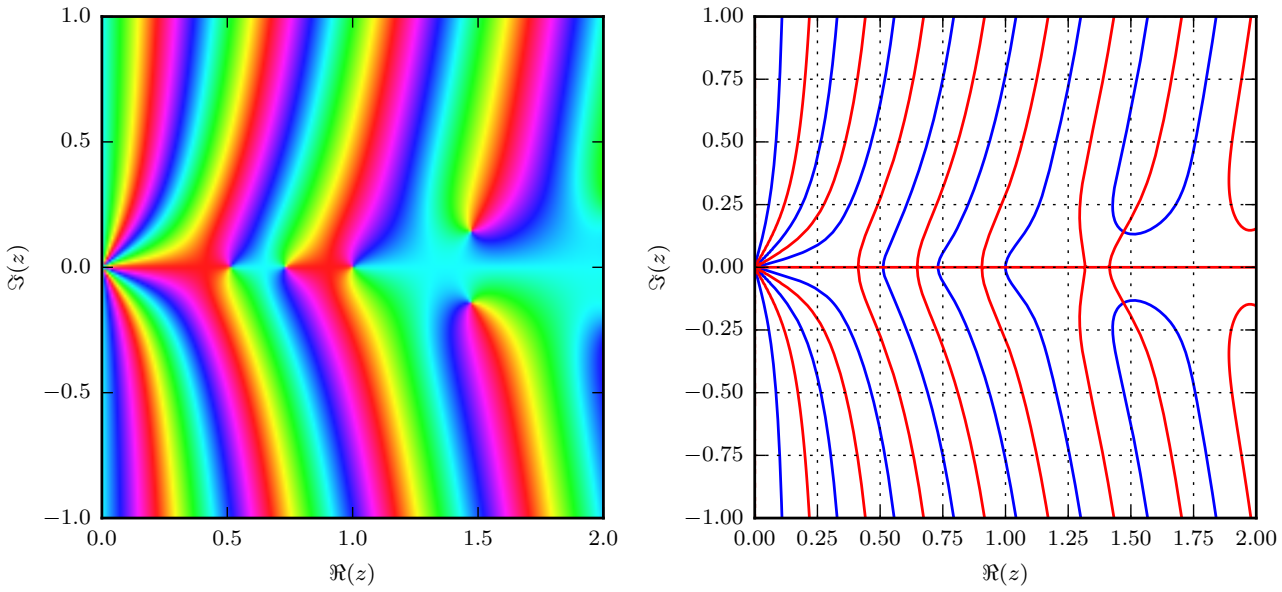

Figure 16: (i) V-notch, $2\alpha = 60°$. On the left-hand side there is the graph of $f(z) = \det(\mathbf{A}(\lambda))$. On the right-hand side a contour plot, the blue curve stands for $\Re\{\det(\mathbf{A}(\Re\{\lambda_k\}))\} = 0$ and the red one for $\Im\{\det(\mathbf{A}(\Im\{\lambda_k\}))\} = 0$.

k	λ_k	M_k	$\bar{N}_k$	I_k	$\bar{L}_k$
1	0.512221	$-0.638227 + 0.049107i$	$0.640113 + 0.000006i$	$-0.997054 + 0.076707i$	1
2	0.730901	$-0.136430 + 1.131423i$	$-1.139619 + 0.000001i$	$0.119715 - 0.992808i$	1
3	$1.471028 + 0.141853i$	$2.554167 - 1.346322i$	$-0.930264 - 0.732678i$	$-2.397982 - 0.441407i$	1
4	$2.074826 + 0.229426i$	$2.157055 - 7.658169i$	$-1.275639 + 1.383938i$	$-3.768504 + 1.914963i$	1

Table 1: (i) V-notch, $2\alpha = 60°$. First four eigenvalues λ_k and eigenvector's v_k coefficients M_k, $\bar{N}_k$, I_k and $\bar{L}_k$.

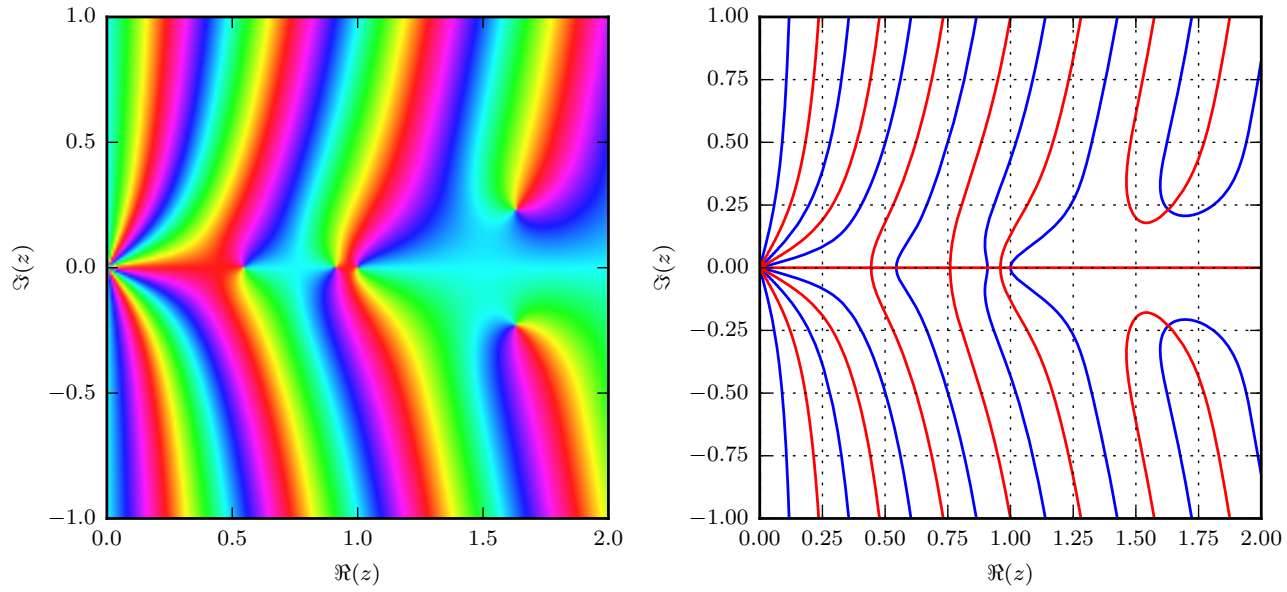

Figure 17: (ii) V-notch, $2\alpha = 90°$. On the left-hand side there is the graph of $f(z) = \det(\mathbf{A}(\lambda))$. On the right-hand side contour plot, the blue curve stands for $\Re\{\det(\mathbf{A}(\Re\{\lambda_k\}))\} = 0$ and the red curve for $\Im\{\det(\mathbf{A}(\Im\{\lambda_k\}))\} = 0$.

k	λ_k	M_k	$\bar{N}_k$	I_k	$\bar{L}_k$
1	0.544484	$-0.806223 + 0.231396i$	$0.838773 - 0.000002i$	$-0.961193 + 0.275878i$	1
2	0.908529	$0.350695 + 0.227131i$	-0.417822	$-0.839339 - 0.543608i$	1
3	$1.629257 + 0.231251i$	$-3.174859 - 4.719311i$	$-0.290233 + 1.298170i$	$-2.941565 + 3.103293i$	1
4	$2.301327 + 0.315837i$	$-15.145801 + 2.378337i$	$-0.349757 + 2.078146i$	$2.305751 + 6.900075i$	1

Table 2: (ii) V-notch, $2\alpha = 90°$. First four eigenvalues λ_k and eigenvector's v_k coefficients M_k, $\bar{N}_k$, I_k and $\bar{L}_k$.

As mentioned earlier, the stresses near the tip of a V-notch are proportional to the r^{-p_k} where $p_k = 1 - \lambda_k$, Eq. (14) on p. 15. It is obvious that with increasing opening angle the strength of singularity decreases as the value of eigenvalue λ_k increases (singular terms considered). This can be illustrated by plotting function r^{-p_1} for the calculated geometries (i), (ii) and (iii) as in Figure 19. Function r^{-p_1} corresponds to the opening mode of the symmetrical V-notch. For the geometries considered throughout the study, the first term of the series which contains the exponent of singularity p_1 is always singular. Nevertheless, the second term, which contains the exponent p_2, is singular only in cases (i) and (ii), since the case (iii) has $\Re\{\lambda_2\} > 1$. This particular term vanishes as $r \to 0$ as illustrated in Figure 20. Function r^{-p_2} corresponds to the in-plane shear mode of the symmetrical V-notch. As explained in previous section, once the eigenvalues λ_k and eigenvectors v_k are determined, it is possible to construct eigenfunctions $f_{ijk}(\theta)$ and $f_{ik}(\theta)$ for stress and displacement series respectively (or their complex conjugates $\bar{f}_{ijk}(\theta)$ and $\bar{f}_{ik}(\theta)$). For the most common case of the V-notch with right angle, i.e. (ii) $2\alpha = 90°$, the stress eigenfunctions $f_{ijk}(\theta)$ for $k = 1, 2, 3, 4$ are displayed in Figure 21. Similarly the displacement eigenfunctions $f_{ik}(\theta)$ for $k = 1, 2, 3, 4$ are constructed and shown in Figure 22. Please note that illustrated eigenfunctions are normalized per equation (38) and the presumed crack initiation angle is due to symmetry of the problem $\theta_0 = 180°$. Also note that the stress and displacement eigenfunctions of the V-notch are symmetric or anti-symmetric relative to the axis or point where $\theta = 180°$. To obtain general dependence of $\lambda_k(2\alpha)$, eigenvalues for angles $2\alpha \in (0°, 360°)$ were determined. Such general dependence of eigenvalues λ_k on the opening angle 2α is shown in Figure 23. Note, that for angle $2\alpha \sim 103°$ the eigenvalue $\lambda_2 = 1$. For larger angles 2α, the term associated with eigenvalue λ_2 is always a non-singular one. This is in accordance with results of Ayatollahi and Nejati in [36] who report the angle value of 102.55°.

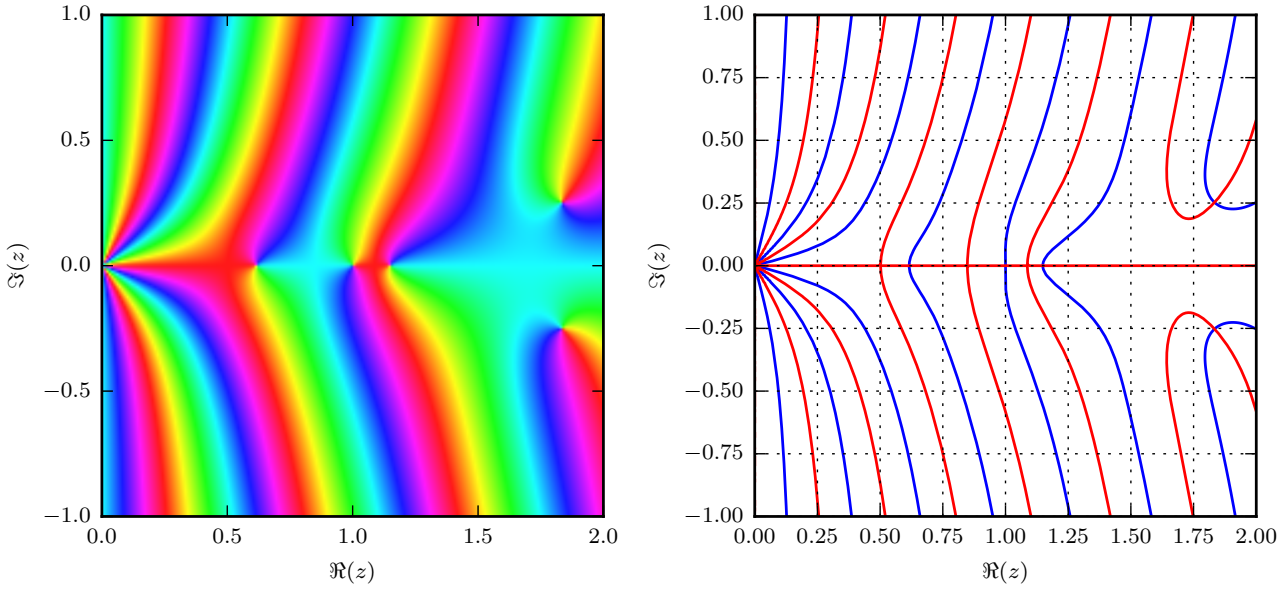

Figure 18: (iii) V-notch, $2\alpha = 120°$. On the left-hand side there is the graph of $f(z) = \det(\mathbf{A}(\lambda))$. On the right-hand side contour plot, the blue curve stands for $\Re\{\det(\mathbf{A}(\Re\{\lambda_k\}))\} = 0$ and the red curve for $\Im\{\det(\mathbf{A}(\Im\{\lambda_k\}))\} = 0$.

k	λ_k	M_k	$\bar{N}_k$	I_k	$\bar{L}_k$
1	0.615731	$-0.861987 + 0.767009i$	1.153830	$-0.747066 + 0.664750i$	1
2	1.148913	$-0.400153 + 0.542926i$	0.674456	$-0.593297 + 0.804984i$	1
3	$1.833549 + 0.252251i$	$-4.230350 + 6.048695i$	$0.638263 + 1.371624i$	$2.445221 + 4.222029i$	1
4	$2.589479 + 0.348375i$	$17.643684 + 11.953875i$	$0.958586 + 2.186906i$	$7.551600 - 4.757790i$	1

Table 3: (iii) V-notch, $2\alpha = 120°$. First four eigenvalues λ_k and eigenvector's v_k coefficients M_k, $\bar{N}_k$, I_k and $\bar{L}_k$.

Numerical example B: Eigenvalues, eigenvectors and eigenfunctions of bi-material notch. The bi-material notch as shown in Figure 10 on p. 16 is considered with geometrical configuration of $2\alpha = 90°$, ($\gamma_1 = 45°, \gamma_2 = 180°, \gamma_3 = 315°$) and bi-material configurations of (i) $E_1/E_2 = 0.50$, (ii) $E_1/E_2 = 0.25$, (iii) $E_1/E_2 = 0.10$. In all cases, $E_1 = 20$ GPa and $\nu_1 = \nu_2 = 0.25$. The eigenvalues λ_k and eigenvectors v_k are determined from the mathematical point of view as described in previous sub-section. From the computational point of view the procedure is identical to the one described in the Numerical example A. The resulting eigenvalues λ_k are listed in Table 4. The coefficients of eigenvector v_k were listed in Numerical example A for the sake of completeness, i.e. for illustration and the validation of other researchers' results. We intentionally omit those in the Numerical example B. All studied geometrical and material configurations lead to 2 singular terms of the stress expansion. We see that with increasing contrast in Young's moduli, the strength of singularity of the first term decreases as shown in Figure 25. However, again with increasing contrast in Young's moduli, the strength of the singularity of the second term increases as shown in Figure 26. The stress eigenfunctions $f_{ijk}(\theta)$ for the case (iii) with the highest contrast in Young's moduli are plotted in Figure 27. In similar manner the displacement eigenfunctions $f_{ik}(\theta)$ for the same case (iii) are shown in Figure 28. Note that these eigenfunctions are no longer symmetrical or anti-symmetrical as in the case of a V-notch. Another important fact is that the radial stress eigenfunction $f_{rrk}(\theta)$ is discontinuous at the material interface Γ, i.e. $\theta = 180°$. Again, these eigenfunctions are normalized per equation (38) with chosen angle $\theta_0 = 270°$. To obtain general dependence of $\lambda_k(2\alpha)$, eigenvalues for angles $2\alpha \in (0°, 360°)$ for some particular configuration, e.g. (ii) were determined. Such general dependence of eigenvalues λ_k on opening angle 2α is shown in Figure 24.

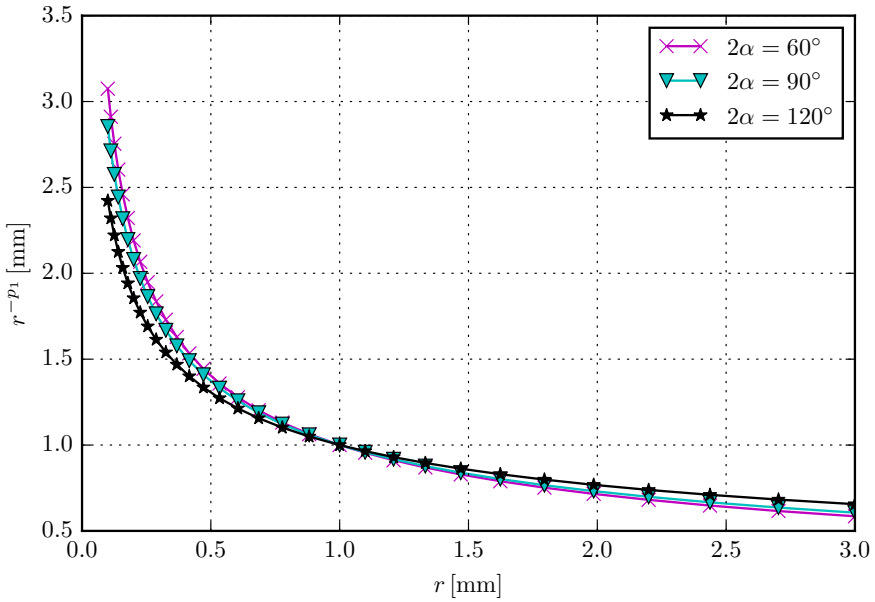

Figure 19: The function r^{-p_1} of the V-notch plotted on a radial distance of $r \in (0.1; 3)$ mm. The exponents of singularity of the first term are: (i) $p_1^{60°} = 0.488$, (ii) $p_1^{90°} = 0.456$ and (iii) $p_1^{120°} = 0.384$. With the increasing of the notch opening angle 2α the strength of stress singularity decreases.

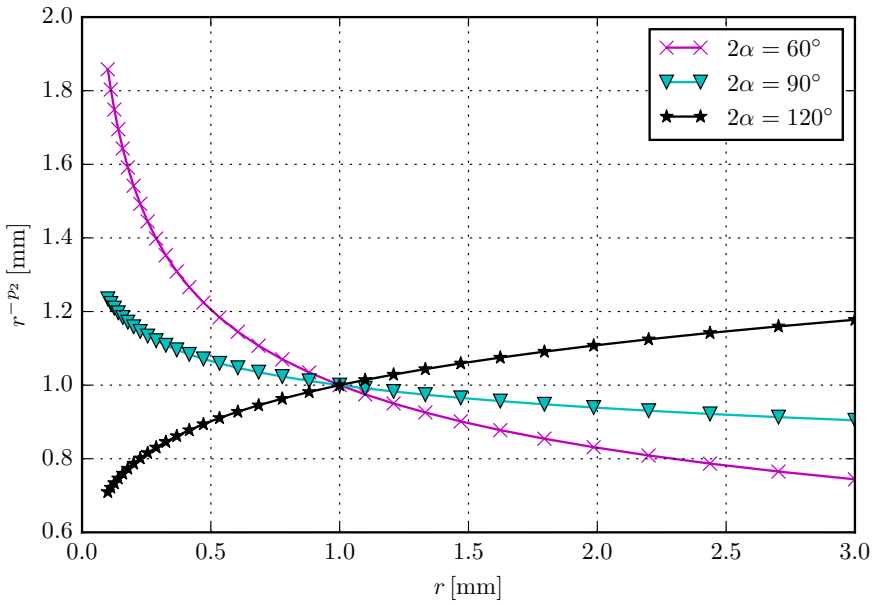

Figure 20: The function r^{-p_2} of the V-notch plotted on a radial distance of $r \in (0.1; 3)$ mm. The exponents of singularity of the second term are: (i) $p_2^{60°} = 0.269$, (ii) $p_2^{90°} = 0.091$ and (iii) $p_2^{120°} = -0.149$. With the increasing of the notch opening angle 2α the strength of stress singularity decreases.

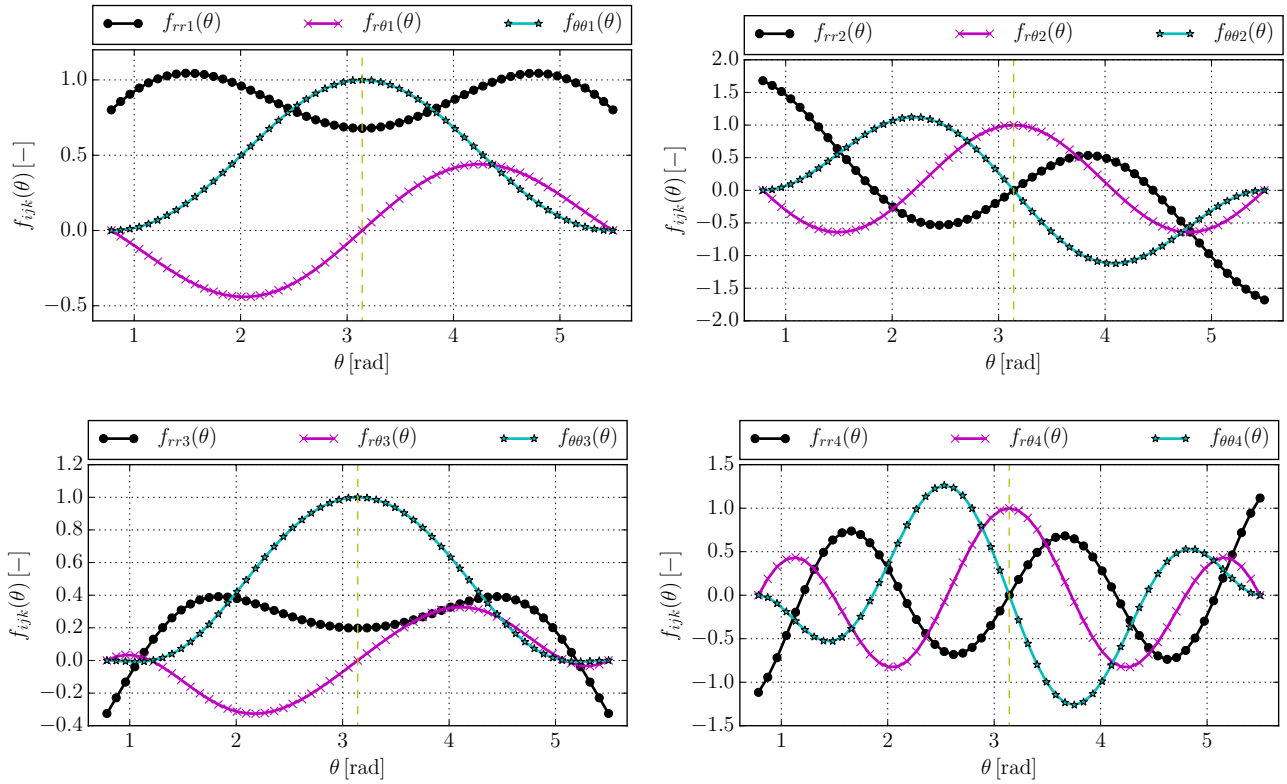

Figure 21: Stress eigenfunctions $f_{ijk}(\theta)$ for $k = 1, 2, 3, 4$ of the V-notch (ii), $2\alpha = 90°$. The yellow dashed line represents the axis of symmetry of the notch.

	$E_1/E_2 = 0.5$	$E_1/E_2 = 0.25$	$E_1/E_2 = 0.10$
λ_1	0.552239	0.572603	0.608051
λ_2	0.894288	0.859567	0.806539
λ_3	$1.645612 \pm 0.225305i$	$1.693610 \pm 0.206185i$	1.770118
λ_4	$2.298183 \pm 0.288001i$	$2.294796 \pm 0.16466i$	$2.577451 \pm 0.219431i$

Table 4: Bi-material notch $2\alpha = 90°$, $(\gamma_1 = 45°, \gamma_2 = 180°, \gamma_3 = 315°)$ and bi-material configuration of (i) $E_1/E_2 = 0.5$, (ii) $E_1/E_2 = 0.25$, (iii) $E_1/E_2 = 0.1$.

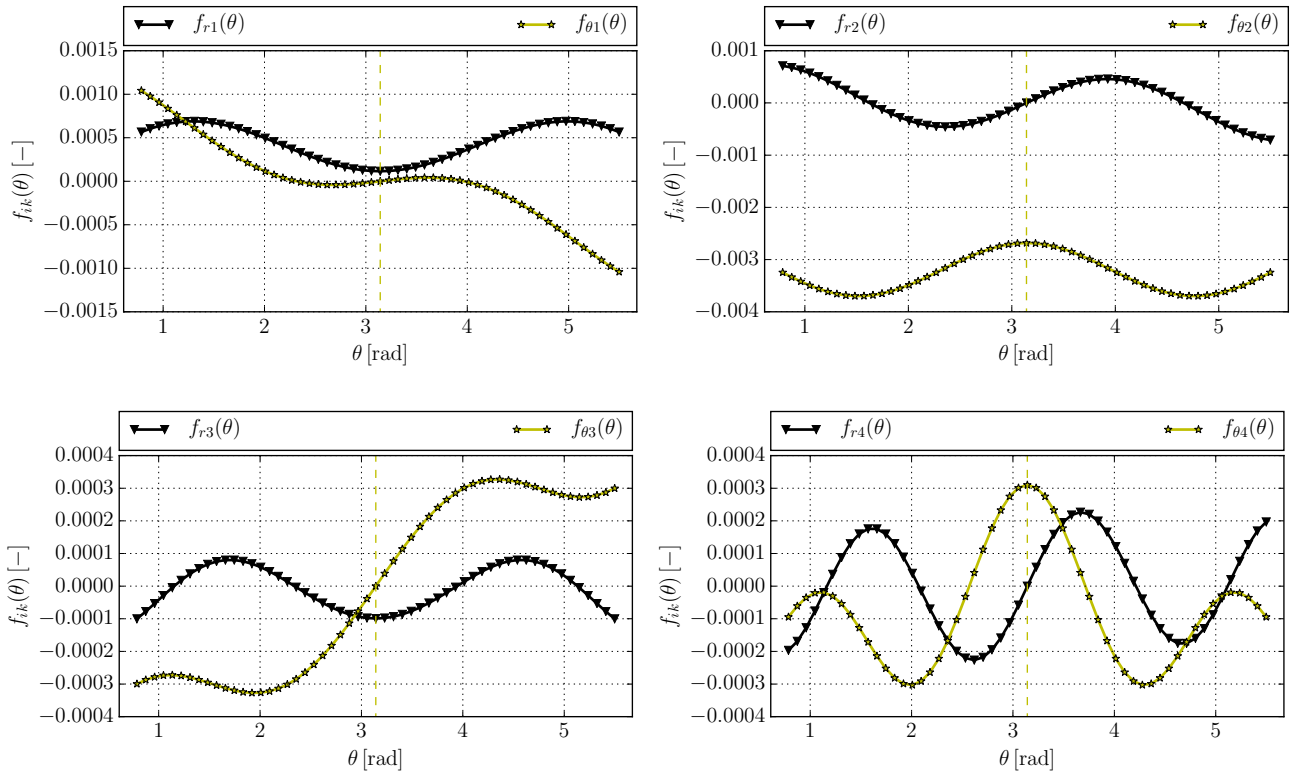

Figure 22: Displacement eigenfunctions $f_{ik}(\theta)$ for $k = 1, 2, 3, 4$ of the V-notch (ii), $2\alpha = 90°$. The yellow dashed line represents the axis of symmetry of the notch.

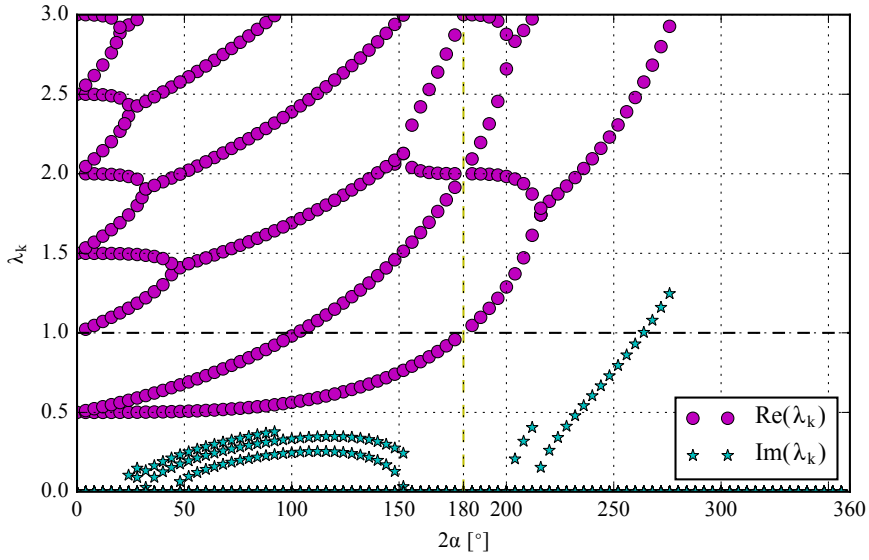

Figure 23: Dependence of eigenvalues λ_k of the V-notch on the opening angle 2α. The black dashed line divides the graph into fields where singular and non-singular eigenvalues are found. The yellow dashed line represents notch free plate.

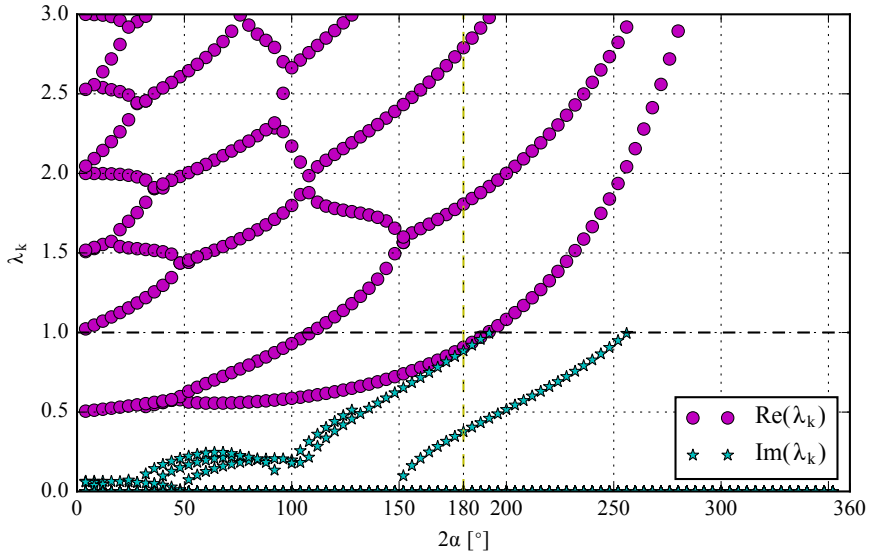

Figure 24: Dependence of eigenvalues λ_k of the bi-material notch on the opening angle 2α. The black dashed line divides the graph into fields where singular and non-singular eigenvalues are found. The yellow dashed line represents the free edge singularity. The geometry of studied case is $\gamma_1 = \alpha$, $\gamma_2 = \pi$, $\gamma_3 = 2\pi - \alpha$. The Young's moduli ratio is $E_1/E_2 = 0.25$ and Poisson's ratio is $\nu_1 = \nu_2 = 0.25$.

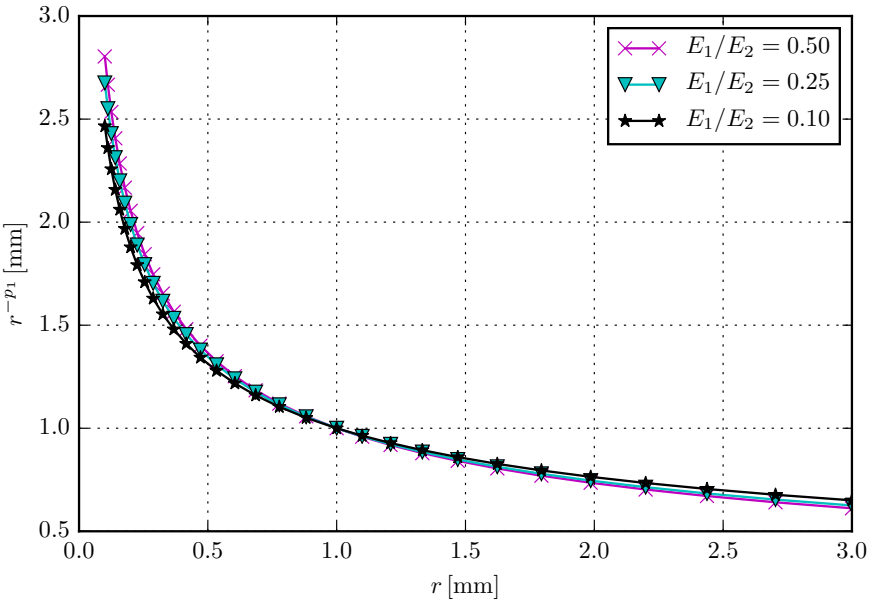

Figure 25: The function r^{-p_1} of the bi-material notch plotted on a radial distance of $r \in (0.1; 3)$ mm. The exponents of singularity of the first term are: (i) $p_1^{0.50} = 0.448$, (ii) $p_1^{0.25} = 0.427$ and (iii) $p_1^{0.10} = 0.392$, where the superscript denotes E_1/E_2.

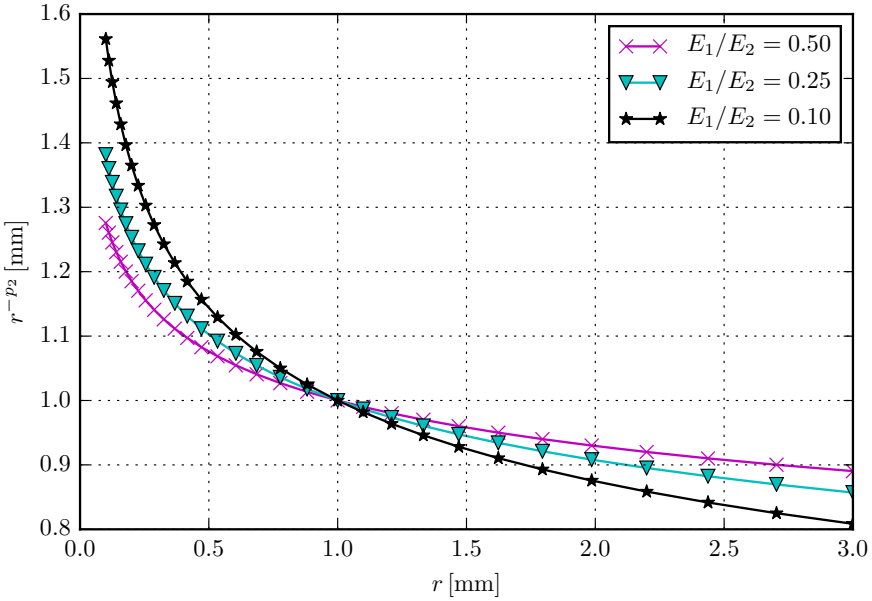

Figure 26: The function r^{-p_2} of the bi-material notch plotted on a radial distance of $r \in (0.1; 3)$ mm. The exponents of singularity of the first term are: (i) $p_2^{0.50} = 0.106$, (ii) $p_2^{0.25} = 0.140$ and (iii) $p_2^{0.10} = 0.193$, where the superscript denotes E_1/E_2.

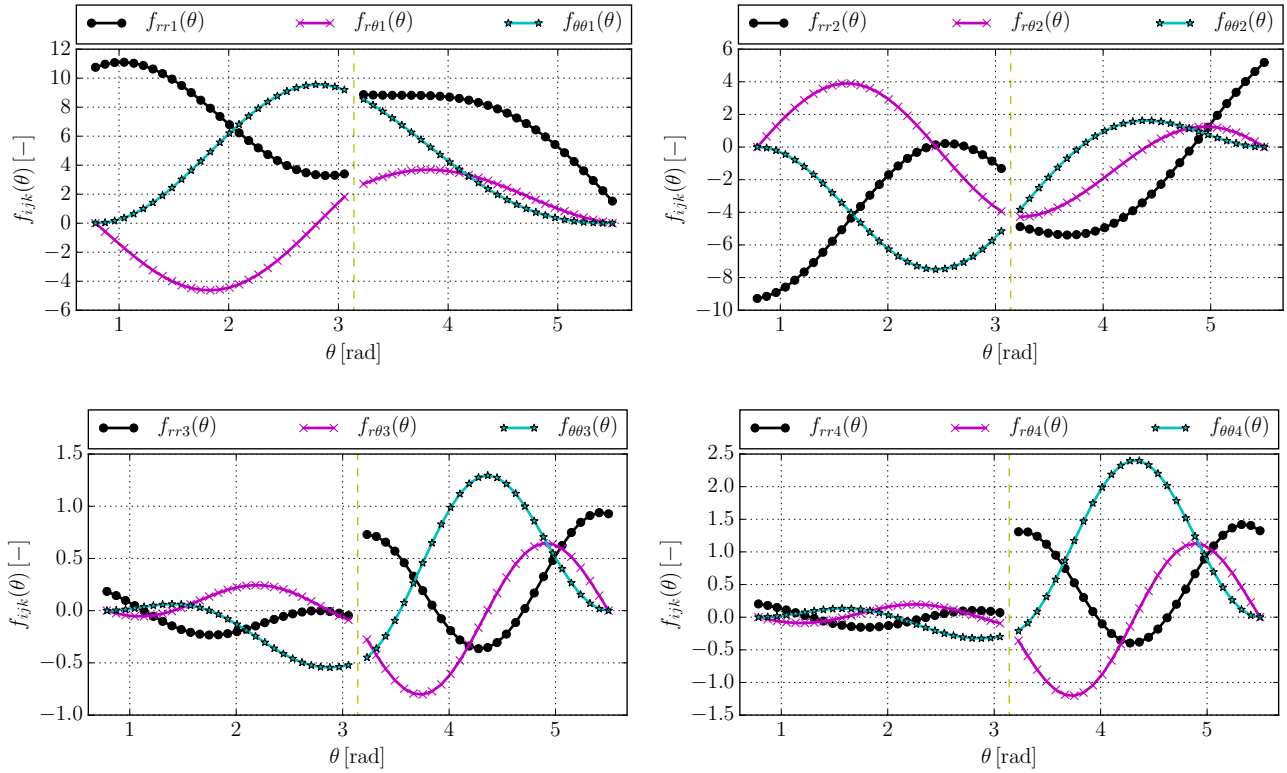

Figure 27: Stress eigenfunctions $f_{ijk}(\theta)$ for $k = 1, 2, 3, 4$ of the bi-material notch (iii), $2\alpha = 90°$, $E_1/E_2 = 0.1$.

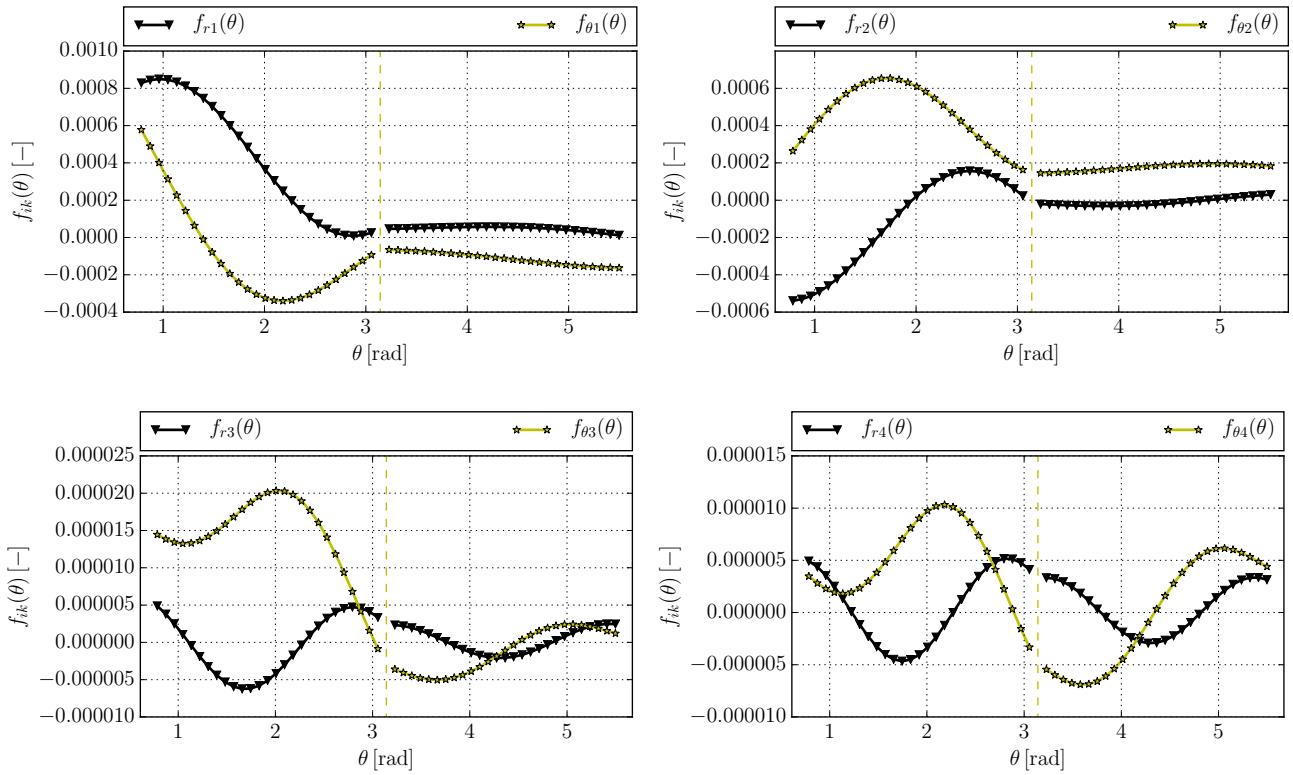

Figure 28: Displacement eigenfunctions $f_{ik}(\theta)$ for $k = 1, 2, 3, 4$ of the bi-material notch (iii), $2\alpha = 90°$, $E_1/E_2 = 0.1$.

Calculation of stress terms factors

Determination of GSIFs by the Ψ-integral

This part of the text describes a derivation of the path independent Ψ-integral for a V-notch or a bi-material notch problem. The employment of the Ψ-integral is a convenient way for determination of the Generalized Stress Intensity Factors (GSIFs) H_k. By use of the Ψ-integral also another necessary parameter for the Leguillon's coupled stress-energy criterion, the scaling coefficient $A(2\alpha, \theta_0)$ can be determined as it will be shown in the following chapter. For the theoretical description of Leguillon criterion see p. 58. The derivation of the Ψ-integral will be shown on the more general case of a bi-material notch. However, analogically it can be performed for the simpler V-notch problem. First, let us consider a zero difference due to symmetry of the elastic tensor C:

$$\int_{\mathcal{D}} (C\colon \nabla U : \nabla V - C : \nabla V : \nabla U)\mathrm{d}x \quad = \quad 0. \tag{40}$$

where U and V are two elastic solutions dependent on 2 coordinates (x, y) in Cartesian coordinate system or (r, θ) in polar coordinate system and ∇ is gradient. $\mathcal{D}$ is an arbitrary closed domain within the material domains Ω_1 and Ω_2 as shown in Figure 29. According to the Hooke's law in following form:

$$\sigma(U) \quad = \quad C\nabla U, \tag{41}$$

the equation (40) becomes:

$$\int_{\mathcal{D}} (\sigma(U)\nabla V - \sigma(V)\nabla U)\mathrm{d}x \quad = \quad 0, \tag{42}$$

where $\sigma(U)$ and $\sigma(V)$ are stress fields associated with U and V respectively. By applying the Green's theorem to the equation (42) we obtain:

$$-\int_{\mathcal{D}} \nabla\sigma(U)V\mathrm{d}x + \int_{\partial\mathcal{D}} \sigma(U)nV\mathrm{d}s + \int_{\mathcal{D}} \nabla\sigma(V)U\mathrm{d}x - \int_{\partial\mathcal{D}} \sigma(V)nU\mathrm{d}s \quad = \quad 0, \tag{43}$$

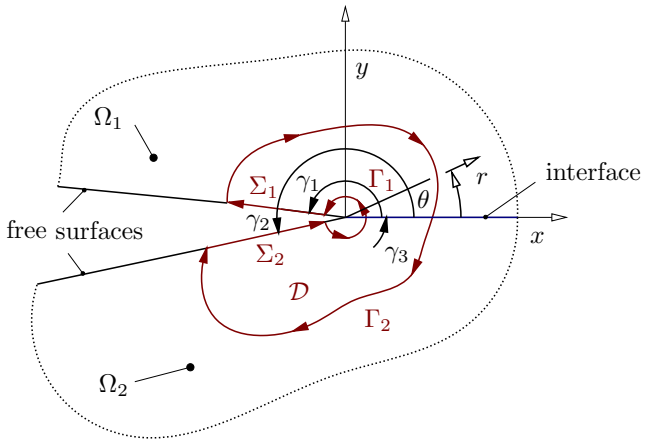

Figure 29: The path integral surrounding the tip of the bi-material notch. The integration path $\partial\mathcal{D}$, the boundary of $\mathcal{D}$, consists of the paths: Γ_1, Γ_2, Σ_1, Σ_2.

where $\partial\mathcal{D}$ denotes the boundary of the domain $\mathcal{D}$ and n is the normal of the contour $\partial\mathcal{D}$. If equilibrium conditions apply, the first and the third term of equation (43) are equal to zero, therefore we can write:

$$\int_{\partial\mathcal{D}} (\sigma(U)nV - \sigma(V)nU)\mathrm{d}s \quad = \quad 0. \tag{44}$$

Since the negatively oriented boundary $\partial\mathcal{D}$ consists of 4 contours $\partial\mathcal{D} = \Gamma_1 \cup \Gamma_2 \cup \Sigma_1 \cup \Sigma_2$, the integral (44) can be written as a sum of the following 4 contour integrals[6]:

$$\begin{aligned} &\int_{\Gamma_1} (\sigma(U)nV - \sigma(V)nU)\mathrm{d}s + \int_{\Sigma_1} (\sigma(U)nV - \sigma(V)nU)\mathrm{d}s + \\ &\int_{\Gamma_2} (\sigma(U)nV - \sigma(V)nU)\mathrm{d}s + \int_{\Sigma_2} (\sigma(U)nV - \sigma(V)nU)\mathrm{d}s \quad = \quad 0, \end{aligned} \tag{45}$$

see Figure 29. Because of zero traction on the notch surfaces, for some terms we write:

$$\begin{aligned} \int_{\Sigma_1} (\sigma(U)nV - \sigma(V)nU)\mathrm{d}s \quad &= \quad 0, \\ \int_{\Sigma_2} (\sigma(U)nV - \sigma(V)nU)\mathrm{d}s \quad &= \quad 0, \end{aligned}$$

and equation (45) becomes:

$$\int_{\Gamma_1} (\sigma(U)nV - \sigma(V)nU)\mathrm{d}s + \int_{\Gamma_2} (\sigma(U)nV - \sigma(V)nU)\mathrm{d}s \quad = \quad 0.$$

Let's denote the $\Gamma_A = \Gamma_1$ and change orientation of the path $\Gamma_B = -\Gamma_2$, so both of the curves are positively oriented as in Figure 30. We obtain:

$$\int_{\Gamma_A} (\sigma(U)nV - \sigma(V)nU)\mathrm{d}s \quad = \quad \int_{\Gamma_B} (\sigma(U)nV - \sigma(V)nU)\mathrm{d}s,$$

which proves that the integral is path independent. There are important implications of the integral path independence. Let's denote such path independent integral as:

$$\Psi(U,V) \quad = \quad \frac{1}{2}\int_{\Gamma} (\sigma(U)nV - \sigma(V)nU)\mathrm{d}s, \tag{46}$$

[6]The symbols Γ_1, Γ_2, Γ_A and Γ_B in this sub-chapter always stay for integration path, not to be confused with Γ_i which denotes material interface in all other parts of this work.

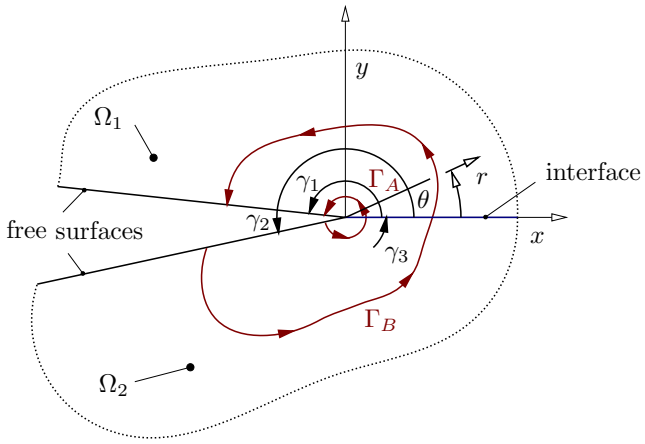

Figure 30: Two positively oriented contours surrounding the tip of the bi-material notch, the Γ_A and Γ_B.

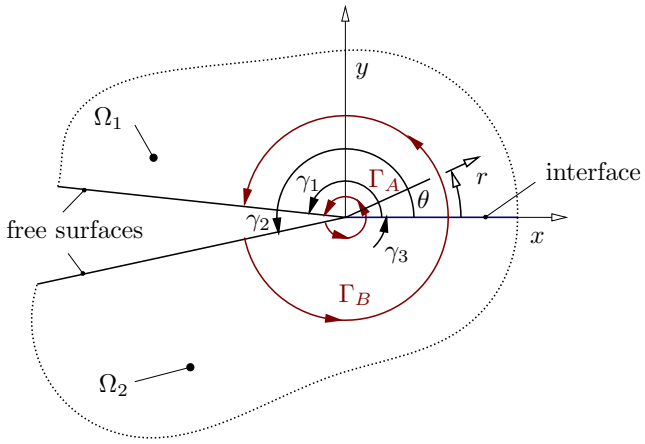

Figure 31: Two positively oriented circular contours surrounding the tip of the bi-material notch, the Γ_A and Γ_B.

which path Γ is a circle of radius R (such as Γ_A or Γ_B in Figure 31). The relations for stress and displacement near the singular point are:

$$\begin{aligned} U &= R^{\alpha} f_{ijk}(\theta), \\ V &= R^{\beta} g_{ijl}(\theta), \\ \sigma(U) &= R^{\alpha-1} f_{ik}(\theta), \\ \sigma(V) &= R^{\beta-1} g_{il}(\theta), \end{aligned}$$

where $f_{ijk}(\theta)$, $g_{ijl}(\theta)$ and $f_{ik}(\theta)$, $g_{il}(\theta)$ are the angular eigenfunctions for stress and displacement respectively. The α and β are the eigenvalues forming the exponents of singularity. By substitution of relations for displacements and stress near the singular point to (46) the integral becomes:

$$\begin{aligned} \int_{\Gamma} (R^{\alpha-1} f_{ik}(\theta) n R^{\beta} g_{ijl}(\theta) - R^{\beta-1} g_{il}(\theta) n R^{\alpha} f_{ijk}(\theta)) R \mathrm{d}\theta &= \\ \int_0^{2\pi} (R^{\alpha} f_{ik}(\theta) n R^{\beta} g_{il}(\theta) - R^{\beta} g_{il}(\theta) n R^{\alpha} f_{ijk}(\theta)) \mathrm{d}\theta &= \\ R^{\alpha+\beta} \int_0^{2\pi} (f_{ik}(\theta) n g_{ijl}(\theta) - g_{il}(\theta) n f_{ijk}(\theta)) \mathrm{d}\theta. & \end{aligned} \tag{47}$$

The integral as we defined it has to be independent of R. If $\alpha \neq -\beta$ in (47), the integral:

$$\int_0^{2\pi} (f_{ik}(\theta) n g_{ijl}(\theta) - g_{il}(\theta) n f_{ijk}(\theta)) \mathrm{d}\theta = 0, \tag{48}$$

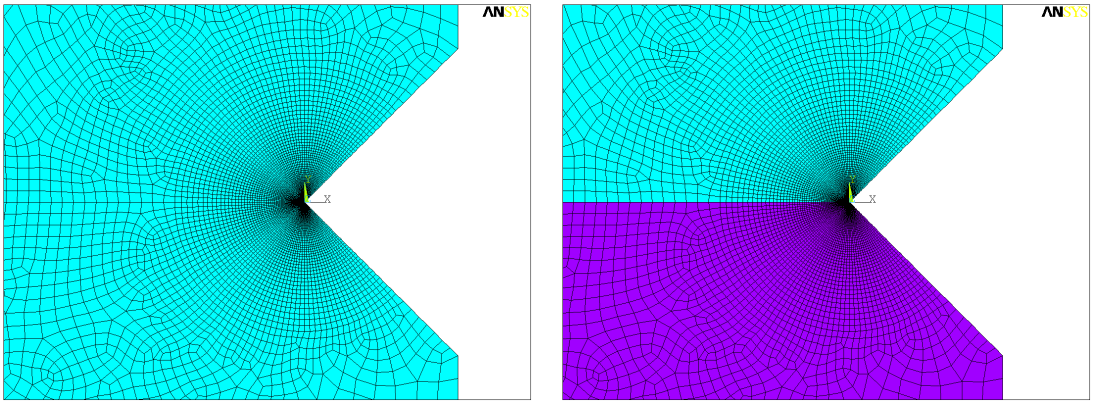

Figure 32: Area of refined mapped mesh near the singular point of the V-notch and bi-material notch.

since it is the only way for the integral to remain path independent. Determination of the GSIFs using the Ψ-integral is shown in the following text. The admissible solution of eigenequation (36) on p. 28 are also roots λ_k for which $\Re\{\lambda_k\} < 0$. These negative eigenvalues are called auxiliary, denoted $\lambda_k^- = -\lambda_k$ and they remain without a direct physical interpretation. However, they play an important role in the GSIFs determination. The Ψ-integral applied to the finite element solution and to an auxiliary eigenvalue solution $\lambda_k^- = -\lambda_k$ can be written:

$$\Psi(u^{\mathrm{FE}}(\theta), r^{-\lambda_1} f_{i1}^-(\theta)) = \Psi(C + H_1 r^{\lambda_1} f_{i1}(\theta) + H_2 r^{\lambda_2} f_{i2}(\theta) + \ldots + H_n r^{\lambda_n} f_{in}(\theta), r^{-\lambda_1} f_{i1}^-(\theta)), \tag{49}$$

where C represents the rigid body translation and $f_{ik}^-(\theta)$ is the auxiliary eigenfunction of the auxiliary displacement expansion. It is constructed analogically as ordinary eigenfunction $f_{ik}(\theta)$, only with consideration of auxiliary eigenvalue λ_k^-. The above-mentioned integral (49) can be rearranged into separate integrals:

$$\begin{aligned}\Psi(u^{\mathrm{FE}}(\theta), r^{-\lambda_1} f_{i1}^-(\theta)) &= \Psi(C, r^{-\lambda_1} f_{i1}^-(\theta)) + H_1 \Psi(r^{\lambda_1} f_{i1}(\theta), r^{-\lambda_1} f_{i1}^-(\theta)) + H_2 \Psi(r^{\lambda_2} f_{i2}(\theta), r^{-\lambda_1} f_{i1}^-(\theta)) + \ldots \\ &\quad \ldots + H_n \Psi(r^{\lambda_n} f_{in}(\theta), r^{-\lambda_1} f_{i1}^-(\theta)).\end{aligned} \tag{50}$$

Since property (48) applies, the terms with λ_k and λ_l^- where $k \neq l$ vanish. The expression above becomes:

$$\Psi(u^{\mathrm{FE}}(\theta), r^{-\lambda_1} f_{i1}^-(\theta)) = H_1 \Psi(r^{\lambda_1} f_{i1}(\theta), r^{-\lambda_1} f_{i1}^-(\theta)), \tag{51}$$

by which the generalized stress intensity factor H_1 can be calculated as:

$$H_1 = \frac{\Psi(u^{\mathrm{FE}}(\theta), r^{-\lambda_1} f_{i1}^-(\theta))}{\Psi(r^{\lambda_1} f_{i1}(\theta), r^{-\lambda_1} f_{i1}^-(\theta))}. \tag{52}$$

Thus, in general the kth factor can be calculated as:

$$H_k = \frac{\Psi(u^{\mathrm{FE}}(\theta), r^{-\lambda_k} f_{ik}^-(\theta))}{\Psi(r^{\lambda_k} f_{ik}(\theta), r^{-\lambda_k} f_{ik}^-(\theta))}. \tag{53}$$

Because of the Ψ-integral path independence the analytical term in denominator $\Psi_k^{\mathrm{analyt}} = \Psi(r^{\lambda_k} f_{ik}(\theta), r^{-\lambda_k} f_{ik}^-(\theta))$ can be calculated once for all for given problem. The term in the numerator $\Psi_k^{\mathrm{FE}} = \Psi(u^{\mathrm{FE}}(\theta), r^{-\lambda_k} f_{ik}^-(\theta))$ is calculated from the finite element results. From the computational point of view the FE results are calculated (in this work) in FEM code ANSYS. The vicinity of the singular point at the 2D model consists of refined mapped mesh as shown in Figure 32. The numerical values of stress and displacement components are extracted from nodes which lay on a circle that surrounds the singular point (any closed curve can be used, however the author of this dissertation finds the circular curve the simplest way to obtain results). The model is meshed with standard quadratic plane elements (in ANSYS denoted as PLANE183). The size of radius of the integration path denoted as r_1 is optional, nevertheless it is recommended to take results reasonably far from the singularity i.e. $r_1 > 1.0$ mm in order to avoid error caused by the nature of FEM. In the Numerical example C (see p. 43), the effect of integration path radius on the leading term H_1 value was always less than 1 % of the resulting value when the integral was calculated on radii between 1 and 3 mm. The model created by the author of this work enables the user to choose the size of area of refined mesh by choice of parameters r_0 and r_2 as shown in Figure 33. It is

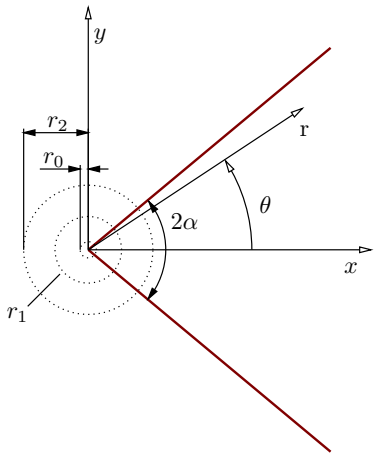

Figure 33: Area of refined mapped mesh near the singular point of the V-notch and bi-material notch.

possible to extract the entire stress and displacement field on this area. It can be either used for calculation of the integral Ψ_k^{FE} on all contours between r_0 and r_2 or later used as a 2D FEM reference to calculated asymptotic field. The circle of radius r_0 surrounds the area where the stress becomes theoretically unbounded and the FE numerical error is significant. This area is not of particular interest in terms of the Ψ-integral calculation. Furthermore there are no special elements found at the notch tip (as those used for fracture mechanics of cracks, depicted in Fig. 8 on p. 14). As the FE calculation is complete, just before writing of the values into data files, the rigid body translation C of the notch tip is subtracted of all nodal displacement values. Then, the values of all in-plane stress components $\sigma_{rr}^{\mathrm{FE}}(r,\theta)$, $\sigma_{r\theta}^{\mathrm{FE}}(r,\theta)$, $\sigma_{\theta\theta}^{\mathrm{FE}}(r,\theta)$ and displacement components $u_r^{\mathrm{FE}}(r,\theta)$, $u_\theta^{\mathrm{FE}}(r,\theta)$ in polar coordinate system are stored in data files. The computation proceeds with an execution of Python script. The first part of the Python script calculates the desired number n of eigenvalues λ_k based on the local geometry and material properties of the problem, constructs the corresponding eigenvectors v_k and eigenfunctions $f_{ijk}(\theta)$ and $f_{ik}(\theta)$ for stress and displacement components respectively. By considering $\lambda_k^- = -\lambda_k$ in a similar manner, the auxiliary eigenvectors v_k^- and eigenfunctions $f_{ijk}^-(\theta)$ and $f_{ik}^-(\theta)$ are obtained. For the term in numerator in Eq. (53) the infinitesimal value of the term in numerator as written in the Python script is:

$$\mathrm{d}\Psi_k^{\mathrm{FE}} = r_1^{\lambda_k^-}\left(u_r^{\mathrm{FE}}(\theta)f_{rrk}^-(\theta) + u_\theta^{\mathrm{FE}}(\theta)f_{r\theta k}^-(\theta) - r_1 f_{rk}^-(\theta)\sigma_{rr}^{\mathrm{FE}}(\theta) - r_1 f_{\theta k}^-(\theta)\sigma_{r\theta}^{\mathrm{FE}}(\theta)\right)\mathrm{d}\theta,$$

and the infinitesimal value of the analytical term in denominator, Eq. (53) is written:

$$\mathrm{d}\Psi_k^{\mathrm{analyt}} = \left(f_{rk}(\theta)f_{rrk}^-(\theta) + f_{\theta k}(\theta)f_{r\theta k}^-(\theta) - f_{rk}^-(\theta)f_{rrk}(\theta) - f_{\theta k}^-(\theta)f_{r\theta k}(\theta)\right)\mathrm{d}\theta.$$

After the script loads the FE results (stress and displacement component values), the numerical integration is conducted by the trapezoidal rule:

$$\Psi_k^{\mathrm{FE}} = \sum_{n=1}\frac{\left(\mathrm{d}\Psi_k^{\mathrm{FE}}(\theta_{n-1}) + \mathrm{d}\Psi_k^{\mathrm{FE}}(\theta_n)\right)\Delta\theta}{2},$$

$$\Psi_k^{\mathrm{analyt}} = \sum_{n=1}\frac{\left(\mathrm{d}\Psi_k^{\mathrm{analyt}}(\theta_{n-1}) + \mathrm{d}\Psi_k^{\mathrm{analyt}}(\theta_n)\right)\Delta\theta}{2},$$

where the numerical integration step, the $\Delta\theta$ is dependent on the circle division by elements (node to node distance). The script finally returns the resultant kth GSIFs:

$$H_k = \frac{\Psi_k^{\mathrm{FE}}}{\Psi_k^{\mathrm{analyt}}}.$$

Circle division by 5° or 2.5° (for notch of $2\alpha = 90°$ i.e. 54 or 108 integration points) both give results of solid computational convergence. As shown in the Numerical example C that follows, the choice of the integration step

	λ_1	λ_2	λ_3	λ_4
$2\alpha = 60°$	0.556318	0.678908	$1.495694 \pm 0.126455i$	$2.056555 \pm 0.196967i$
$2\alpha = 90°$	0.572603	0.859567	$1.693610 \pm 0.206185i$	$2.294796 \pm 0.164660i$
$2\alpha = 120°$	0.627362	1.098829	1.779801	$2.119643 \pm 0.380189i$

Table 5: Bi-material notch with bi-material configuration of $E_1/E_2 = 0.25$ and 3 geometric configurations $2\alpha = 60°$, $90°$, $120°$

	$H_1^{\Delta\theta=2.5°}$			$s^{\Delta\theta=2.5°}$	$H_1^{\Delta\theta=5.0°}$			$s^{\Delta\theta=5.0°}$
2α	$r = 1$ mm	$r = 3$ mm	avg.	avg.	$r = 1$ mm	$r = 3$ mm	avg.	avg.
60°	49.074983	49.348909	49.122359	0.071201	49.105613	49.153084	49.043314	0.039942
90°	51.320719	51.158123	51.234381	0.043204	51.366651	51.145435	51.199755	0.083277
120°	54.323977	53.909335	54.152227	0.114307	54.384717	53.867149	54.161656	0.143541

Table 6: V-notch Ψ-integral results for various 2α geometries. The values of leading term factor H_1 determined on multiple radii with finer integration step of $\Delta\theta = 2.5°$ are listed in the left part of the table and coarser integration step of $\Delta\theta = 5.0°$ in the right side of the table. Both the cases are supplemented by standard deviation of the averaged value denoted by s.

from 54 to 108 integration steps changes the value of leading term H_1 by less than 0.5 % in all tested cases. In Figure 32 a detail of meshed model with element edge division by 2.5° is shown. For the case of the double root $\lambda_1 = \lambda_2 = \lambda$ the stress intensity factors H_1 and H_2 are obtained by solving the system of two equations:

$$\begin{aligned}\Psi(u^{\mathrm{FE}}, r^{-\lambda} f_{i1}^{-}(\theta)) &= H_1 \Psi(r^{\lambda} f_{i1}(\theta), r^{-\lambda} f_{i1}^{-}(\theta)) + H_2 \Psi(r^{\lambda} f_{i2}(\theta), r^{-\lambda} f_{i1}^{-}(\theta)),\\ \Psi(u^{\mathrm{FE}}, r^{-\lambda} f_{i2}^{-}(\theta)) &= H_1 \Psi(r^{\lambda} f_{i1}(\theta), r^{-\lambda} f_{i2}^{-}(\theta)) + H_2 \Psi(r^{\lambda} f_{i2}(\theta), r^{-\lambda} f_{i2}^{-}(\theta)).\end{aligned}$$

From the equations as we defined it follows, that we need to do final adjustment for generalized stress intensity factors.

$$H_k := \begin{cases} H_k & \text{for } \Im\{\lambda_k\} \neq 0 \\ H_k/2 & \text{for } \Im\{\lambda_k\} = 0 \end{cases}$$

Numerical example C: Integration step and path independence of the Ψ-integral for notches. The test example consists of the Ψ-integral calculation for 3 geometric configurations of the V-notch $2\alpha = 60°$, $90°$, $120°$ ($\gamma_1 = \alpha$, $\gamma_2 = 360° - \alpha$) and 3 geometric configurations of the bi-material notch $2\alpha = 60°$, $90°$, $120°$ ($\gamma_1 = \alpha, \gamma_2 = 180°, \gamma_3 = 360° - \alpha$) with $E_1/E_2 = 0.25$, $E_1 = 20$ GPa and $\nu_1 = \nu_2 = 0.25$. The eigenvalues for the case of a V-notch were calculated in Numerical example A on p. 30. The first four eigenvalues for the bi-material notch are found in Table 5. In both the V-notch and bi-material notch test example the effect of integration step size $\Delta\theta$ is shown on multiple integration radii. The circles of multiple radii have been taken into account to another test example purpose, to validate the Ψ-integral path independence. Geometry of the model is identical to the one in Numerical example E on p. 50 in the case of the V-notch and to the one in Numerical example F on p. 53 in the case of the bi-material notch. In both cases, the model is loaded with force $F = 100N$ (per 1 mm of specimen thickness b). The leading term factor H_1 for the symmetrically loaded V-notch and leading term factors H_1 and H_2 for the case of the bi-material notch are calculated on $r_1 = 1$ mm, $r_2 = 3$ mm and as an average on all the radii between r_1 and r_2 (the script adjust the mesh automatically, so there are 10 circles in the case of larger integration step and 22 circles in the case of smaller integration step). The results for the V-notch are listed in Table 6. The results for the bi-material notch are found in Tables 7 and 8. In both cases, the left part of the table consists of smaller integration step results obtained by finer element division by $\Delta\theta = 2.5°$. The right side of the tables represents larger integration step results obtained with coarser element division by$\Delta\theta = 5.0°$. The results are supplemented by standard deviation of the average value denoted by $s^{\Delta\theta=2.5°}$ or $s^{\Delta\theta=5.0°}$. The choice of number of the integration steps from 54 to 108 integration steps changes the value of leading term factor H_1 by less than 0.5 % in both tested cases. The effect of the integration step on the resulting value of second leading term factor H_2 in the case of the bi-material notch is more profound especially towards the large 2α. For such cases, the standard deviation value s is decreased by using a finer integration step. Therefore the choice of the finer integration step is beneficial. The effect of integration path radius on the leading term factor H_1 value was always less than 1 % of the resulting

	$H_1^{\Delta\theta=2.5°}$			$s^{\Delta\theta=2.5°}$	$H_1^{\Delta\theta=5.0°}$			$s^{\Delta\theta=5.0°}$
2α	$r = 1$ mm	$r = 3$ mm	avg.	avg.	$r = 1$ mm	$r = 3$ mm	avg.	avg.
60°	2.948757	2.935656	2.936589	0.000437	2.978178	2.950140	2.952096	0.001021
90°	9.159032	9.113595	9.123140	0.004574	9.200633	9.108610	9.125289	0.008979
120°	7.235544	7.210268	7.214646	0.002019	7.262257	7.209313	7.217978	0.004529

Table 7: Bi-material notch Ψ-integral results for various 2α geometries. The values of leading term factor H_1 determined on multiple radii with finer integration step of $\Delta\theta = 2.5°$ are listed in the left part of the table and coarser integration step of $\Delta\theta = 5.0°$ in the right side of the table. Both the cases are supplemented by standard deviation of the averaged value denoted by s.

	$H_2^{\Delta\theta=2.5°}$			$s^{\Delta\theta=2.5°}$	$H_2^{\Delta\theta=5.0°}$			$s^{\Delta\theta=5.0°}$
2α	$r = 1$ mm	$r = 3$ mm	avg.	avg.	$r = 1$ mm	$r = 3$ mm	avg.	avg.
60°	8.196698	8.218343	8.186926	0.018445	7.779961	7.808389	7.755549	0.032715
90°	3.197018	3.283971	3.230628	0.032228	2.845325	2.998096	2.906699	0.058189
120°	0.080194	0.226453	0.153295	0.046779	−0.280710	−0.014312	−0.142072	0.085072

Table 8: Bi-material notch Ψ-integral results for various 2α geometries. The values of leading term factor H_2 determined on multiple radii with finer integration step of $\Delta\theta = 2.5°$ are listed in the left part of the table and coarser integration step of $\Delta\theta = 5.0°$ in the right side of the table. Both the cases are supplemented by standard deviation of the averaged value denoted by s.

value. The trends in the dependence of the integration radius are shown in graphs in Figure 34. Although the trend is plotted only for one geometric and bi-material configuration, it represents standard behavior of H_k calculation convergence by the Ψ-integral. We see that the leading term factors H_1 and H_2 show solid convergence on all integration radii, whereas the higher order term factors converge towards larger integration radii. We therefore recommend to determine the higher order term factors on the larger distances such as $r_2 = 3$ mm. To check that the radius to determine GSIFs was chosen correctly, we can compare the reconstructed analytical solution with pure FE solution (either on particular radius of interest or on the whole field, e.g. 0.1 mm - 3 mm) as it will be shown in Numerical example E and F on p. 50 and 53 respectively.

Determination of GSIFs by overdeterministic method

The overdeterministic method (ODM) belongs to so called direct methods and is based on the least-squares solution of overdetermined system of linear equations. The method was firstly proposed by Seweryn in [34] under a name of method of analytical constraints. In [35] Ayatollahi and Nejati applied this method to calculate SIFs of a crack problem. In an article that followed, they applied the ODM to the sharp notch problem [36]. Next Ayatollahi et al. studied ODM in application to the bi-material notch problem in [55], however they studied effect of first and real non-singular term only. The ODM is chosen especially because of its minimal requirements for the FE software (no need for special elements). The ODM takes large number of results, namely displacements from FEM to compute chosen number of GSIFs (stress components can also be used for GSIFs determination by the ODM). The displacements are usually preferred because the majority of FE codes is displacement based, which leads to increased inherent precision. The method can be used for calculation of $H_k \in \mathbb{R}$ when the real form of the stress Eq. (28) and displacement series Eq. (30) on p. 26 is considered. As stated above, the goal of the ODM is to find n GSIFs as a least square method solution of an overdetermined system of linear equations. These equations can be written in a matrix form as:

$$\begin{bmatrix} f^*_{r1}(\theta_1)\, r^{\lambda_1} & f^*_{r2}(\theta_1)\, r^{\lambda_2} & \dots & f^*_{rn}(\theta_1)\, r^{\lambda_n} \\ f^*_{r1}(\theta_2)\, r^{\lambda_1} & f^*_{r2}(\theta_2)\, r^{\lambda_2} & \dots & f^*_{rn}(\theta_2)\, r^{\lambda_n} \\ \vdots & \vdots & & \vdots \\ f^*_{r1}(\theta_m)\, r^{\lambda_1} & f^*_{r2}(\theta_m)\, r^{\lambda_2} & \dots & f^*_{rn}(\theta_m)\, r^{\lambda_n} \\ f^*_{\theta 1}(\theta_1)\, r^{\lambda_1} & f^*_{\theta 2}(\theta_1)\, r^{\lambda_2} & \dots & f^*_{\theta n}(\theta_1)\, r^{\lambda_n} \\ f^*_{\theta 1}(\theta_2)\, r^{\lambda_1} & f^*_{\theta 2}(\theta_2)\, r^{\lambda_2} & \dots & f^*_{\theta n}(\theta_2)\, r^{\lambda_n} \\ \vdots & \vdots & & \vdots \\ f^*_{\theta 1}(\theta_m)\, r^{\lambda_1} & f^*_{\theta 2}(\theta_m)\, r^{\lambda_2} & \dots & f^*_{\theta n}(\theta_m)\, r^{\lambda_n} \end{bmatrix} \begin{bmatrix} H_1 \\ H_2 \\ \vdots \\ H_n \end{bmatrix} = \begin{bmatrix} u^{\mathrm{FE}}_{r1}(r,\theta_1) \\ u^{\mathrm{FE}}_{r2}(r,\theta_2) \\ \vdots \\ u^{\mathrm{FE}}_{rm}(r,\theta_m) \\ u^{\mathrm{FE}}_{\theta 1}(r,\theta_1) \\ u^{\mathrm{FE}}_{\theta 2}(r,\theta_2) \\ \vdots \\ u^{\mathrm{FE}}_{\theta m}(r,\theta_m) \end{bmatrix} \tag{54}$$

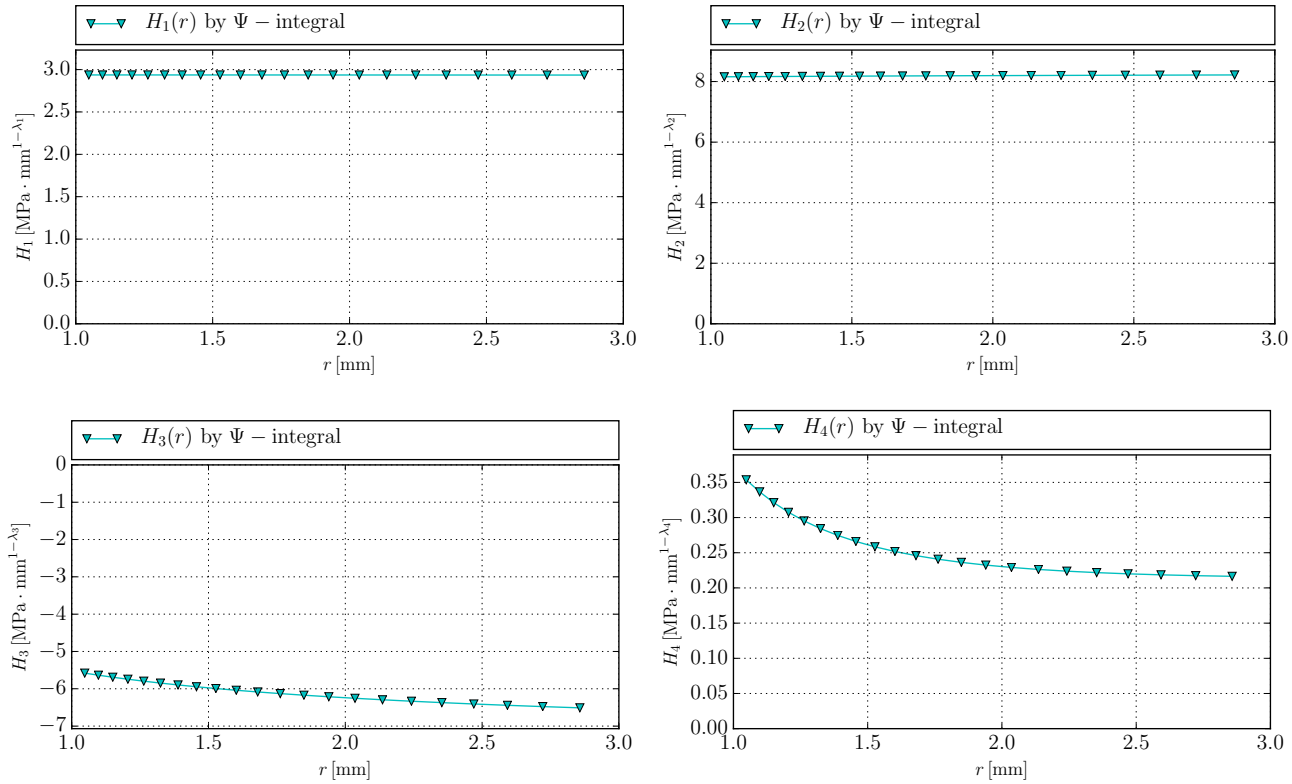

Figure 34: Dependence of the H_k on the radial distance r. The bi-material notch, $2\alpha = 60°$, $E_1/E_2 = 0.25$. Calculation by the Ψ-integral.

On the left-hand side the eigenfunctions of the first n displacement series term factors are listed in $2m$ lines which form the matrix[7]. First the m lines of this matrix are filled with the eigenfunctions for the radial displacement components. These are followed by m lines of eigenfunctions for tangential displacement components. The vector on the left-hand side is composed of n unknown GSIFs H_k. Finally, a vector of $2m$ length composed of FEA calculated m radial displacements and m tangential displacements stays on the right-hand side. For an overdetermined system of linear equations (54), in a short form written:

$$\mathbf{F}_{[2m\times n]}\mathbf{H}_{[n]} \quad = \quad \mathbf{u}^{\mathrm{FE}}_{[2m]}, \tag{55}$$

no exact solution exists, since $2m > n$. The approximation of solution (vector $\mathbf{H}_{[n]}$ that contains n GSIFs) is found by minimizing the residual vector:

$$\mathbf{r} \quad = \quad \mathbf{F}_{[2m\times n]}\mathbf{H}_{[n]} - \mathbf{u}^{\mathrm{FE}}_{[2m]} \tag{56}$$

by the least square method. In the general case of $H_k \in \mathbb{C}$, the complex form of the stress and displacement series is Eq. (20) and displacement series Eq. (24) on p. 25 is considered. According to [34], the series is decomposed to

[7]The index m used in this sub-chapter does not correspond to the index m for mth material region. Identical index is used because of lack of useful indices.

real and imaginary part which is written in the matrix form as:

$$\begin{bmatrix} \Re\left\{f_{r1}\left(\theta_1\right)r^{\lambda_1}\right\} & \Im\left\{f_{r1}\left(\theta_1\right)r^{\lambda_1}\right\} & \dots & \Re\left\{f_{rn}\left(\theta_1\right)r^{\lambda_n}\right\} & \Im\left\{f_{rn}\left(\theta_1\right)r^{\lambda_n}\right\} \\ \Re\left\{f_{r1}\left(\theta_2\right)r^{\lambda_1}\right\} & \Im\left\{f_{r1}\left(\theta_2\right)r^{\lambda_1}\right\} & \dots & \Re\left\{f_{rn}\left(\theta_2\right)r^{\lambda_n}\right\} & \Im\left\{f_{rn}\left(\theta_2\right)r^{\lambda_n}\right\} \\ \vdots & \vdots & & \vdots & \vdots \\ \Re\left\{f_{r1}\left(\theta_m\right)r^{\lambda_1}\right\} & \Im\left\{f_{r1}\left(\theta_m\right)r^{\lambda_1}\right\} & \dots & \Re\left\{f_{rn}\left(\theta_m\right)r^{\lambda_n}\right\} & \Im\left\{f_{rn}\left(\theta_m\right)r^{\lambda_n}\right\} \\ \Re\left\{f_{\theta 1}\left(\theta_1\right)r^{\lambda_1}\right\} & \Im\left\{f_{\theta 1}\left(\theta_1\right)r^{\lambda_1}\right\} & \dots & \Re\left\{f_{\theta n}\left(\theta_1\right)r^{\lambda_n}\right\} & \Im\left\{f_{\theta n}\left(\theta_1\right)r^{\lambda_n}\right\} \\ \Re\left\{f_{\theta 1}\left(\theta_2\right)r^{\lambda_1}\right\} & \Im\left\{f_{\theta 1}\left(\theta_2\right)r^{\lambda_1}\right\} & \dots & \Re\left\{f_{\theta n}\left(\theta_2\right)r^{\lambda_n}\right\} & \Im\left\{f_{\theta n}\left(\theta_2\right)r^{\lambda_n}\right\} \\ \vdots & \vdots & & \vdots & \vdots \\ \Re\left\{f_{\theta 1}\left(\theta_m\right)r^{\lambda_1}\right\} & \Im\left\{f_{\theta 1}\left(\theta_m\right)r^{\lambda_1}\right\} & \dots & \Re\left\{f_{\theta n}\left(\theta_m\right)r^{\lambda_n}\right\} & \Im\left\{f_{\theta n}\left(\theta_m\right)r^{\lambda_n}\right\} \end{bmatrix} \begin{bmatrix} \Re\left\{H_1\right\} \\ \Im\left\{H_1\right\} \\ \Re\left\{H_2\right\} \\ \Im\left\{H_2\right\} \\ \vdots \\ \Re\left\{H_n\right\} \\ \Im\left\{H_n\right\} \end{bmatrix} = \mathbf{u}^{\mathrm{FE}}_{[2m]},$$

where $n' = 2n$ and the FE vector $\mathbf{u}^{\mathrm{FE}}_{[2m]}$ is identical to the previous real case. The equation is in matrix form written analogically to (55) i.e. $\mathbf{F}_{[2m\times n']}\mathbf{H}_{[n']} = \mathbf{u}^{\mathrm{FE}}_{[2m]}$ and the solution is found also by minimizing residual vector analogically to (56) i.e. $\mathbf{r} = \mathbf{F}_{[2m\times n']}\mathbf{H}_{[n']} - \mathbf{u}^{\mathrm{FE}}_{[2m]}$. The resulting GSIFs are finally reconstructed as:

$$H_k = \Re\left\{H_k\right\} + i\Im\left\{H_k\right\}. \tag{57}$$

The nodal displacements in both radial and tangential directions are again taken from nodal points lying on a circle surrounding the singular point r_1, see Figure 33. These nodal points are therefore characterized by the fixed radial coordinate r_1 and variable angular coordinate $\theta_j \in (1; m)$ as shown in Figure 33, which describes the FE results extraction. As for the Ψ-integral calculation, the ODM can be calculated on any circle between r_0 and r_2. Furthermore the method does not require to take values from nodes laying on a circle. Values from basically any pattern can be used to calculate unknown GSIFs H_k by the ODM. Choice of circle is again seen by the author as the simplest mean of H_k computation. However, there are some setbacks related to the displacement based ODM. By the form of the ODM used in this work, the valid results are obtained for symmetrical problems (in terms of geometry and loading) of a V-notch and bi-material junction. The problem of a bi-material notch is always a non-symmetrical one. In the symmetrical cases the rigid body rotation of the specimen is equal to zero and does not enter into the calculation H_k . If the problem is non-symmetrical, the rigid body rotation is present. Please note that it cannot be as easily subtracted from the FE displacements as the rigid body translation can be. The rigid body rotation may be included in the displacement series by adding a term with $\lambda_k^{\mathrm{rot}} = 1$, which describes it, as in [35, 36, 55]. The general determination of this term is nevertheless difficult. By substitution of the unit eigenvalue back into matrix $\mathbf{A}(\lambda)$, one is unable to obtain the needed eigenfunction, since there is no solution of reduced system of equations $\mathbf{A}^{\mathrm{red}}(\lambda_k^{\mathrm{rot}})$. The development of method to include rigid body rotation of a general problem in terms of methods of plane elasticity used in this work could be a subject of further research. Therefore, in the author's opinion, in non-symmetrical cases it is recommended to use the stress based ODM, which completely eliminates the problem. We consider the stress series, Eq. (28) as in p. 26. Similarly as in the displacement based ODM, we need to find a approximation of a solution of an overdetermined system of linear equations, which in the case of $H_k \in \mathbb{R}$ is:

$$\begin{bmatrix} f^*_{rr1}\left(\theta_1\right)r^{\lambda_1} & f^*_{rr2}\left(\theta_1\right)r^{\lambda_2} & \dots & f^*_{rrn}\left(\theta_1\right)r^{\lambda_n} \\ f^*_{rr1}\left(\theta_2\right)r^{\lambda_1} & f^*_{rr2}\left(\theta_2\right)r^{\lambda_2} & \dots & f^*_{rrn}\left(\theta_2\right)r^{\lambda_n} \\ \vdots & \vdots & & \vdots \\ f^*_{rr1}\left(\theta_m\right)r^{\lambda_1} & f^*_{rr2}\left(\theta_m\right)r^{\lambda_2} & \dots & f^*_{rrn}\left(\theta_m\right)r^{\lambda_n} \\ f^*_{r\theta 1}\left(\theta_1\right)r^{\lambda_1} & f^*_{r\theta 2}\left(\theta_1\right)r^{\lambda_2} & \dots & f^*_{r\theta n}\left(\theta_1\right)r^{\lambda_n} \\ f^*_{r\theta 1}\left(\theta_2\right)r^{\lambda_1} & f^*_{r\theta 2}\left(\theta_2\right)r^{\lambda_2} & \dots & f^*_{r\theta n}\left(\theta_2\right)r^{\lambda_n} \\ \vdots & \vdots & & \vdots \\ f^*_{r\theta 1}\left(\theta_m\right)r^{\lambda_1} & f^*_{r\theta 2}\left(\theta_m\right)r^{\lambda_2} & \dots & f^*_{r\theta n}\left(\theta_m\right)r^{\lambda_n} \\ f^*_{\theta\theta 1}\left(\theta_1\right)r^{\lambda_1} & f^*_{\theta\theta 2}\left(\theta_1\right)r^{\lambda_2} & \dots & f^*_{\theta\theta n}\left(\theta_1\right)r^{\lambda_n} \\ f^*_{\theta\theta 1}\left(\theta_2\right)r^{\lambda_1} & f^*_{\theta\theta 2}\left(\theta_2\right)r^{\lambda_2} & \dots & f^*_{\theta\theta n}\left(\theta_2\right)r^{\lambda_n} \\ \vdots & \vdots & & \vdots \\ f^*_{\theta\theta 1}\left(\theta_m\right)r^{\lambda_1} & f^*_{\theta\theta 2}\left(\theta_m\right)r^{\lambda_2} & \dots & f^*_{\theta\theta n}\left(\theta_m\right)r^{\lambda_n} \end{bmatrix} \begin{bmatrix} H_1 \\ H_2 \\ \vdots \\ H_n \end{bmatrix} = \begin{bmatrix} \sigma^{\mathrm{FE}}_{rr1}\left(r,\theta_1\right) \\ \sigma^{\mathrm{FE}}_{rr2}\left(r,\theta_2\right) \\ \vdots \\ \sigma^{\mathrm{FE}}_{rrm}\left(r,\theta_m\right) \\ \sigma^{\mathrm{FE}}_{r\theta 1}\left(r,\theta_1\right) \\ \sigma^{\mathrm{FE}}_{r\theta 2}\left(r,\theta_2\right) \\ \vdots \\ \sigma^{\mathrm{FE}}_{r\theta m}\left(r,\theta_m\right) \\ \sigma^{\mathrm{FE}}_{\theta\theta 1}\left(r,\theta_1\right) \\ \sigma^{\mathrm{FE}}_{\theta\theta 2}\left(r,\theta_2\right) \\ \vdots \\ \sigma^{\mathrm{FE}}_{\theta\theta m}\left(r,\theta_m\right) \end{bmatrix}. \tag{58}$$

The matrix on the left-hand side is formed of the known analytical eigenfunctions. On the left-hand side we also find the unknown vector of n GSIFs. The right-hand side vector consists of radial, shear and tangential stress

components, determined by FE. For an overdetermined system of stress based linear equations (58) that is in a short form written:

$$\mathbf{F}_{[3m\times n]}\mathbf{H}_{[n]} \quad = \quad \mathbf{S}^{\mathrm{FE}}_{[3m]}, \tag{59}$$

as in the previous case of the displacement based ODM, since $3m > n$ no exact solution exists. The approximation of the solution is found by minimizing the residual vector:

$$\mathbf{r} \quad = \quad \mathbf{F}_{[3m\times n]}\mathbf{H}_{[n]} - \mathbf{S}^{\mathrm{FE}}_{[3m]}$$

by the least square method. In the general case of $H_k \in \mathbb{C}$ the system has the following form:

$$\begin{bmatrix}
\Re\left\{f_{rr1}\left(\theta_1\right)r^{\lambda_1}\right\} & \Im\left\{f_{rr1}\left(\theta_1\right)r^{\lambda_1}\right\} & \dots & \Re\left\{f_{rrn}\left(\theta_1\right)r^{\lambda_n}\right\} & \Im\left\{f_{rrn}\left(\theta_1\right)r^{\lambda_n}\right\} \\
\Re\left\{f_{rr1}\left(\theta_2\right)r^{\lambda_1}\right\} & \Im\left\{f_{rr1}\left(\theta_2\right)r^{\lambda_1}\right\} & \dots & \Re\left\{f_{rrn}\left(\theta_2\right)r^{\lambda_n}\right\} & \Im\left\{f_{rrn}\left(\theta_2\right)r^{\lambda_n}\right\} \\
\vdots & \vdots & & \vdots & \vdots \\
\Re\left\{f_{rr1}\left(\theta_m\right)r^{\lambda_1}\right\} & \Im\left\{f_{rr1}\left(\theta_m\right)r^{\lambda_1}\right\} & \dots & \Re\left\{f_{rrn}\left(\theta_m\right)r^{\lambda_n}\right\} & \Im\left\{f_{rrn}\left(\theta_m\right)r^{\lambda_n}\right\} \\
\Re\left\{f_{r\theta1}\left(\theta_1\right)r^{\lambda_1}\right\} & \Im\left\{f_{r\theta1}\left(\theta_1\right)r^{\lambda_1}\right\} & \dots & \Re\left\{f_{r\theta n}\left(\theta_1\right)r^{\lambda_n}\right\} & \Im\left\{f_{r\theta n}\left(\theta_1\right)r^{\lambda_n}\right\} \\
\Re\left\{f_{r\theta1}\left(\theta_2\right)r^{\lambda_1}\right\} & \Im\left\{f_{r\theta1}\left(\theta_2\right)r^{\lambda_1}\right\} & \dots & \Re\left\{f_{r\theta n}\left(\theta_2\right)r^{\lambda_n}\right\} & \Im\left\{f_{r\theta n}\left(\theta_2\right)r^{\lambda_n}\right\} \\
\vdots & \vdots & & \vdots & \vdots \\
\Re\left\{f_{r\theta1}\left(\theta_m\right)r^{\lambda_1}\right\} & \Im\left\{f_{r\theta1}\left(\theta_m\right)r^{\lambda_1}\right\} & \dots & \Re\left\{f_{r\theta n}\left(\theta_m\right)r^{\lambda_n}\right\} & \Im\left\{f_{r\theta n}\left(\theta_m\right)r^{\lambda_n}\right\} \\
\Re\left\{f_{\theta\theta1}\left(\theta_1\right)r^{\lambda_1}\right\} & \Im\left\{f_{\theta\theta1}\left(\theta_1\right)r^{\lambda_1}\right\} & \dots & \Re\left\{f_{\theta\theta n}\left(\theta_1\right)r^{\lambda_n}\right\} & \Im\left\{f_{\theta\theta n}\left(\theta_1\right)r^{\lambda_n}\right\} \\
\Re\left\{f_{\theta\theta1}\left(\theta_2\right)r^{\lambda_1}\right\} & \Im\left\{f_{\theta\theta1}\left(\theta_2\right)r^{\lambda_1}\right\} & \dots & \Re\left\{f_{\theta\theta n}\left(\theta_2\right)r^{\lambda_n}\right\} & \Im\left\{f_{\theta\theta n}\left(\theta_2\right)r^{\lambda_n}\right\} \\
\vdots & \vdots & & \vdots & \vdots \\
\Re\left\{f_{\theta\theta1}\left(\theta_m\right)r^{\lambda_1}\right\} & \Im\left\{f_{\theta\theta1}\left(\theta_m\right)r^{\lambda_1}\right\} & \dots & \Re\left\{f_{\theta\theta n}\left(\theta_m\right)r^{\lambda_n}\right\} & \Im\left\{f_{\theta\theta n}\left(\theta_m\right)r^{\lambda_n}\right\}
\end{bmatrix}
\begin{bmatrix}
\Re\{H_1\} \\ \Im\{H_1\} \\ \Re\{H_2\} \\ \Im\{H_2\} \\ \vdots \\ \Re\{H_n\} \\ \Im\{H_n\}
\end{bmatrix}
= \mathbf{S}^{\mathrm{FE}}_{[3m]},$$

where $n' = 2n$ and the FE vector $\mathbf{S}^{\mathrm{FE}}_{[3m]}$ is identical to the previous real case. The resulting GSIFs are constructed using Eq. (57). Since the factors are determined on particular radius r, it is recommended to check if the dependence $H_k\left(r\right)$ exists. If the strong and linear dependence exists, the singular leading term factors H_k can be extrapolated to $r \to 0$ by the linear regression (it is not recommended to calculate the GSIFs directly on a radius too close to singularity because of a significant numerical error). The method of calculation of H_k by the linear regression is in accordance to the definition of the stress intensity factor by a limit. If the dependence exists in the case of higher order terms the averaged value can be calculated however, in the author's experience, when the GSIFs are calculated reasonably far from singularity, the radial dependence is in general week, which will be shown and commented in numerical examples. To make sure that the used methodology is valid, we can compare the reconstructed analytical solution with pure FE solution (again as in the case of the Ψ-integral, the comparison can be made on particular radius of interest or on the whole stress field). From mathematical point of view, the values of factors H_k should be dependent on the vector $\mathbf{H}_{[n']}$ length (number n of factors being calculated). This effect is investigated in following numerical example with foundation that the first two terms factors H_1 and H_2 converge when $n' > 4$ and the higher order terms H_3 and H_4 when $n' > 16$. Although the behavior is demonstrated only on one numerical example, it is a general one and is in accordance with results published by Ayatollahi and Nejati in [36]. We therefore recommend to chose $n' > 16$ when the higher order terms are of interest.

To conclude, we now compare the advantages and disadvantages of the ODM and Ψ-integral. General advantage of the ODM is its simplicity and its low computational cost. The general disadvantage of the ODM is its dependency on the number of term factors to be determined, which origins from the mathematical foundation of the method. Such effect will be examined in the following Numerical example D. The main advantage of the Ψ-integral is, that the H_k are determined mutually independently. In any case it is beneficial to compare results calculated by both methods with each other to prevent random errors. The comparison of results determined by both methods is shown in Numerical example D.

Numerical example D: Determination of GSIFs by the ODM. We consider the identical bi-material notch as in previous Numerical example C on p. 43 with $2\alpha = 60°$, $90°$, $120°$ and $E_1/E_2 = 0.25$. The leading singular terms with H_1 and H_2 and higher order terms with H_3 and H_4 are calculated by the stress based overdeterministic method. Since we calculate the singular and non-singular term factors, the radius for the ODM determination is chosen as $r_1 \in (0.2 - 1)$ mm which is the area where the above mentioned singular and non-singular terms prevail. In addition, for the model created in this work, this area is characterized by low FE error. The effect of element

	$H_1^{\Delta\theta=2.5°}$			$s^{\Delta\theta=2.5°}$	$H_1^{\Delta\theta=5.0°}$			$s^{\Delta\theta=5.0°}$
2α	$r = 0.2$ mm	$r = 1$ mm	avg.	avg.	$r = 0.2$ mm	$r = 1$ mm	avg.	avg.
60°	2.918742	2.940974	2.917949	0.000630	2.911692	2.958155	2.909008	0.002037
90°	9.116427	9.177946	9.113761	0.001769	9.104589	9.230813	9.093580	0.006558
120°	7.210331	7.249287	7.208264	0.001346	7.207143	7.286563	7.199797	0.005228

Table 9: Bi-material notch results for $2\alpha = 60°$, 90°, 120° geometries and $E_1/E_2 = 0.25$. Values of leading term factor H_1 determined on multiple radii with finer division $\Delta\theta = 2.5°$ are listed in the left part of the table and coarser division $\Delta\theta = 5.0°$ on the right-hand side of the table. The both cases are supplemented by the standard deviation of the averaged value denoted by $s^{\Delta\theta=2.5°}$ and $s^{\Delta\theta=5.0°}$.

	$H_2^{\Delta\theta=2.5°}$			$s^{\Delta\theta=2.5°}$	$H_2^{\Delta\theta=5.0°}$			$s^{\Delta\theta=5.0°}$
2α	$r = 0.2$ mm	$r = 1$ mm	avg.	avg.	$r = 0.2$ mm	$r = 1$ mm	avg.	avg.
60°	8.627544	8.696743	8.630076	0.003981	8.581582	8.732149	8.585571	0.004568
90°	3.558906	3.575628	3.558123	0.001460	3.545283	3.573771	3.538515	0.002979
120°	0.461848	0.461554	0.461771	0.000072	0.464420	0.457764	0.461831	0.002264

Table 10: Bi-material notch results for $2\alpha = 60°$, 90°, 120° geometries and $E_1/E_2 = 0.25$. Values of leading term factor H_2 determined on multiple radii with finer division $\Delta\theta = 2.5°$ are listed in the left part of the table and coarser division $\Delta\theta = 5.0°$ on the right-hand side of the table. The both cases are supplemented by the standard deviation of the averaged value denoted by $s^{\Delta\theta=2.5°}$ and $s^{\Delta\theta=5.0°}$.

edge length division by 2.5° and 5.0° is studied. The resulting values are listed in Tables 9 and 10. The transition from coarser to finer element length has very low effect on the resulting value of leading GSIFs, with change less than 0.3 % in averaged H_1 and less than 0.6 % change in averaged H_2 for all studied configurations of 2α. The radial dependence of calculated leading singular terms factors H_1 and H_2 is shown in Figure 35. The graphs show that very slight linear dependence of the values exists (see values listed in tables above). Thus the singular terms factors extrapolation to $r \to 0$ is performed using the linear regression with resulting values shown in Table 9 and 10. This is in accordance to the fact, that the values of H_k calculated too close to the singular point may be heavily distorted by FE numerical error. Figure 36 shows radial dependence for non-singular terms factors H_3 and H_4. Non-singular terms factors show solid convergence towards $r = 1$ mm. The Table 11 and 12 compare values determined by the Ψ-integral (averaged) and ODM (linear regression extrapolated) with highest discrepancy of 22.1 % in the case of H_2 calculation and coarser mesh. This discrepancy is reduced to 10.2 % when finer mesh is used. The first singular term factor is calculated with almost identical values by both methods with maximum difference of 1.4 %. In all cases by mesh refinement, values with lower difference are obtained. We therefore recommend to use finer element division. Next, the effect of number of terms in vector $\mathbf{H}_{[n']}$ is studied, with results shown in Figure 37 for singular terms and in Figure 38 for non-singular terms. The results show that the first two terms factors H_1 and H_2 converge when $n' > 4$, as the difference between subsequent values of factor H_1 is always less

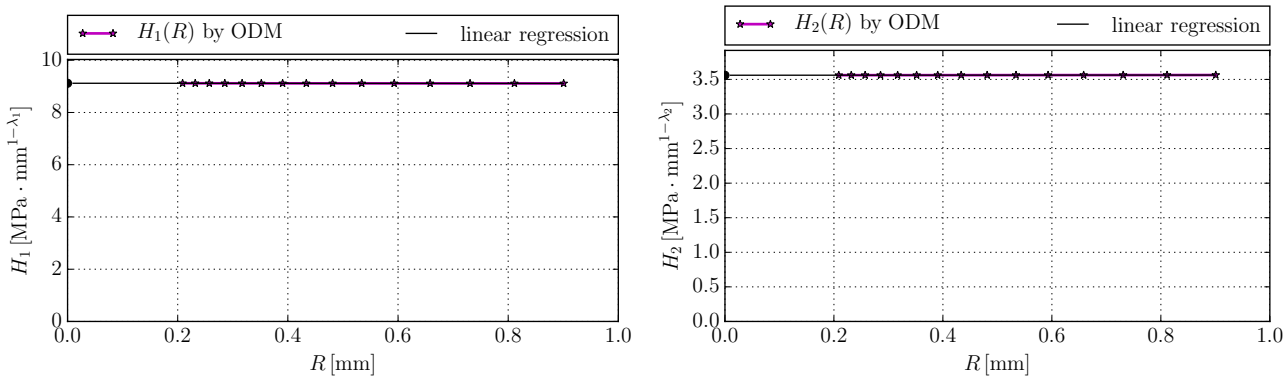

Figure 35: Dependence of the leading singular terms factors H_1 and H_2 on the radial distance r and fitted curve by the linear regression. The bi-material notch, $2\alpha = 90°$, $E_1/E_2 = 0.25$. Calculation by the ODM.

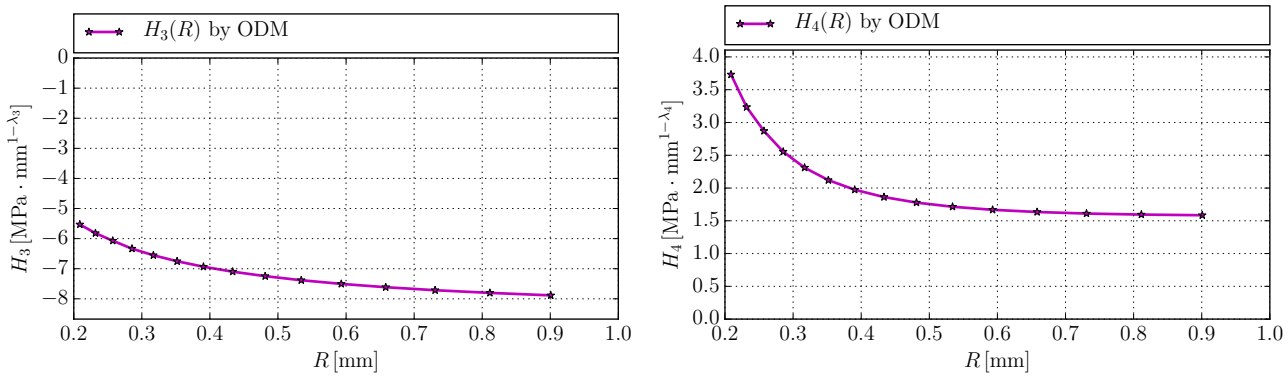

Figure 36: Dependence of the non-singular terms factors H_3 and H_4 on the radial distance r. The bi-material notch, $2\alpha = 90°$, $E_1/E_2 = 0.25$. Calculation by the ODM.

	$H_1^{\Delta\theta=2.5°}$			$H_1^{\Delta\theta=5.0°}$		
2α	ODM extrap.	$\Psi-$integral avg.	difference	ODM extrap.	$\Psi-$integral avg.	difference
60°	2.919937	2.936589	0.6 %	2.916078	2.952096	1.4 %
90°	9.118604	9.12314	0.1 %	9.111950	9.125289	0.2 %
120°	7.211273	7.214646	0.1 %	7.211940	7.217978	0.1 %

Table 11: Bi-material notch results for $2\alpha = 60°$ geometry. Values of leading term factor H_1 determined by the ODM extrapolation and as averaged value of the Ψ-integral. Both determined with finer division $\Delta\theta = 2.5°$ in the left part of the table and coarser division $\Delta\theta = 5.0°$ in the right part of the table.

than 0.5 % and the difference in H_2 subsequent values is always less than 1.5 %. In the case of higher order terms, the convergence rate of first non-singular term under 1.5 % is achieved with $n' > 8$. The second non-singular term H_4 convergence rate under 1.75 % is achieved with $n' > 16$. For researchers interested particularly in non-singular terms, we recommend the size of vector $\mathbf{H}_{[n']}$ at least $n' = 16$.

	$H_2^{\Delta\theta=2.5°}$			$H_2^{\Delta\theta=5.0°}$		
2α	ODM extrap.	$\Psi-$integral avg.	difference	ODM extrap.	$\Psi-$integral avg.	difference
60°	8.641101	8.186926	5.6 %	8.623311	7.755549	10.2 %
90°	3.560358	3.230628	10.2 %	3.548921	2.906699	22.1 %
120°	N/A	0.153295	N/A	N/A	−0.142072	N/A

Table 12: Bi-material notch results for $2\alpha = 60°$ geometry. Values of leading term factor H_2 determined by the ODM extrapolation and as averaged value of the Ψ-integral. For the case of $2\alpha = 120°$ the regression is not performed since the term factor H_2 is this case is non-singular. Both determined with finer division $\Delta\theta = 2.5°$ in the left part of the table and coarser division $\Delta\theta = 5.0°$ in the right part of the table.

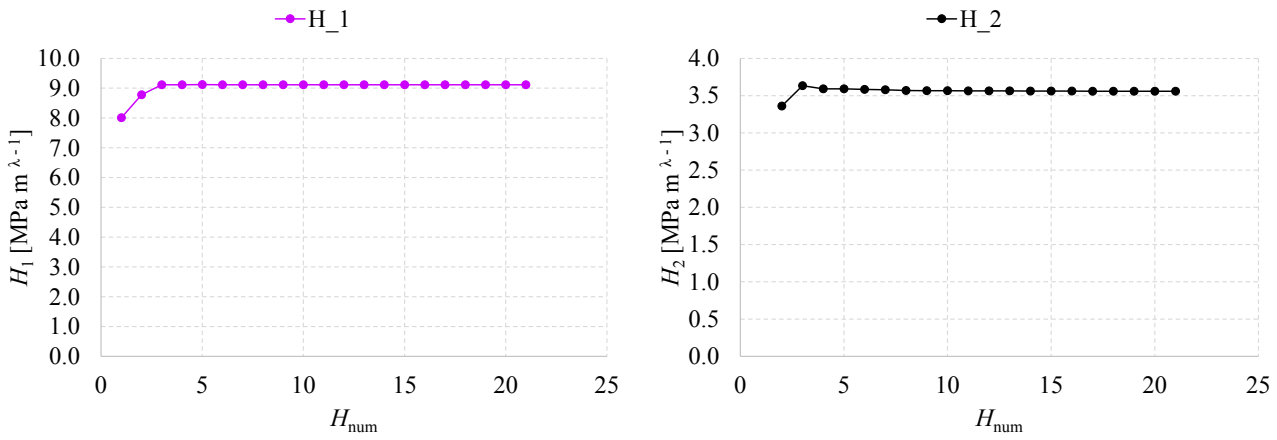

Figure 37: Dependence of the H_k value on the number of terms in vector H_n. The bi-material notch, $2\alpha = 90°$, $E_1/E_2 = 0.25$.

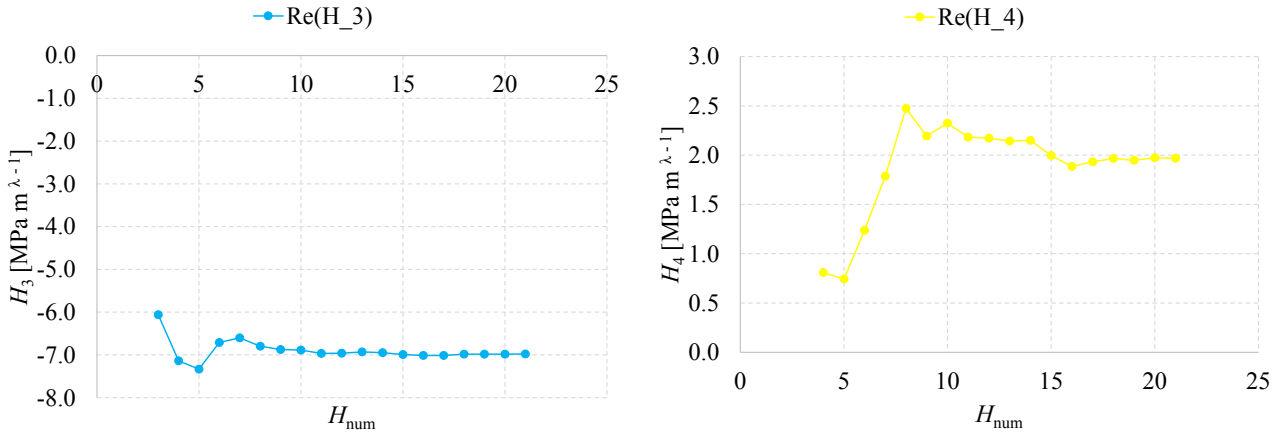

Figure 38: Dependence of the H_k value on the number of terms in vector H_n. The bi-material notch, $2\alpha = 90°$, $E_1/E_2 = 0.25$.

Numerical example E: Stress reconstruction for a V-notch. The specimen with the V-notch is modeled in 2D as shown in Figure 39 and it is characterized by the following dimensions: $L = 76.2$ mm, $h = 17.8$ mm, $a = 3.56$ mm, so the notch depth to height ratio is $a/h = 0.2$. The notch opening angle is $2\alpha = 90°$ ($\gamma_1 = \alpha, \gamma_2 = 180°, \gamma_3 = 360° - \alpha$). The specimen is modeled with PMMA (polymethyl methacrylate) material model, $E = 2.3$ GPa, $\nu = 0.34$ and loaded with force of $F = 1$ N (per 1 mm of specimen thickness b). Plane strain state is chosen. The first five GSIFs H_k are calculated by the Ψ-integral, with integration radius $r = 3$ mm and by the linear regression extrapolated displacement and stress based ODM with $r = 0.2 \div 1$ mm. The eigenfunctions are normalized per Eq. (38) on p. 29 with $\theta_0 = 180°$ where the coordinate system is shown in Figure 39. The parameters which form the mapped mesh near singular point as in Figure 33 are chosen as: $r_0 = 0.01$ mm, $r_1 = 1$ mm and $r_2 = 3$ mm and the element edge division is by 2.5°. The results are found in Table 13. We see that both methods for GSIFs calculation return values of the leading term factor H_1 close to each other (within 0.3 % comparing the Ψ-integral and the stress based ODM and 0.1 % comparing the Ψ-integral and the displacement based ODM). Because of symmetry of the problem, the odd terms factors of the expansion should be zero. This is true for H_2 since both methods give a number smaller than 10^{-5}. The higher order terms factors H_3, H_4 and H_5 values are complex and determined by both methods with signs of solid computational convergence. The factor H_3 value of both methods is close to each other, within 4.6 % when the stress based method is considered. For both methods, the odd term factor H_4 is again in terms of numerical methods equal to zero as it should be. To see how the asymptotic solution fits the pure FE solution, we can plot individual $\sigma_{ij}(r, \theta)$ on desired distance. Then

we can compare the FE solution with singular terms solution H_1, H_2 or with singular and non-singular solution $H_1 \div H_5$. The results can be even compared on a polar plot and the error between FE and asymptotic quantified as in [22]. First, lets take the GSIFs determined by the Ψ-integral. The stress field solution is reconstructed on radius $r = 1$ mm as in Figure 40. The FE solution is represented by the black squares. The singular terms solution is given dominantly by the singular term with λ_1 (the blue line), the consideration of second singular term containing λ_2 (the yellow line) does not lead to any change (as expected since $H_2 \approx 0$). The overall trend of the singular terms solution is close to the trend of FE solution. The consideration of non-singular terms however increases the precision of stress reconstruction. The highest increase in precision is given by considering the first non-singular term with λ_3 (magenta line). Employment of higher order terms with λ_4 (the cyan line) and the term with λ_5 (the red line) does not lead to significant precision increase as all the three lines overlap each other. As expected, the fourth term with λ_4 does not increase precision of the analytical solution since $H_4 \approx 0$. The H_5 does not make significant change because the stress is reconstructed on a relatively small distance from the singular point. The contribution of the fifth term would become significant on larger distances. In conclusion, the analytical solution given by the Ψ-integral with consideration of non-singular terms highly increases the precision of stress description and almost perfectly overlaps the FE solution. Next, a comparison of analytical solution with GSIFs determined by the stress based ODM is shown in Figure 41. We see a similar trend as in the previous case, that the singular terms provide solid stress description on this particular radius, nevertheless the precision is increased by the employment of higher order terms. Since we have seen in the Table 13 that both methods gave GSIFs close to each other and seen that the stress reconstruction by the Ψ-integral fits the FE quite well, such results are not very surprising. In conclusion, the singular terms determined by both methods approximate the FE solution well in terms of the overall stress trend. The higher order terms provide a slight increase in precision (see σ_{rr} stress component for the highest increase in precision). Both methods can be recommended for GSIFs calculation and the following fracture mechanics analysis. The choice of a particular method in this case is left to the preferences of the researcher.

k	λ_k	H_k^{Ψ}	$H_k^{\mathrm{ODM},\sigma_{ij}}$	H_k^{ODM,u_i}
1	0.544484	0.511508	0.512873	0.512086
2	0.908529	$6e-06$	$-3e-06$	$7e-06$
3	$1.629257 \pm 0.231251i$	$-0.031952 \pm 0.016126i$	$-0.06112 \pm 0.041541i$	$-0.047005 \pm 0.02195i$
4	$2.301327 \pm 0.315837i$	$-5e-06 \pm 2e-06i$	$-1.1e-05 \pm 4e-06i$	$-2.6e-05 \pm 0.00019i$
5	$2.971844 \pm 0.373931i$	$-0.000438 \pm 0.000577i$	$0.003176 \pm 0.000503i$	$0.05861 \pm 0.059737i$

Table 13: V-notch, first three eigenvalues λ_k and GSIFs H_k calculated by the Ψ-integral and the stress and displacement based ODM.

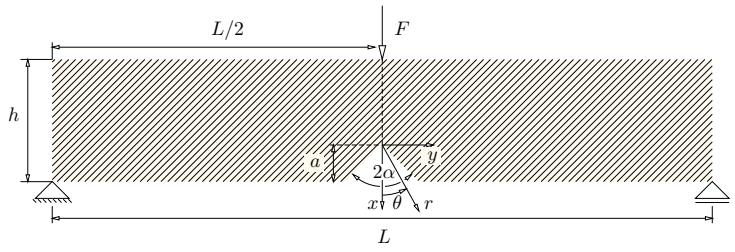

Figure 39: Model of V-notched specimen subjected to 3 point bending.

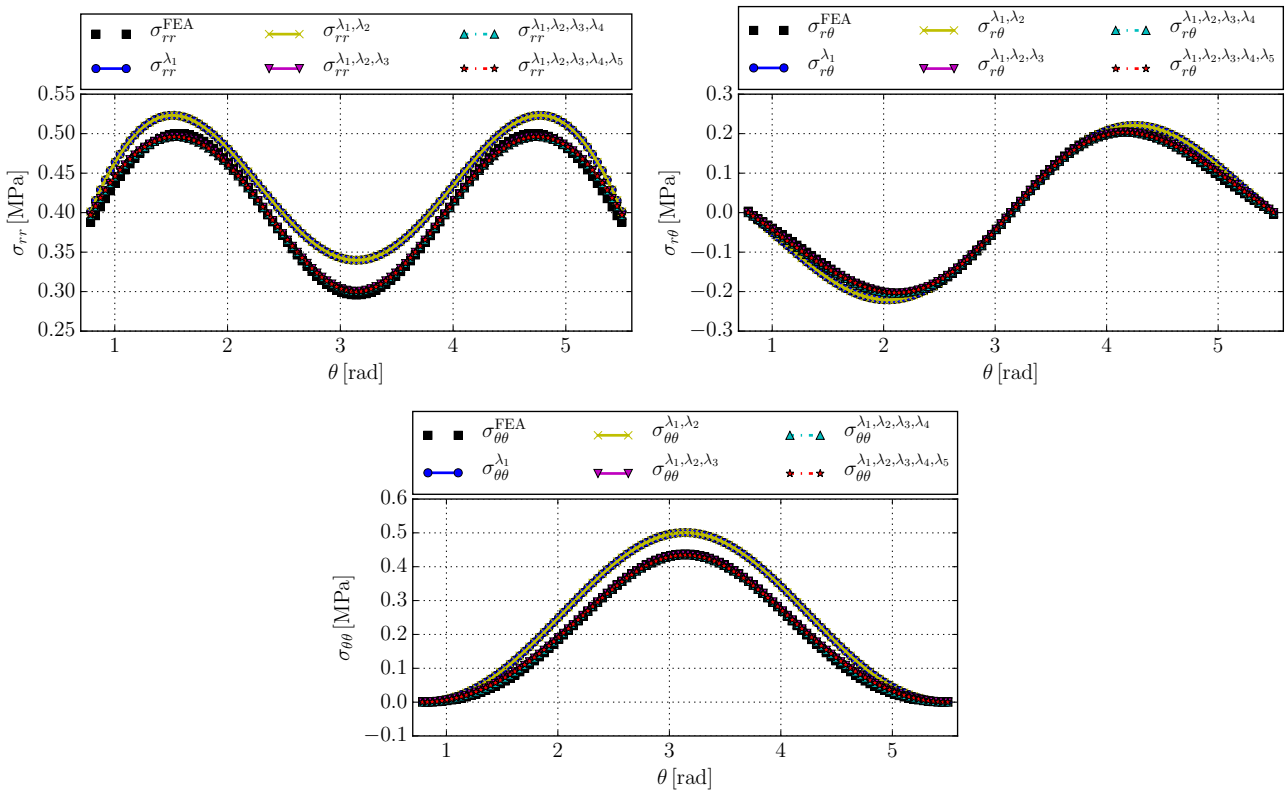

Figure 40: Reconstruction of σ_{rr}, $\sigma_{r\theta}$ and $\sigma_{\theta\theta}$ on $r = 1$ mm. The V-notch $2\alpha = 90°$. The GSIFs by the Ψ-integral.

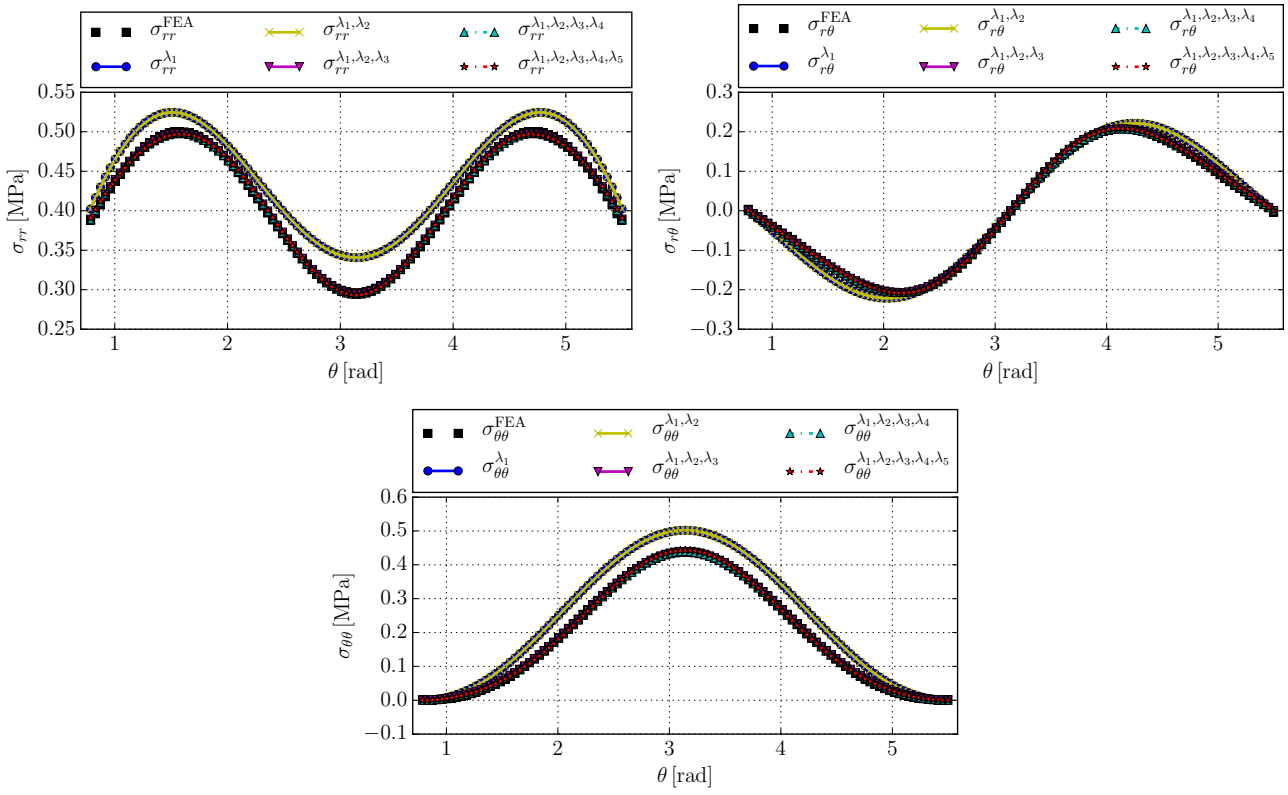

Figure 41: Reconstruction of σ_{rr}, $\sigma_{r\theta}$ and $\sigma_{\theta\theta}$ on $r = 1$ mm. The V-notch $2\alpha = 90°$. The GSIFs by the ODM.

k	λ_k	H_k^{Ψ}	$H_k^{\mathrm{ODM},\sigma_{ij}}$
1	0.574837	0.103935	0.103929
2	0.846410	0.017645	0.020187
3	1.601034	0.059421	0.053779
4	$1.886466 \pm 0.328683i$	$-0.025273 \pm 0.008627i$	$-0.055768 \pm 0.024402i$
5	$2.578256 \pm 0.363686i$	$-0.001147 \pm 0.000857i$	$-0.001897 \pm 0.006968i$

Table 14: Bi-material notch, first three eigenvalues λ_k and GSIFs H_k calculated by the Ψ-integral and ODM.

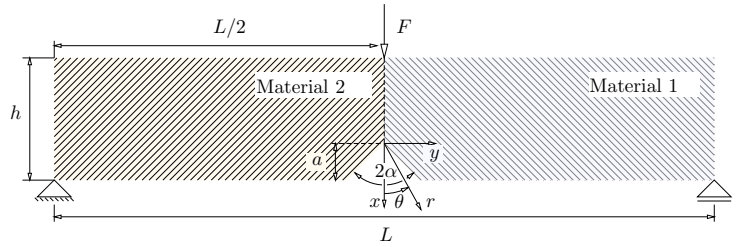

Figure 42: Model of the bi-material notch specimen subjected to 3 point bending.

Numerical example F: Stress reconstruction for a bi-material notch. The specimen with the bi-material notch (BMN) is modeled in 2D as depicted in Figure 42. The dimensions of the model in this numerical example are identical as in the previous Numerical example E, i.e. $L = 76.2$ mm, $h = 17.8$ mm, $a = 3.56$ mm, so the notch depth to width ratio is $a/h = 0.2$. The notch opening angle is $2\alpha = 90°$ ($\gamma_1 = \alpha, \gamma_2 = 180°, \gamma_3 = 360° - \alpha$). The material region 1 is modeled with PMMA material properties $E_1 = 2.3$ GPa, $\nu_1 = 0.34$ and the material region 2 with aluminum material model $E_2 = 69$ GPa, $\nu_2 = 0.33$. The Young's moduli ratio in this case is $E_1/E_2 = 0.033$. Ideal adhesion on the interface is assumed. The model is loaded with force of $F = 1$ N (per 1 mm of specimen thickness b) and plane strain state is chosen. The eigenfunctions are normalized per Eq. (38) on p. 29 with $\theta_0 = 270°$, where the coordinate system is shown in Figure 42. This angle is chosen and does not represent the expected crack initiation angle, which is yet unknown. The parameters which form the mapped mesh near singular point as in Figure 33 are chosen as: $r_0 = 0.01$ mm, $r_1 = 1$ mm and $r_2 = 3$ mm and the element division is by 2.5°. The first five GSIFs H_k are calculated by the Ψ-integral, with integration radius $r = 3$ mm and the linear regression extrapolated H_1, H_2 or the averaged ODM $H_3 \div H_5$ with $r = 0.2 \div 1$ mm. The first two terms factors were extrapolated since slight linear dependence existed for $H_k(r)$. The higher order terms factors were averaged since the linear regression is not applicable for these. For the reason discussed in theoretical part discussing the ODM, only the stress based determination is used. The results are found in Table 14. We see that both methods for GSIFs calculation for the singular leading terms factors H_1 and H_2 return values very close to each other (0.01 % for H_1 and 12.6 % for H_2). In case of non-singular terms, good agreement is also found (10.5 % for H_3, 9.4 % for H_4 and 20.9 % for H_5). The method for calculation of GSIFs for a given problem should be chosen by the comparison of reconstructed analytical solution by each method and pure FE solution. This is shown in Figures 43 and 44, where stress solution on a radial distance $r = 1$ mm is compared. In the first set of graphs in Figure 43, the H_k were determined by the Ψ-integral method. Since the problem is not symmetric, contrary to the problem in the previous numerical example, both the singular term with H_1 (the blue line) and with H_2 (the yellow line) are needed to obtain the right trend of the stress distribution (solely the first singular term with H_1 marked as a the blue line does not approximate the FE solution trend well). When we plot the solution by singular and only the first non-singular term, which contains λ_3, we actually obtain solution which is in the material region 2 of less quality than singular solution only. However, when we add to the singular solution the first (which contains λ_3) and also the second non-singular term which contains λ_4 and is denoted by magenta line, we obtain great match to the FE. The fifth term, which contains λ_5 does not increase precision on the distance of 1 mm by any means. The same is true for analytical solution obtained by the ODM, which gives results of high quality (in accordance to the to the previous case of the V-notch). In conclusion, both methods produce results which correspond to the FE solution very well. In case of both methods used, the employment of non-singular terms leads to increased precision of stress description. The choice of the method in this case is again left to the researcher.

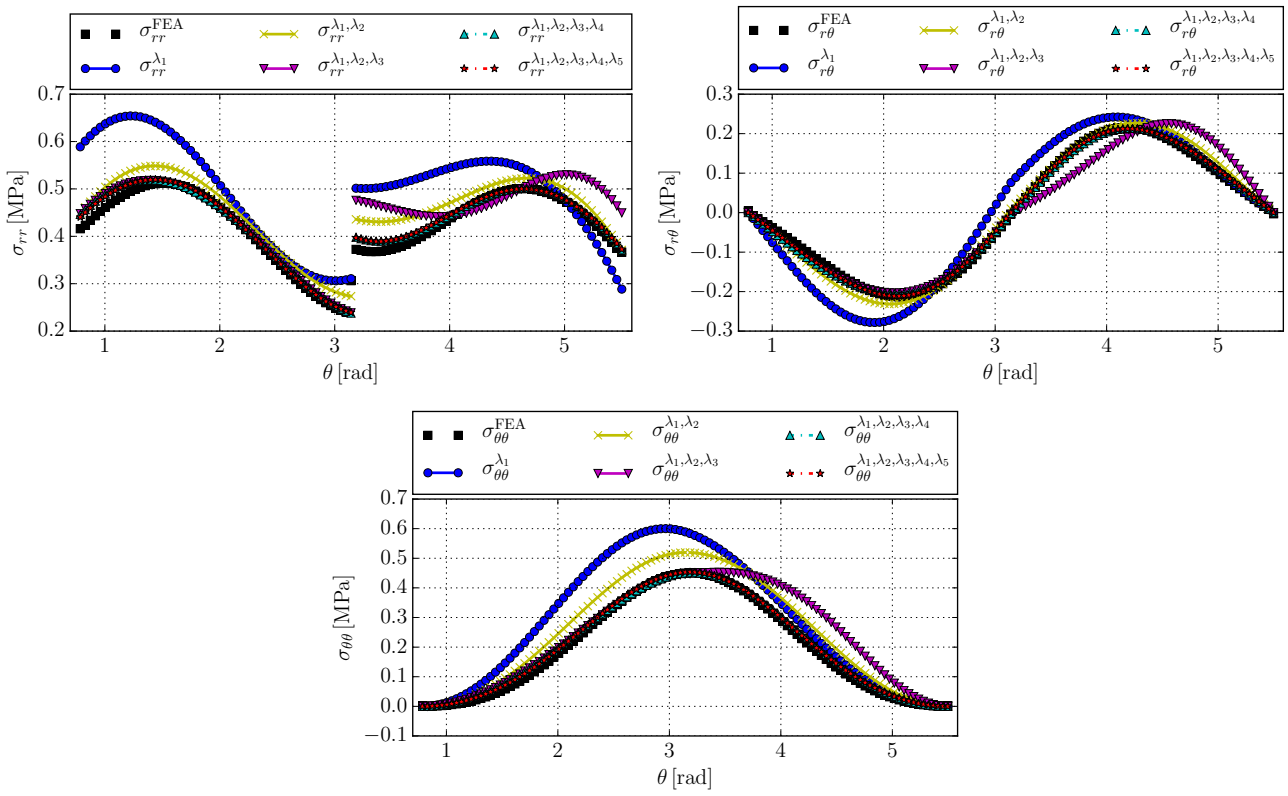

Figure 43: Reconstruction of σ_{rr}, $\sigma_{r\theta}$ and $\sigma_{\theta\theta}$ on $r = 1$ mm for the BMN, $E_1/E_2 = 0.033$, H_k by the Ψ-integral.

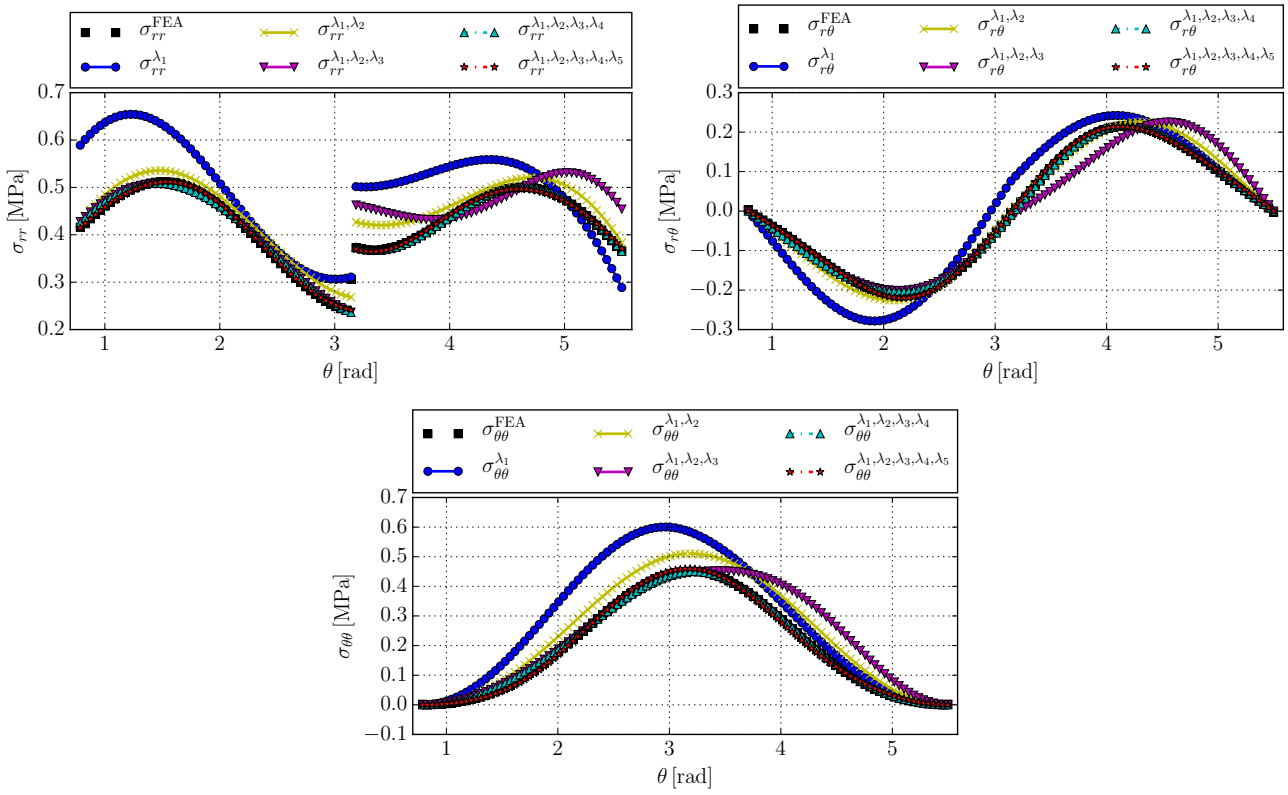

Figure 44: Reconstruction of σ_{rr}, $\sigma_{r\theta}$ and $\sigma_{\theta\theta}$ on $r = 1$ mm for the BMN with $E_1/E_2 = 0.033$, H_k by the ODM.

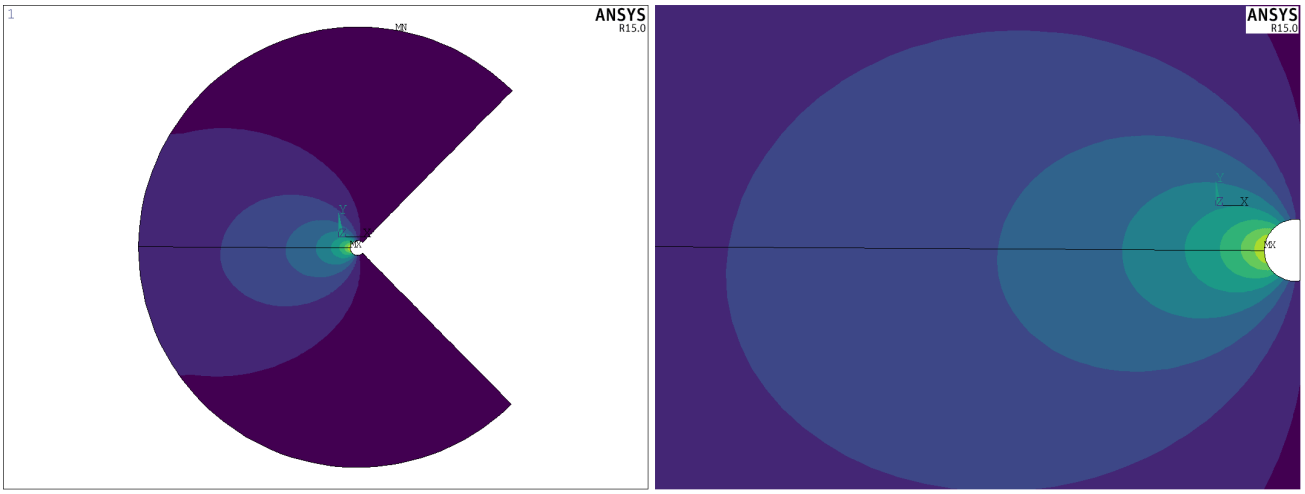

Figure 45: Tangential stress near the tip of the bi-material notch, area $0.1 - 3$ mm. The results of this numerical example shows qualitative character of the problem, so the values of $\sigma_{\theta\theta}$ represented by individual contours are intentionally omitted.

Criteria of crack initiation direction and stability criteria

The criterion of maximum of average tangential stress

As described in sub-section 2.2 on p. 14, the maximum tangential stress criterion states that the crack will initiate in the direction of maximal tangential stress. Contrary to the case of a crack, direction of maximum of tangential stress near tip of a bi-material notch is dependent on the radial distance. This can be observed in Figure 45, where tangential stress on area $r = 0.1 - 3$ mm near the singular point is shown by FE analysis. As the distance increases, the maximum changes its direction as shown in Figure 46, where the results of the same FE analysis are plotted in the graph. The geometry, bi-material combination and loading is identical to Numerical example F on p. 53. In order to mitigate the radial dependence of the maximum in tangential stress, an average value over specific distance d which is fracture mechanism or material microstructure related can be calculated as:

$$\overline{\sigma}_{\theta\theta}(\theta) = \frac{1}{d}\int_0^d \sigma_{\theta\theta}(r,\theta)\,\mathrm{d}r. \tag{60}$$

Then, the maximum value is found by search for function extreme:

$$\left(\frac{\partial\overline{\sigma}_{\theta\theta}}{\partial\theta}\right) = 0, \tag{61}$$

and by complying to the condition:

$$\left(\frac{\partial^2\overline{\sigma}_{\theta\theta}}{\partial\theta^2}\right) < 0.$$

Substituting the tangential stress component as in expansion (20) on p. 24, into equation (60) we obtain:

$$\overline{\sigma}_{\theta\theta}(\theta) = H_1\sum_{k=1}^{n}\Gamma_{k1}\frac{d^{\lambda_k-1}}{\lambda_k}f_{\theta\theta k}(\theta) + \bar{H}_1\sum_{k=1}^{n}\bar{\Gamma}_{k1}\frac{d^{\bar{\lambda}_k-1}}{\bar{\lambda}_k}\bar{f}_{\theta\theta k}(\theta) = 2\Re\left\{H_1\sum_{k=1}^{n}\Gamma_{k1}\frac{d^{\lambda_k-1}}{\lambda_k}f_{\theta\theta k}(\theta)\right\}, \tag{62}$$

where the Γ_{k1} is the ratio between individual GSIFs:

$$\Gamma_{k1} = \frac{H_k}{H_1}. \tag{63}$$

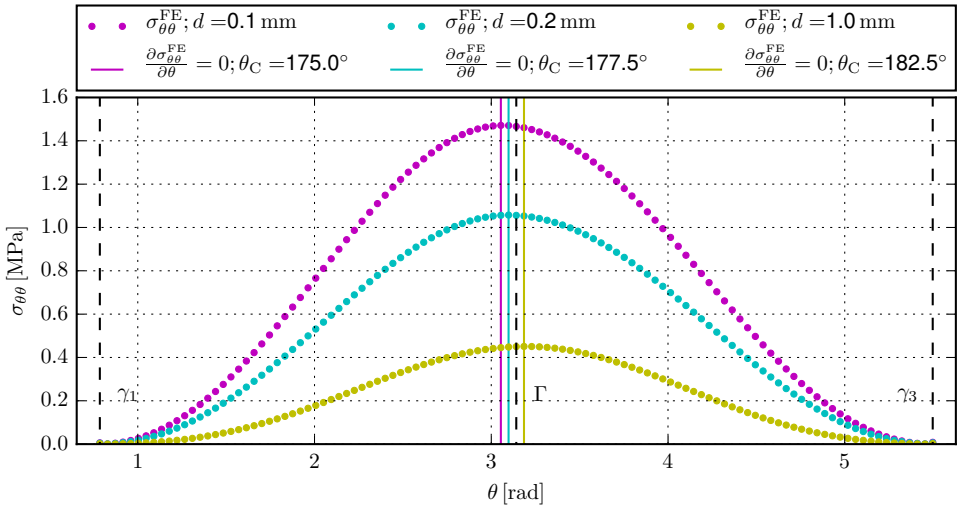

Figure 46: Tangential stress calculated by pure FEM plotted on three radii: 0.1 mm, 0.2 mm and 1 mm. Please note the difference in predicted angles of crack initiation θ_0 when different d is considered.

Deriving the equation (62) with respect to θ and by forming equation as in Eq. (61) and considering only one part of the equation (62) we get:

$$\sum_{k=1}^{n} \Gamma_{k1} \frac{d^{\lambda_k}}{\lambda_k} \frac{\partial f_{\theta\theta k}(\theta)}{\partial\theta} = 0, \tag{64}$$

by which we will find the angle θ, where the tangential stress has its global extreme, which can occur in material 1 or 2. Please note that detailed derivation of this equation and first and second derivative of eigenfunction $f_{\theta\theta k}(\theta)$ with respect to θ is found at the Appendix A.2 on p. 107. We presume the crack initiation mechanism to be identical as in the case of a crack propagation in homogeneous media. The critical value of average tangential stress follows from the case of crack propagation in material m subjected to mode I loading [40]:

$$\overline{\sigma}_{\theta\theta\mathrm{C}}(\theta_{0,m}) = \frac{2K_{\mathrm{IC},m}}{\sqrt{2\pi d}}.$$

Comparing this equation with equation (62), the critical value of GSIF for a notch problem is for complex λ_k and H_k:

$$H_{1\mathrm{C},m} = \frac{K_{\mathrm{IC},m}}{\sqrt{2\pi}\Re\left\{\sum_{k=1}^{n}\Gamma_{k1}\frac{d^{\lambda_k-\frac{1}{2}}}{\lambda_k} f_{\theta\theta k}(\theta_{0,m})\right\}} \tag{65}$$

As introduced by Eq. (15) on p. 17, the generalized fracture toughness $H_{1\mathrm{C},m}$ depends on the fracture toughness $K_{\mathrm{IC},m}$ of the material m. In the case of a bi-material notch, there are two materials in which the crack can initiate. If the value $H_{1\mathrm{C},1}$ is lower than $H_{1\mathrm{C},2}$, crack initiation is expected into the material 1, otherwise it onsets in the material 2. The third option is the crack initiation in the interface. The value $H_{1\mathrm{C,interface}}$ is determined based on fracture toughness of the interface, $K_{\mathrm{IC,interface}}$. Note that for all the critical values $H_{1\mathrm{C},1}$, $H_{1\mathrm{C},2}$ and $H_{1\mathrm{C,interface}}$, the shape functions $f_{\theta\theta k}(\theta)$ shall contain corresponding angle of potential crack initiation $\theta_{0,m}(m = 1, 2, \mathrm{interface})$. The angle $\theta_{0,m}$ is determined by Eq. (64) for the case when the material contains the global maximum of $\overline{\sigma}_{\theta\theta}(\theta)$ and equals to γ_2 for the remaining cases of local maximum of $\overline{\sigma}_{\theta\theta}(\theta)$ of the interface failure. Then, the crack initiation occurs if the following stability criterion is violated [20]:

$$H_1 < \{H_{1\mathrm{C},1}, H_{1\mathrm{C},2}, H_{1\mathrm{C,interface}}\}. \tag{66}$$

In general, the criteria always compare value H_1 with critical values $H_{1\mathrm{C},m}$. This is true for approach when only the singular terms factors are employed as well as for the multi-parameter approach. There is no need to compute critical values for other terms H_k since they are dependent on H_1 by the ratio Γ_{k1}. Finally the critical load for crack onset from a bi-material notch can be calculated:

$$\sigma_{\mathrm{C}} = \sigma_{\mathrm{appl}} \frac{\min\left(H_{1\mathrm{C},1}\left(\theta_{0,1}\right), H_{1\mathrm{C},2}\left(\theta_{0,2}\right), H_{1\mathrm{C},\mathrm{interface}}\left(\theta_{0,\mathrm{interface}}\right)\right)}{H_1\left(\sigma_{\mathrm{appl}}\right)}. \tag{67}$$

The average strain energy density factor criterion

In the linear elastic fracture mechanics of cracks, Sih's strain energy density factor (SEDF) criterion can be used to predict crack propagation conditions [57]. This approach can also be applied for the same purpose on other cases of stress concentration [58]. The case of a crack is characterized by independence of the extreme (minimum) of the SEDF on radial distance. General cases however show the radial distance dependence. Therefore, a mean value of the SEDF over distance d, which is a distance related to fracture mechanism or material microstructure, is used. In [18] Klusák and Knésl applied mean value of the SEDF to assess the stability of bi-material notches. No instances of the SEDF criterion employment with consideration of not only singular but also higher non-singular terms are found in the literature to the best of author's knowledge. As shown in the dissertation, some cases of V-notches and bi-material notches are characterized by rather weak singularities in comparison to crack problems (e.g. notches with $2\alpha > 120°$). In such cases, the singular terms may describe stress field precisely only on distances smaller than distance d related to fracture mechanism or material microstructure. Because of that, the SEDF criteria without consideration of higher order terms may give either overconservative or underestimated failure load prediction. In order to mitigate such discrepancy, the SEDF can be calculated using n singular and non-singular terms. The definition of the SEDF is [57]:

$$\Sigma = r\frac{\mathrm{d}W}{\mathrm{d}V} = r\int_0^{\varepsilon} \sigma \mathrm{d}\varepsilon,$$

where the $\frac{\mathrm{d}W}{\mathrm{d}V}$ represents strain energy density (strain energy per volume). When considering the brittle fracture the crack initiates when the SEDF reaches its critical value:

$$\Sigma = \Sigma_{\mathrm{C}},$$

where Σ_{C} is material parameter determined in relation to the fracture toughness of given material $K_{\mathrm{IC},m}$. Let's recall Eq. (13) on p. 15. For crack problems:

$$\Sigma_{\mathrm{C},m} = \frac{k_m K_{\mathrm{IC},m}^2}{4\pi\mu_m}. \tag{68}$$

In the case of a bi-material notch, the SEDF will be determined for both material regions and the interface, thus for index $m = 1, 2, \mathrm{interface}$. As discussed above, to account for dependence of the SEDF on radial distance, its mean value $\overline{\Sigma}_m$ over specific distance d is determined as:

$$\overline{\Sigma}_m = \frac{1}{d}\int_0^d \Sigma_m \mathrm{d}r. \tag{69}$$

Let's recall the formula for calculation of the SEDF for plane problems, Eq. (10) on p. 14:

$$\Sigma_m = r\left[2\sigma_{\theta\theta m}\sigma_{rrm}(k_m - 1) + (\sigma_{\theta\theta m}^2 + \sigma_{rrm}^2)(k_m + 1) + 4\sigma_{r\theta m}^2\right]\frac{1}{8\mu_m}, \tag{70}$$

in which the material constant k_m is defined in Eq. (11) on p. 14. Let's substitute for each stress component its stress series form of n terms and integrate the equation over specific distance d. By doing that, the final form of the formula for the mean value of the SEDF is:

$$\overline{\Sigma}_m = \Re\left\{\frac{H_1^2}{2\mu_m}\sum_{k=1}^{n}\sum_{l=k}^{n}\Gamma_{k1}\Gamma_{l1}\frac{d^{\lambda_k+\lambda_l-1}}{\lambda_k+\lambda_l}U_{kl}\left(\theta\right)\right\} \tag{71}$$

in which the Γ_{l1} is ratio between GSIFs defined:

$$\Gamma_{l1} \quad = \quad \frac{H_l}{H_1},$$

and the augmented shape functions in the following form:

$$U_{kl}\left(\theta\right) \quad = \quad \begin{cases} 2f_{\theta\theta k}\left(\theta\right) f_{rrk}\left(\theta\right)\left(k_m-1\right)+\left(f^2_{\theta\theta k}\left(\theta\right)+f^2_{rrk}\left(\theta\right)\right)\left(k_m+1\right)+4f^2_{r\theta k}\left(\theta\right) & k=l \\ 2(f_{\theta\theta k}\left(\theta\right) f_{rrl}\left(\theta\right)+f_{\theta\theta l}\left(\theta\right) f_{rrk}\left(\theta\right))\left(k_m-1\right)+2(f_{\theta\theta k}\left(\theta\right) f_{\theta\theta l}\left(\theta\right)+ & k\neq l \\ \quad +f_{rrk}\left(\theta\right) f_{rrl}\left(\theta\right))\left(k_m+1\right)+8f_{r\theta k}\left(\theta\right) f_{r\theta l}\left(\theta\right). & \end{cases}$$

The detailed derivation of Eq. (71) is found in the Appendix A, p. 108. The crack initiation angle θ_0 is found as a minimum of mean value of the SEDF. Mathematically, the function extreme is:

$$\left(\frac{\partial\overline{\Sigma}_m}{\partial\theta}\right) \quad = \quad 0, \tag{72}$$

and for the function minimum:

$$\left(\frac{\partial^2\overline{\Sigma}_m}{\partial\theta^2}\right) \quad > \quad 0.$$

By substitution of Eq. (71) into Eq. (72) we finally obtain equation by which we will find the crack initiation angle θ_0:

$$\sum_{k=1}^{n}\sum_{l=k}^{n}\Gamma_{k1}\Gamma_{l1}\frac{d^{\lambda_k+\lambda_l-1}}{\lambda_k+\lambda_l}\frac{\partial U_{kl}\left(\theta\right)}{\partial\theta} \quad = \quad 0. \tag{73}$$

The derivative of $U_{kl}\left(\theta\right)$ is found in the Appendix A, Eq. 109 on p. 110. We assume that the crack initiation process in the case of a bi-material notch is identical to the crack propagation process in the case of a crack in homogeneous media. The employment of equation (71) for mean value of the SEDF together with equation (68) for critical value of the SEDF leads to formula for determination of critical value of GSIF:

$$H_{1\mathrm{C},m} \quad = \quad K_{\mathrm{IC},m}\sqrt{\frac{k_m}{2\pi\Re\left\{\sum_{k=1}^{n}\sum_{l=k}^{n}\Gamma_{k1}\Gamma_{l1}\frac{d^{\lambda_k+\lambda_l-1}}{\lambda_k+\lambda_l}U_{kl}\left(\theta\right)\right\}}}. \tag{74}$$

Note that all the critical values $H_{1C,1}$, $H_{1C,2}$ and $H_{1\mathrm{C,interface}}$ should be evaluated for calculated corresponding angles of crack initiation $\theta_{0,1}$, $\theta_{0,2}$ and $\theta_{0,\mathrm{interface}}$ respectively, which were determined earlier by Eq. (73). Once the critical fracture toughness values are known, in order to assess stability, the generalized stability condition as stated in equation (15) is used. The condition of stability for the case of a bi-material notch is written identically as in Eq. (66) in the MTS criterion section, since it is a general one. The crack onset load is then calculated by Eq. (67).

The coupled stress-energy criterion

The coupled stress-energy criterion developed by Leguillon [23] states that both the energy and stress criteria are necessary conditions for fracture but neither one nor the other are sufficient. The fracture occurs when the two criteria are fulfilled simultaneously, together they form a sufficient one. The energy criterion, which is commonly used in fracture mechanics of brittle solids is:

$$-\frac{\delta W_{\mathrm{p}}}{\delta S} \quad \geqslant \quad G_{\mathrm{C}}, \tag{75}$$

where δS is newly created crack surface and G_C is fracture energy per unit surface, the fracture toughness. The incremental form of this criterion is the foundation of Finite fracture mechanics (FFM). It requires the knowledge of the crack increment surface δS [23]. The differential form of this criterion is known as Griffith criterion. Let's

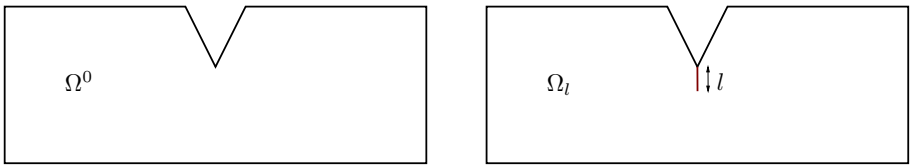

(a) (b)

Figure 47: Unperturbed and perturbed problem.

consider the symmetrically loaded V-notch which is characterized by single real governing term of the stress expansion (with GSIF H and eigenvalue λ). The potential energy change at a crack onset in the direction θ_0 is written [24]:

$$-\delta W_{\mathrm{p}} \quad = \quad H^2 A\left(2\alpha, \theta_0\right) l^{2\lambda} d + \ldots, \tag{76}$$

where $A\left(2\alpha, \theta_0\right)$ is the scaling term dependent on local geometry (2α) and the direction of crack initiation θ_0. Its computation is commented in following sub-chapter. The l is length of the newly created crack and d is the width of the specimen. The GSIF H is proportional to the applied load σ_∞ thus $H = c\sigma_\infty$. Combining equations (75) and (76), the lower bound for the crack increment length is:

$$l^{2\lambda-1} \quad \geqslant \quad \frac{G_{\mathrm{C}}}{A\left(2\alpha, \theta_0\right) c^2 \sigma_\infty^2}. \tag{77}$$

Since the applied load σ_∞ cannot be infinitely large, the increment length l at crack onset cannot be infinitely small. The crack jumps from 0 to l_0, which is the illustration of FFM. The tangential stress at a distance l from the tip in the direction θ_0 is:

$$\sigma_{\theta\theta}\left(l, \theta_0\right) \quad = \quad H l^{\lambda-1} f_{\theta\theta}\left(\theta_0\right) + \ldots$$

considering the stress failure condition:

$$\sigma_{\theta\theta}\left(l, \theta_0\right) \quad \geqslant \quad \sigma_{\mathrm{C}},$$

where σ_{C} is the critical tension, i.e. material strength. The upper bond for the increment length l is:

$$l^{\lambda-1} \quad \leqslant \quad \frac{c\sigma_\infty f_{\theta\theta}\left(\theta_0\right)}{\sigma_{\mathrm{C}}}. \tag{78}$$

The increment length l_0 is derived by combining (77) and (78), so we get:

$$l_0 \quad = \quad \frac{G_{\mathrm{C}} f_{\theta\theta}^2\left(\theta_0\right)}{A\left(2\alpha, \theta_0\right) \sigma_{\mathrm{C}}^2}. \tag{79}$$

The crack onset criterion can be obtain by substituting Eq. (79) into Eq. (76), thus:

$$H \quad < \quad \left(\frac{G_{\mathrm{C}}}{A\left(2\alpha, \theta_0\right)}\right)^{1-\lambda} \left(\frac{\sigma_{\mathrm{C}}}{f_{\theta\theta}\left(\theta_0\right)}\right)^{2\lambda-1}.$$

Matched asymptotic expansion for the coupled stress-energy criterion

Let's consider a domain Ω^l which is slightly perturbed by a small crack of length l as illustrated in Figure 47b. The solution $U^l(x_1, x_2)$ can be expressed as the unperturbed solution $U^0(x_1, x_2)$ defined in Ω^0, see Figure 47a, (Ω^0 is a limit of Ω^l as $l \to 0$) plus a small correction:

$$U^l(x_1, x_2) \quad = \quad U^0(x_1, x_2) + g_1(l) U^1(x_1, x_2), \tag{80}$$

where $g_1(l) \to 0$ as $l \to 0$. This expansion above (80) is called outer and it is valid in the whole domain Ω^0 (or Ω^l) except near the corner point where the geometry is perturbed [23]. The singular solution $U^0(x_1, x_2)$ at the corner point can be written as:

$$U^0(x_1, x_2) \quad = \quad U^0(0,0) + Hr^\lambda u(\theta) + \dots \tag{81}$$

Where the term $U^0(0,0)$ represents the rigid body translation. It is assumed for simplicity that the leading singular term is single real one (therefore we denote $H_1 = H$, $\lambda_1 = \lambda$ and $u_1(\theta) = u(\theta)$). In order to have description of near fields, the domain Ω^l is stretched ($\times 1/l$) and as $l \to 0$ it leads to unbounded inner domain Ω^{in} where $y_1 = x_1/l$, $y_2 = x_2/l$ and $\rho = r/l$. The crack length is chosen as $l = 1$, so the inner expansion is:

$$U^l(x_1, x_2) \quad = \quad U^l(ly_1, ly_2) = G_0(l)V^0(y_1, y_2) + G_1(l)V^1(y_1, y_2), \tag{82}$$

where $G_1(l)/G_0(l) \to 0$ as $l \to 0$. The behavior of outer terms in (80) when approaching to the singular point must match the behavior of the inner terms in (82) at infinity. The asymptotic character of (81) leads to:

$$G_0(l) = 1, \quad V^0(y_1, y_2) = U^0(0,0) = C, \quad G_1(l) = Hl^\lambda.$$

In addition it is prescribed that $V^1(y_1, y_2) \sim \rho^\lambda u(\theta)$ as $\rho \to \infty$. By using the superposition principle the function $V^1(y_1, y_2)$ is written:

$$V^1(y_1, y_2) \quad = \quad \rho^\lambda u(\theta) + \hat{V}(y_1, y_2),$$

where $\hat{V}(y_1, y_2)$ is the complementary term. Therefore the inner expansion of perturbed problem is:

$$U^l(y_1, y_2) \quad = \quad C + H_1 l^\lambda (\rho^\lambda u(\theta) + \hat{V}(y_1, y_2)) + \dots$$

and the inner expansion of unperturbed problem:

$$U^0(y_1, y_2) \quad = \quad C + Hl^\lambda \rho^\lambda u(\theta) + \dots$$

The difference in strain energy thus is:

$$W_{\text{p}}(0) - W_{\text{p}}(l) \quad = \Psi(U^0, U^l) = \quad \Psi(C + Hl^\lambda(\rho^\lambda u(\theta) + \hat{V}(y_1, y_2)) + \dots, C + Hl^\lambda \rho^\lambda u(\theta) + \dots),$$

which can be expanded in individual Ψ-integrals:

$$\begin{aligned} W_{\text{p}}(0) - W_{\text{p}}(l) \quad = \quad & \Psi(C, C) + Hl^\lambda C\Psi(C, \rho^\lambda u(\theta)) + Hl^\lambda C\Psi(\rho^\lambda u(\theta), C) + H^2 l^{2\lambda}\Psi(\rho^\lambda u(\theta), \rho^\lambda u(\theta)) \\ & + Hl^\lambda \Psi(\hat{V}, C) + H^2 l^{2\lambda}\Psi(\hat{V}, \rho^\lambda u(\theta)). \end{aligned}$$

As the properties $\Psi(u, u) = 0$ and $\Psi(u, v) = -\Psi(v, u)$ apply, all the terms expect the last one are equal to zero. Equality $Hl^\lambda \psi(\hat{V}, C) = 0$ can be also proven [25]. The final form of the equation for difference in potential energy is

$$W_{\text{p}}(0) - W_{\text{p}}(l) \quad = \quad AH^2 l^{2\lambda}, \tag{83}$$

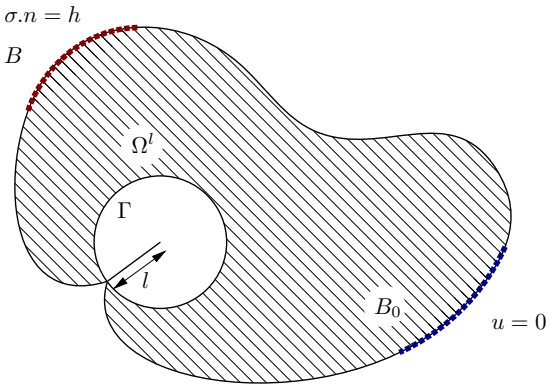

Figure 48: Domain with a small crack of length l.

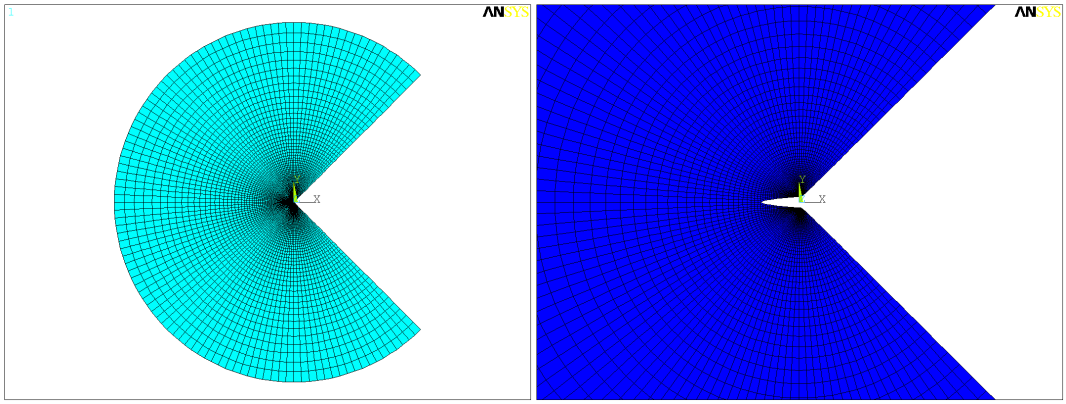

Figure 49: On the left: FE model of the inner domain for a calculation of the scaling coefficient $A\,(2\alpha = 90°, \theta_0 = 180°)$ of the V-notch. On the right: the crack with unit length after deformation.

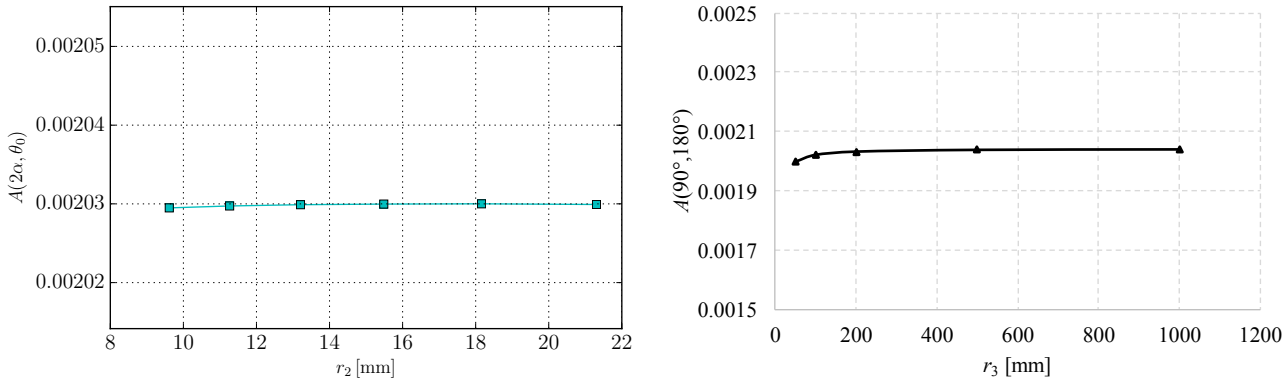

Figure 50: The left-hand side shows the convergence study of the scaling coefficient $A\,(2\alpha = 90°, \theta_0 = 180°)$ for the V-notch in dependence of integration path radius r_2. The right-hand side shows the convergence study of the scaling coefficient $A\,(2\alpha = 90°, \theta_0 = 180°)$ for the V-notch in dependence of the inner domain size r_3.

in which the term A is:

$$A \quad = \quad \Psi(\hat{V}, \rho^{\lambda} u(\theta)) = \frac{1}{2} \int_{\Gamma} (\sigma(\hat{V}) n \rho^{\lambda} u(\theta) - \sigma(\rho^{\lambda} u(\theta)) n \hat{V}) \tag{84}$$

and the Γ is any contour surrounding the singular point as shown in Figure 48. We refer to A as to scaling coefficient. It is dependent on the general singular stress concentrator local geometry and the crack initiation angle. Thus we denote it as $A\,(2\alpha, \theta_0)$.

Numerical example G: Scaling coefficient $A\,(2\alpha, \theta_0)$ of the coupled stress-energy criterion. The values of scaling coefficient $A\,(2\alpha, \theta_0)$ are calculated for the V-notch with geometry as shown in Figure 9 on p. 15. The V-notch is symmetrically loaded so the crack initiation angle is known, $\theta_0 = 180°$. The parameter $A\,(2\alpha, \theta_0)$ is calculated by matched asymptotic expansion, which is theoretically explained in the previous sub-chapter 4.2 on p. 59. Circular domain is modeled by FEM code ANSYS with a small crack of unit length at its origin (with orientation of crack initiation angle θ_0). The FE model is shown in Figure 49. The crack faces are loaded with function $r^{\lambda_1 - 1} f_{\theta\theta 1}\,(\theta)$, which is normalized as in Eq. (38) on p. 29. The assumption for the inner domain is, that it has boundaries in infinity. This can not be modeled by FEM, therefore the domain has to be modeled large compared to the crack length of $l = 1$ mm. The nodes of elements laying on the outer edge of the domain are fixed in radial and tangential direction. Then, the scaling coefficient is determined by numerical integration of expression (84). Circular integration path Γ as shown in Figure 48 is chosen to fully surround the crack and the integration radius is denoted r_2. The values of stress and displacement components are extracted from nodes found on this circle. The expression for an infinitesimal value of the integral as written in python script is:

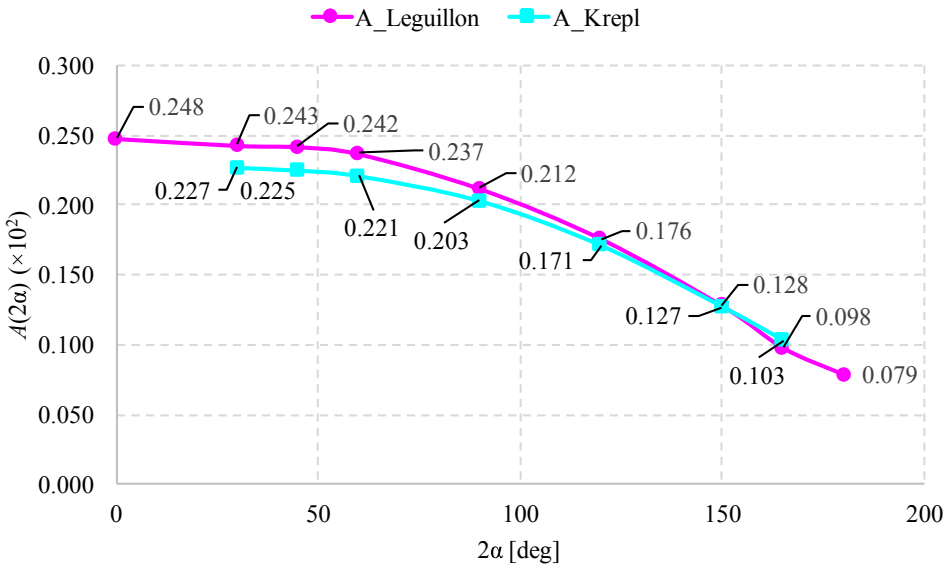

Figure 51: Scaling coefficient $A\,(2\alpha)$ resulting values comparison. The magenta line represents results calculated by Leguillon, the cyan line represents author's results [23].

$$\mathrm{d}A_k(\theta) \quad = \quad r_2^{\lambda_k}\left(r_2 f_{rk}(\theta)\sigma_{rr}^{\mathrm{FE}}(\theta) + r_2 f_{\theta k}(\theta)\sigma_{r\theta}^{\mathrm{FE}}(\theta) - u_r^{\mathrm{FE}}(\theta) f_{rrk}(\theta) - u_\theta^{\mathrm{FE}}(\theta) f_{r\theta k}(\theta)\right)\mathrm{d}\theta,$$

which is later integrated by the trapezoidal rule:

$$A_k \quad = \quad \sum_{n=1} \frac{\left(\mathrm{d}A_k\left(\theta_{n-1}\right) + \mathrm{d}A_k\left(\theta_n\right)\right)\Delta\theta}{2}.$$

As in the case of the Ψ-integral applied on the V-notch of $2\alpha = 90°$, circle division $\Delta\theta$ by 5° or 2.5° leads to 54 or 108 integration points respectively. The choice of the finer integration step results in a very small change of coefficient (by 0.5 % or less). To prove the integral path independence, the integral is calculated on various circular paths with r_2 between 10 and 25 mm. The results which are shown in chart on the left side of Figure 50 show satisfactory convergence. The size of inner domain is chosen as $r_3 = 200$ mm. This large dimension should represent behavior of the domain as if it had boundaries in infinity. The convergence study shows that further increasing of its size does not significantly affect the resulting scaling coefficient, see left chart in Figure 50. The calculated values of scaling parameter for the V-notch are compared with values calculated by Leguillon in [23]. Graph in Figure 51 shows the resulting values of scaling coefficient for variety V-notch opening angles 2α. Good match in results is found (within 7 %).

Failure load predictions vs. experimental data. Experiments on three point bending specimens made of polymethyl methacrylate (PMMA) with a V-notch were conducted by Dunn et al. in [64]. The geometry of specimen is identical to the one modeled in Numerical example E on p. 50. The actual thickness of specimen is $b = 12.7$ mm. Dunn et al. tested specimens with notch opening angle 2α of 60°, 90° and 120°. They also varied the notch depth, so the specimens with a/h ratio of 0.1, 0.2, 0.3 and 0.4 were tested. In [64] Dunn et al. measured fracture toughness of PMMA as an average value $K_{\mathrm{IC}} = 1.02$ MPa$\sqrt{\mathrm{m}}$ with standard deviation of 0.12 MPa$\sqrt{\mathrm{m}}$ and the average strength $\sigma_u = 124$ MPa. They reported on failure strength σ_f of notched specimens of individual geometric configuration. By knowledge of failure strength the failure force can be easily calculated by formula:

$$F_f \quad = \quad \frac{2\sigma_f b h^2}{3L}.$$

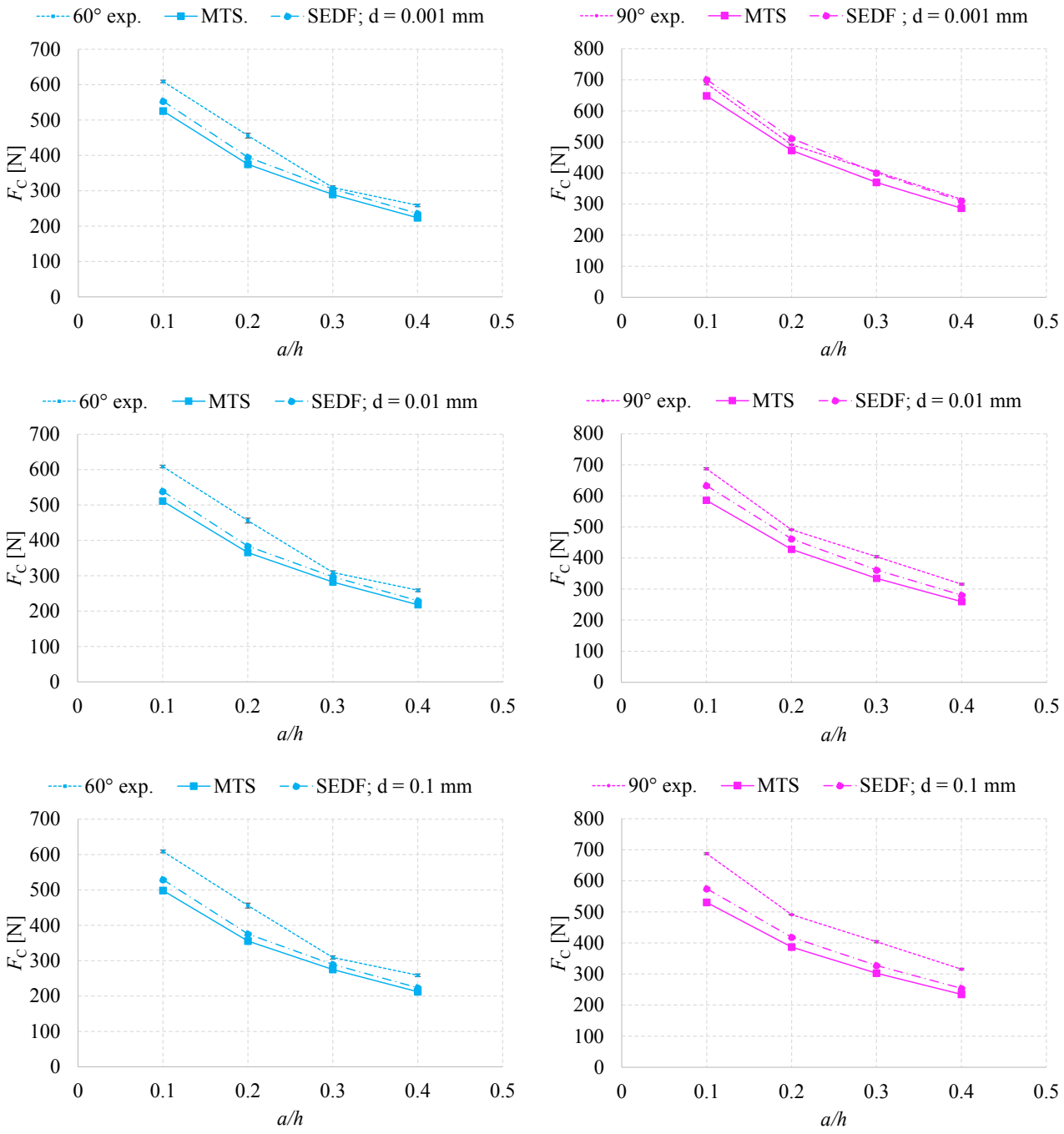

Figure 52: Comparison of experimental failure forces [64], the MTS and SEDF criterion predicted critical forces for a V-notch. The cyan color represents results of $2\alpha = 60°$ and the magenta color represents results of $2\alpha = 90°$.

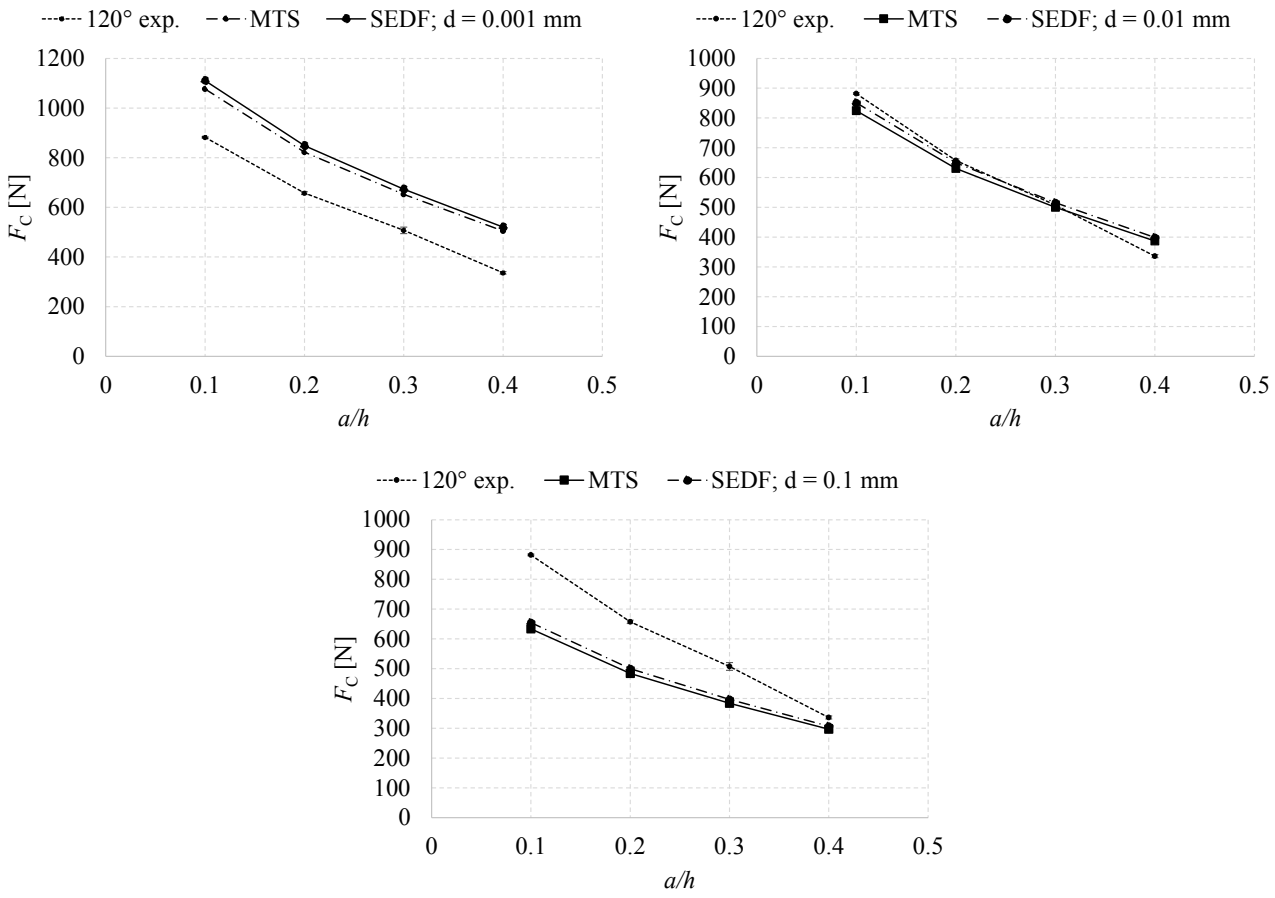

Figure 53: Comparison of experimental failure forces [64], the MTS and SEDF criterion predicted critical forces for a V-notch. Results of $2\alpha = 120°$.

We predict F_C by simple modification of Eq. (67) on p. 57:

$$F_C = F_{appl} \frac{H_{1C}(\theta_0)}{H_1(F_{appl})}.$$

Whereas the $H_{1C,m}$ are determined by Eq. (65) on p. 56 in the case of criterion of maximum of average tangential stress or by Eq. (74) on p. 58 in the case of average strain energy density factor criterion. The generalized fracture toughness is computed by the above stated K_{IC} of PMMA. The crack initiation angle is assumed to be $\theta_0 = 180°$ because of problem symmetry. The parameter d related to microstructure or fracture mechanism was varied, so the charts show predictions with $d = 0.001$ mm, $d = 0.01$ mm and $d = 0.1$ mm. The results for specimens with notch opening angle $2\alpha = 60°$ and $2\alpha = 90°$ are found in Figure 52 and the results for $2\alpha = 120°$ in Figure 53.

The review of results show, that the very good agreement between experimental data and theoretical predictions occur for $d = 0.01$ mm especially in the case of the largest opening angle 120°. The use of the above mentioned criteria and parameter $d = 0.01$ mm leads to results which underestimate the actual failure load. From the engineering point of view, it is a desirable situation, since the results lay on so called safe side. The chosen length $d = 0.01$ mm has the same order of magnitude by the material length parameter used by Taylor in [59]:

$$d = \frac{1}{\pi}\left(\frac{K_{IC}}{\sigma_u}\right)^2 = \frac{1}{\pi}\left(\frac{1.02\,\text{MPa}\sqrt{\text{m}}}{124\,\text{MPa}}\right)^2 \doteq 0.0215\,\text{mm}$$

The criteria used to predict the failure force are multi-parameter, nevertheless on distances in order of 10^{-2} mm, the contribution of higher order terms is small. The difference in failure loads predicted by the single-parameter criteria and multi-parameter criteria is in units of percents. The higher order terms contribution would become significant for materials and configurations where larger d is necessary.

k	1	2	3	4
λ_k	0.598793	1.142299	1.544159	$2.098344 + 0.580010i$
H_k	0.077091	−0.011036	0.018588	$-0.004002 + 0.007523i$

Table 15: Eigenvalues λ_k and GSIFs H_k of the bi-material notch with $2\alpha = 120°$ and $E_1/E_2 = 0.033$.

Numerical example H: Crack initiation direction and crack initiation load in the case of a bi-material notch.

Part 1 The three point bending specimen with the bi-material notch is modeled. The studied problem is identical to the Numerical example F on p. 53 with only one difference, the notch opening angle is $2\alpha = 120°$. As in Numerical example F, the Young's moduli ratio is $E_1/E_2 = 0.033$. The GSIFs are calculated by the Ψ-integral method and listed in Table 15. Let's predict the crack initiation direction and the critical value of GSIF by (a) criterion of maximum of average tangential stress and (b) average strain energy density factor criterion. The crack initiation angle and failure load will be calculated using (i) singular terms, (ii) singular and non-singular terms. Case (i) contains one singular term thus $n = 1$, case (ii) contains one singular and three non-singular terms thus $n = 4$. We have seen in Numerical example F on p. 53, that the employment of the fifth term does not increase precision by any means, this is also true for this geometric configuration.

(a) The criterion of maximum of average tangential stress. The crack initiation direction is predicted using the formula (64) on p. 56 to find the extreme of $\overline{\sigma}_{\theta\theta}(\theta)$. The results are illustrated in Figure 54, where the graph shows averaged stress $\overline{\sigma}_{\theta\theta}(\theta)$ over distance $d = 1$ mm using (i) singular term (the blue dotted line), singular and non-singular terms (the cyan dotted line). The blue and cyan vertical line shows the maximum of $\overline{\sigma}_{\theta\theta}(\theta)$ determined by (i) singular term and (ii) singular together with non-singular terms respectively. In addition, the blue and cyan solid line with markers represents the $\sigma_{\theta\theta}(r, \theta)$ reconstruction on particular distance d. The black squares denote the FE solution. When (i) only the singular term is used, the global maximum lays in material 2, which is aluminum. In case (ii) when singular and non-singular terms are used, the global maximum is again found in material 2. The difference in the angles of global maxima determined by (i) and (ii) is 2.3°. By varying the value of d, the angles of global maxima slightly changes (for $d = 0.3$ mm the difference is 1.8° and for $d = 3.0$ mm it is 1.2°). Therefore the averaging distance should be chosen carefully in relation to the fracture mechanism or microstructure of a particular problem. Since the purpose of this numerical example is only to provide illustration of application of the criteria, the critical distance will remain $d = 1$ mm. Furthermore the choice of d related to mechanism or microstructure is beyond scope of this work. The fracture toughness of PMMA is $K_{\mathrm{IC}}^{\mathrm{PMMA}} = 1.02$ MPa$\sqrt{\mathrm{m}}$ [64]. The fracture toughness of aluminum is $14 \div 28$ MPa$\sqrt{\mathrm{m}}$ depending on the particular alloy and treatment. We choose aluminum alloy (7075) with $K_{\mathrm{IC}}^{\mathrm{Al}} = 24$ MPa$\sqrt{\mathrm{m}}$. Without an experiment with the particular bi-material configuration, it is uneasy to estimate fracture toughness of the interface. In [65] Shatil and Shaimoto tested aluminum/PMMA bi-material 3PB specimens, however they do not provide value regarding fracture toughness of the interface. To bond the materials together they use epoxy adhesive. Experimental evaluation in [67, 66] show that the fracture toughness of interface can vary widely depending on conditions and particular configuration of materials to be bonded. Our estimation for this numerical example therefore is $K_{\mathrm{IC}}^{\mathrm{interface}} = 0.75$ MPa$\sqrt{\mathrm{m}}$. The generalized fracture toughness is calculated by Eq. (65) for global maximum, local maximum and the interface. The results calculated by (i) singular term are shown in Table 16 and by (ii) singular and non singular terms in Table 17. Please recall the stability condition (66) on p. 56. According to (i) the global maximum lays in $m = 2$, which is the aluminum with the crack initiation angle of $\theta_{0,1} = 183.3°$. The corresponding generalized fracture toughness value $H_{1\mathrm{C},2}$ is the highest one since aluminum has ~ 20 times higher fracture toughness than PMMA. Crack is expected to initiate rather to direction of local maximum, in PMMA or to the interface. When we asses the local maximum, we see that the lowest value corresponds to the interface, therefore the crack is expected to initiate in this direction. According to (ii) the global maximum also lays in $m = 2$ with the crack initiation angle of $\theta_{0,2} = 181.0°$. The lowest value of generalized fracture toughness value also corresponds to the interface. The difference in this generalized fracture toughness value determined by (i) and (ii) is 1.8 %.

	$\theta_{0,m}$	m	$H_{1\mathrm{C},m}$
global maximum	183.3°	1 ≡ aluminum	26.405477
local maximum	180.0°	2 ≡ PMMA	1.124533
local maximum	180.0°	interface	0.826863

Table 16: The generalized fracture toughness $H_{1\mathrm{C},m}$ for global maximum, local maximum and the interface determined by (i) singular term and (a) criterion of maximum of average tangential stress.

	$\theta_{0,m}$	m	$H_{1\mathrm{C},m}$
global maximum	181.0°	1 ≡ aluminum	26.940646
local maximum	180.0°	2 ≡ PMMA	1.145156
local maximum	180.0°	interface	0.842027

Table 17: The generalized fracture toughness $H_{1\mathrm{C},m}$ for global maximum, local maximum and the interface determined by (ii) singular and non-singular terms and (a) criterion of maximum of average tangential stress.

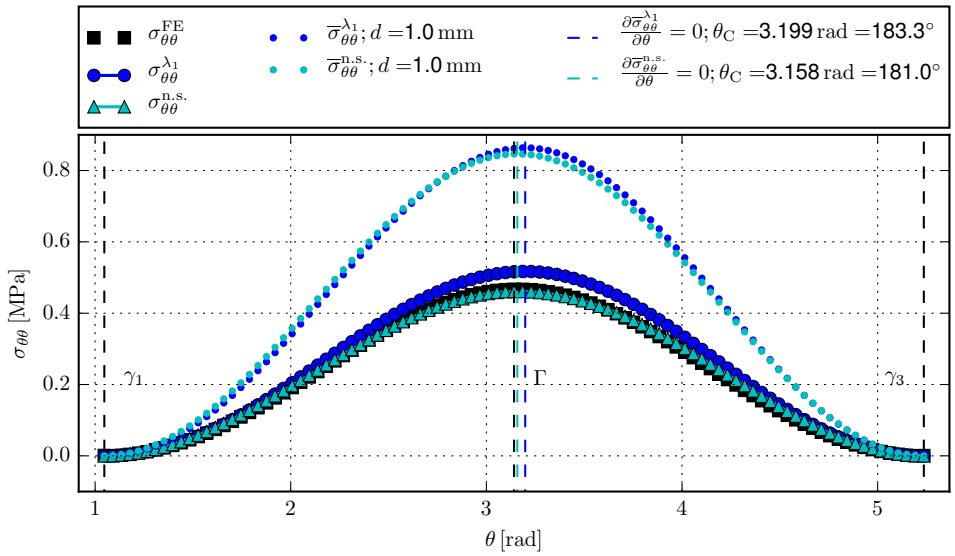

Figure 54: Mean value of the $\overline{\sigma}_{\theta\theta}(\theta)$ plotted by (i) singular term: the blue dotted line, (ii) singular and non-singular terms: the cyan dotted line. The blue and cyan vertical line denotes the corresponding crack initiation angle. The black dashed vertical lines denote the interface and the free surfaces.

(b) The average strain energy density factor criterion. The crack initiation direction is predicted using the formula to find the extreme of $\overline{\Sigma}(\theta)$ Eq. (73) on p. 58. The results are illustrated in Figure 55, where the graph shows averaged strain energy density $\overline{\Sigma}(\theta)$ over distance d using (i) singular term (the blue line with markers), (ii) singular and non-singular terms (the cyan line with markers). The blue and cyan vertical lines show extreme values (global minimum) determined by (i) and (ii) respectively. Both (i) and (ii) show the global minimum in material $m = 2$, which is aluminum. There is difference of 2.9° in direction of global minimum predicted by (i) and (ii). Because of much higher fracture toughness of aluminum in comparison to PMMA, the crack is expected to initiate rather to direction of local minimum of $\overline{\Sigma}(\theta)$ or to the interface. The results are summarized in Tables 18 and 19. Per stability condition (66) on p. 56, the lowest value of $H_{1\mathrm{C},m}$ corresponds to the local minimum of $\overline{\Sigma}(\theta)$ and the interface. Thus crack initiation in interface in the direction $\theta_0 = 180.0°$ is expected. The difference in general fracture toughness value determined by (i) and (ii) is 5.2 %.

	$\theta_{0,m}$	m	$H_{1\mathrm{C},m}$
global minimum	184.5°	1 ≡ aluminum	27.711504
local minimum	180.0°	2 ≡ PMMA	1.169967
local minimum	180.0°	interface	0.860270

Table 18: The generalized fracture toughness $H_{1\mathrm{C},m}$ for global minimum, local minimum and the interface determined by (i) singular term and (b) average strain energy density factor criterion.

	$\theta_{0,m}$	m	$H_{1\mathrm{C},m}$
global minimum	181.6°	1 ≡ aluminum	28.83614
local minimum	180.0°	2 ≡ PMMA	1.230542
local minimum	180.0°	interface	0.904810

Table 19: The generalized fracture toughness $H_{1\mathrm{C},m}$ for global minimum, local minimum and the interface determined by (ii) singular and non-singular terms and (b) average strain energy density factor criterion.

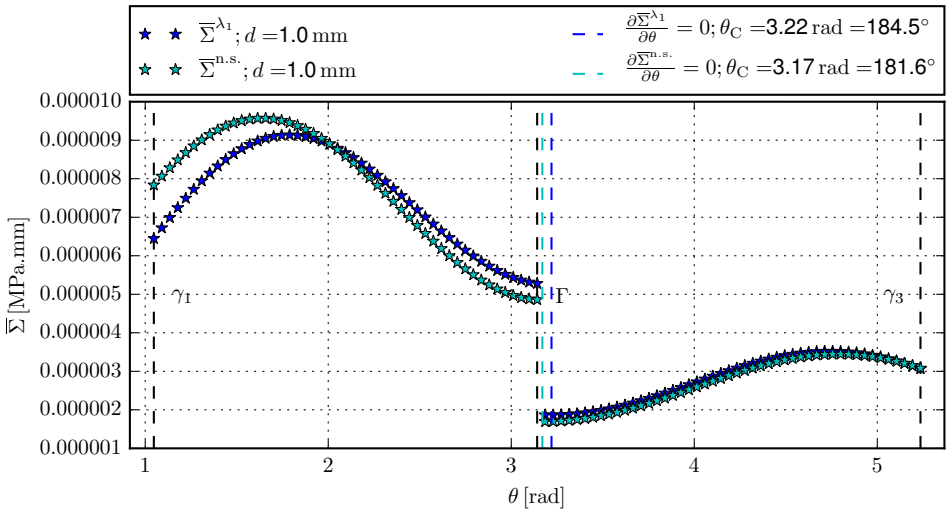

Figure 55: Mean value of the $\overline{\Sigma}(\theta)$ plotted by (i) singular term: the blue line, by (ii) singular and non-singular terms: the cyan line. The blue and cyan vertical line denotes the corresponding crack initiation angle. The black dashed vertical lines denote the interface and the free surfaces. Please note that in the interval (Γ, γ_3) the value $\overline{\Sigma}(\theta)$ is multiplied by factor of 10.

Part 2 A free edge singularity as shown in Figure 56 is studied. The dimensions of the modeled specimen are $L = 38.1$ mm, $h = 14.24$ mm and the plane strain state is considered. The angles which define the free edge singularity by a bi-material notch model are $\gamma_1 = 90°$, $\gamma_2 = 180°$ and $\gamma_3 = 270°$. The material region 1 consists of Aluminum material model, while the material region 2 consists of PMMA material model. The elastic constants are identical to those of Numerical example F on p. 53 thus the Young's moduli ratio is $E_1/E_2 = 30$. The fracture parameters are identical to those in Part 1 of this numerical example. The force of 0.1 N/mm applied on a line is constantly distributed on the length h of the upper edge under direction of ζ (per 1 mm of specimen thickness b). This particular configuration of a bi-material notch has only one singular term with $\lambda_1 = 0.721100$. The second term is non-singular with $\lambda_2 = 1.721014 \pm 0.575276$. Higher order terms have $\Im\{\lambda_k\} > 1$ and do not significantly add to the precision on $d = 1$ mm. Both the eigenfunction are normalized by the angle 240°. The crack initiation direction and material in which the crack initiates is calculated by criterion of maximum of average tangential stress. According to the theory, when only the singular term is used for prediction of crack initiation direction $\theta_{0,m}$, this direction should be independent of external loading direction ζ. The reason is apparent from examination of the

formula for crack initiation direction calculation Eq. (64) on p. 56. To account for the different loading of particular problem, the formulae contain ratio Γ_{k1}. However, when only one singular term is used, this ratio remain constant and single one. Apparently, the angle of crack initiation should be dependent on the angle of external loading. With employment of the first non-singular term, the crack initiation angle changes as it should be. The distance d is again chosen as a 1 mm for the reasons discussed above. The results related to the criterion of maximum of average tangential stress for the case when $\zeta = 180°$ are shown in Figure 57. The blue line with markers represents the (i) singular term solution of $\sigma_{\theta\theta}(r, \theta)$ and the yellow line with markers represents (ii) singular and non-singular term solution of $\sigma_{\theta\theta}(r, \theta)$ on distance d. The blue and yellow line represents the averaged distributions $\overline{\sigma}_{\theta\theta}(\theta)$ by (i) and (ii) respectively. The dashed vertical lines represents the global maxima. The results for different ζ determined by (a) are summarized in Table 20. The highest discrepancy in location of global maximum of $\overline{\sigma}_{\theta\theta}(\theta)$ determined by (i) and (ii) occurs when $\zeta = 180°$ and with a value of 6.0°. The results of generalized fracture toughnesses for the case $\zeta = 90°$ determined by (i) and (ii) are listed in Table 21. In similar manner, the Table 22 summarizes the results for $\zeta = 180°$. According to the stability condition (66) on p. 56, the lowest value in both (i) and (ii) is $H_{1\mathrm{C,interface}}$. Therefore the crack is expected to be initiated in the direction of local maximum to the interface i.e. $\theta_{0,\mathrm{interface}} = 180°$. The difference in calculated critical value of $H_{1\mathrm{C,interface}}$ by (i) and (ii) is 5.5 % when $\zeta = 90°$ and 20.4 % when $\zeta = 180°$.

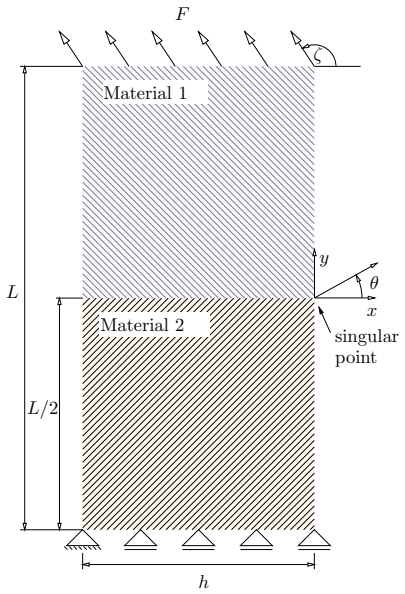

Figure 56: Bi-material plate with a free edge singularity, loaded with load of variable direction ζ.

	(i) singular term	(ii) singular and non-singular terms	
ζ	θ_0	θ_0	discrepancy
90°	169.9°	171.0°	1.1°
112.5°	169.9°	174.2°	4.3°
135°	169.9°	175.0°	5.1°
180°	169.9°	175.9°	6.0°

Table 20: Variation of the crack initiation angle θ_0 on the external loading angle ζ for free edge singularity. Values determined by (a) criterion of maximum of average tangential stress.

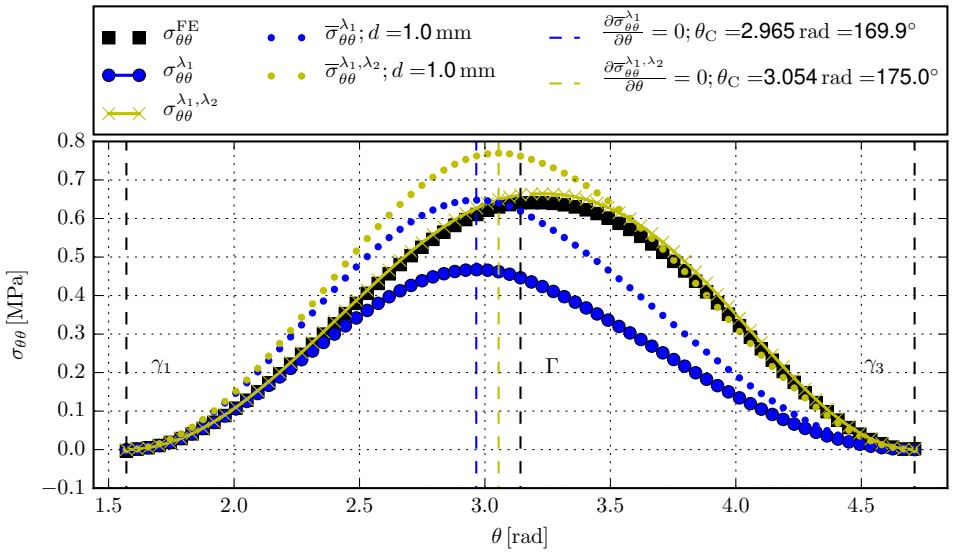

Figure 57: Mean value of the $\overline{\sigma}_{\theta\theta}(\theta)$ plotted by (i) singular term: the blue line, by (ii) singular and non-singular terms: the yellow line. The black dashed lines denote the interface and the free surfaces. The external load direction for this case is $\zeta = 180°$.

	(i) singular term			(ii) singular and non-singular terms		
$\zeta = 90°$	θ_0	m	$H_{1\mathrm{C},m}$	θ_0	m	$H_{1\mathrm{C},m}$
global maximum	169.9°	$1 \equiv$ aluminum	35.844833	171.0°	$1 \equiv$ aluminum	34.219002
local maximum	180.0°	$2 \equiv$ PMMA	1.594816	180.0°	$2 \equiv$ PMMA	1.507462
local maximum	180.0°	interface	1.172659	180.0°	interface	1.108428

Table 21: The generalized fracture toughness $H_{1\mathrm{C},m}$ determined by (a) criterion of maximum of average tangential stress for a free edge singularity with $\zeta = 90°$.

	(i) singular term			(ii) singular and non-singular terms		
$\zeta = 180°$	θ_0	m	$H_{1\mathrm{C},m}$	θ_0	m	$H_{1\mathrm{C},m}$
global maximum	169.9°	$1 \equiv$ aluminum	35.844833	175.7°	$1 \equiv$ aluminum	29.665253
local maximum	180.0°	$2 \equiv$ PMMA	1.594816	180.0°	$2 \equiv$ PMMA	1.269263
local maximum	180.0°	interface	1.172659	180.0°	interface	0.933282

Table 22: The generalized fracture toughness $H_{1\mathrm{C},m}$ determined by (a) criterion of maximum of average tangential stress for a free edge singularity with $\zeta = 180°$.

4.3. Formulation of multi-parameter fracture mechanics approaches for a sharp material inclusion

Stress terms exponents determination and study

A sharp material inclusion is modeled as a bi-material junction which is shown in Figure 11 on p. 18. The boundary conditions of the problem are:

$$\begin{aligned}
\sigma_{\theta\theta k1}(r,\gamma_1) &= \sigma_{\theta\theta k2}(r,\gamma_1) \\
\sigma_{r\theta k1}(r,\gamma_1) &= \sigma_{r\theta k2}(r,\gamma_1) \\
u_{\theta k1}(r,\gamma_1) &= u_{\theta k2}(r,\gamma_1) \\
u_{rk1}(r,\gamma_1) &= u_{rk2}(r,\gamma_1) \\
\sigma_{\theta\theta k2}(r,\gamma_2) &= \sigma_{\theta\theta k1}(r,\gamma_0) \\
\sigma_{r\theta k2}(r,\gamma_2) &= \sigma_{r\theta k1}(r,\gamma_0) \\
u_{\theta k2}(r,\gamma_2) &= u_{\theta k1}(r,\gamma_0) \\
u_{rk2}(r,\gamma_2) &= u_{rk1}(r,\gamma_0)
\end{aligned} \tag{85}$$

From the equations above it follows that the traction and displacement continuity is enforced at both interfaces Γ_1 and $\Gamma_0 = \Gamma_2$. By substituting equations for stress components (18) and displacement components (19) on p. 24 into 8 equations of boundary conditions above and by simple rearrangement we obtain the matrix $\mathbf{A}(\lambda)$ analogical to a V-notch problem, Eq. (33), p. 28. Again, the system of equations can be written as in Eq. (35), i.e.:

$$\mathbf{A}(\lambda)\, v = 0.$$

The system is characterized by 9 unknowns, the eigenvalue λ_k and 8 complex constants in the eigenvector v_k, which has the same form as the eigenvector for a bi-material notch Eq. (34). From the mathematical point of view, the system is solved in accordance to the means described in detail in sub-section 4.2 p. 27. Brief recall of the approach is following. Eigenvalue λ_k is found as a solution of the characteristic equation rising from determinant of matrix $\mathbf{A}(\lambda)$ as in Eq. (36) on p. 28. The kth eigenvalue λ_k a is inserted back into the matrix in order to obtain eigenvector v_k. One complex coefficient of the eigenvector is chosen as 1 and the reduced system of equations is solved, see Eq. (37) and remaining coefficients of eigenvector determined. As the eigenvector v_k is constructed, eigenfunctions for stress $f_{ijk}(\theta)$ and displacement series $f_{ik}(\theta)$, Eq. (23) and (27) respectively, are fully defined. Normalization of eigenfunctions is conducted as in (38) or (39) on p. 29 in the assumed direction of crack initiation θ_0 or another angle of choice. Contrary to the case of a V-notch, for eigenfunctions of a bi-material junction does not apply, that the odd eigenfunctions are with $k = 1, 3, 5\ldots$ and even eigenfunction with $k = 2, 4, 6\ldots$ Therefore, in such case it is investigated if the function is odd or even and it is normalized accordingly. However, straightforward division to odd and even function is applicable only for symmetrical problems of a bi-material junction, i.e. when $|\gamma_1| = |\gamma_0|$. General non-symmetrical problem of a bi-material junction is analogical to a bi-material notch, where each eigenfunction $f_{ijk}(\theta)$ contains both odd and even functions. In such cases, the normalization should be performed on individual basis.

Numerical example J: Eigenvalues, eigenvectors and the eigenfunctions of the bi-material junction (case of inclusion more compliant than matrix). The bi-material junction as shown in Figure 11 on p. 18 is considered. Let's study three geometrical configurations, i.e. (i) $2\alpha = 60°$, (ii) $2\alpha = 90°$, (iii) $2\alpha = 120°$ (for all cases: $\gamma_0 = -\alpha, \gamma_1 = \alpha, \gamma_2 = 2\pi - \alpha$) . The material properties are defined by $E_1/E_2 = 0.25$, $E_1 = 20$ GPa and $\nu_1 = \nu_2 = 0.25$. This numerical example represents the case of the sharp material inclusion more compliant than matrix. The eigenvalues λ_k and eigenvectors v_k are determined as described theoretically in the previous sub-section. From the computational point of view, the search for roots is conducted with the same procedure as in the case of a bi-material notch, which is in detail described in the Numerical example B on p. 32. The eigenvalues are roots of the characteristic equation which are being found on a complex plane by solving system of two equations. Where both the real and imaginary part of the eigenequation is zero a root is found (location where the red and blue curve intersect). Again it is advised to check if the found value truly represents a root by inserting it back into the characteristic equation. The resulting value should be close to zero. For the first geometric configuration (i) $2\alpha = 60°$ the solution is described in the graph in Figure 58 and the resulting eigenvalues listed in Table 23. For the first geometrical configuration in this numerical example, the complex coefficients of eigenvector v_k are for the sake of completeness listed in Table 24 for the first material region and in Table 25 for the second material region (eigenvectors of first four eigenvalues are considered). For the second geometric configuration (ii) of this numerical

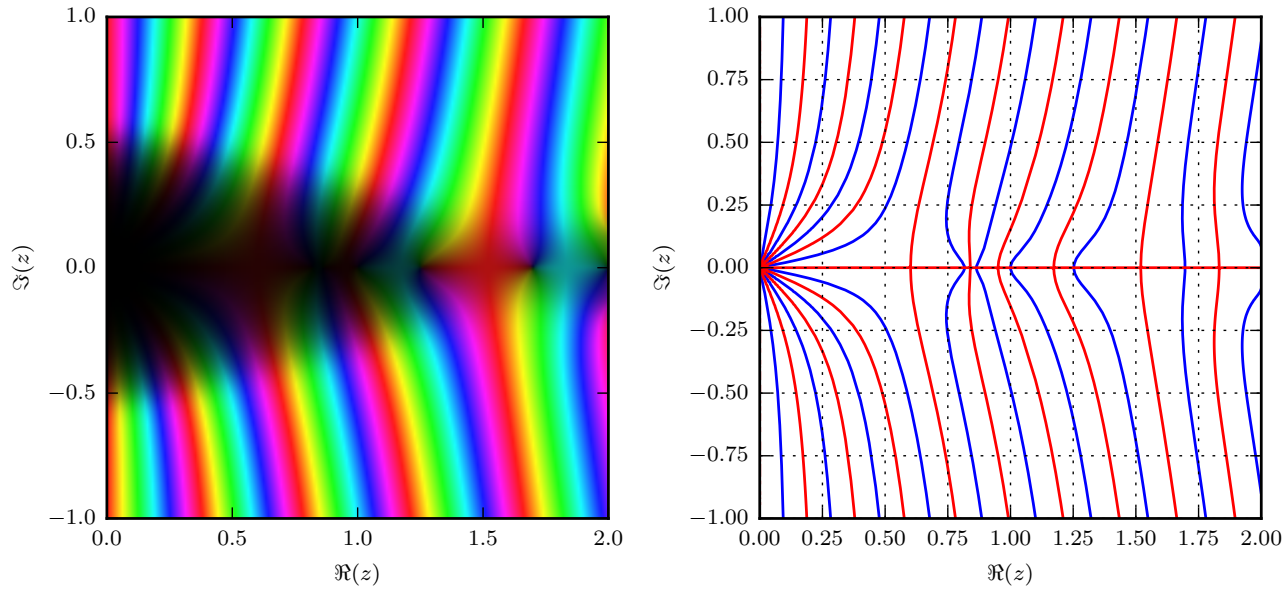

Figure 58: (i) Bi-material junction, $2\alpha = 60°$, $E_1/E_2 = 0.25$. On the left-hand side there is the graph of $f(z) = \det(\mathbf{A}(\lambda))$. On the right-hand side contour plot, the blue curve stays for $\Re\{\det(\mathbf{A}(\Re\{\lambda_k\}))\} = 0$ and the red curve for $\Im\{\det(\mathbf{A}(\Im\{\lambda_k\}))\} = 0$.

k	1	2	3	4	5	6
λ_k	0.816623	0.863720	1.252661	1.696219	2.000000	$2.058139 \pm 0.154775i$

Table 23: (i) Bi-material junction, $2\alpha = 60°$, $E_1/E_2 = 0.25$. First six eigenvalues λ_k.

example, the eigenvalues are found graphically as shown in Figure 59 and the eigenvalues listed in Table 26. The last geometrical configuration (iii) has the graphical solution of eigenvalues in Figure 60 and the eigenvalues listed in Table 27. As explained theoretically in the previous section, once the eigenvalues λ_k and eigenvectors v_k are determined, one is able to construct eigenfunctions $f_{ijk}(\theta)$ and $f_{ik}(\theta)$ for stress and displacement series respectively (and their complex conjugates). For the most common case of the bi-material junction, i.e. (ii) $2\alpha = 90°$, the stress eigenfunctions $f_{ijk}(\theta)$ for $k = 1, 2, 3, 4$ are displayed in Figure 61. Similarly the displacement eigenfunctions $f_{ik}(\theta)$ for $k = 1, 2, 3, 4$ are constructed and shown in Figure 62. The yellow dashed line denotes the location of the interface Γ_1. The eigenfunctions are normalized with consideration of the $\theta_0 = 180°$. We see that the eigenfunctions with $k = 1, 3, 4$ are odd and eigenfunction with $k = 2$ is even in terms of radial and tangential stress[8]. Analogically to a bi-material notch, the radial stress eigenfunction is discontinuous, in the case of a bi-material junction on two interfaces. The strength of singularity varies from case to case and a straightforward conclusion similar to case of a V-notch or bi-material notch cannot be proclaimed. A general understanding may be provided by plotting the dependence of λ_k on the 2α for particular bi-material configuration. Such dependence of eigenvalues for bi-material configuration of $E_1/E_2 = 0.25$ is shown in Figure 63.

Numerical example K: Eigenvalues, eigenvectors and the eigenfunctions of the bi-material junction (case of inclusion stiffer than matrix) Similarly as in the Numerical example J, the bi-material junction as shown in Figure 11 on p. 18 is considered. Again, let's study three geometrical configurations, i.e. (i) $2\alpha = 60°$, (ii) $2\alpha = 90°$, (iii) $2\alpha = 120°$ (for all cases: $\gamma_0 = -\alpha, \gamma_1 = \alpha, \gamma_2 = 2\pi - \alpha$). The material properties are defined by $E_1/E_2 = 4$, $E_1 = 80$ GPa and $\nu_1 = \nu_2 = 0.25$. Thus, the numerical example represents the case of the sharp material inclusion stiffer than matrix. The eigenvalues λ_k are determined in the same way as described in the previous sub-section. The solution is plotted only for case (ii) which is a representative one, see Figure 64. The graphical solution of other cases has similar characteristics. The resulting eigenvalues are listed for the geometric

[8]By referring to the eigenfunction as odd or even we mean that it is odd or even in part on each of two material domains, see Figure 73.

k	M_{k1}	$\bar{N}_{k1}$	I_{k1}	$\bar{L}_{k1}$
1	$0.715493 + 0.464786i$	$0.715492 + 0.464787i$	$0.533424 + 0.346514i$	$0.533424 - 0.346515i$
2	$0.436009 + 0.198952i$	$-0.435969 - 0.199039i$	$-0.284583 - 0.1299269i$	$0.284611 - 0.129867i$
3	$-0.582004 + 0.591817i$	$-0.582004 + 0.591817i$	$0.191283 - 0.194508i$	$0.191283 + 0.19450i$
4	$0.300250 + 0.423752i$	$0.300250 + 0.423752i$	$0.157338 + 0.222056i$	$0.157338 - 0.222056i$

Table 24: (i) Bi-material junction, $2\alpha = 60°$, $E_1/E_2 = 0.25$. First four eigenvector's v_k coefficients M_{k1}, $\bar{N}_{k1}$, I_{k1} and $\bar{L}_{k1}$.

k	M_{k2}	$\bar{N}_{k2}$	I_{k2}	$\bar{L}_{k2}$
1	$0.321620 + 0.722903i$	$0.791219 + 0.000002i$	$0.406484 + 0.913658i$	1
2	$0.723878 + 0.834526i$	$-1.104732 - 0.000094i$	$-0.655188 - 0.755466i$	1
3	$0.026795 + 1.602508i$	-1.602732	$-0.016719 - 0.999860i$	1
4	$0.044471 - 0.126556i$	-0.134142	$-0.331519 + 0.943448i$	1

Table 25: (i) Bi-material junction, $2\alpha = 60°$, $E_1/E_2 = 0.25$. First four eigenvector's v_k coefficients M_{k2}, $\bar{N}_{k2}$, I_{k2} and $\bar{L}_{k2}$.

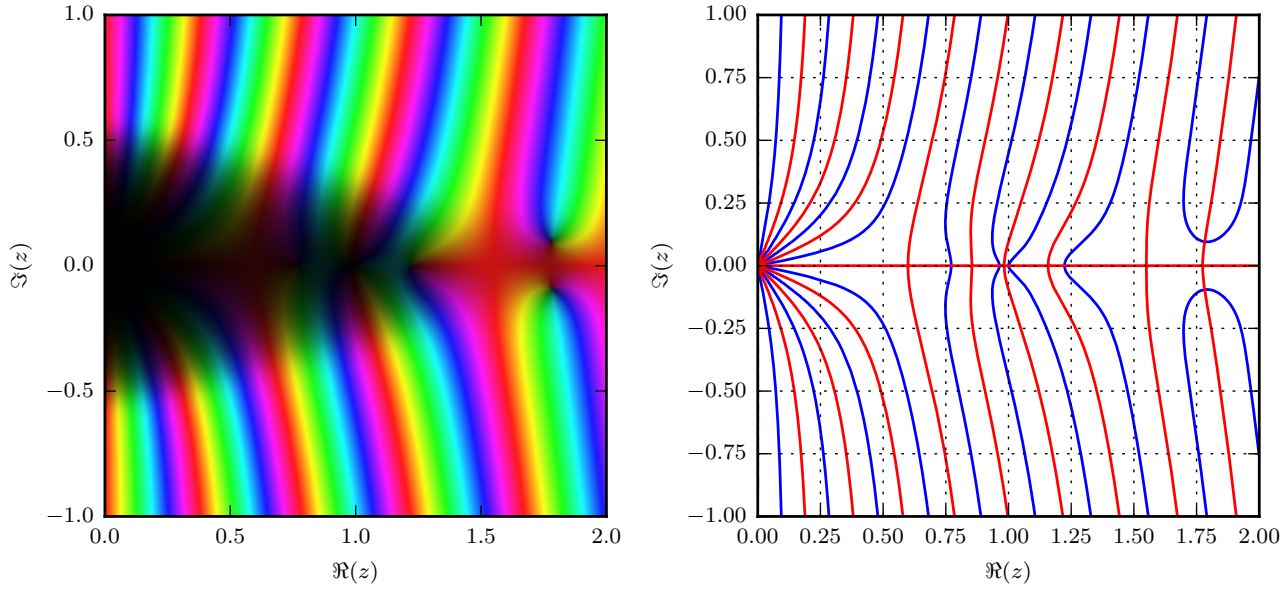

Figure 59: (ii) Bi-material junction, $2\alpha = 90°$. On the left-hand side there is the graph of $f(z) = \det(\mathbf{A}(\lambda))$. On the right-hand side contour plot, the blue curve stays for $\Re\{\det(\mathbf{A}(\Re\{\lambda_k\}))\} = 0$ and the red curve for $\Im\{\det(\mathbf{A}(\Im\{\lambda_k\}))\} = 0$.

k	1	2	3	4	5	6
λ_k	0.771662	0.963713	1.223471	$1.782013 \pm 0.095427i$	$2.229579 \pm 0.152656i$	$2.906718 \pm 0.380536i$

Table 26: (ii) Bi-material junction, $2\alpha = 90°$, $E_1/E_2 = 0.25$. First six eigenvalues λ_k.

k	1	2	3	4	5	6
λ_k	0.778634	1.093457	1.124854	$1.900225 \pm 0.157971i$	2.000000	2.25895762

Table 27: (iii) Bi-material junction, $2\alpha = 120°$, $E_1/E_2 = 0.25$. First six eigenvalues λ_k.

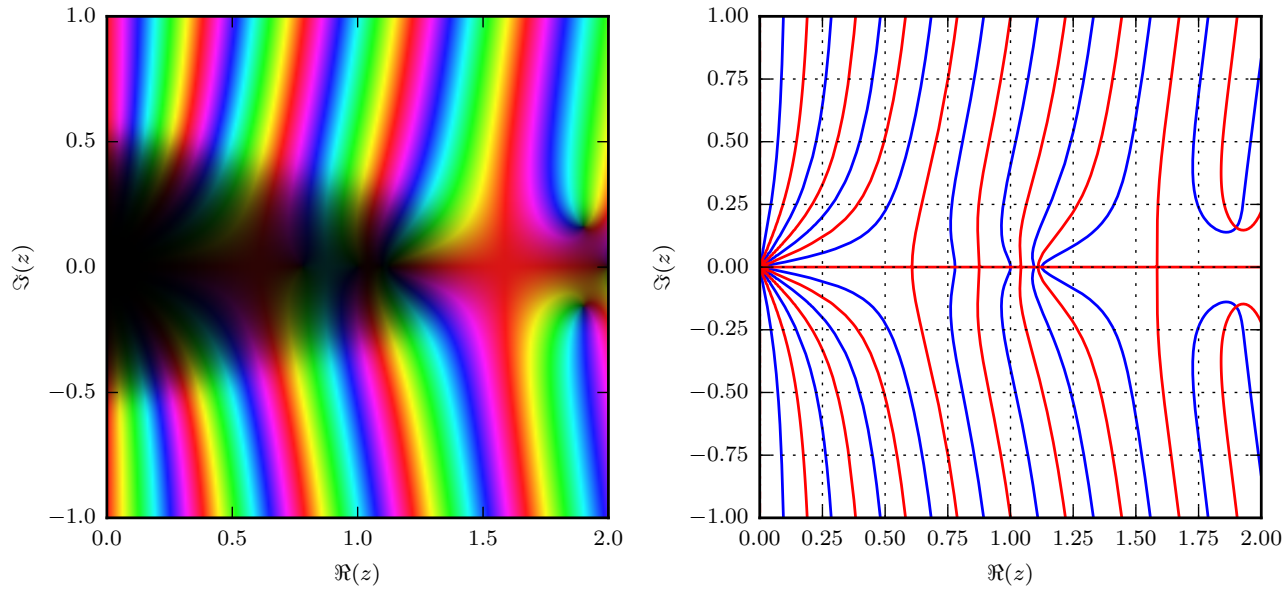

Figure 60: (iii) Bi-material junction, $2\alpha = 120°$, $E_1/E_2 = 0.25$. On the left-hand side there is the graph of $f(z) = \det(\mathbf{A}(\lambda))$. On the right-hand side contour plot, the blue curve stays for $\Re\{\det(\mathbf{A}(\Re\{\lambda_k\}))\} = 0$ and the red curve for $\Im\{\det(\mathbf{A}(\Im\{\lambda_k\}))\} = 0$.

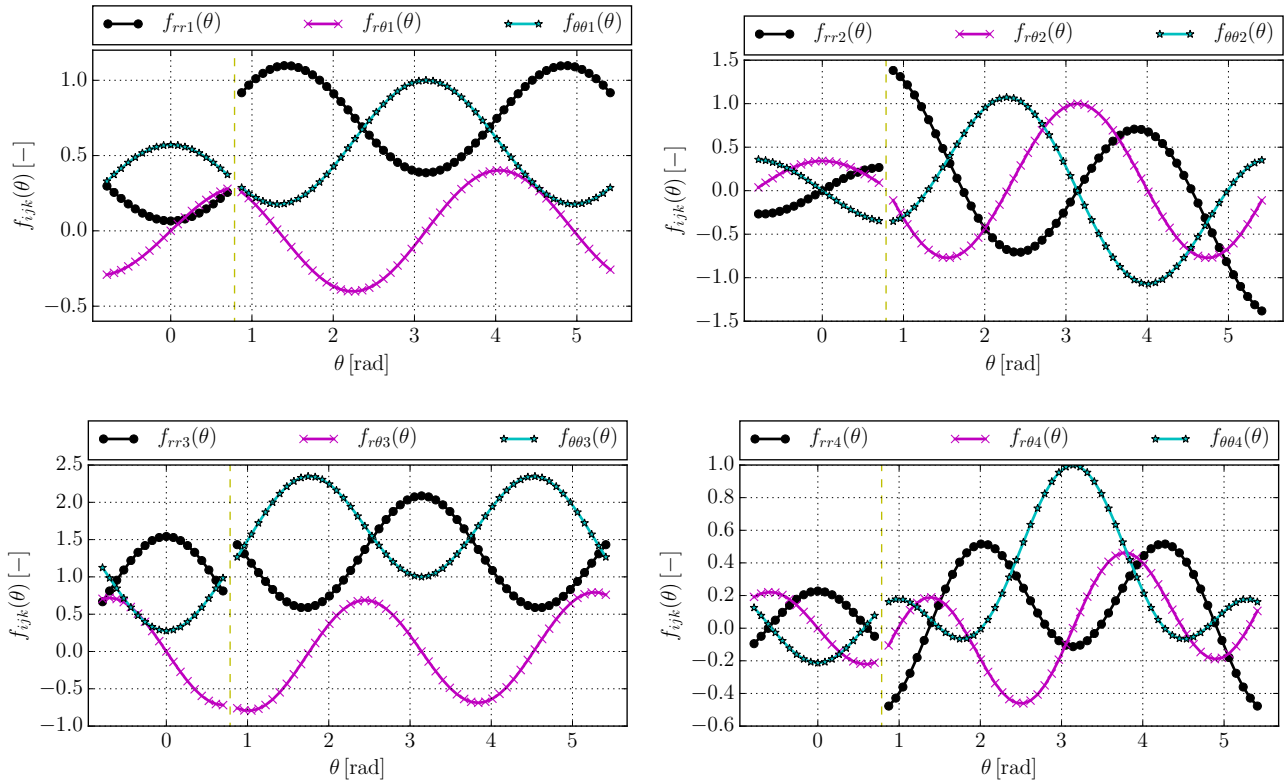

Figure 61: (ii) Bi-material junction, $2\alpha = 90°$, $E_1/E_2 = 0.25$. Stress eigenfunctions $f_{ijk}(\theta)$ for $k = 1, 2, 3, 4$.

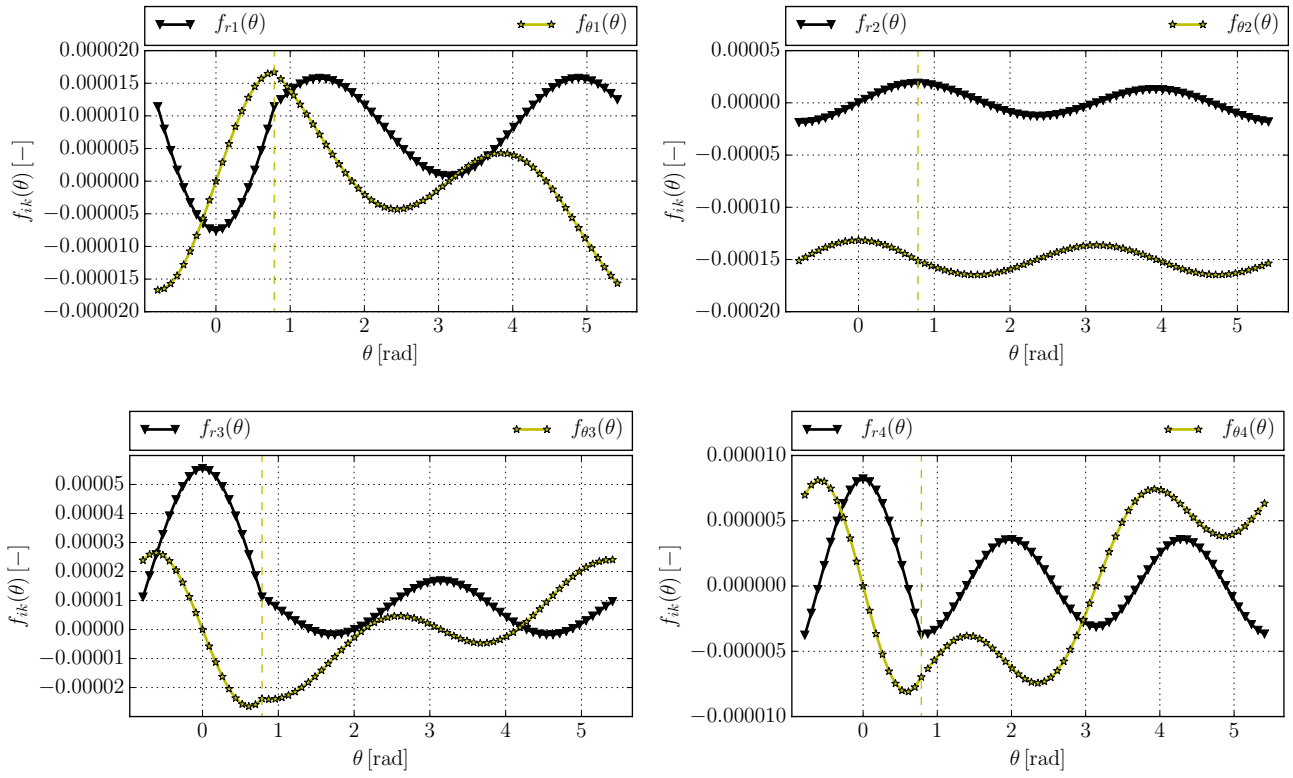

Figure 62: (ii) Bi-material junction, $2\alpha = 90°$, $E_1/E_2 = 0.25$. Displacement eigenfunctions $f_{ik}(\theta)$ for $k = 1, 2, 3, 4$.

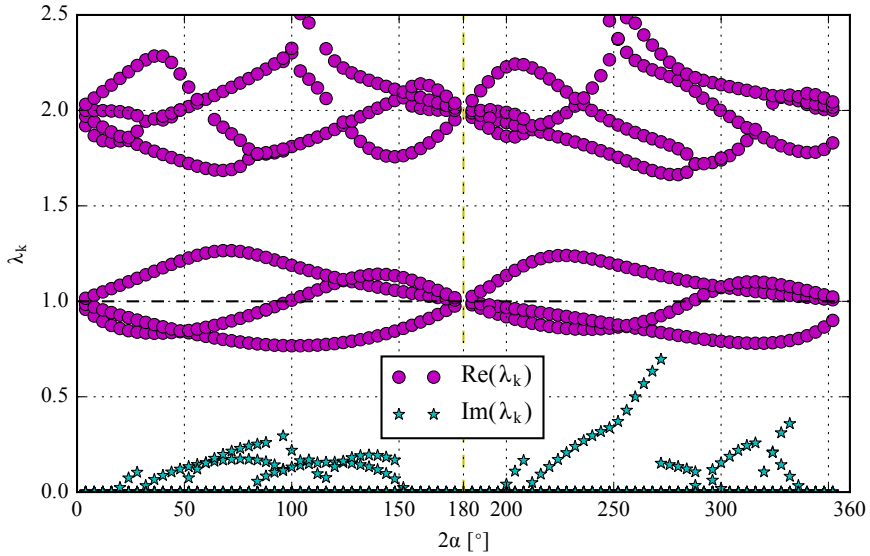

Figure 63: Dependence of eigenvalues λ_k the opening angle 2α. The geometry of the studied bi-material junction is defined: $\gamma_0 = -\alpha$, $\gamma_1 = \alpha$, $\gamma_2 = 2\pi - \alpha$. The Young's moduli ratio is $E_1/E_2 = 0.25$ and Poisson's ratios are $\nu_1 = \nu_2 = 0.25$.

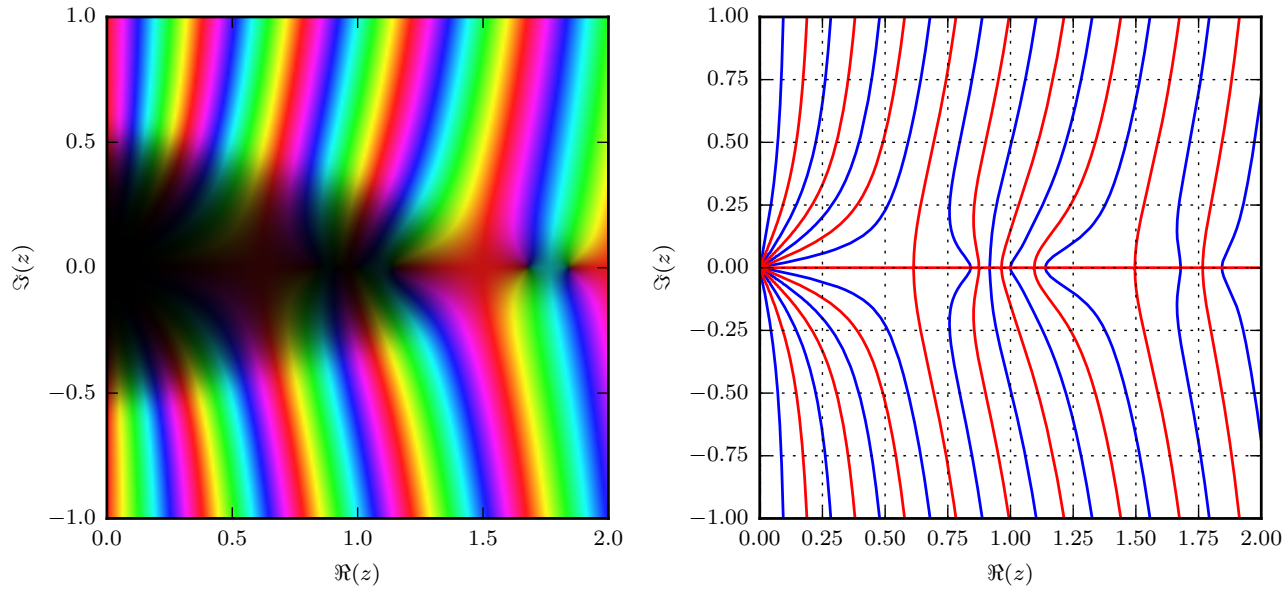

Figure 64: (i) Bi-material junction, $2\alpha = 90°$, $E_1/E_2 = 4$. On the left-hand side there is the graph of $f(z) = \det(\mathbf{A}(\lambda))$. On the right-hand side contour plot, the blue curve stays for $\Re\{\det(\mathbf{A}(\Re\{\lambda_k\}))\} = 0$ and the red curve for $\Im\{\det(\mathbf{A}(\Im\{\lambda_k\}))\} = 0$.

configuration (i), (ii) and (iii) in Table 28, 29 and 30 respectively. Note that the first three eigenvalues were real for all studied bi-material configurations. We have seen this also in the Numerical example J. In fact, the chart in Figure 63 with dependence $\lambda_k(2\alpha)$ shows that it is true for all admissible 2α (including both cases of inclusion more compliant than matrix and inclusion stiffer than matrix). As in the previous numerical example, the stress and displacement eigenfunctions are plotted in Figures 65 and 66 respectively, where the yellow dashed line denotes the location of the interface Γ_1.

k	1	2	3	4	5	6
λ_k	0.790989	1.071939	1.076264	$1.740424 \pm 0.154158i$	2.000000	2.134734

Table 28: (i) Bi-material junction, $2\alpha = 60°$, $E_1/E_2 = 4$. First six eigenvalues λ_k.

k	1	2	3	4	5	6
λ_k	0.840513	0.916435	1.139804	1.678525	1.843408	2.203158

Table 29: (ii) Bi-material junction, $2\alpha = 90°$, $E_1/E_2 = 4$. First six eigenvalues λ_k.

k	1	2	3	4	5	6
λ_k	0.853884	0.899008	1.221628	1.804944	2.000000	2.117332 ± 0.295848

Table 30: (iii) Bi-material junction, $2\alpha = 120°$, $E_1/E_2 = 4$. First six eigenvalues λ_k.

Calculation of stress terms factors

Determination of GSIFs by Ψ-integral

This part of the text describes a derivation of the path independent Ψ-integral for the bi-material junction problem. As in the case of a V-notch and bi-material notch, the employment of the Ψ-integral is a convenient

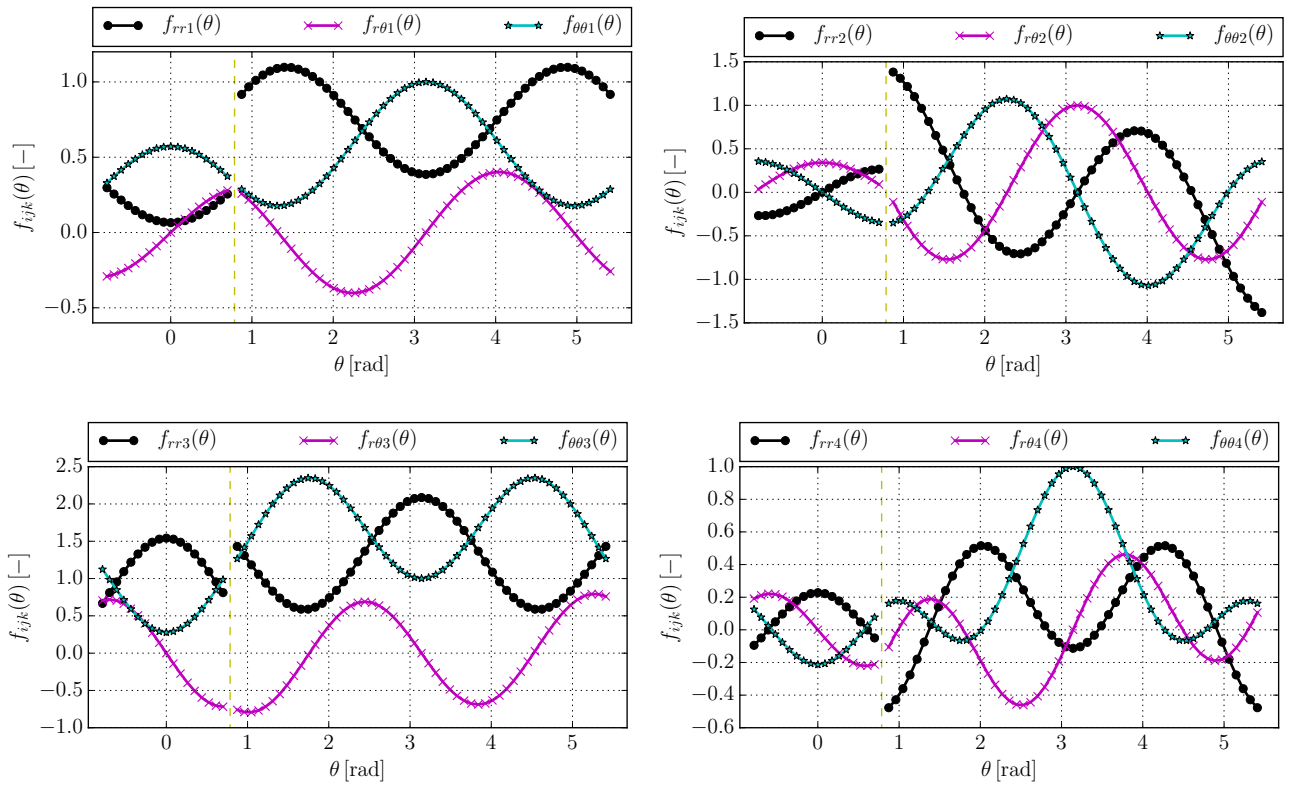

Figure 65: (ii) Bi-material junction, $2\alpha = 90°$, $E_1/E_2 = 4$. Stress eigenfunctions $f_{ijk}(\theta)$ for $k = 1, 2, 3, 4$.

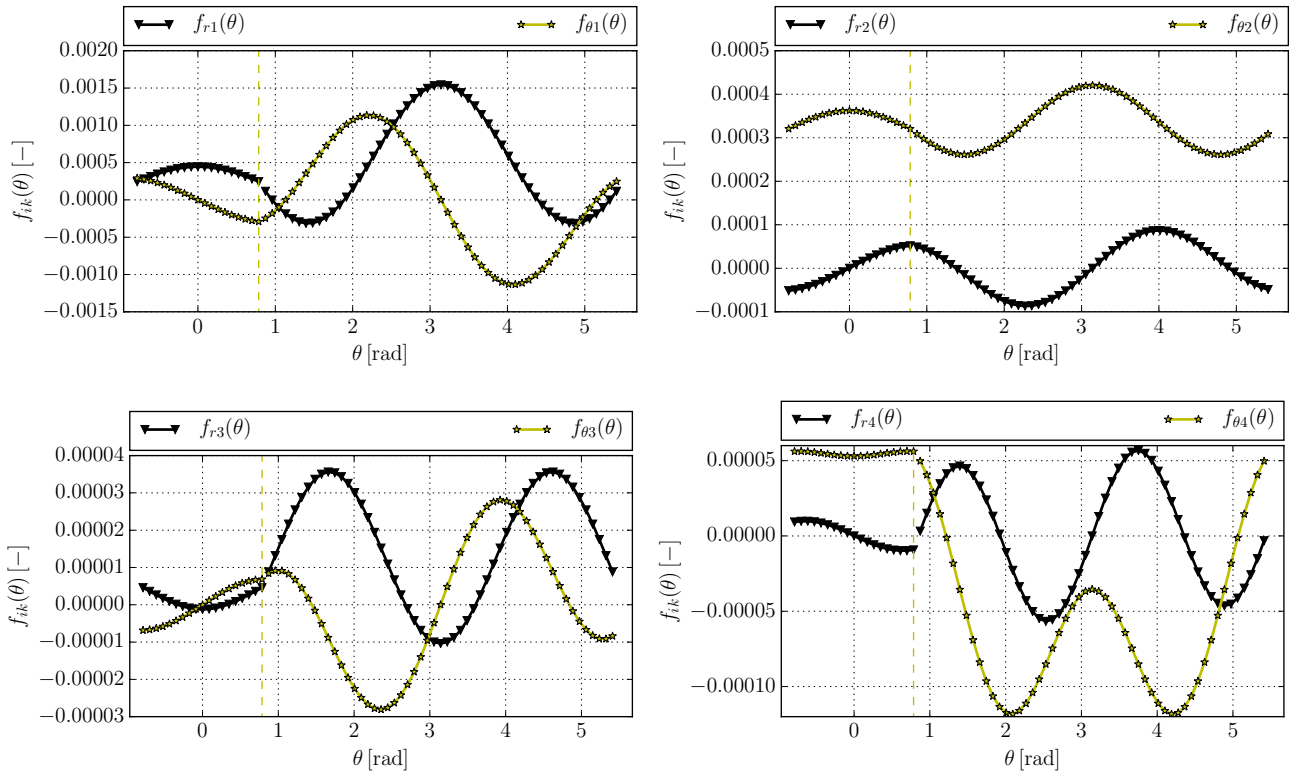

Figure 66: (ii) Bi-material junction, $2\alpha = 90°$, $E_1/E_2 = 4.0$. Displacement eigenfunctions $f_{ik}(\theta)$ for $k = 1, 2, 3, 4$.

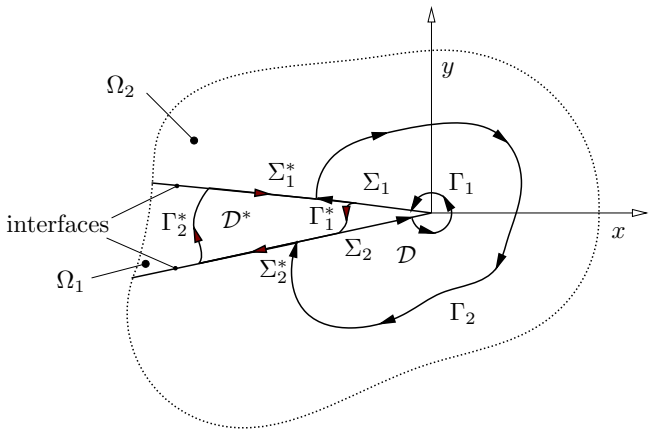

Figure 67: Two paths defined on two domains $\mathcal{D}$ and $\mathcal{D}^*$ of the bi-material junction which consists of material regions Ω_1 and Ω_2. The integration path $\partial\mathcal{D}$, the boundary of $\mathcal{D}$, consists of paths: Γ_1, Γ_2, Σ_1 and Σ_2. The other integration path $\partial\mathcal{D}^*$, the boundary of $\mathcal{D}^*$, consists of paths: Γ_1^*, Γ_2^*, Σ_1^* and Σ_2^*.

way for determination of Generalized Stress Intensity Factors (GSIFs) H_k. Similarly to the notch problem, a scaling coefficient $A(2\alpha, \theta_C)$ (necessary parameter for the Leguillon's coupled stress-energy criterion) can also be determined by the Ψ-integral. First, let recall equations (40)-(41) on p. 38. We consider a zero difference due to symmetry of the elastic tensor C:

$$\int_{\mathcal{D}} (C\colon \nabla U : \nabla V - C : \nabla V : \nabla U)\mathrm{d}x \quad = \quad 0. \tag{86}$$

where U and V are two elastic solutions dependent on 2 coordinates (x, y) in Cartesian coordinate system or (r, θ) in polar coordinate system and ∇ is gradient. $\mathcal{D}$ is an arbitrary closed domain within the material domains Ω_2 as shown in Figure 67. According to the Hooke's law in the following form:

$$\sigma(U) \quad = \quad C\nabla U,$$

the equation (86) becomes:

$$\int_{\mathcal{D}} (\sigma(U)\nabla V - \sigma(V)\nabla U)\mathrm{d}x \quad = \quad 0, \tag{87}$$

where $\sigma(U)$ and $\sigma(V)$ are stress fields associated with U and V respectively. By applying the Green's theorem to the equation (87) we obtain:

$$-\int_{\mathcal{D}} \nabla\sigma(U)V\mathrm{d}x + \int_{\partial\mathcal{D}} \sigma(U)nV\mathrm{d}s + \int_{\mathcal{D}} \nabla\sigma(V)U\mathrm{d}x - \int_{\partial\mathcal{D}} \sigma(V)nU\mathrm{d}s \quad = \quad 0, \tag{88}$$

where $\partial\mathcal{D}$ denotes the boundary of the domain $\mathcal{D}$ and n is the normal of the contour $\partial\mathcal{D}$. If equilibrium conditions apply, the first and the third term of equation (88) are equal to zero, therefore we can write:

$$\int_{\partial\mathcal{D}} (\sigma(U)nV - \sigma(V)nU)\mathrm{d}s \quad = \quad 0. \tag{89}$$

Since the negatively oriented boundary $\partial\mathcal{D}$ consists of 4 contours $\partial\mathcal{D} = \Gamma_1 \cup \Gamma_2 \cup \Sigma_1 \cup \Sigma_2$, the integral (89) can be written as sum of following 4 contour integrals:

$$\begin{aligned} &\int_{\Gamma_1} (\sigma(U)nV - \sigma(V)nU)\mathrm{d}s + \int_{\Sigma_1} (\sigma(U)nV - \sigma(V)nU)\mathrm{d}s + \\ &\int_{\Gamma_2} (\sigma(U)nV - \sigma(V)nU)\mathrm{d}s + \int_{\Sigma_2} (\sigma(U)nV - \sigma(V)nU)\mathrm{d}s \quad = \quad 0. \end{aligned} \tag{90}$$

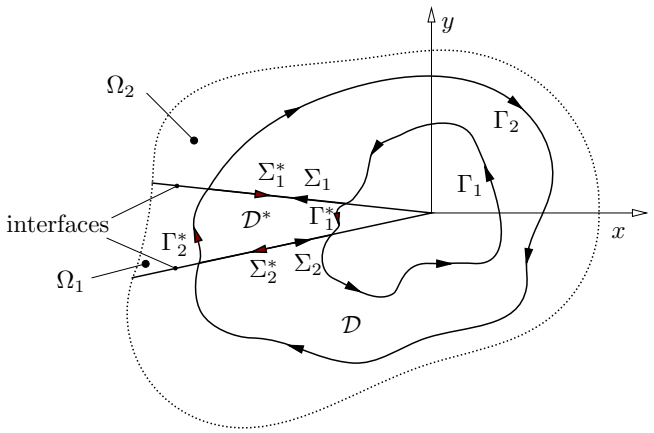

Figure 68: Paths of two integrals overlap on the interfaces, namely the Σ_1 with Σ_1^* and Σ_2 with Σ_2^*.

Let us consider another contour integral which is defined by arbitrary boundary $\partial\mathcal{D}^*$ laying within the other material domain Ω_1 as illustrated in Figure 67:

$$\int_{\partial\mathcal{D}^*} (\sigma(U)n^*V - \sigma(V)n^*U)\mathrm{d}s \quad = \quad 0. \tag{91}$$

Similarly as done previously we can subdivide the contour $\partial\mathcal{D}^*$ into four parts and the contour integral (91) becomes:

$$\begin{aligned}\int_{\Gamma_1^*} (\sigma(U)n^*V - \sigma(V)n^*U)\mathrm{d}s + \int_{\Sigma_1^*} (\sigma(U)n^*V - \sigma(V)n^*U)\mathrm{d}s + \\ \int_{\Gamma_2^*} (\sigma(U)n^*V - \sigma(V)n^*U)\mathrm{d}s + \int_{\Sigma_2^*} (\sigma(U)n^*V - \sigma(V)n^*U)\mathrm{d}s \quad = \quad 0.\end{aligned} \tag{92}$$

Let's lead both the path $\partial\mathcal{D}$ and $\partial\mathcal{D}^*$ in a way that Σ_1 and Σ_1^* as well as Σ_2 and Σ_2^* perfectly overlap, see Figure 68. To obtain the same orientation of the path for these overlapping contours a sign of the integral has to be changed, since $n^* = -n$. Therefore both integral equations (45) and (92) become:

$$\int_{\Gamma_1} (\sigma(U)nV - \sigma(V)nU)\mathrm{d}s + \int_{\Gamma_2} (\sigma(U)nV - \sigma(V)nU)\mathrm{d}s \quad = \quad -\int_{\Sigma_1} (\sigma(U)nV - \sigma(V)nU)\mathrm{d}s - \int_{\Sigma_2} (\sigma(U)nV - \sigma(V)nU)\mathrm{d}s, \tag{93}$$

$$\int_{\Gamma_1^*} (\sigma(U)n^*V - \sigma(V)n^*U)\mathrm{d}s + \int_{\Gamma_2^*} (\sigma(U)n^*V - \sigma(V)n^*U)\mathrm{d}s \quad = \quad \int_{\Sigma_1} (\sigma(U)nV - \sigma(V)nU)\mathrm{d}s + \int_{\Sigma_2} (\sigma(U)nV - \sigma(V)nU)\mathrm{d}s. \tag{94}$$

Because U, V, $\sigma(U)$ and $\sigma(V)$ are continuous through the interface, by adding (93) and (94) and a simple rearrangement we obtain:

$$\begin{aligned}\int_{\Gamma_1} (\sigma(U)nV - \sigma(V)nU)\mathrm{d}s + \int_{\Gamma_2} (\sigma(U)nV - \sigma(V)nU)\mathrm{d}s \quad + \\ + \int_{\Gamma_1^*} (\sigma(U)n^*V - \sigma(V)n^*U)\mathrm{d}s + \int_{\Gamma_2^*} (\sigma(U)n^*V - \sigma(V)n^*U)\mathrm{d}s \quad = \quad 0.\end{aligned} \tag{95}$$

Since $\Gamma_A = \Gamma_1 + \Gamma_1^*$ and $\Gamma_B^* = \Gamma_2 + \Gamma_2^*$ the equation (95) becomes:

$$\int_{\Gamma_A} (\sigma(U)nV - \sigma(V)nU)\mathrm{d}s + \int_{\Gamma_B^*} (\sigma(U)n^*V - \sigma(V)n^*U)\mathrm{d}s \quad = \quad 0,$$

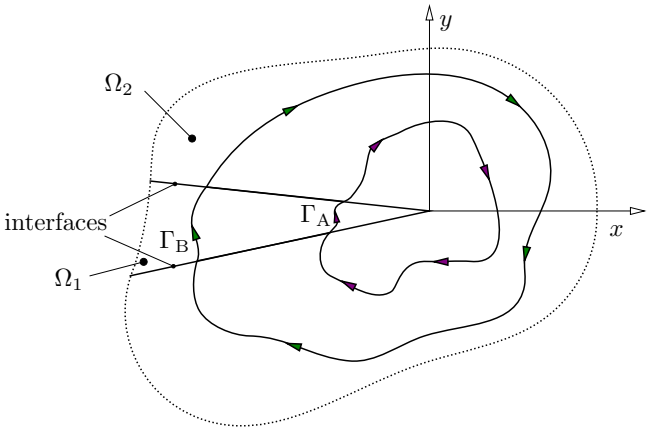

Figure 69: Paths of the integrals Γ_{A} and Γ_{B} .

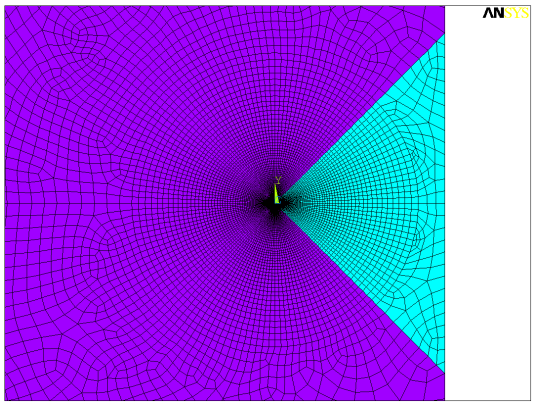

Figure 70: Area of refined mapped mesh near singular point of the bi-material junction.

or for negatively oriented curves Γ_A and Γ_B which are depicted in Figure 69 we finally get:

$$\int_{\Gamma_A} (\sigma(U)nV - \sigma(V)nU)\mathrm{d}s \quad = \quad \int_{\Gamma_B} (\sigma(U)nV - \sigma(V)nU)\mathrm{d}s,$$

which shows that this integral is path independent. The implications of the integral path independence are in detail commented in the previous sub-chapter on p. 39. As in the case of a bi-material notch (or any notch problem), definition of the integral as in Eq. (46) on p. 39 and properties as in Eq. (47)-(52) leads identically to the fact that the GSIFs in the case of a bi-material junction can be calculated by equation (53) on p. 41. To obtain term Ψ_k^{FE} the stresses and displacements are analogically calculated in FEM code ANSYS (in this work). The vicinity of the bi-material junction tip 2D model consists of refined mapped mesh as shown in Figure 70.

Numerical example M: Path independence and integration step effect for the Ψ-integral. Let's consider the geometric configuration of the bi-material junction $2\alpha = 90°$, which represents the most common case of the rectangular sharp material inclusion. In this numerical example, two bi-material configurations will be studied, the inclusion more compliant than matrix with (a) $E_1/E_2 = 0.25$ and inclusion stiffer than matrix with (b) $E_1/E_2 = 4$. In the former case $E_1 = 20$ GPa, in the latter case $E_1 = 80$ GPa and for both configurations $\nu_1 = \nu_2 = 0.25$. The eigenvalues, which were calculated previously in Numerical examples J and K are listed in Table 26 on p. 72 for the case (a) and in Table 29 on p. 75 for the case (b). The geometry of the studied problem is in both cases identical to Numerical example O, as shown in Figure 75 on p. 84. The loading for this numerical example is $F = 100$ N (per 1 mm of specimen thickness b). The problem is a symmetrical one. In such case we are mainly interested in terms with even eigenfunctions. As discussed in the theoretical section and shown in Numerical example J, the parity of k does not have to correspond to the the kth eigenfunction symmetry (odd or even properties of the function). In

this numerical example, in the case (a) we find the even eigenfunctions when $k = 1, 3, 4$. In the case (b) the even eigenfunctions are with $k = 1, 3$. The Ψ-integral is calculated with integration step of $\Delta\theta = 2.5°$ and $\Delta\theta = 5.0°$. The integration is conducted on $r = 1$ mm, $r = 3$ mm and as an average between these radii (since the mesh is adjusted automatically to keep right shape of individual elements, there are 10 circles in the case of larger integration step and 22 circles in the case of smaller integration step). The results of the configuration (a) are listed in Table 31. When we consider the dominant terms with even eigenfunctions, the change in H_k by decreasing the integration step is low, with maximum of 9.0 % in average value of the fourth term. The terms factors H_1 and H_3 show low standard deviation value in both cases of integration step size. The term factor H_2 with odd eigenfunction should have value close to zero, because of the problem symmetry. Its value is significantly closer to zero, when the finer integration step is used. Therefore results of better quality are obtained by smaller integration step size. Solid computational convergence is achieved as shown in Figure 71. We see that the term factor H_4 tends to converge on larger distances as seen in the same figure. For the case (b), the dominant (even) terms are with H_1 and with H_3. The results are listed in Table 32. The decrease in integration step size results in very low change in GSIFs of 0.5 % maximum (average of H_1). Considering the dominant terms, both cases of integration step size show very low standard deviation values. The odd term shows values much closer to zero again when we use smaller integration step. For the case of finer integration step a good computational convergence is achieved as shown in Figure 72, with an exception of small valued negative H_2.

	$H_k^{\Delta\theta=2.5°}$			$s^{\Delta\theta=2.5°}$
	$r = 1$ mm	$r = 3$ mm	avg.	avg.
H_1	31.711096	31.671537	31.685866	0.006926
H_2	-0.526437	-0.414348	-0.471664	0.033578
H_3	-0.986715	-1.036437	-1.015922	0.013186
H_4	$-2.607539 - 1.858953i$	$-2.323283 - 1.819121i$	$-2.437986 - 1.833683i$	0.081679

	$H_k^{\Delta\theta=5.0°}$			$s^{\Delta\theta=5.0°}$
	$r = 1$ mm	$r = 3$ mm	avg.	avg.
H_1	31.841465	31.756351	31.785227	0.01576
H_2	-1.117199	-0.908541	-1.014935	0.066322
H_3	-0.909882	-0.984984	-0.956533	0.019120
H_4	$-3.191347 - 1.831145i$	$-2.551828 - 1.797279i$	$-2.796666 - 1.806883i$	0.177578

Table 31: Bi-material junction Ψ-integral results for (a), $2\alpha = 90°$, $E_1/E_2 = 0.25$. Values of terms factors H_k determined on multiple radii with finer integration step of $\Delta\theta = 2.5°$ in the upper table and coarser integration step of $\Delta\theta = 5.0°$ in the lower table. The both cases are supplemented by standard deviation of the averaged value denoted by s.

	$H_k^{\Delta\theta=2.5°}$			$s^{\Delta\theta=2.5°}$	$H_k^{\Delta\theta=5.0°}$			$s^{\Delta\theta=5.0°}$
	$r = 1$ mm	$r = 3$mm	avg.	avg.	$r = 1$ mm	$r = 3$ mm	avg.	avg.
H_1	-0.266383	-0.265541	-0.265972	0.000204	-0.265262	-0.263983	-0.264565	0.000304
H_2	-0.030557	-0.059586	-0.041799	0.008569	-0.079073	-0.133025	-0.101129	0.017091
H_3	14.666912	14.672885	14.673597	0.000304	14.60914	14.634184	14.628421	0.003402
H_4	0.018563	0.016835	0.016957	0.000667	0.035951	0.032162	0.033113	0.001354

Table 32: Bi-material junction Ψ-integral results for (b), $2\alpha = 90°$, $E_1/E_2 = 4$. Values of terms factors H_k determined on multiple radii with finer integration step of $\Delta\theta = 2.5°$ in the left part of the table and coarser integration step of $\Delta\theta = 5.0°$ in the right part of the table. Both the cases are supplemented by standard deviation of the averaged value denoted by s.

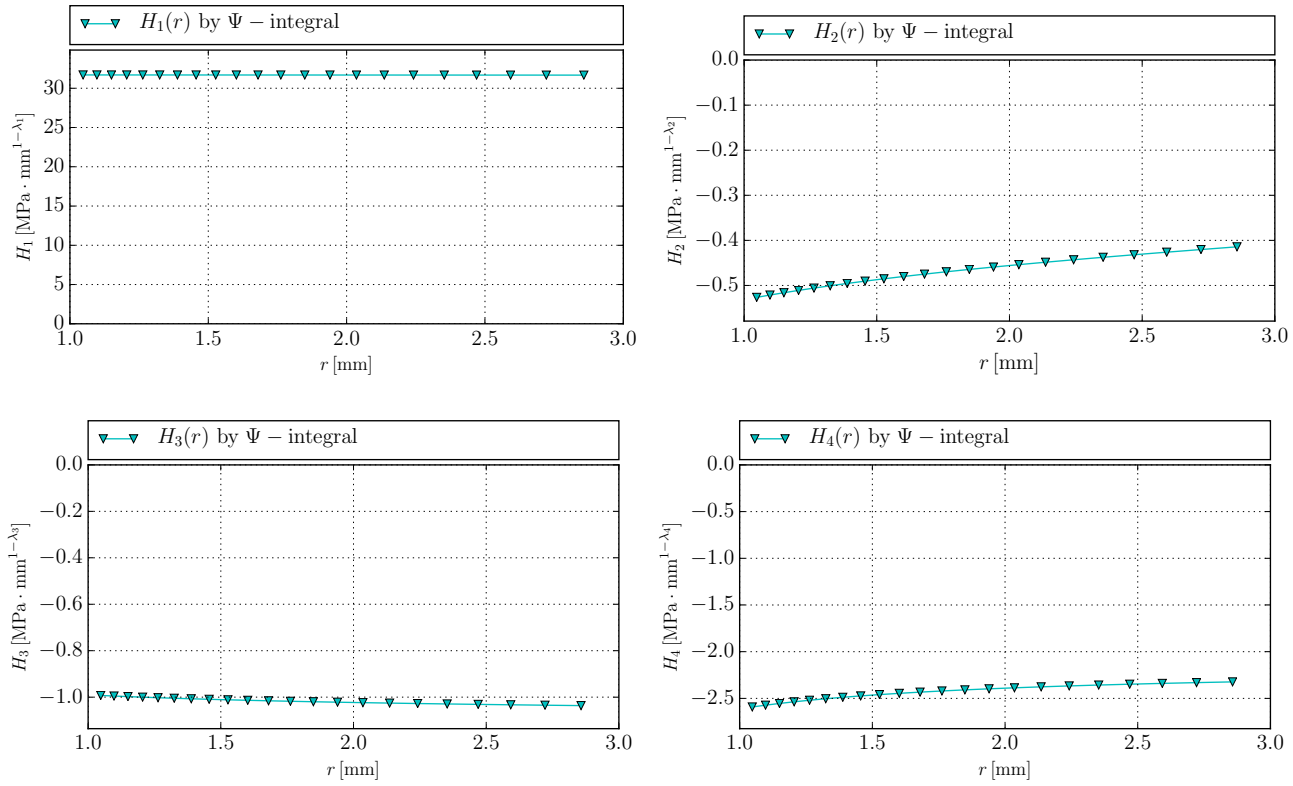

Figure 71: Dependence of the H_k on r. Bi-material junction (a), $2\alpha = 90°$, $E_1/E_2 = 0.25$. H_k by the Ψ-integral.

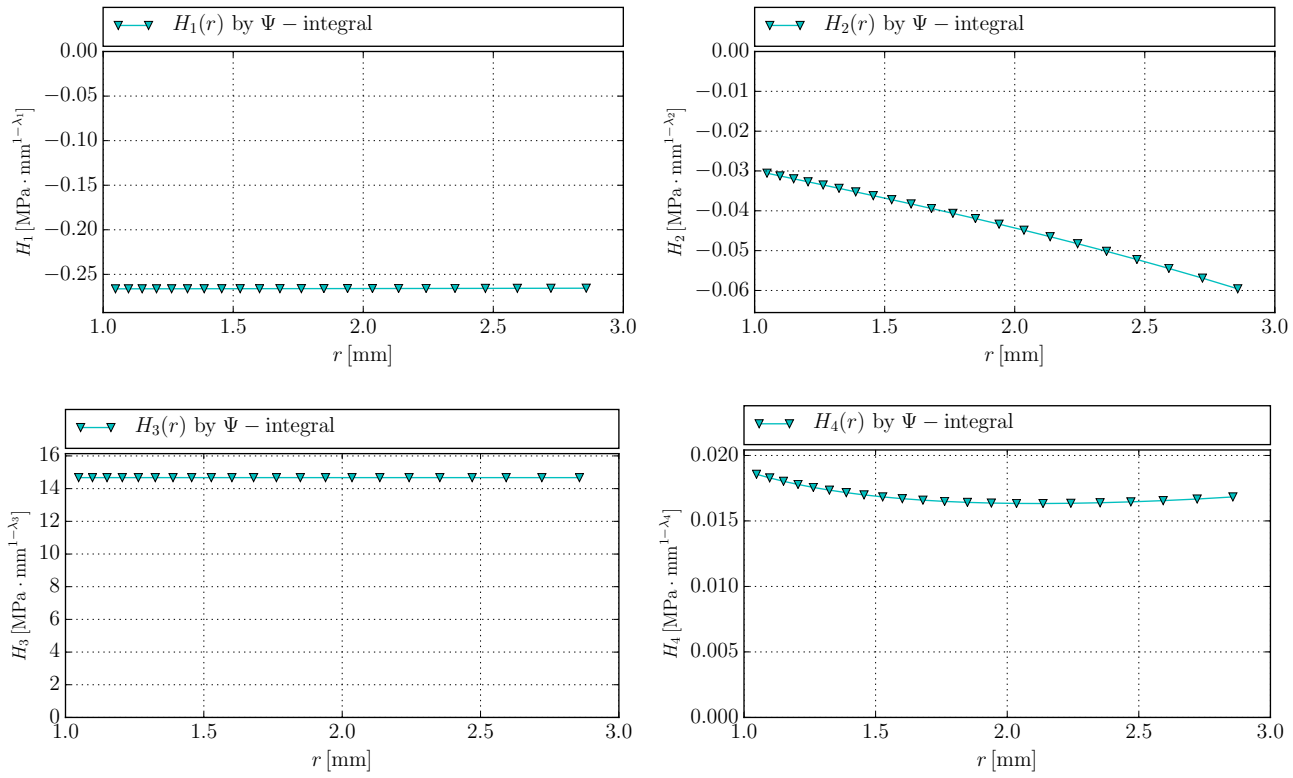

Figure 72: Dependence of the H_k on r. Bi-material junction (b), $2\alpha = 90°$, $E_1/E_2 = 4$. H_k by the Ψ-integral.

Determination of GSIFs by overdeterministic method

The ODM is mathematically easy and robust method of GSIFs determination. It is based on a least square solution of overdetermined system of linear equations. Inputs from the FEA can be either displacements or stresses. First let's recall the displacement based method and rewrite the Eq. (55) on p. 45:

$$\mathbf{F}_{[2m\times n]}\mathbf{H}_{[n]} \quad = \quad \mathbf{u}^{\mathrm{FE}}_{[2m]}.$$

The displacement based method is applicable only on symmetrical problems since we have not found a way to subtract the rigid body rotations or to account for them analytically in the displacement series. Rigid body rotations are typical for the case of non-symmetric problem as discussed in application of the ODM on the bi-material notch problem on p. 44. The advantage of stress based method is its straightforward applicability on non-symmetric problems. Let's rewrite the equation (59) on p. 47:

$$\mathbf{F}_{[3m\times n]}\mathbf{H}_{[n]} \quad = \quad \mathbf{S}^{\mathrm{FE}}_{[3m]}.$$

The Numerical example E on p. 50 has shown that the application of both methods give similar results (as it was tested in the case of symmetrical problem, when the comparison of methods is possible). The stress based method will be used further regardless of the problem symmetry.

Numerical example N: Determination of the GSIFs by the ODM. In this numerical example, the GSIFs will be determined by stress based Overdeterministic method. The geometry, bi-material configuration and loading in this study is identical as in Numerical example M on p. 79. In the first case denoted (a) we calculate first four GSIFs for rectangular inclusion more compliant than matrix of which the dominant (even) are H_1, H_3 and H_4 . In the second case denoted (b) again first four terms factors are calculated for the rectangular inclusion stiffer than matrix of which dominant are the terms factors H_1 and H_3. The use of smaller element edge length and subsequent input higher amount of input data leads to a 0.2 % change in averaged H_1, a 5.1 % change in averaged H_3, a 14.6 % change in averaged H_4 and decrease in standard deviation values in all cases. The odd term with H_2 shows values closer to zero in case of finer integration step. There is very slight linear trend in $H_k\,(r)$ so the value can be extrapolated to the point $r = 0$. This is illustrated in Figure 73. The case (b) shows a 0.5 % change in averaged H_1 and less than 0.1 % difference in averaged H_3. Again smaller values of non-dominant terms factors are better achieved by using smaller element edge length. The radial dependence of H_k is shown in Figure 74. The radial dependence of the second term factor may seem to have little signs of the convergence, however it is necessary to put it in the context of values it acquires ($\backsim 10^{-5}$ in comparison to $10^{-1} \div 10^{1}$ of the dominant terms factors). The H_2 is practically equal to zero.

	$H_k^{\Delta\theta=5.0^\circ}$				$s^{\Delta\theta=5.0^\circ}$
	regression	$r = 0.2$ mm	$r = 1$ mm	avg.	avg.
H_1	31.754646	31.740088	31.910209	31.715068	0.017126
H_2	−0.006831	−0.006823	−0.006791	−0.006812	$8e-06$
H_3	N/A	−0.982626	−1.026875	−1.019643	0.022973
H_4	N/A	$-6.618669 - 3.382666i$	$-4.784998 - 3.466781i$	$-5.634971 - 3.438265i$	0.555423

	$H_k^{\Delta\theta=2.5^\circ}$				$s^{\Delta\theta=2.5^\circ}$
	regression	$r = 0.2$ mm	$r = 1$ mm	avg.	avg.
H_1	31.654585	31.651782	31.737581	31.645112	0.004243
H_2	−0.001675	−0.001676	−0.001676	−0.001676	$8e-06$
H_3	N/A	−1.055008	−1.076553	−1.07387	0.010588
H_4	N/A	$-5.435045 - 3.564461i$	$-4.541765 - 3.560535i$	$-4.916542 - 3.564503i$	0.259246

Table 33: Bi-material junction ODM results for (a), $2\alpha = 90^\circ$, $E_1/E_2 = 0.25$. Values of singular terms factors H_1, H_2 and non-singular terms factors H_3 and H_4 determined on multiple radii with finer element edge division by $\Delta\theta = 2.5^\circ$ in the upper table and coarser element edge division by $\Delta\theta = 5.0^\circ$ in the lower table. In the first column there is the value obtained by the linear regression. Both the cases are supplemented by the average value and the standard deviation of the averaged value denoted by s.

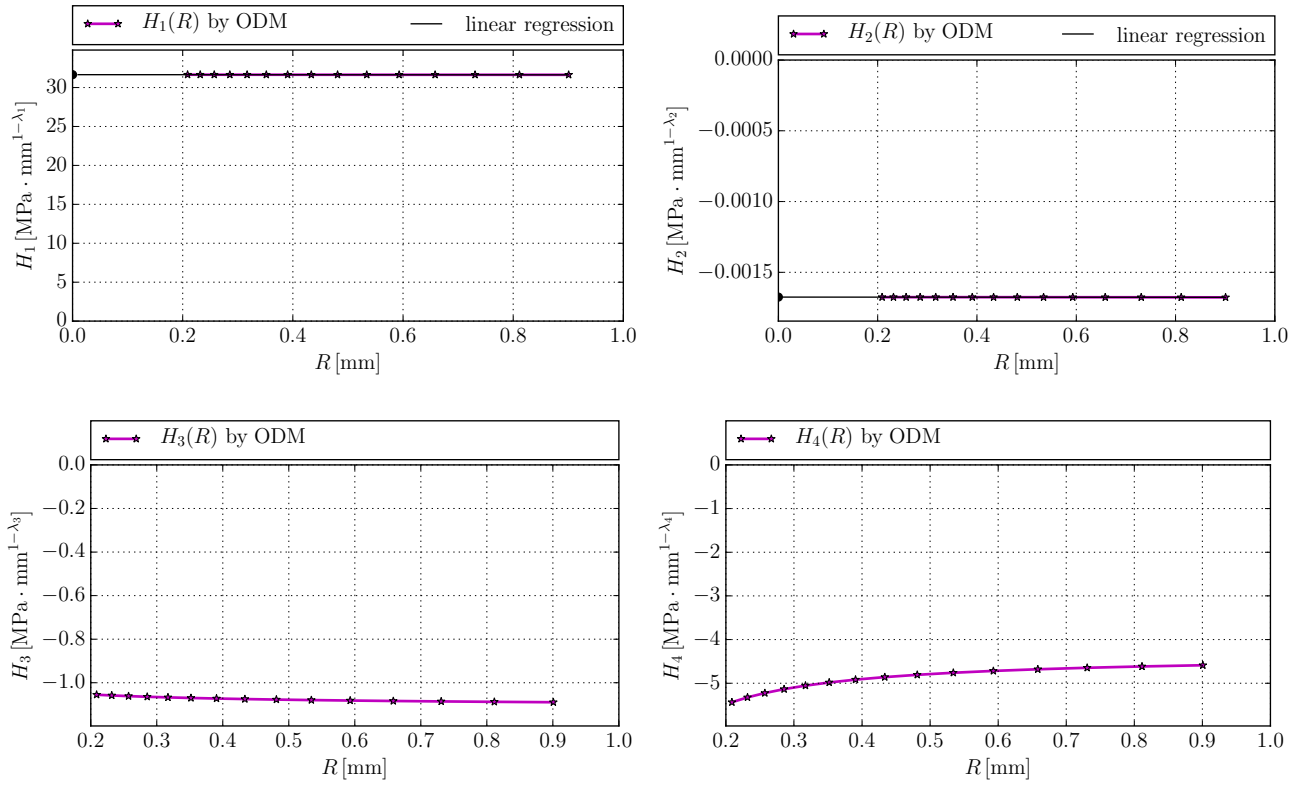

Figure 73: Dependence of the H_k on the radial distance r. The bi-material junction (a), $2\alpha = 90°$, $E_1/E_2 = 0.25$. GSIFs calculated by the ODM.

	$H_k^{\Delta\theta=5.0°}$				$s^{\Delta\theta=5.0°}$
	regression	$r = 0.2$ mm	$r = 1$ mm	avg.	avg.
H_1	−0.266041	−0.26581	−0.267448	−0.26562	0.000181
H_2	−0.002643	−0.002777	−0.001786	−0.002969	0.000141
H_3	N/A	14.679851	14.63162	14.689146	0.007211
H_4	N/A	0.013506	−0.001887	0.006484	0.003380

	$H_k^{\Delta\theta=2.5°}$				$s^{\Delta\theta=2.5°}$
	regression	$r = 0.2$ mm	$r = 1$mm	avg.	avg.
H_1	−0.266972	−0.266914	−0.267815	−0.266899	$3.6e-05$
H_2	$-4.3e-05$	−0.000115	0.000876	$-6.9e-05$	$3.4e-05$
H_3	N/A	14.707765	14.679417	14.708479	0.001195
H_4	N/A	0.007971	−0.002087	0.002714	0.002203

Table 34: Bi-material junction ODM results for (b), $2\alpha = 90°$, $E_1/E_2 = 4$. Values of leading terms factors H_1 and H_3 determined on multiple radii with finer element edge division by $\Delta\theta = 2.5°$ in the left part of the table and coarser element edge division by $\Delta\theta = 5.0°$ in the right side of the table. In the first column there is the value obtained by the linear regression. Both the cases are supplemented by the average value and the standard deviation of the averaged value denoted by s.

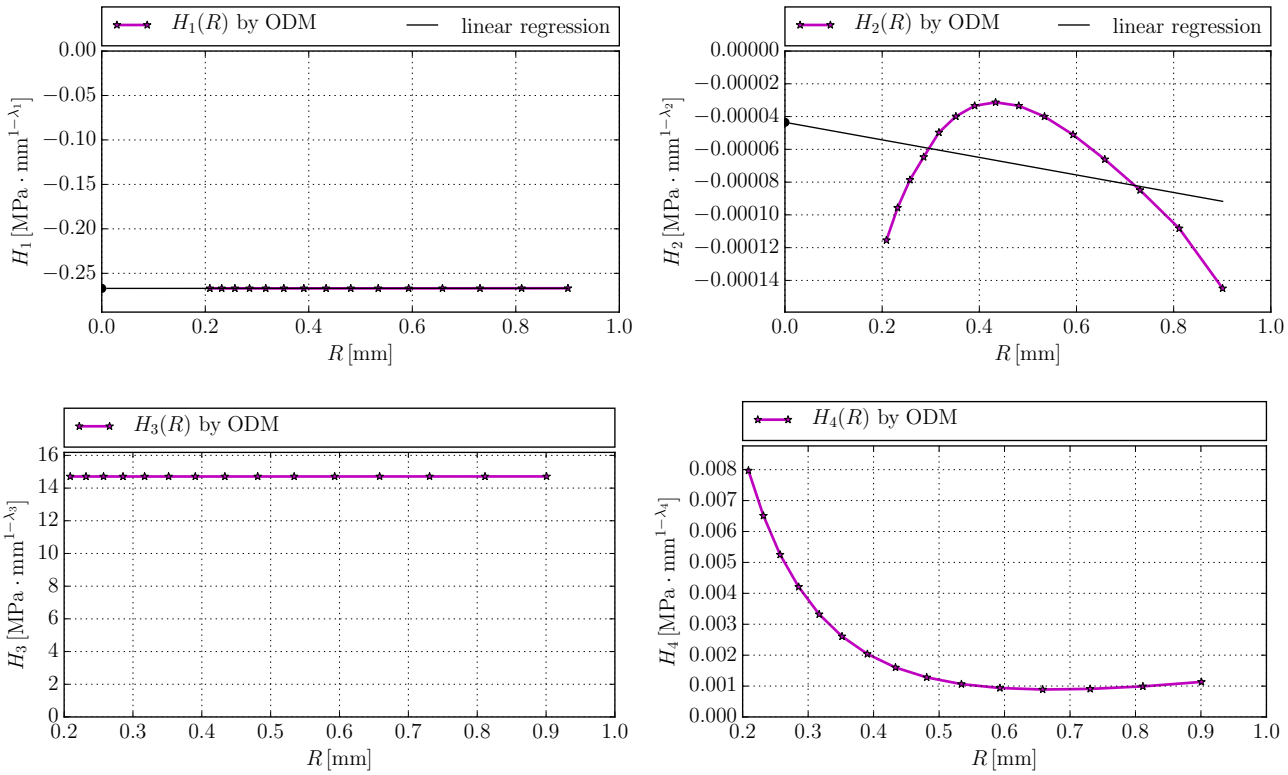

Figure 74: Dependence of the H_k on the radial distance r. The bi-material junction (b), $2\alpha = 90°$, $E_1/E_2 = 4$. GSIFs calculated by the ODM.

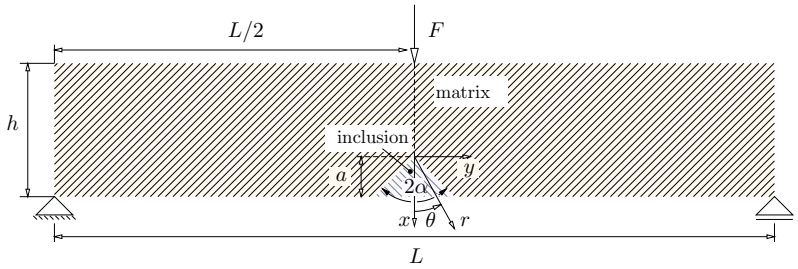

Figure 75: Model of the sharp material inclusion specimen subjected to 3 point bending.

Numerical example O: Stress reconstruction for the Sharp Material Inclusion more compliant than matrix. The three point bending specimen that contains the sharp material inclusion is modeled in 2D as shown in Figure 75. The dimensions of the model are identical as in previous examples for notches, i.e. $L = 76.2$ mm, $h = 17.8$ mm, $a = 3.56$ mm, so the inclusion depth to width ratio is $a/h = 0.2$. The bi-material junction model is used with the opening angle $2\alpha = 90°$ ($\gamma_0 = -\alpha, \gamma_1 = \alpha, \gamma_2 = 360° - \alpha$). The material region 1, which represents the inclusion, is modeled with PMMA material properties $E_1 = 2.3$ GPa, $\nu_1 = 0.34$ and the material region 2, which represents matrix, with aluminum material model characterized by $E_2 = 69$ GPa, $\nu_2 = 0.33$. The Young's moduli ratio in this case is $E_1/E_2 = 0.033$, thus it is the case of an inclusion more compliant than matrix. Ideal adhesion on the interfaces is assumed. The model is loaded with force of $F = 1$ N (per 1 mm of specimen thickness b) and plane strain state is chosen. The eigenfunctions are normalized per Eq. (38) with $\theta_0 = 180°$, which is due to the problem symmetry the predicted angle of crack initiation. The reference coordinate system is shown in Figure 75. The parameters which form the mapped mesh near singular point as in Figure 33 are chosen as: $r_0 = 0.01$ mm, $r_1 = 1$ mm and $r_2 = 3$ mm and the element edge division is by 2.5°. The first five GSIFs H_k are calculated by the Ψ-integral, with integration radius $r = 3$ mm and the linear regression extrapolated H_1, H_2 or the averaged ODM

$H_3 \div H_5$. The universal stress based ODM is used. The results are found in Table 35. The difference in those two methods is 0.6 % for the first term factor H_1 and 13% for the H_4, nevertheless the ODM returns values of non-dominant terms factors H_2 and H_5 closer to zero. The stress is reconstructed on the radius of 1 mm as shown in Figure 76 with terms factors calculated by the ODM. We can see that the stress distribution within $\gamma_1 \div \gamma_2$ by shape of the curves corresponds to the stress distribution of a V-notch. It is not difficult to explain why. When the more compliant material fills the V-notch area, which is normally a free space, it acts like compliant reinforcement. Overall behavior of the notch in terms of mechanics however remains. By overall trend the analytical solution corresponds well to the FE solution. In the case when only singular terms with H_1 and H_2 are used we see some difference between analytical solution and FE solution among all stress components. The first non-singular term with H_3 (magenta line) does not increase precision by any observable means. Next non-singular term with H_4 (the cyan line) however increases precision in a way that it fits FEA excellently. Employment of following term with H_5 (the red line) does not add any more precision as its line lays on the cyan line of H_4 . We can identify a pattern in this behavior. Remember that this is a symmetrical problem and as commented in numerical example the odd terms are with H_1, H_3 and H_4. The terms H_1 and H_4 which contribute to the solution for most are found among these and furthermore they are the two with the maximal absolute values.

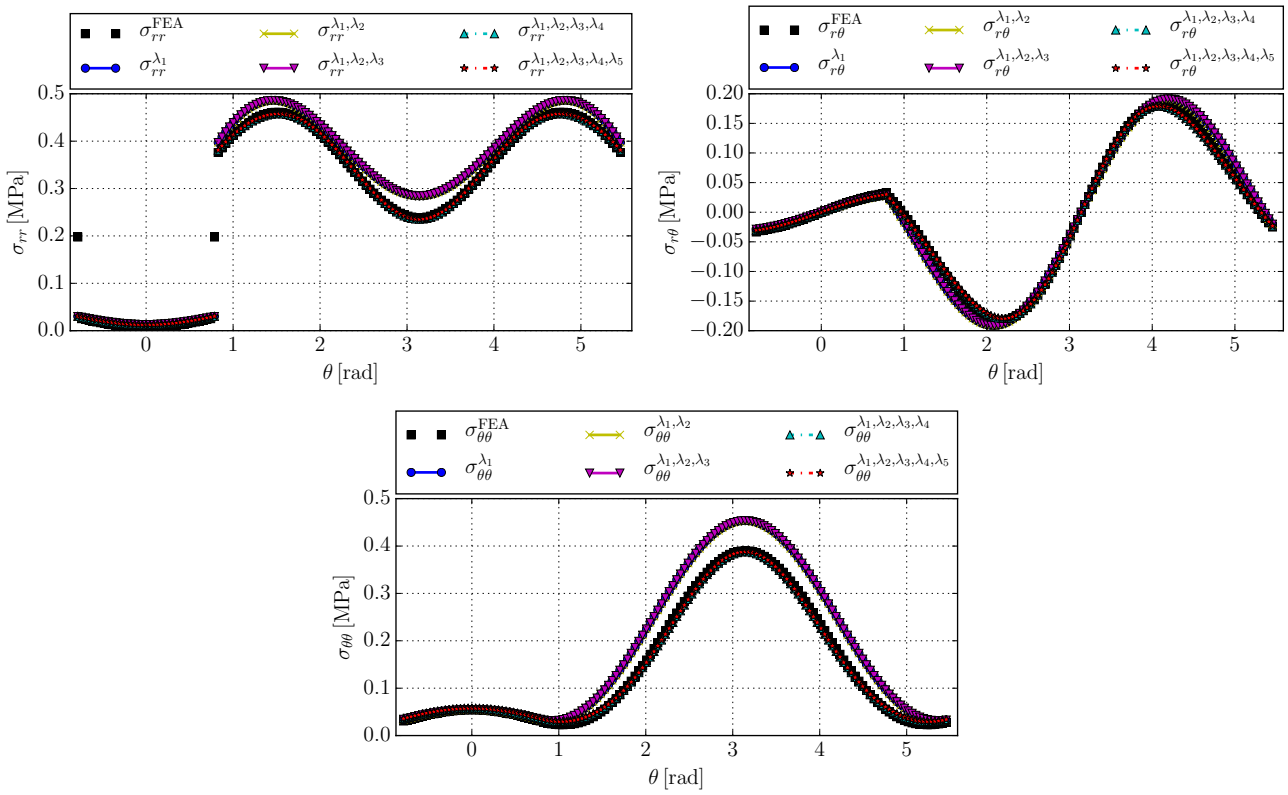

Figure 76: Stress reconstruction of $\sigma_{rr}(r,\theta)$, $\sigma_{r\theta}(r,\theta)$ and $\sigma_{\theta\theta}(r,\theta)$ on $r = 1$ mm for the bi-material junction with $2\alpha = 90°$ and $E_1/E_2 = 0.033$. The GSIFs for an analytical solution determined by the ODM.

k	λ_k	H_k^{Ψ}	$H_k^{\mathrm{ODM},\sigma_{ij}}$
1	0.589566	0.465328	0.462405
2	0.918297	-0.006971	$-8e-06$
3	1.342835	-0.007708	-0.000275
4	$1.648027 + 0.2047i$	$-0.027841 - 0.018909i$	$-0.063994 - 0.048784i$
5	$2.295327 + 0.294341i$	$0.002336 - 0.001035i$	$-7e-06 + 4e-06i$

Table 35: Eigenvalues λ_k and H_k by the Ψ-integral and ODM. Bi-material junction, $2\alpha = 90°$, $E_1/E_2 = 0.033$.

Numerical example P: Stress reconstruction for the Sharp Material Inclusion stiffer than matrix. This numerical example is analogical to the Numerical example O. Only the material region 1, which represents the inclusion, is modeled with aluminum material properties 69 GPa, $\nu_1 = 0.33$ and the material region 2, which represents matrix, with PMMA model $E_2 = 2.3$ GPa, $\nu_2 = 0.34$. The Young's moduli ratio in this case is $E_1/E_2 = 30$, thus it is a case of inclusion stiffer than matrix. Ideal adhesion on the interfaces is assumed. The GSIFs were calculated by the Ψ-integral and the ODM. If we examine the eigenfunctions, we found that the functions with $k = 2, 3$ are even. Therefore, the terms with even eigenfunctions should be non-zero. The results are listed in Table 36. Difference in the second term factor H_2 calculated by different methods is 3.6 % and the difference in the third term factor H_3 is 7.5%. For the remaining terms values closer to zero are obtained by use of the ODM. The stress is reconstructed on the radius of 0.5 mm as shown in Figure 77. The stress distribution is typical for examples when the inclusion is stiffer than matrix (with consideration of three point bending or tension loading). Such stress distribution is different both from the case of notches and more compliant inclusion. The explanation is, that the stiffer inclusion acts like a reinforcement, which bears the load. The analytical stress distribution by first singular term with H_1 (the blue line) is completely off relative to the FE solution. By employing the second singular term with H_2 (the yellow line), the analytical solution by trend becomes closer to FE solution. When we take into account also the first non-singular term with H_3 (the magenta line), the analytical solution fits FE solution with very good precision. Use of higher order terms with H_4 (the cyan line) and H_5 (the red line) does not add to the precision by any observable means as all the lines lay on each other. For a symmetric problem like this one, the even terms are the most significant. As shown in Table 36, these are also terms with highest absolute values. In conclusion, the singular terms do not describe the solution well even on 0.5 mm. In fact, even if we decrease the radial distance to the nanometers, the singular terms still does not describe the stress well [22]. Only by employment of higher order terms, the stress description begins to match FEA.

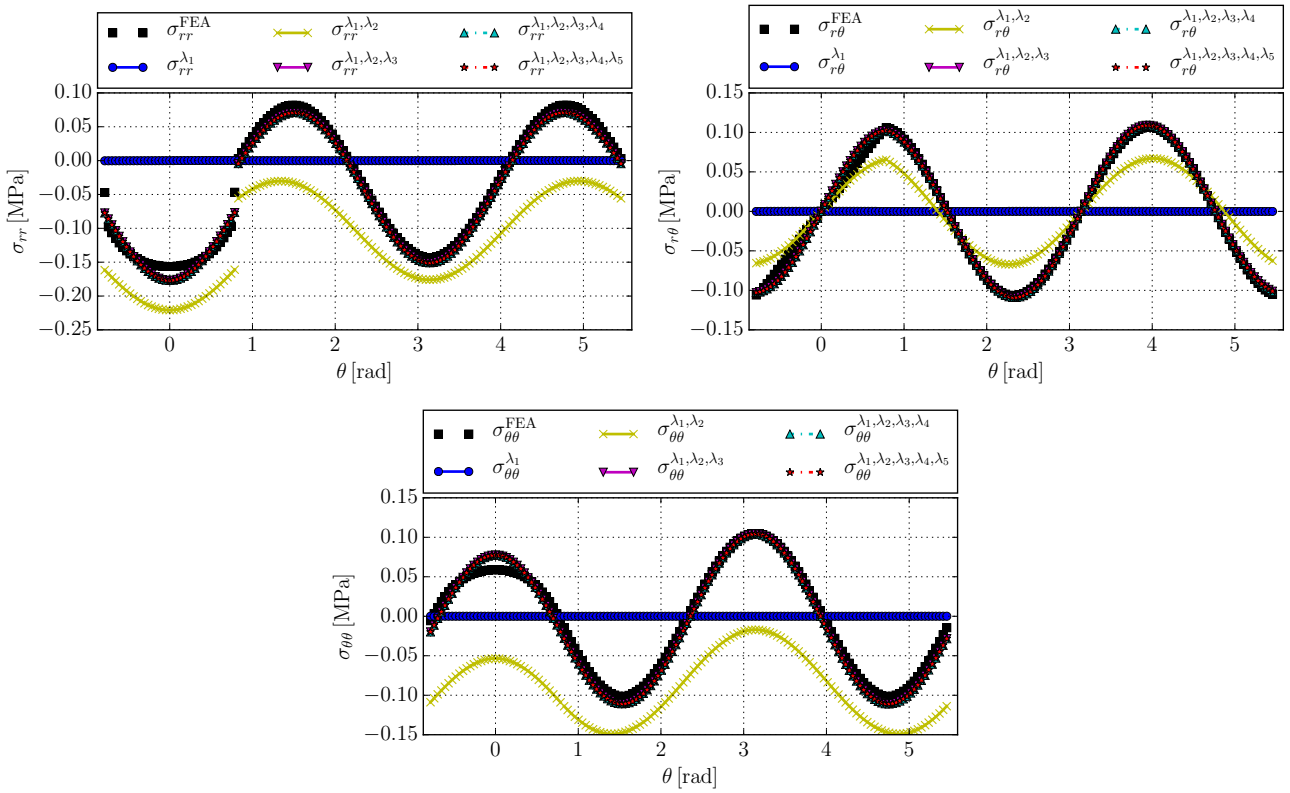

Figure 77: Stress reconstruction of $\sigma_{rr}(r,\theta)$, $\sigma_{r\theta}(r,\theta)$ and $\sigma_{\theta\theta}(r,\theta)$ on $r = 0.5$ mm for the bi-material junction with $2\alpha = 90°$ and $E_1/E_2 = 30$. The GSIFs for an analytical solution determined by the ODM.

k	λ_k	H_k^{Ψ}	$H_k^{\mathrm{ODM},\sigma_{ij}}$
1	0.667580	-0.000136	$1.8e-05$
2	0.783669	-0.014298	-0.013803
3	1.159292	0.146576	0.136358
4	1.628595	$5e-06$	$1.6e-05$
5	1.676726	$-1e-05$	$-4.2e-05$

Table 36: First five eigenvalues λ_k and GSIFs H_k calculated by the Ψ-integral and ODM. The bi-material junction, $2\alpha = 90°$, $E_1/E_2 = 30$.

	inclusion more compliant than matrix ($E_1 < E_2$)			inclusion stiffer than matrix ($E_1 > E_2$)		
loading	case	description by s. t.:	use of n. s. t.:	case	description by s. t.:	use of n. s. t.:
vertical	(i)	good	increased precision	(ii)	poor	necessary
vertical	(iii)	good	increased precision	(iv)	poor	necessary
horizontal	(v)	poor	necessary	(vi)	good	increased precision
horizontal	(vii)	poor	necessary	(viii)	good	increased precision

Table 37: Summary of results, the particular cases are shown in Figure 78. The acronym s. t. stands for singular terms and n. s. t. for non-singular terms.

Criteria of crack initiation direction and stability criteria

When we consider sharp rectangular material inclusion, there are 8 possible cases of loading direction and bi-material stiffness ratio variation. This determines the character of singularity, which exists at the singular concentrator tip. These 8 possible configurations are illustrated in Figure 78. For some cases, the singular terms describe the singular solution with solid accuracy (as in Numerical example O on p. 84), in other instances, the employment of higher order terms is essential (as in Numerical example P on p. 86). Let's analyse the configurations with the vertical loading, cases (i)-(iv). The Young's modulus of inclusion is denoted by E_1 and the modulus of matrix by E_2. The cases (i) and (iii) both act like a V-notch, since the inclusion acts like a compliant reinforcement. In the former case loaded in tension and the latter case in compression. In both cases the singular terms describe the stress state well. Employment of higher order terms increases precision on larger distances from the tip. On the other hand, we have configurations (ii) and (iv) which represent inclusion stiffer than matrix. The case (ii) is similar to Numerical example O, where the stress is not described well by singular terms. The case (iv) is its equivalent in compression, characterized also by poor description of the stress field by singular terms. Employment of higher order terms is essential to obtain stresses that truly represents the stress state near the inclusion tip. The configurations with horizontal tension (v)-(viii) show a different pattern. The cases (v) and (vii), i.e. cases of inclusion more compliant than matrix are characterized by poor stress description by singular terms. To obtain results that represent the actual stress field, employment of higher order terms is necessary. In contrast, in the cases (vi) and (vii) with inclusion stiffer than matrix singular terms describe the stress state well. Again, precision is increased by use of higher order terms. The Table 37 provides a summary of the cases. The general load of an engineering component is a combined one. Moreover, the orientation of an inclusion in composite is random (depending on the composite type). Therefore, we can not state that the singular terms only are sufficient for the case of an inclusion more compliant than matrix and that the non-singular terms are crucial for the case of inclusion stiffer than matrix. By comparing e.g. the cases (i) and (v) it is obvious, that even for cases of an inclusion more compliant than matrix, the non-singular terms do not describe the stress precisely enough.

The criterion of maximum of average tangential stress

As described in the sub-section 2.3 on p. 17, the maximum tangential stress criterion states that the crack will initiate in the direction of maximal tangential stress. General case of a bi-material junction (non-symmetrical) is characterized by radial dependence of the direction of maximum $\sigma_{\theta\theta}(r,\theta)$. To mitigate this dependence, as in the case of a bi-material notch, we determine the average value of tangential stress $\overline{\sigma}_{\theta\theta}(\theta)$ over some specific distance d. This distance d is established by the relation to microstructure or fracture mechanism. The derivation of the multi-parameter formula to assess stability of a bi-material junction is analogical to the case of a bi-material notch, see p. 55. Thus we can rewrite the equation (64):

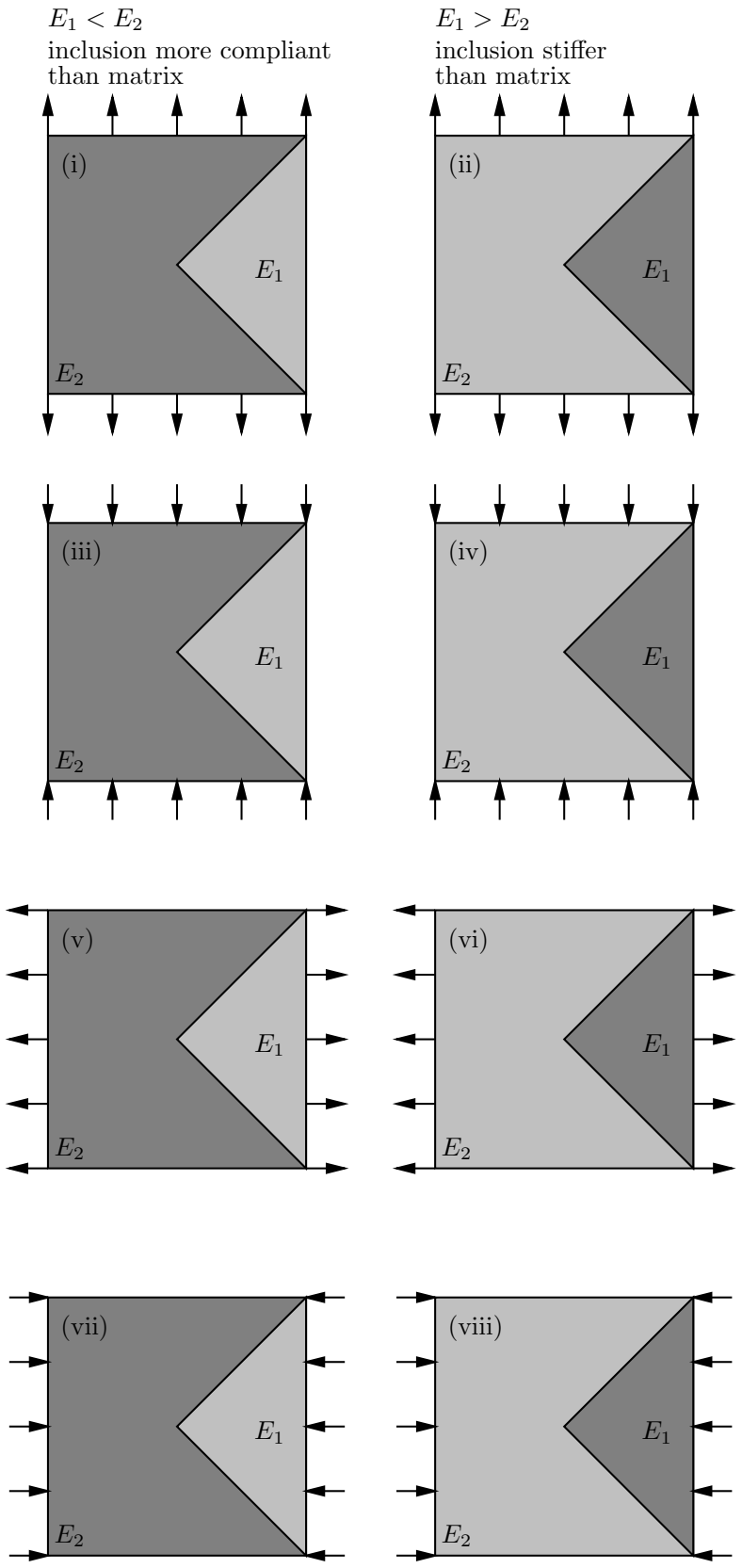

Figure 78: 8 possible cases of rectangular inclusion loading and bi-material variation

$$\sum_{k=1}^{n} \Gamma_{k1} \frac{d^{\lambda_k}}{\lambda_k} \frac{\partial f_{\theta\theta k}(\theta)}{\partial \theta} = 0, \tag{96}$$

by which we find the global maximum of $\overline{\sigma}_{\theta\theta}(\theta)$ (and also the local one). Recall that Γ_{k1} is the ratio between GSIFs defined as $\Gamma_{k1} = H_k/H_1$. In the equation above, the angle of global maximum is the only unknown. In the case of a bi-material junction, there are three possible directions of crack onset. The crack can onset into direction with global maximum of $\overline{\sigma}_{\theta\theta}(\theta)$, into a local maximum, or in one of the interfaces. These three depend on the fracture toughness of inclusion, matrix and the interface, the $K_{\mathrm{IC},1}$, $K_{\mathrm{IC},2}$ and $K_{\mathrm{IC,interface}}$ respectively. Based on an assumption that the crack initiation mechanism is the same as in the case of a crack propagation in homogeneous media, we compute the generalized critical value of fracture toughness as:

$$H_{1\mathrm{C},m} = \frac{K_{\mathrm{IC},m}}{\sqrt{2\pi}\Re\left\{\sum_{k=1}^{n} \Gamma_{k1} \frac{d^{\lambda_k - \frac{1}{2}}}{\lambda_k} f_{\theta\theta k}(\theta_{0,m})\right\}} \tag{97}$$

The generalized fracture toughness of the matrix, inclusion and the interface $H_{1C,1}$, $H_{1C,2}$ and $H_{1\mathrm{C,interface}}$ have to be calculated on corresponding angles of crack onset $\theta_{0,1}$, $\theta_{0,2}$ and $\theta_{0,\mathrm{interface}}$ respectively. The condition of stability is a general one, common for both cases of a bi-material notch and junction, as written in Eq. (66) on p. 56. The critical load is calculated by Eq. (67) on p. 57.

The average strain energy density factor criterion

The strain energy density factor (SEDF) criterion, developed by Sih, found many applications in assessment of crack problems. The problem of a sharp material inclusion, modeled as a bi-material junction can be assessed by this criterion as well. The theoretical multi-parameter approach is identical to the case of a bi-material notch. The global minimum (and the local as well) of the SEDF is found as a potential crack initiation direction. Thus we rewrite the formula (68) on p. 57:

$$\sum_{k=1}^{n} \sum_{l=k}^{n} \Gamma_{k1}\Gamma_{l1} \frac{d^{\lambda_k+\lambda_l-1}}{\lambda_k+\lambda_l} \frac{\partial U_{kl}(\theta)}{\partial \theta} = 0. \tag{98}$$

Based on the SEDF approach, we determine the generalized fracture toughness for all potential crack onset directions, the global minimum, local minimum and the interface. This is achieved by Eq. (74) on p. 58, written as:

$$H_{1\mathrm{C},m} = K_{\mathrm{IC},m} \sqrt{\frac{k_m}{\pi\Re\left\{\sum_{k=1}^{n}\sum_{l=k}^{n} \Gamma_{k1}\Gamma_{l1} \frac{d^{\lambda_k+\lambda_l-1}}{\lambda_k+\lambda_l} U_{kl}(\theta)\right\}}}. \tag{99}$$

The condition of stability is a general one, common to all general singular stress concentrators, stated in Eq. (66) on p. 56. Finally the formula for critical load, also a general one, is given by Eq. (67) on p. 57.

Numerical example Q: Crack initiation direction and initiation load in the case of a bi-material junction

Part 1 First, we consider a problem described in Numerical example O on p. 84, which represents a three point bending specimen with rectangular inclusion more compliant than matrix where $E_1/E_2 = 0.033$. To assess crack initiation direction we use (a) criterion of maximum of average tangential stress and (b) average strain energy density criterion. The fracture parameters are identical to those in Numerical example H on p. 65.

(a) The criterion of maximum of average tangential stress. The tangential stress is averaged over a specific distance d, which is chosen as 1 mm. The averaged tangential stress calculated by (i) singular terms (the yellow dotted line) and by (ii) singular and non-singular terms (the cyan dotted line) is shown in Figure 79. The yellow line with markers represents the solution of $\sigma_{\theta\theta}(r,\theta)$ on $d = 1$ mm by singular terms. In similar manner, the cyan line with markers represents the singular and non-singular terms solution. For this particular bi-material and geometrical configuration there are two singular terms. Regarding the singular and non-singular terms solution, two singular and two non-singular terms are considered (as shown in Numerical example O, the fifth term does not significantly contribute to the precision on 1 mm). Please recall the formula to find potential crack initiation directions (96) on p. 89. We see that there are two extremes in the tangential stress angular distribution, the global maximum (occurs in the matrix, $m = 2$) and the local maximum (occurs in the inclusion, $m = 1$). In both cases, the singular terms solution of extreme (represented by the vertical yellow solid line) and the non-singular terms solution of extreme (represented by the vertical cyan dashed line) has the same direction (both in the local and global average tangential stress maximum). The potential crack initiation direction in the global maximum is $\theta_0^{\text{glb.}} = 180°$ and in local maximum $\theta_0^{\text{loc.}} = 0°$ which is apparent because of the problem symmetry. Nevertheless, as the solution by employment of non-singular terms is more precise, increase in precision of the critical parameters is also expected. In the previous theoretical chapter we stated that the crack initiation can occur in the inclusion, matrix or the interface, whereas each of them possesses a particular material parameter $K_{1\text{C},m}$ and therefore different $H_{1\text{C},m}$. We calculate these critical values by Eq. (97). The results (i) singular terms solution are found in Table 38 and results of (ii) non-singular terms solution in Table 39. The methods (i) and (ii) lead to difference of 5.94 % in $H_{1\text{C},2}$ which is in global maximum, 1.72 % in $H_{1\text{C},1}$ which is in local maximum and 0.83 % in interface critical GSIF value. The minimum value of $H_{1\text{C},m}$ is found in the PMMA. By criterion of maximum of average tangential stress the crack is therefore predicted to initiate in this direction and material. Remember, that we assume interface with perfect adhesion, which allows full traction transmission. If the actual interface does not comply to this assumption and crack may not initiate in this predicted direction.

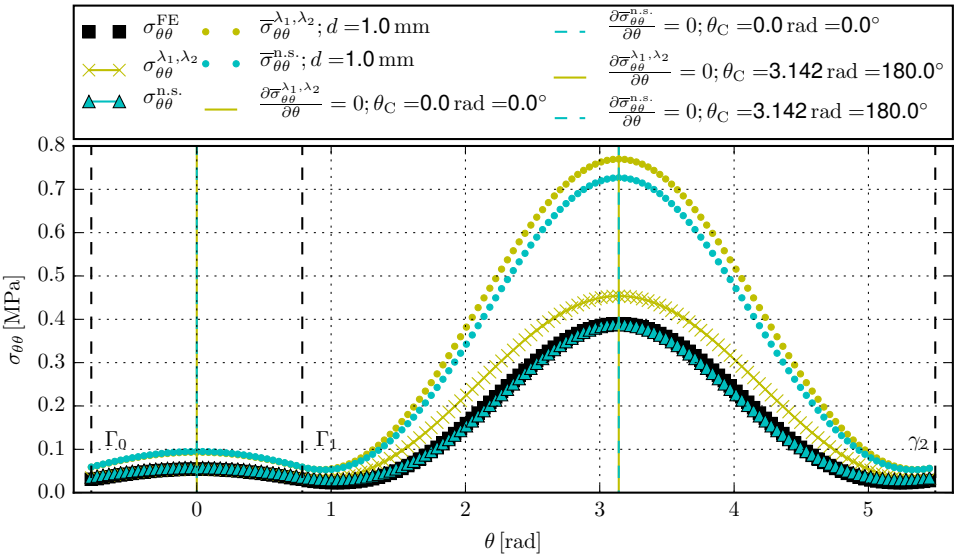

Figure 79: Average value of the $\overline{\sigma}_{\theta\theta}(\theta)$ plotted by (i) singular terms: the yellow line, by (ii) singular and non-singular terms: the cyan line. The black dashed lines denote the interfaces.

	$\theta_{0,m}$	m	$H_{1\text{C},m}$
global maximum	180.0°	2 ≡ aluminum	177.765048
local maximum	0.0°	1 ≡ PMMA	62.32677
interface	±45.0°	interface	72.968331

Table 38: The generalized fracture toughness $H_{1\text{C},m}$ for global minimum, local minimum and the interface determined by (i) singular terms and (a) criterion of maximum of average tangential stress.

	$\theta_{0,m}$	m	$H_{1\mathrm{C},m}$
global maximum	180.0°	2 ≡ aluminum	188.317388
local maximum	0.0°	1 ≡ PMMA	61.254716
interface	±45.0°	interface	72.359732

Table 39: The generalized fracture toughness $H_{1\mathrm{C},m}$ for global minimum, local minimum and the interface determined by (ii) singular and non-singular terms and (a) criterion of maximum of average tangential stress.

(b) The average strain energy density factor criterion. The averaged strain energy density factor over distance $d = 1$ mm is plotted in Figure 80. The yellow line represents solution by (i) two singular terms and the cyan line represents solution by (ii) two singular and two non-singular terms. We see that there is a global minimum and a local one, found by solving Eq. (98). Both (i) and (ii) return identical angular values corresponding to these points. However some offset of $\overline{\Sigma}(\theta)$ between solutions exists, therefore difference in critical parameters is expected. The generalized fracture toughnesses are calculated by formula (99). The results (i) singular terms solution are found in Table 40 and results of (ii) non-singular terms solution in Table 41. The methods (i) and (ii) leads to the difference of 9.6 % in $H_{1\mathrm{C},2}$ which corresponds to local minimum, 2.9 % in $H_{1\mathrm{C},1}$ for global minimum and 2.2 % in interface critical GSIF value prediction. The lowest value of generalized fracture toughness corresponds to the interface, thus the crack is expected to initiate in this direction. We see that the crack initiation direction and material predicted by (a) and (b) is different as in the former case the crack is predicted to initiate in PMMA with $\theta_0^{\mathrm{glb.}} = 0°$ and the latter case it is predicted to initiate in the interface with $\theta_{0,\mathrm{interface}} = \pm 45°$. In (a) only the tangential stress component is used to calculate $H_{1\mathrm{C},m}$ whereas in (b) all stress components are employed. The level of tangential stress acting on the interfaces is low, leading to higher value of $H_{1\mathrm{C},\mathrm{interface}}$ calculated by (a) than by (b).

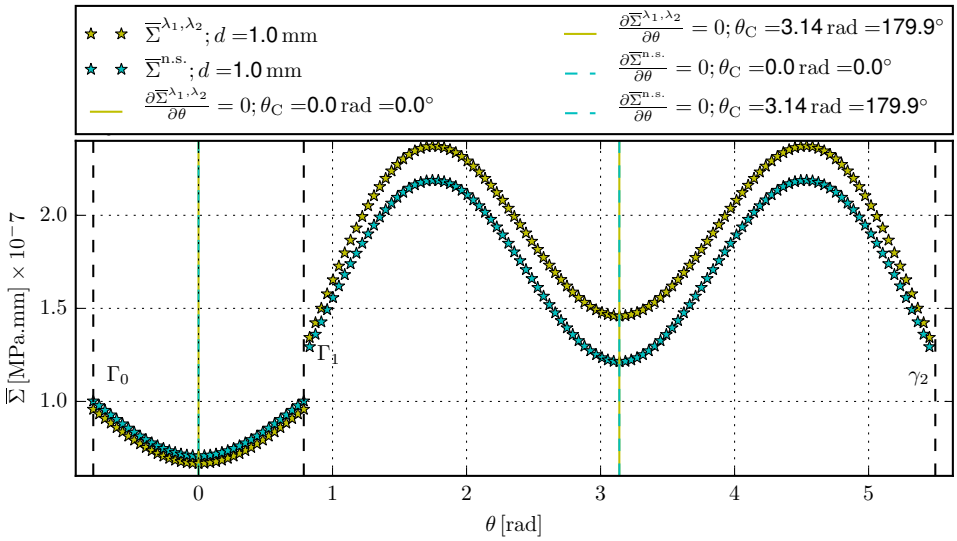

Figure 80: Average value of the $\overline{\Sigma}(\theta)$ plotted by (i) singular terms: the yellow line, by (ii) singular and non-singular terms (the cyan line). The black dashed lines denote the interfaces.

	$\theta_{0,m}$	m	$H_{1\mathrm{C},m}$
global minimum	0.0°	1 ≡ PMMA	62.786943
local minimum	179.9°	2 ≡ aluminum	187.279553
interface	±45.0°	interface	39.704644

Table 40: The generalized fracture toughness $H_{1\mathrm{C},m}$ for global minimum, local minimum and the interface determined by (i) singular terms and (b) average strain energy density criterion.

	$\theta_{0,m}$	m	$H_{1\mathrm{C},m}$
global minimum	0.0°	1 ≡ PMMA	60.974337
local minimum	179.9°	2 ≡ aluminum	205.32978
interface	±45.0°	interface	38.813687

Table 41: The generalized fracture toughness $H_{1\mathrm{C},m}$ for global minimum, local minimum and the interface determined by (ii) singular and non-singular terms and (b) average strain energy density criterion.

Part 2 We consider a problem described in Numerical example P on p. 86, which represents a three point bending specimen with rectangular inclusion stiffer than matrix where $E_1/E_2 = 30$. Again, to assess crack initiation direction and critical value of GSIF we use (a) the criterion of maximum of average tangential stress and (b) the average strain energy density criterion. In the part 2 of the numerical example, we use averaging distance $d = 0.5$ mm.

(a) The criterion of maximum of average tangential stress. The distribution of $\overline{\sigma}_{\theta\theta}(\theta)$ is shown in Figure 81, where the yellow dotted line represents the averaged tangential stress solution given by (i) two singular terms. The cyan line represents the solution given by (ii) two singular and two non-singular terms. In addition, the stress on particular distance d is plotted by (i) and (ii) and denoted by lines with markers. Please note that the tangential stress given by (i) is compressive for all θ. The black squares represents the FE solution. As in the previous case, we see two extremes of $\overline{\sigma}_{\theta\theta}(\theta)$ represented by vertical lines, the yellow in case of (i) and the cyan in case of (ii). Both singular and non-singular solution predict identical angles of crack initiation, i. e. $\theta_0^{\mathrm{glb.}} = 180°$ and $\theta_0^{\mathrm{loc.}} = 0°$. The difference in stress description by (i) and (ii) is severe, therefore significant difference in value of critical parameters is expected. The results by (i) are listed in Table 42. The results given by (ii) is summarized in Table 43. When (i) only the singular terms are taken as an input for critical GSIF calculation a negative valued $H_{1\mathrm{C},m}$ are obtained (since the $\overline{\sigma}_{\theta\theta}(\theta)$ is compressive). For (ii), the minimum value is $H_{1\mathrm{C},2}$ and the crack is expected to initiate in the direction of global maximum found in PMMA.

	$\theta_{0,m}$	m	$H_{1\mathrm{C},m}$
global maximum	180.0°	2 ≡ PMMA	(-0.015640)
local maximum	0.0°	1 ≡ aluminum	(-0.117511)
interface	±45.0°	interface	(-0.001800)

Table 42: The generalized fracture toughness $H_{1\mathrm{C},m}$ for global minimum, local minimum and the interface determined by (i) singular terms and (a) criterion of maximum of average tangential stress.

	$\theta_{0,m}$	m	$H_{1\mathrm{C},m}$
global maximum	180.0°	2 ≡ PMMA	0.004104
local maximum	0.0°	1 ≡ aluminum	0.178545
interface	±45.0°	interface	(-0.004031)

Table 43: The generalized fracture toughness $H_{1\mathrm{C},m}$ for global minimum, local minimum and the interface determined by (ii) singular and non-singular terms and (a) criterion of maximum of average tangential stress.

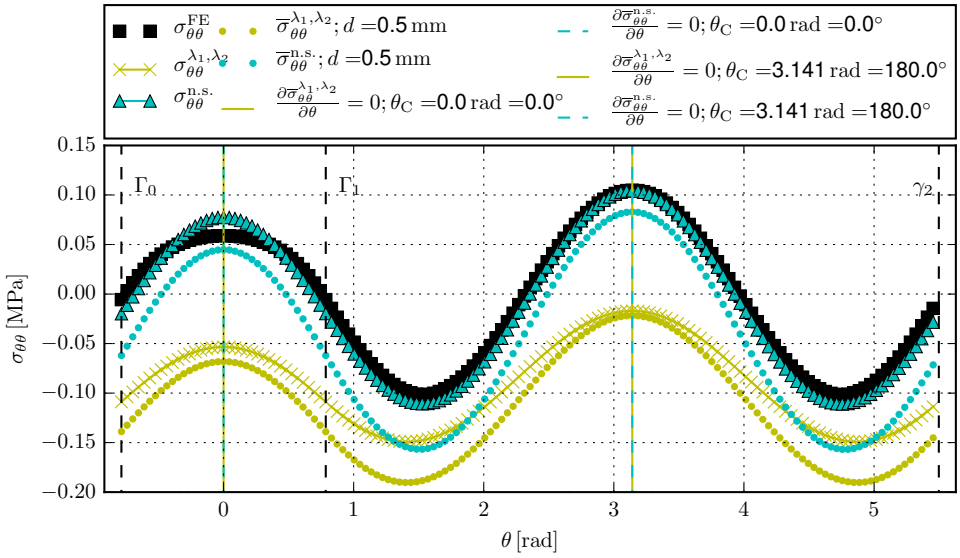

Figure 81: Average value of the $\sigma_{\theta\theta}^{-}(\theta)$ plotted by (i) singular terms: the yellow line, by (ii) singular and non-singular terms (the cyan line). The black dashed lines denote the interfaces.

(b) The average strain energy density factor criterion. The angular distribution of strain energy density factor $\overline{\Sigma}(\theta)$ is shown in Figure 82. The yellow line represents (i) two singular terms solution. The cyan line represents (ii) two singular and two non-singular terms solution. Because the problem is a symmetric one, there are two directions where global minimum and local minimum are found. The yellow and cyan vertical lines represent the locations of local minima. The global minima are found at the interfaces. The results by (i) are listed in Table 44 and by (ii) in Table 45. The difference in $H_{1\mathrm{C},m}$ by (i) and (ii) is 1.1 % for the global minimum, 10.7 % for local minimum and 1.1 % for the interface. The lowest value of $H_{1\mathrm{C},m}$ is found at the interface, therefore it is the expected angle of crack initiation.

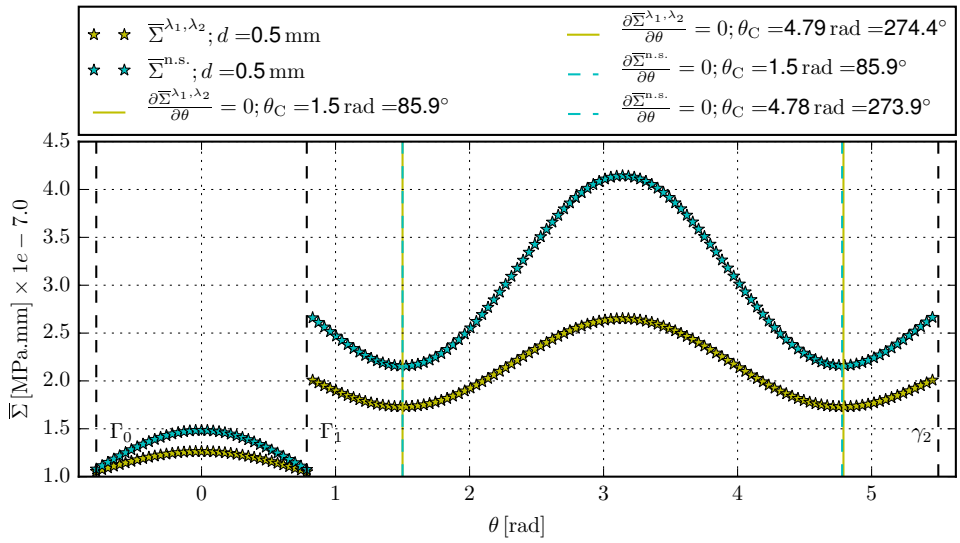

Figure 82: Average value of the $\bar{\Sigma}(\theta)$ plotted by (i) singular terms: the yellow line, by (ii) singular and non-singular terms: the cyan line. The black dashed lines denote the interfaces. In the region of inclusion, i.e. the $\bar{\Sigma}(\theta)$ is multiplied by factor of 10.

	$\theta_{0,m}$	m	$H_{1\mathrm{C},m}$
global minimum	$\pm 45.0°$	$1 \equiv$ aluminum	0.027674
local minimum	85.9°, 274.4°	$2 \equiv$ PMMA	0.001334
interface	$\pm 45.0°$	interface	0.000865

Table 44: The generalized fracture toughness $H_{1\mathrm{C},m}$ for global minimum, local minimum and the interface determined by (i) singular terms and (b) average strain energy density criterion.

	$\theta_{0,m}$	m	$H_{1\mathrm{C},m}$
global minimum	$\pm 45.0°$	$1 \equiv$ aluminum	0.027360
local minimum	85.9°, 273.9°	$2 \equiv$ PMMA	0.001477
interface	$\pm 45.0°$	interface	0.000855

Table 45: The generalized fracture toughness $H_{1\mathrm{C},m}$ for global minimum, local minimum and the interface determined by (ii) singular and non-singular terms and (b) average strain energy density criterion.

The angle and material of expected crack initiation is different from (a), but as discussed in first part of this example, the possible explanation is that the SEDF uses all the stress components rather than tangential stress only. The thorough explanation of such behavior will be a subject of following research as well as experimental evaluation of the problem.

4.4. Formulation of approaches for a general problem

The multi-material notch or multi-material junction problem can be approached in general way by forming sparse structure matrix $\mathbf{A}(\lambda)$ as in Eq. (35) on p. 28 from sub-matrices $\mathbf{N}_\theta^{km}$ for multi-material notch problem:

$$\mathbf{N}_\theta^{km} = \begin{bmatrix} \frac{\lambda_k e^{i\theta(\lambda_k+1)}}{2} & \frac{\lambda_k e^{-i\theta(\lambda_k+1)}}{2} & \frac{\lambda_k(\lambda_k+1)e^{i\theta(\lambda_k-1)}}{2} & \frac{\lambda_k(\lambda_k+1)e^{-i\theta(\lambda_k-1)}}{2} \\ \frac{\lambda_k e^{i\theta(\lambda_k+1)}}{2i} & -\frac{\lambda_k e^{-i\theta(\lambda_k+1)}}{2i} & \frac{\lambda_k(\lambda_k-1)e^{i\theta(\lambda_k-1)}}{2i} & -\frac{\lambda_k(\lambda_k-1)e^{-i\theta(\lambda_k-1)}}{2i} \end{bmatrix},$$

and $\mathbf{M}_\theta^{km}$ for multi-material junction problem:

$$\mathbf{M}_\theta^{km} = \begin{bmatrix} \frac{\lambda_k e^{i\theta(\lambda_k+1)}}{2} & \frac{\lambda_k e^{-i\theta(\lambda_k+1)}}{2} & \frac{\lambda_k(\lambda_k+1)e^{i\theta(\lambda_k-1)}}{2} & \frac{\lambda_k(\lambda_k+1)e^{-i\theta(\lambda_k-1)}}{2} \\ \frac{\lambda_k e^{i\theta(\lambda_k+1)}}{2i} & -\frac{\lambda_k e^{-i\theta(\lambda_k+1)}}{2i} & \frac{\lambda_k(\lambda_k-1)e^{i\theta(\lambda_k-1)}}{2i} & -\frac{\lambda_k(\lambda_k-1)e^{-i\theta(\lambda_k-1)}}{2i} \\ -\frac{e^{i\theta(\lambda_k+1)}}{4\mu_i} & -\frac{e^{-i\theta(\lambda_k+1)}}{4\mu_i} & \frac{(\kappa_i-\lambda_k)e^{i\theta(\lambda_k-1)}}{4\mu_i} & \frac{(\kappa_i-\lambda_k)e^{-i\theta(\lambda_k-1)}}{4\mu_i} \\ \frac{e^{i\theta(\lambda_k+1)}}{4i\mu_i} & -\frac{e^{i\theta(\lambda_k+1)}}{4i\mu_i} & \frac{(\kappa_i+\lambda_k)e^{i\theta(\lambda_k-1)}}{4i\mu_i} & \frac{(\kappa_i+\lambda_k)e^{-i\theta(\lambda_k-1)}}{4i\mu_i} \end{bmatrix}.$$

In the simple case of a homogeneous notch, studied in this work, the matrix $\mathbf{A}(\lambda)$ is:

$$\mathbf{A}(\lambda) = \begin{bmatrix} \mathbf{N}_{\gamma_1}^1 \\ \mathbf{N}_{\gamma_2}^1 \end{bmatrix},$$

Similarly for the studied case of a bi-material notch, the matrix $\mathbf{A}(\lambda)$ can be written:

$$\mathbf{A}(\lambda) = \begin{bmatrix} \mathbf{N}_{\gamma_1}^1 & \mathbf{0} \\ \mathbf{M}_{\gamma_2}^1 & -\mathbf{M}_{\gamma_2}^2 \\ \mathbf{0} & \mathbf{N}_{\gamma_3}^2 \end{bmatrix}.$$

For a problem of crack terminating at the bi-material interface as shown in Figure 12 on p. 19, the matrix $\mathbf{A}(\lambda)$ can be written:

$$\mathbf{A}(\lambda) = \begin{bmatrix} \mathbf{M}_{\gamma_1}^1 & -\mathbf{M}_{\gamma_1}^2 & \mathbf{0} \\ \mathbf{0} & \mathbf{N}_{\gamma_2}^2 & \mathbf{0} \\ \mathbf{0} & \mathbf{0} & \mathbf{N}_{\gamma_0}^2 \end{bmatrix}.$$

As another example serves the case of the tri-material notch

$$\mathbf{A}(\lambda) = \begin{bmatrix} \mathbf{N}^1_{\gamma_1} & \mathbf{0} & \mathbf{0} \\ \mathbf{M}^1_{\gamma_2} & -\mathbf{M}^2_{\gamma_2} & \mathbf{0} \\ \mathbf{0} & \mathbf{M}^2_{\gamma_3} & -\mathbf{M}^3_{\gamma_3} \\ \mathbf{0} & \mathbf{0} & \mathbf{N}^3_{\gamma_4} \end{bmatrix},$$

which is a special case of a multi-material notch. In fact, multi-material notch consisting of even more material regions can be described by this approach, such as the last example, the quad-material notch:

$$\mathbf{A}(\lambda) = \begin{bmatrix} \mathbf{N}^1_{\gamma_1} & \mathbf{0} & \mathbf{0} & \mathbf{0} \\ \mathbf{M}^1_{\gamma_2} & -\mathbf{M}^2_{\gamma_2} & \mathbf{0} & \mathbf{0} \\ \mathbf{0} & \mathbf{M}^2_{\gamma_3} & -\mathbf{M}^3_{\gamma_3} & \mathbf{0} \\ \mathbf{0} & \mathbf{0} & \mathbf{M}^3_{\gamma_4} & -\mathbf{M}^4_{\gamma_4} \\ \mathbf{0} & \mathbf{0} & \mathbf{0} & \mathbf{N}^4_{\gamma_5} \end{bmatrix},$$

For the problem of a bi-material junction, studied in previous chapter, the matrix $\mathbf{A}(\lambda)$ is:

$$\mathbf{A}(\lambda) = \begin{bmatrix} \mathbf{M}^1_{\gamma_1} & -\mathbf{M}^2_{\gamma_1} \\ -\mathbf{M}^1_{\gamma_0} & \mathbf{M}^2_{\gamma_2} \end{bmatrix}.$$

A junction of three material domains, the tri-material junction is described by the following sparse structure matrix:

$$\mathbf{A}(\lambda) = \begin{bmatrix} \mathbf{M}^1_{\gamma_1} & -\mathbf{M}^2_{\gamma_1} & \mathbf{0} \\ \mathbf{0} & \mathbf{M}^2_{\gamma_2} & -\mathbf{M}^3_{\gamma_2} \\ -\mathbf{M}^1_{\gamma_0} & \mathbf{0} & \mathbf{M}^3_{\gamma_3} \end{bmatrix}$$

and as the last example, the quad-material junction is characterized by the following matrix:

$$\mathbf{A}(\lambda) = \begin{bmatrix} \mathbf{M}^1_{\gamma_1} & -\mathbf{M}^2_{\gamma_1} & \mathbf{0} & \mathbf{0} \\ \mathbf{0} & \mathbf{M}^2_{\gamma_2} & -\mathbf{M}^3_{\gamma_2} & \mathbf{0} \\ \mathbf{0} & \mathbf{0} & \mathbf{M}^3_{\gamma_3} & -\mathbf{M}^4_{\gamma_3} \\ -\mathbf{M}^1_{\gamma_0} & \mathbf{0} & \mathbf{0} & \mathbf{M}^4_{\gamma_4} \end{bmatrix}.$$

In conclusion, a problem of any number of material domains can be easily described in this way. As the sparse structure matrix is formed, the eigenequation is obtained by Eq. (36) on p. 28.

4.5. Developing a complete description of crack initiation and propagation near the sharp material inclusion

This chapter examines possible scenarios of crack behavior near the sharp material inclusion embedded in matrix. Crack in matrix terminating at inclusion/matrix interface is shown left-hand side of Figure 83. Similarly, the crack in inclusion terminating at the inclusion/matrix interface is shown in right-hand side of Figure 83. This case can be modeled as a crack with its tip at a bi-material interface. The geometry of problem is shown in Figure 12 on p. 19 and the methods are identical as those on p. 27. The crack that terminated at the interface can either propagate to the other material or propagate through the inclusion/matrix interface. The latter situation is examined further in Figure 84, where crack propagating through the inclusion/matrix interface is shown. In the left-hand side of the Figure 84 the crack originates in matrix and in the left-hand side of the Figure 84 it originates in inclusion. These cases is modeled as interfacial cracks (special case of the bi-material notch model with $2\alpha = 0°$ and e.g. $\gamma_1 = 0°$, $\gamma_2 = 180°$ and $\gamma_3 = 360°$, see p. 27). Another situation occurs when the crack reaches the end point of the sharp material inclusion, as shown in Figure 85 (another special case of the bi-material notch model with $2\alpha = 0°$ and e.g. $\gamma_1 = 0°$, $\gamma_2 = 270°$ and $\gamma_3 = 360°$, see p. 27). Figure 86 shows crack initiated at the tip of the sharp material inclusion in the matrix (left-hand side) or in the inclusion (right-hand side). This case is modeled as a bi-material junction (see p. 70). Above mentioned situations capture complete crack behavior near the sharp material inclusion and all can be modeled by methods described in this dissertation.

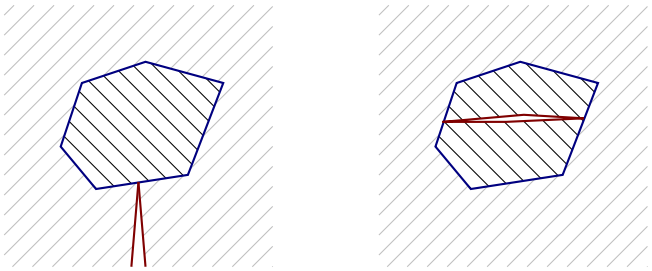

Figure 83: Crack terminating at the inclusion/matrix interface. On the left-hand side the crack originates in matrix. On the right-hand side the crack originates in the inclusion.

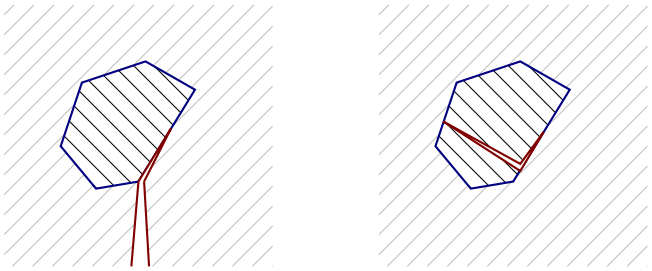

Figure 84: Crack propagating through the inclusion/matrix interface. On the left-hand side the crack originates in matrix. On the right-hand side the crack originates in the inclusion.

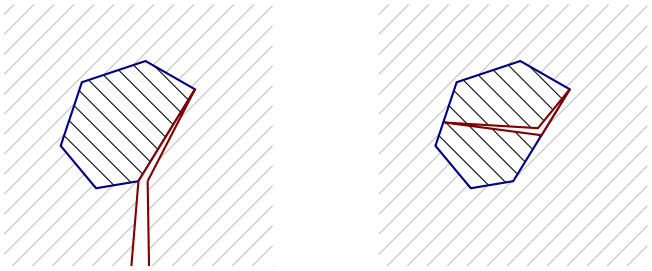

Figure 85: Crack propagated to the end point of inclusion/matrix interface. On the left-hand side the crack originates in matrix. On the right-hand side the crack originates in the inclusion.

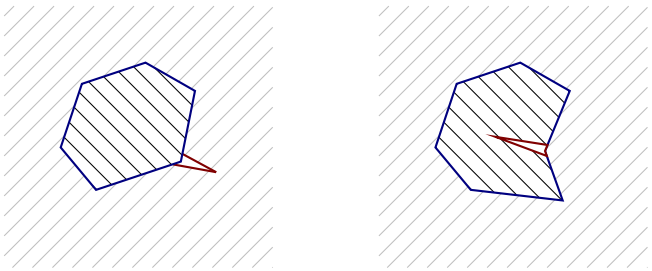

Figure 86: Crack initiated at the tip of the sharp material inclusion. On the left-hand side the crack initiates in matrix. On the right-hand side the crack initiates in matrix.

5. Conclusions

Methods of the classical fracture mechanics can not be directly applied on general singular stress concentrators and its generalization is the current objective of many researchers. The identical motivation stays behind this thesis. Although the presented work is primarily theoretical, it provides the researchers with the framework in order to fully assess generalized singular stress concentrators in terms of the multi-parameter criteria proposed herein. Experiments to verify the theory on general singular stress concentrators different from a V-notch are the next step to be conducted. For this purpose the specimens modeled in this work can be used.

This work presents methods to determine the eigenvalues to form the exponents of singular and non-singular stress terms in cases of general singular stress concentrators. When the eigenvalues are determined, the angular eigenfunction can be easily formed. The cases of a V-notch, bi-material notch and bi-material junction are studied in detail. However, the methods presented herein allow researchers to determine the order of singularity for any type of multi-material general singular stress concentrator (for example quad-material notch or quad-material junction). In the following part, application of two different methods to determine generalized stress intensity factors of singular and non-singular terms are studied. The main advantage of the Ψ-integral method is, that it allows independent determination of kth generalized stress intensity factor. The overdeterministic method is simpler and computationally less expensive. When some requirements are fulfilled, i.e. if the integration path is far enough from singular point in the case of the Ψ-integral, or number of terms n to be determined is high enough in the case of the ODM, both methods return results very close to each other. By the knowledge of the eigenvalues and generalized stress intensity factors, stress field near singular point can be reconstructed. The analytical solution can be compared with pure finite element solution. When we are interested in the stress field on distances such as $0.1 - 1$ mm, the employment of non-singular terms leads either to significant increase in precision (notches and inclusion more compliant than matrix) or provides the only means to describe the stress field well (inclusion stiffer than matrix).

The dissertation also presents stability criteria modified to contain higher order terms. These multi-parameter criteria are namely the criterion of maximum of average tangential stress and the average strain energy density factor criterion. Both criteria are applied on problems of V-notch, bi-material notch and bi-material junction. In the case of V-notch, comparison of the predicted failure loads and experimental data show very good agreement. In other cases, the crack initiation direction and critical parameters are calculated. Use of the multi-parameter criteria leads to change in the predicted critical parameters in order of percents. The experimental validation of proposed criteria will be a subject of further research.

6. References

[1] Pook, L. *Linear elastic fracture mechanics for engineers: theory and applications.* Boston: WIT Press, 2000, 154 p. ISBN1853127035.

[2] Anderson, T.L. *Fracture mechanics: fundamentals and applications.* Second Edition. Boca Raton: CRC Press, 1995, 669 p. ISBN 0849342600.

[3] Sun, C., Jin J. *Fracture mechanics.* Waltham, MA: Academic Press, 2012, xvii, 311 p. ISBN0123850010.

[4] Muskhelishvili N.I. *Some Basic Problems of the Mathematical Theory of Elasticity*, Noordhoff, Groningen, 1953.

[5] England, A.H. *Complex Variable Methods in Elasticity*, Donver Publications, New York, 2003.

[6] Kaw, A.K. *Mechanics of composite materials.* 2nd ed. Boca Raton, FL: Taylor & Francis, 2006, 466 p. Mechanical engineering series (Boca Raton, Fla.), v. 29. ISBN 9780849313431.

[7] Hwu, Ch. *Anisotropic Elastic Plates*, Spinger, Verlag US, 2010, 673 p. ISBN 978-1-4419-5914-0.

[8] Williams, M.L., Stress singularities resulting from various boundary conditions in angular corners of plates in extensions, Journal of Applied Mechanics 19 (1952) 526 – 528.

[9] Williams, M.L, On the Stress Distribution at the Base of Stationary Crack, Journal of Applied Mechanics, 24 (1957) 109-114.

[10] Hein, V.L., Erdogan, F., Stress Singularities in a Two-Material Wedge, International Journal of Fracture Mechanics 7 (1971) 317-330.

[11] Paris, P.C., Erdogan, F. A critical analysis of crack propagation laws, Journal of Basic Engineering, ASME, 85 (1963) 528-534.

[12] Hutař, P., Seitl, S., Knésl, Z. Quantification of the effect of specimen geometry on the fatigue crack growth response by two-parameter fracture mechanics, Materials Science and Engineering 387–389 (2004) 491-494.

[13] Tong, J., T-stress and its implications for crack growth, Engineering Fracture Mechanics 69 (2002) 1325–1337.

[14] Seitl, S., Knésl, Z., Two parameter fracture mechanics: Fatigue crack behavior under mixed mode conditions, Engineering Fracture Mechanics 75 (2008) 857-865.

[15] Moon, H.J., Earmme, Y.Y., Calculation of elastic T stresses near interface crack tip under in-plane and antiplane loading, Int. J. Fracture 91 (1998) 179-195.

[16] Kotousov, A., On stress singularities at angular corners of plates of arbitrary thickness under tension, International Journal of Fracture 132 (2005) 29-36.

[17] Klusák, J., Profant, T., Kotoul, M., Study of the stress distribution around an orthotropic bi-material notch tip, Key Engineering Materials 417-418 (2010) 385-388.

[18] Klusák, J., Knésl, Z., Reliability assessment of a bi-material notch: Strain energy density factor approach, Theoretical and Applied Fracture Mechanics 53 (2010) 89-93.

[19] Klusák, J., Profant, T., Kotoul, M., Determination of the threshold values of orthotropic bi-material notches, Procedia Engineering 2 (2010) 1635–1642.

[20] Klusák, J., Profant, T., Knésl, Z., Kotoul, M., The influence of discontinuity and orthotropy of fracture toughness on conditions of fracture initiation in singular stress concentrators, Engineering Fracture Mechanics 110 (2013) 438–447.

[21] Krepl, O., Klusák, J., Reconstruction of a 2D stress field around the tip of a sharp material inclusion, Procedia Struct. Integrity 2 (2016) 1920–1927.

[22] Krepl, O., Klusák, J., The influence of non-singular terms on the precision of stress description near a sharp material inclusion tip, Theoretical and Applied Fracture Mechanics 90 (2017) 85-99.

[23] Leguillon, D., Strength or toughness? A criterion for crack onset at a notch, European Journal of Mechanics A/Solids 21 (2002) 61–72.

[24] Leguillon, D., Calcul du taux de restitution de l'énergie au voisinage d'une singularité. C. R. Acad. Sci. Paris Sér. II 309 (1989) 945–950.

[25] Leguillon, D., Asymptotic and numerical analysis of a crack branching in non-isotropic materials, Eur. J. Mech. A Solids 12 (1993) 33-51.

[26] Erdogan, F., Sih, G.C., On the crack extension in plates under plane loading and transverse shear, Int. J. Basic Engineering 85 (1963) 519 – 527.

[27] Ayatollahi, M. R., Dehghany, M., On T-stresses near V-notches, Int. J. Fract. 165 (2010) 121–126.

[28] Náhlík, L., Knésl, Z., Klusák, J.: Crack initiation criteria for singular stress concentrations, Part III: An Application to a Crack Touching a Bimaterial Interface, Engineering Mechanics 15 (2008) 99 – 114.

[29] Qian, Z.Q., Akisania, A.R., Wedge corner stress behaviour of bonded dissimilar materials, Theoretical and Applied Fracture Mechanics 32 (1999) 209-222.

[30] Dundurs, J., Effect of elastic constants on stress in composite under plane deformation, Journal of Composite Materials 1 (1967) 310-322.

[31] Seweryn, A. Molski, K., Elastic stress singularitiesand corresponding generalized stress intensity factors for angular corners under various boundary conditions, Engineering Fracture Mechanics 55 (1996) 529-556.

[32] Klusák, J., Knésl, Z., Náhlík, L., Crack initiation criteria for singular stress concentrations, Part II: Stability of sharp and bi-material notches, Engineering mechanics, Vol. 14, 2007, 6, p. 409-422.

[33] Profant T., Ševeček O., Kotoul M., Calculation of K-factor and T-stress for cracks in anisotropic bimaterials, Engineering Fracture Mechanics 75 (2008) 3707-3726.

[34] Seweryn, A., Modeling of singular stress fields using finite element method, International Journal of Solids and Structures 39 (2002) 4787-4804.

[35] Ayatollahi, M.R., Nejati, M., An over-deterministic method for calculation of coefficients of crack tip asymptotic field from finite element analysis, Fatigue and Fracture of Engineering Materials and Structures 34 (2010) 159-176.

[36] Ayatollahi, M.R., Nejati, M., Determination of NSIFs and coefficients of higher order terms for sharp notches using finite element method, International Journal of Mechanical Sciences 53 (2011) 164–177.

[37] Hilton, P.D., Sih, G.C., Applications of the finite element method to the calculations of stress intensity factors, 1973. In: Sih., G. C., Mechanics of Fracture – Methods of analysis and solutions of crack problems, Noordhoff International Publishing, Leyden, 426-477.

[38] Owen D.R.J, Fawkes A.J., *Engineering Fracture Mechanics: Numerical Methods and Applications.* Pineridge Press Ltd, Swansea, 1983.

[39] Vu-Quoc, L., Tran, V.-X.: Singular analysis and fracture energy-release rate for composites: Piecewise homogenous-anisotropic materials, Comput. Methods Appl. Mech. Eng. 195 (2006) 5162–5197.

[40] Knésl, Z.: A criterion of V-notch stability. International Journal of Fracture 48 (1991) 79-83.

[41] Knésl, Z., Klusák, J. Náhlík, L., Crack initiation criteria for singular stress concentrations, Part I: A universal assessment of singular stress concentrations, Engineering Mechanics 14 (2007) 399-408.

[42] Pageau, S., Joseph, P., Biggers S.: The order of stress singularities for bonded and disbonded three-material junctions, Int. J. Solid Structures 31 (1994) 2979-2997.

[43] Paggi, M., Carpinteri, A., On the stress singularities at multimaterial interfaces and related analogies with fluid dynamics and diffusion, Appl. Mech. Rev. 61 (2008) 1–22.

[44] Yang, Y., Munz D., Stress Intensity Factor and stress distribution in a joint with an interface corner under thermal and mechanical loading, Computers & Structures 57 (1995) 467 – 476.

[45] Larsson, S.G. and Carlsson, A.J., Influence of non-singular stress terms and specimen geometry on small scale yielding at crack tips in elastic-plastic materials, Journal of the Mechanics and Physics of Solids 21 (1973) 263-277.

[46] Bétegon, C., Hancock, J.W., Two-parameter characterization of elastic-plastic crack-tip fields, Journal of Applied Mechanics 58 (1991) 104–110.

[47] Ayatollahi, M.R., Pavier, M.J. and Smith, D.J. Mode I cracks subjected to large T-stresses, International Journal of Fracture 117 (2002) 159-174.

[48] Cotterell, B, Rice, J.R. Slightly curved or kinked cracks, International Journal of Fracture 16 (1980) 155-169.

[49] Kfouri, A. P., Some evaluations of the elastic T-term using Eshelby's method, Int. J. Fracture 30 (1986) 301-315.

[50] Sládek, J., Sládek, V., Evaluations of the T-stress for interface cracks by the boundary element method, Engineering Fracture Mechanics 56 (1997) 813-825.

[51] Profant, T., Ševeček, O., Kotoul, M., Calculation of K-factor and T-stress for cracks in anisotropic bimaterials, Engineering Fracture Mechanics 75 (2008) 3707-3726.

[52] Kim, J.K., Cho, S.B., Effect of second non-singular term of mode I near the tip of a V-notched crack, Fatigue and Fracture of Engineering Materials and Structures 32 (2009) 346-356.

[53] Ayatollahi, M.R., Dehghany, M., Nejati, M., Fracture analysis of V-notched components – Effects of first non-singular stress term, Int. J. Solids Struct. 48 (2011) 1579-1589.

[54] Ayatollahi, M.R., Mirsayar, M.M., Dehghany, M., Experimental determination of stress field parameters in bi-material notches using photoelasticity, Materials and Design 32 (2011) 4901–4908.

[55] Ayatollahi, M.R., Mirsayar, M.M., Nejati, M.: Evaluation of first non-singular stress term in bi-material notches, Computational Materials Science 50 (2010) 752–760

[56] Farris, F.A. (2017). Visualizing complex-valued functions in the plane | Mathematical Association of America. [online] Maa.org. Available at: https://www.maa.org/visualizing-complex-valued-functions-in-the-plane [Accessed 22 Nov. 2017].

[57] Sih, G.C., A special theory of crack propagation, in: G. C. Sih (Ed.), Mechanics of Fracture - Methods of analysis and solutions of crack problems, Noordhoff Internation Publishing, Leyden, The Netherlands, 1973, pp. XXI-XLV.

[58] Sih, G.C., Mechanics of Fracutre Initiation and Propagation, Kluwer Academic Publishing, Boston, 1991.

[59] Taylor, D., The theory of critical distances, Engineering Fracture Mechanics 75 (2008) 1696–1705

[60] Docs.scipy.org. (2017). Optimization and root finding (scipy.optimize) — SciPy v1.0.0 Reference Guide. [online] Available at: https://docs.scipy.org/doc/scipy/reference/optimize.html [Accessed 22 Nov. 2017].

[61] Math.utah.edu. (2017). minpack.html. [online] Available at: https://www.math.utah.edu/software/minpack/minpack.html [Accessed 22 Nov. 2017].

[62] Matplotlib.org. (2017). Matplotlib: Python plotting — Matplotlib 2.1.0 documentation. [online] Available at: https://matplotlib.org/ [Accessed 22 Nov. 2017].

[63] Plane Stress and Plane Strain Analysis (2017) College of Engineering - UC Santa Barbara. [online]. Available at: https://engineering.ucsb.edu/~hpscicom/projects/stress/introge.pdf [Accessed 22 Nov. 2017].

[64] Dunn, M.L., Suwito, W., Cunningham, S., Fracture initiation at sharp notches: correlation using critical stress intensities, Int. J. Solid Structures. 34 No. 29 (1997) 3873-3883.

[65] Shatil, G., Saimoto A., Ductile-Brittle Fatigue and Fracture Behaviour of aluminium/PMMA Bimaterial 3PB Specimens, Gruppo Frattura [online]. Available at: http://www.gruppofrattura.it/pdf/cp/cp2006/78.pdf [Accessed 22 Nov. 2017].

[66] Bo, Z., Jing-wei, L., Shu-guang, L., Yi-hui, L., Ju-tau, H., Relationship between fracture toughness and temperature in epoxy coatings, Polimery 60 No. 4 (2015) 258-263.

[67] Sun, Z., Hu, X., Chen, H., Effects of aramid-fibre toughening on interfacial fracture toughness of epoxy adhesive joint between carbon-fibre face sheet and aluminium substrate, Int. J. of Adhesion & Adhesives 48 (2014) 288–294.

7. Nomenclature

a	half of the crack length
$A\left(2\alpha,\theta_0\right)$	scaling coefficient of the coupled stress-energy criterion
A_k, B_k, C_k, D_k	constants of the solution of bi-harmonic equation
$\mathbf{A}\left(\lambda\right)$	characteristic matrix of a problem
$\mathbf{A}^{\mathrm{red}}\left(\lambda\right)$	reduced characteristic matrix of a problem
α	half of the notch/junction opening angle
α, β	eigenvalues (only in Ψ-integral sub-chapter)
C	elastic tensor
$\mathcal{D}$, $\mathcal{D}^*$	domain
$\partial\mathcal{D}$, $\partial\mathcal{D}^*$	curve surrounding domain $\mathcal{D}$ or $\mathcal{D}^*$
$\Delta\theta$	element angular length / integration step size
ε_{ij}	strain tensor component
E_m	Young's moduli of mth material
$F_k\left(\theta\right)$	kth eigenfunction of Williams' stress function
$f_{ij}\left(\theta\right)$, $g_{ijk}\left(\theta\right)$	Williams' series angular functions
$f_{ijk}\left(\theta\right)$	kth stress eigenfunction for ijth stress component
$f^*_{ijk}\left(\theta\right)$	kth real stress eigenfunction for ijth stress component
$f_{ik}\left(\theta\right)$	kth displacement eigenfunction for ith displacement component
$f^*_{ik}\left(\theta\right)$	kth real displacement eigenfunction for ith displacement component
$f^-_{ijk}\left(\theta\right)$	kth auxilary stress eigenfunction for ijth stress component
$f^-_{ik}\left(\theta\right)$	auxilary displacement eigenfunction for ith displacement component
$\mathbf{F}_{[2m\times n]}$	matrix of eigenfunctions of $2m$ rows and n columns
Φ	Airy's stress function
$g_{ijl}\left(\theta\right)$	lth stress eigenfunction for ijth stress component (only in Ψ-integral subchapter)
$g_{il}\left(\theta\right)$	displacement eigenfucntion for ith displacement component (only in Ψ-integral subchapter)
G_{C}	material toughness
γ_i	angular parameter
Γ_i	ith bi-material interface
Γ_1, Γ_2, Γ_A, Γ_B	integration paths (only in Ψ-integral subchapter)
Γ_{k1}, Γ_{l1}	ratios between individual GSIFs and first GSIF
H_k	generalized stress intensity factor
$H_{1\mathrm{C},m}$	generalized fracture toughness
$\mathbf{H}_{[n]}$	unknown vector of n generalized stress intensity factors
$\Im\left\{z\right\}$	imaginary part of the complex number z
i	imaginary unit
I_{km}, L_{km}, M_{km}, N_{km}	complex constants
K_{I}	stress intensity factor of mode I
K_{Icrit}	critical value of stress intensity factor
K_{IC}	fracture toughness
K_{Ith}	threshold value for fatigue crack propagation
k_m	elastic constant (in terms of Poisson's ratio)
k_k	stress intensity factor in Williams' stress series
κ_m	Kolosov's constant of mth material
l	crack length in pertubated domain
L	controling variable
L, h, b, a	dimensions of the modeled specimen (only in numerical examples)
λ_k	kth eigenvalue
λ^*	material constant (in terms of Kolosov's and shear modulus)
μ	shear modulus
n	normal
$\mathbf{N}^{km}_{\theta}$	sub-matrix of a multi-material notch problem to form a characteristic matrix $\mathbf{A}\left(\lambda\right)$
ν_m	Poisson's ratio of mth material
$\mathbf{N}^{km}_{\theta}$	sub-matrix of a multi-material junciton problem to form a characteristic matrix $\mathbf{A}\left(\lambda\right)$
∇	gradient

∇^2	Laplace operator
$O\left(r^{1/2}\right)$	higher order term of the Williams series
Ω_m	mth material region
$\Omega\left(z\right)$, $\chi\left(z\right)$, $\omega\left(z\right)$	analytic functions (complex potentials) in general
Ω_1, Ω_2	material domains
Ω^{in}	unbounded inner domain
$\Omega_{km}\left(z\right)$, $\omega_{km}\left(z\right)$	analytic functions for kth eigenvalue and mth material region
p_k	stress singularity exponent
$\Psi\left(U,V\right)$	path independent Ψ-integral
Ψ_k^{FE}	Ψ-integral of FE solution
Ψ_k^{analyt}	Ψ-integral of analytical solution
r, θ	polar coordinates
r_0, r_1, r_2	FE radial parameters
$\Re\left\{z\right\}$	real part of the complex number z
s	standard deviation of generalized stress intensity factor average
$\mathbf{S}_{[3m]}^{\mathbf{FE}}$	vector of FE stresses
σ_{ij}	stress tensor
σ_∞	far field loading
σ_{appl}	applied stress
σ_{C}	material strength
$\overline{\sigma}_{\theta\theta}\left(\theta\right)$	averaged value of the tangential stress (averaged over r)
Σ_m	strain energy density factor of mth material
$\overline{\Sigma}_m$	averaged value of the strain energy density factor of mth material (averaged over r)
Σ_{crit}	critical value of strain energy density factor
$\Sigma_{\text{C},m}$	critical value of strain energy density factor of mth material in terms of brittle fracture
Σ_1, Σ_2	integration paths (only in Ψ-integral subchapter)
T	T-stress (constant value term in Williams' expansion)
θ_0	crack initiation angle
$\mathbf{u}_{[2m]}$	vector of FE displacements
U, V	elastic solutions
$U^l\left(x_1,x_2\right)$	perturbed solution
$U^0\left(x_1,x_2\right)$	unperturbed solution
$U_{kl}\left(\theta\right)$	augmented shape functions for average SEDF crigerion
v_k	kth eigenvector
v_k^{red}	reduced kth eigenvector
$\hat{V}$	complementary term in matched asymtotic expansion
W_p	strain energy
$\frac{\text{d}W}{\text{d}V}$	strain energy per volume
x, y	cartesian coordinates
y_1, y_2	stretched coordinates ($\times 1/l$)
$Z\left(z\right)$	Westergaard's stress function
z	complex variable
ζ	external loading angle

List of abbreviations

APDL	Ansys program design language
BMN	bi-material notch
FE	finite element
FEA	finite element analysis
FEM	finite element method
GSIF	generalized stress intensity factor
GSSC	general singular stress concentrator
HSV	hue, saturation, value, color model for a domain coloring
LEFM	linear elastic fracture mechanics
ODM	overdeterministic method
PMMA	polymethyl methacrylate
SIF	stress intensity factor
SEDF	strain energy density factor
3PB	three point bending

A. Detailed derivation of equations

A.1. Kolosov-Muskhelishvili formulas

First, recall the complex analytical functions from (17) on p. 24, i.e.:

$$\begin{aligned}\Omega_{km}(z) &= I_{km}z^{\lambda_k} + L_{km}z^{\bar{\lambda}_k},\\ \omega_{km}(z) &= M_{km}z^{\lambda_k} + N_{km}z^{\bar{\lambda}_k}.\end{aligned}$$

The first derivative of the complex function $\Omega_{km}(z)$ by complex variable z is:

$$\Omega'_{km}(z) = I_{km}\lambda_k z^{\lambda_k-1} + L_{km}\bar{\lambda}_k z^{\bar{\lambda}_k-1} = I_{km}\lambda_k r^{\lambda_k-1}e^{i\theta(\lambda_k-1)} + L_{km}\bar{\lambda}_k r^{\bar{\lambda}_k-1}e^{i\theta\left(\bar{\lambda}_k-1\right)} \tag{100}$$

and by knowing that $\bar{z} = re^{-i\theta}$ its complex conjugate is:

$$\bar{\Omega}'_{km}(z) = \bar{I}_{km}\bar{\lambda}_k \bar{z}^{\bar{\lambda}_k-1} + \bar{L}_{km}\lambda_k \bar{z}^{\lambda_k-1} = \bar{I}_{km}\bar{\lambda}_k r^{\bar{\lambda}_k-1}e^{-i\theta\left(\bar{\lambda}_k-1\right)} + \bar{L}_{km}\lambda_k r^{\lambda_k-1}e^{-i\theta(\lambda_k-1)}. \tag{101}$$

The second derivative of complex function $\Omega_{km}(z)$ by complex variable z is:

$$\begin{aligned}\Omega''_{km}(z) &= I_{km}\lambda_k(\lambda_k-1)z^{\lambda_k-2} + L_{km}\bar{\lambda}_k(\bar{\lambda}_k-1)z^{\bar{\lambda}_k-2} = \\ &= I_{km}\lambda_k\left(\lambda_k-1\right)r^{\lambda_k-2}e^{i\theta(\lambda_k-2)} + L_{km}\bar{\lambda}_k\left(\bar{\lambda}_k-1\right)r^{\bar{\lambda}_k-2}e^{i\theta(\bar{\lambda}_k-2)}\end{aligned} \tag{102}$$

and similarly its complex conjugate is:

$$\begin{aligned}\bar{\Omega}''_{km}(z) &= \bar{I}_{km}\bar{\lambda}_k(\bar{\lambda}_k-1)\bar{z}^{\bar{\lambda}_k-2} + \bar{L}_{km}\lambda_k\left(\lambda_k-1\right)\bar{z}^{\lambda_k-2} = \\ &= \bar{I}_{km}\bar{\lambda}_k(\bar{\lambda}_k-1)r^{\bar{\lambda}_k-2}e^{-i\theta(\bar{\lambda}_k-2)} + \bar{L}_{km}\lambda_k\left(\lambda_k-1\right)r^{\lambda_k-2}e^{-i\theta(\lambda_k-2)}\end{aligned} \tag{103}$$

The first derivative of the complex function $\omega_{km}(z)$ by complex variable z is:

$$\omega'_{km}(z) = M_{km}\lambda_k z^{\lambda_k-1} + N_{km}\bar{\lambda}_k z^{\bar{\lambda}_k-1} = M_{km}\lambda_k r^{\lambda_k-1}e^{i\theta(\lambda_k-1)} + N_{km}\bar{\lambda}_k r^{\bar{\lambda}_k-1}e^{i\theta(\bar{\lambda}_k-1)} \tag{104}$$

and finally its complex conjugate is:

$$\bar{\omega}'_{km}(z) = \bar{M}_{km}\bar{\lambda}_k z^{\bar{\lambda}_k-1} + \bar{N}_{km}\lambda_k z^{\lambda_k-1} = \bar{M}_{km}\bar{\lambda}_k r^{\bar{\lambda}_k-1}e^{-i\theta(\bar{\lambda}_k-1)} + \bar{N}_{km}\lambda_k r^{\lambda_k-1}e^{-i\theta(\lambda_k-1)}. \tag{105}$$

By substitution of (100), (101), (102), (103), (104), (105) into Kolosov-Muskhelishvili equations for stress components (9) on p. 11 we can show derivation of previously shown equations (18), p. 24. For σ_{rrkm} we thus write:

$$\begin{aligned}\sigma_{rrkm}(r,\theta) &= I_{km}\lambda_k r^{\lambda_k-1}e^{i\theta(\lambda_k-1)} + L_{km}\bar{\lambda}_k r^{\bar{\lambda}_k-1}e^{i\theta\left(\bar{\lambda}_k-1\right)} +\\ &+ \bar{I}_{km}\bar{\lambda}_k r^{\bar{\lambda}_k-1}e^{-i\theta\left(\bar{\lambda}_k-1\right)} + \bar{L}_{km}\lambda_k r^{\lambda_k-1}e^{-i\theta(\lambda_k-1)} -\\ &- \frac{re^{-i\theta}}{2}\left[I_{km}\lambda_k\left(\lambda_k-1\right)r^{\lambda_k-2}e^{i\theta(\lambda_k-2)} + L_{km}\bar{\lambda}_k\left(\bar{\lambda}_k-1\right)r^{\bar{\lambda}_k-2}e^{i\theta(\bar{\lambda}_k-2)}\right] -\\ &- \frac{re^{i\theta}}{2}\left[\bar{I}_{km}\bar{\lambda}_k\left(\bar{\lambda}_k-1\right)r^{\bar{\lambda}_k-2}e^{-i\theta(\bar{\lambda}_k-2)} + \bar{L}_{km}\lambda_k\left(\lambda_k-1\right)r^{\lambda_k-2}e^{-i\theta(\lambda_k-2)}\right] -\\ &- \frac{1}{2}\left[M_{km}\lambda_k r^{\lambda_k-1}e^{i\theta(\lambda_k-1)} + N_{km}\bar{\lambda}_k r^{\bar{\lambda}_k-1}e^{i\theta(\bar{\lambda}_k-1)}\right] -\\ &- \frac{1}{2}\left[\bar{M}_{km}\bar{\lambda}_k r^{\bar{\lambda}_k-1}e^{-i\theta(\bar{\lambda}_k-1)} + \bar{N}_{km}\lambda_k r^{\lambda_k-1}e^{-i\theta(\lambda_k-1)}\right]\\ &= \frac{1}{2}\{r^{\lambda_k-1}\left[-I_{km}\lambda_k\left(\lambda_k-3\right)e^{i\theta(\lambda_k-1)} - \bar{L}_{km}\lambda_k\left(\lambda_k-3\right)e^{-i\theta(\lambda_k-1)} - M_{km}\lambda_k e^{i\theta(\lambda_k+1)} - \bar{N}_{km}\lambda_k e^{-i\theta(\lambda_k+1)}\right] +\\ &+ r^{\bar{\lambda}_k-1}\left[-\bar{I}_{km}\bar{\lambda}_k\left(\bar{\lambda}_k-3\right)e^{-i\theta\left(\bar{\lambda}_k-1\right)} - L_{km}\bar{\lambda}_k\left(\bar{\lambda}_k-3\right)e^{i\theta\left(\bar{\lambda}_k-1\right)} - \bar{M}_{km}\bar{\lambda}_k e^{-i\theta\left(\bar{\lambda}_k+1\right)} - N_{km}\bar{\lambda}_k e^{i\theta(\lambda_k+1)}\right]\}.\end{aligned}$$

The expression for $\sigma_{r\theta km}$ is again obtained by substitution of equations (100)-(105) into (9). Therefore we write:

$$\begin{aligned}
\sigma_{r\theta km}(r,\theta) &= \frac{re^{-i\theta}}{2i}\left[I_{km}\lambda_k(\lambda_k-1)r^{\lambda_k-2}e^{i\theta(\lambda_k-2)}+L_{km}\bar{\lambda}_k\left(\bar{\lambda}_k-1\right)r^{\bar{\lambda}_k-2}e^{i\theta\left(\bar{\lambda}_k-2\right)}\right]- \\
&- \frac{re^{i\theta}}{2i}\left[\bar{I}_{km}\bar{\lambda}_k\left(\bar{\lambda}_k-1\right)r^{\bar{\lambda}_k-2}e^{-i\theta\left(\bar{\lambda}_k-2\right)}+\bar{L}_{km}\lambda_k(\lambda_k-1)r^{\lambda_k-2}e^{-i\theta(\lambda_k-2)}\right]+ \\
&+ \frac{1}{2i}\left[M_{km}\lambda_k r^{\lambda_k-1}e^{i\theta(\lambda_k-1)}+N_{km}\bar{\lambda}_k r^{\bar{\lambda}_k-1}e^{i\theta\left(\bar{\lambda}_k-1\right)}\right]- \\
&- \frac{1}{2i}\left[\bar{M}_{km}\bar{\lambda}_k r^{\bar{\lambda}_k-1}e^{-i\theta\left(\bar{\lambda}_k-1\right)}+\bar{N}_{km}\lambda_k r^{\lambda_k-1}e^{-i\theta(\lambda_k-1)}\right] \\
&= \frac{1}{2i}\{r^{\lambda_k-1}\left[I_{km}\lambda_k(\lambda_k-1)e^{i\theta(\lambda_k-1)}-\bar{L}_{km}\lambda_k(\lambda_k-1)e^{-i\theta(\lambda_k-1)}+M_{km}\lambda_k e^{i\theta(\lambda_k+1)}-\bar{N}_{km}\lambda_k e^{-i\theta(\lambda_k+1)}\right]+ \\
&+ r^{\bar{\lambda}_k-1}\left[-\bar{I}_{km}\bar{\lambda}_k\left(\bar{\lambda}_k-1\right)e^{-i\theta\left(\bar{\lambda}_k-1\right)}+L_{km}\bar{\lambda}_k\left(\bar{\lambda}_k-1\right)e^{i\theta\left(\bar{\lambda}_k-1\right)}-\bar{M}_{km}\bar{\lambda}_k e^{-i\theta\left(\bar{\lambda}_k+1\right)}+N_{km}\bar{\lambda}_k e^{i\theta\left(\bar{\lambda}_k+1\right)}\right]\},
\end{aligned}$$

and similarly for $\sigma_{\theta\theta km}$ we write:

$$\begin{aligned}
\sigma_{\theta\theta km}(r,\theta) &= I_{km}\lambda_k r^{\lambda_k-1}e^{i\theta(\lambda_k-1)}+L_{km}\bar{\lambda}_k r^{\bar{\lambda}_k-1}e^{i\theta\left(\bar{\lambda}_k-1\right)}+ \\
&+ \bar{I}_{km}\bar{\lambda}_k r^{\bar{\lambda}_k-1}e^{-i\theta\left(\bar{\lambda}_k-1\right)}+\bar{L}_{km}\lambda_k r^{\lambda_k-1}e^{-i\theta(\lambda_k-1)}+ \\
&+ \frac{re^{-i\theta}}{2}\left[I_{km}\lambda_k(\lambda_k-1)r^{\lambda_k-2}e^{i\theta(\lambda_k-2)}+L_{km}\bar{\lambda}_k\left(\bar{\lambda}_k-1\right)r^{\bar{\lambda}_k-2}e^{i\theta\left(\bar{\lambda}_k-2\right)}\right]+ \\
&+ \frac{re^{i\theta}}{2}\left[\bar{I}_{km}\bar{\lambda}_k\left(\bar{\lambda}_k-1\right)r^{\bar{\lambda}_k-2}e^{-i\theta\left(\bar{\lambda}_k-2\right)}+\bar{L}_{km}\lambda_k(\lambda_k-1)r^{\lambda_k-2}e^{-i\theta(\lambda_k-2)}\right]+ \\
&+ \frac{1}{2}\left[M_{km}\lambda_k r^{\lambda_k-1}e^{i\theta(\lambda_k-1)}+N_{km}\bar{\lambda}_k r^{\bar{\lambda}_k-1}e^{i\theta\left(\bar{\lambda}_k-1\right)}\right]+ \\
&+ \frac{1}{2}\left[\bar{M}_{km}\bar{\lambda}_k r^{\bar{\lambda}_k-1}e^{-i\theta\left(\bar{\lambda}_k-1\right)}+\bar{N}_{km}\lambda_k r^{\lambda_k-1}e^{-i\theta(\lambda_k-1)}\right] \\
&= \frac{1}{2}\{r^{\lambda_k-1}\left[I_{km}\lambda_k(\lambda_k+1)e^{i\theta(\lambda_k-1)}+\bar{L}_{km}\lambda_k(\lambda_k+1)e^{-i\theta(\lambda_k-1)}+M_{km}\lambda_k e^{i\theta(\lambda_k+1)}+\bar{N}_{km}\lambda_k e^{-i\theta(\lambda_k+1)}\right]+ \\
&+ r^{\bar{\lambda}_k-1}\left[\bar{I}_{km}\bar{\lambda}_k\left(\bar{\lambda}_k+1\right)e^{-i\theta\left(\bar{\lambda}_k-1\right)}+L_{km}\bar{\lambda}_k\left(\bar{\lambda}_k+1\right)e^{i\theta\left(\bar{\lambda}_k-1\right)}+\bar{M}_{km}\bar{\lambda}_k e^{-i\theta\left(\bar{\lambda}_k+1\right)}+N_{km}\bar{\lambda}_k e^{i\theta(\lambda_k+1)}\right]\}.
\end{aligned}$$

The displacements are derived in a similar manner, for u_{rkm} we thus write:

$$\begin{aligned}
u_{rkm}(r,\theta) &= \frac{1}{4\mu_m}\{\kappa_m e^{-i\theta}\left[I_{km}r^{\lambda_k}e^{i\theta\lambda_k}+L_{km}r^{\bar{\lambda}_k}e^{i\theta\bar{\lambda}_k}\right]- \\
&- r\left[\bar{I}_{km}\bar{\lambda}_k r^{\bar{\lambda}_k-1}e^{-i\theta\left(\bar{\lambda}_k-1\right)}+\bar{L}_{km}\lambda_k r^{\lambda_k-1}e^{-i\theta(\lambda_k-1)}\right]- \\
&- e^{-i\theta}\left[\bar{M}_{km}r^{\bar{\lambda}_k}e^{-i\theta\bar{\lambda}_k}+\bar{N}_{km}r^{\lambda_k}e^{-i\theta\lambda_k}\right]+ \\
&+ \kappa_m e^{i\theta}\left[\bar{I}_{km}r^{\bar{\lambda}_k}e^{-i\theta\bar{\lambda}_k}+\bar{L}_{km}r^{\lambda_k}e^{-i\theta\lambda_k}\right]- \\
&- r\left[I_{km}\lambda_k r^{\lambda_k-1}e^{i\theta(\lambda_k-1)}+L_{km}\bar{\lambda}_k r^{\bar{\lambda}_k-1}e^{i\theta\left(\bar{\lambda}_k-1\right)}\right]- \\
&- e^{i\theta}\left[M_{km}r^{\lambda_k}e^{i\theta\bar{\lambda}_k}+N_{km}r^{\bar{\lambda}_k}e^{i\theta\bar{\lambda}_k}\right]\} \\
&= \frac{1}{4\mu_m}\{r^{\lambda_k}\left[I_{km}(\kappa_m-\lambda_k)e^{i\theta(\lambda_k-1)}+\bar{L}_{km}(\kappa_m-\lambda_k)e^{-i\theta(\lambda_k-1)}-M_{km}e^{i\theta(\lambda_k+1)}-\bar{N}_{km}e^{-i\theta(\lambda_k+1)}\right]+ \\
&+ r^{\bar{\lambda}_k}\left[\bar{I}_{km}\left(\kappa_m-\bar{\lambda}_k\right)e^{-i\theta\left(\bar{\lambda}_k-1\right)}+L_{km}(\kappa_m-\lambda_k)e^{i\theta(\lambda_k-1)}-\bar{M}_{km}e^{-i\theta(\lambda_k+1)}-N_{km}e^{i\theta(\lambda_k+1)}\right]\},
\end{aligned}$$

and finally for the $u_{\theta km}$ we write:

$$\begin{aligned}
u_{\theta km}(r,\theta) &= \frac{1}{4i\mu_m}\{e^{-i\theta}\kappa_m\left[I_{km}r^{\lambda_k}e^{i\theta\lambda_k}+L_{km}r^{\bar{\lambda}_k}e^{i\theta\bar{\lambda}_k}\right]-\\
&- r\left[\bar{I}_{km}\bar{\lambda}_k r^{\bar{\lambda}_k-1}e^{-i\theta\left(\bar{\lambda}_k-1\right)}+\bar{L}_{km}\lambda_k r^{\lambda_k-1}e^{-i\theta(\lambda_k-1)}\right]-\\
&- e^{-i\theta}\left[\bar{M}_{km}r^{\bar{\lambda}_k}e^{-i\theta\bar{\lambda}_k}+\bar{N}_{km}r^{\lambda_k}e^{-i\theta\lambda_k}\right]-\\
&- e^{i\theta}\kappa_m\left[\bar{I}_{km}r^{\bar{\lambda}_k}e^{-i\theta\bar{\lambda}_k}+\bar{L}_{km}r^{\lambda_k}e^{-i\theta\lambda_k}\right]-\\
&+ r\left[I_{km}\lambda_k r^{\lambda_k-1}e^{i\theta(\lambda_k-1)}+L_{km}\bar{\lambda}_k r^{\bar{\lambda}_k-1}e^{i\theta\left(\bar{\lambda}_k-1\right)}\right]+\\
&+ e^{i\theta}\left[M_{km}r^{\lambda_k}e^{-i\theta\lambda_k}+N_{km}r^{\bar{\lambda}_k}e^{i\theta\bar{\lambda}_k}\right]\}\\
&= \frac{1}{4i\mu_m}\{r^{\lambda_k}\left[I_{km}\left(\kappa_m+\lambda_k\right)e^{i\theta(\lambda_k-1)}-\bar{L}_{km}\left(\kappa_m+\lambda_k\right)e^{-i\theta(\lambda_k-1)}+M_{km}e^{i\theta(\lambda_k+1)}-\bar{N}_{km}e^{-i\theta(\lambda_k+1)}\right]+\\
&+ r^{\bar{\lambda}_k}\left[-\bar{I}_{km}\left(\kappa_m+\bar{\lambda}_k\right)e^{-i\theta\left(\bar{\lambda}_k-1\right)}+L_{km}\left(\kappa_m+\bar{\lambda}_k\right)e^{i\theta\left(\bar{\lambda}_k-1\right)}-\bar{M}_{km}e^{-i\theta\left(\bar{\lambda}_k+1\right)}+N_{km}e^{i\theta\left(\bar{\lambda}_k+1\right)}\right]\}.
\end{aligned}$$

A.2. Criterion of maximum of average tangential stress

The derivation of Eq. (64) on p. 56 is shown by substitution of first 3 stress series terms in complex form, Eq. (20) on p. 24 into equation (61) on p. 55. The equation becomes:

$$\begin{aligned}
\frac{1}{d}\frac{\partial}{\partial\theta}\Bigg[\int_0^d &\left(H_1r^{\lambda_1-1}f_{\theta\theta1}(\theta)+H_2r^{\lambda_2-1}f_{\theta\theta2}(\theta)+H_3r^{\lambda_3-1}f_{\theta\theta3}(\theta)\right)\mathrm{d}r+\\
&+\bar{H}_1r^{\bar{\lambda}_1-1}\bar{f}_{\theta\theta1}(\theta)+\bar{H}_2r^{\bar{\lambda}_2-1}\bar{f}_{\theta\theta2}(\theta)+\bar{H}_3r^{\bar{\lambda}_3-1}\bar{f}_{\theta\theta3}(\theta)\Bigg] = 0,
\end{aligned}$$

which after integration is:

$$H_1\frac{d^{\lambda_1}}{\lambda_1}\frac{\partial f_{\theta\theta1}(\theta)}{\partial\theta}+H_2\frac{d^{\lambda_2}}{\lambda_2}\frac{\partial f_{\theta\theta2}(\theta)}{\partial\theta}+H_3\frac{d^{\lambda_3}}{\lambda_3}\frac{\partial f_{\theta\theta3}(\theta)}{\partial\theta}+\bar{H}_1\frac{d^{\bar{\lambda}_1}}{\bar{\lambda}_1}\frac{\partial\bar{f}_{\theta\theta1}(\theta)}{\partial\theta}+\bar{H}_2\frac{d^{\bar{\lambda}_2}}{\bar{\lambda}_2}\frac{\partial\bar{f}_{\theta\theta2}(\theta)}{\partial\theta}+\bar{H}_3\frac{d^{\bar{\lambda}_3}}{\bar{\lambda}_3}\frac{\partial\bar{f}_{\theta\theta3}(\theta)}{\partial\theta} = 0,$$

where the first derivative of eigenfunction $f_{\theta\theta km}(\theta)$ in terms of complex constants I_{km}, L_{km}, M_{km} and N_{km} is:

$$\begin{aligned}
\frac{\partial f_{\theta\theta km}(\theta)}{\partial\theta} &= \frac{1}{2}i\left[e^{i\theta(\lambda_k-1)}I_{km}\lambda_k\left(\lambda_k-1\right)\left(\lambda_k+1\right)-e^{-i\theta(\lambda_k-1)}\bar{L}_{km}\lambda_k\left(\lambda_k-1\right)\left(\lambda_k+1\right)+\right.\\
&+ \left.e^{i\theta(\lambda_k+1)}M_{km}\lambda_k\left(\lambda_k+1\right)-e^{-i\theta(\lambda_k+1)}\bar{N}_{km}\lambda_k\left(\lambda_k+1\right)\right],
\end{aligned}$$

and similarly for $\bar{f}_{\theta\theta km}(\theta)$ we write:

$$\begin{aligned}
\frac{\partial\bar{f}_{\theta\theta km}(\theta)}{\partial\theta} &= \frac{1}{2}i\left[-e^{-i\theta\left(\bar{\lambda}_k-1\right)}\bar{I}_{km}\bar{\lambda}_k\left(\bar{\lambda}_k-1\right)\left(\bar{\lambda}_k+1\right)+e^{i\theta\left(\bar{\lambda}_k-1\right)}L_{km}\bar{\lambda}_k\left(\bar{\lambda}_k-1\right)\left(\bar{\lambda}_k+1\right)-\right.\\
&- \left.e^{-i\theta\left(\bar{\lambda}_k+1\right)}\bar{M}_{km}\bar{\lambda}_k\left(\bar{\lambda}_k+1\right)+e^{i\theta\left(\bar{\lambda}_k+1\right)}N_{km}\bar{\lambda}_k\left(\bar{\lambda}_k+1\right)\right].
\end{aligned}$$

The GSIF H_1 can be factored out of the equation, so we introduce factors between GSIFs Γ_{k1} as in Eq. (63) on p. 55. Since the crack initiation direction does not depend on GSIFs absolute value, we obtain:

$$\Gamma_{11}\frac{d^{\lambda_1}}{\lambda_1}\frac{\partial f_{\theta\theta1}(\theta)}{\partial\theta}+\Gamma_{21}\frac{d^{\lambda_2}}{\lambda_2}\frac{\partial f_{\theta\theta2}(\theta)}{\partial\theta}+\Gamma_{31}\frac{d^{\lambda_3}}{\lambda_3}\frac{\partial f_{\theta\theta3}(\theta)}{\partial\theta}+\bar{\Gamma}_{11}\frac{d^{\bar{\lambda}_1}}{\bar{\lambda}_1}\frac{\partial\bar{f}_{\theta\theta1}(\theta)}{\partial\theta}+\bar{\Gamma}_{21}\frac{d^{\bar{\lambda}_2}}{\bar{\lambda}_2}\frac{\partial\bar{f}_{\theta\theta2}(\theta)}{\partial\theta}+\bar{\Gamma}_{31}\frac{d^{\bar{\lambda}_3}}{\bar{\lambda}_3}\frac{\partial\bar{f}_{\theta\theta3}(\theta)}{\partial\theta} = 0,$$

which leads to the general form of the equation with n terms, equation (65) on p. 56. The derivation of complex form follows. We can rewrite the stress expansion as:

$$\sigma_{ij} = H_1\sum_{k=1}^{n}\Gamma_{k1}r^{\lambda_k-1}f_{ijk}(\theta)+\bar{H}_1\sum_{k=1}^{n}\bar{\Gamma}_{k1}r^{\bar{\lambda}_k-1}\bar{f}_{ijk}(\theta),$$

which can be analogically derived, integrated and rearranged, so we obtain Eq. (65) on p. 56. For completeness, the second derivative of function $\bar{f}_{\theta\theta km}(\theta)$ in terms of complex constants is:

$$\begin{aligned}\frac{\partial f^2_{\theta\theta km}(\theta)}{\partial\theta^2} &= -\frac{1}{2}\Big[e^{i\theta(\lambda_k-1)}I_{km}\lambda_k(\lambda_k-1)^2(\lambda_k+1)+e^{-i\theta(\lambda_k-1)}\bar{L}_{km}\lambda_k(\lambda_k-1)^2(\lambda_k+1)+\\ &+ e^{i\theta(\lambda_k+1)}M_{km}\lambda_k(\lambda_k+1)^2++e^{-i\theta(\lambda_k+1)}\bar{N}_{km}\lambda_k(\lambda_k+1)^2\Big],\end{aligned}$$

and its complex conjugate:

$$\begin{aligned}\frac{\partial \bar{f}^2_{\theta\theta km}(\theta)}{\partial\theta^2} &= \frac{1}{2}\Big[e^{-i\theta(\bar{\lambda}_k-1)}\bar{I}_{km}\bar{\lambda}_k(\bar{\lambda}_k-1)^2(\bar{\lambda}_k+1)+e^{i\theta(\bar{\lambda}_k-1)}L_{km}\bar{\lambda}_k(\bar{\lambda}_k-1)^2(\bar{\lambda}_k+1)+\\ &+ e^{-i\theta(\bar{\lambda}_k+1)}\bar{M}_{km}\bar{\lambda}_k(\bar{\lambda}_k+1)^2+e^{i\theta(\bar{\lambda}_k+1)}N_{km}\bar{\lambda}_k(\bar{\lambda}_k+1)^2\Big].\end{aligned}$$

A.3. Average strain energy density criterion

The derivation of Eq. (71) on p. 57 for calculation of a mean value of SEDF is shown in following text. Let's consider stress expansion, Eq. (20) on p. 24 in following form:

$$\sigma_{ij} = 2\Re\left\{\sum_{k=1}^{n}H_k r^{\lambda_1-1}f_{ijk}(\theta)\right\}.$$

The derivation is shown on a series containing first 3 terms only. General form for n terms follows later on. First, each stress component in its expansion form is substituted into formula for calculation SEDF on mth material region in case of a plane problem, Eq. (70) on p. 57:

$$\begin{aligned}\Sigma_m &= \Re\Big\{r\frac{1}{2\mu_m}\big[2\left(H_1r^{\lambda_1-1}f_{\theta\theta1}(\theta)+H_2r^{\lambda_2-1}f_{\theta\theta2}(\theta)+H_3r^{\lambda_3-1}f_{\theta\theta3}(\theta)\right)\\ &\quad\left(H_1r^{\lambda_1-1}f_{rr1}(\theta)+H_2r^{\lambda_2-1}f_{rr2}(\theta)+H_3r^{\lambda_3-1}f_{rr3}(\theta)\right)(k_m-1)+\\ &+\Big(\left(H_1r^{\lambda_1-1}f_{\theta\theta1}(\theta)+H_2r^{\lambda_2-1}f_{\theta\theta2}(\theta)+H_3r^{\lambda_3-1}f_{\theta\theta3}(\theta)\right)^2+\\ &+\left(H_1r^{\lambda_1-1}f_{rr1}(\theta)+H_2r^{\lambda_2-1}f_{rr2}(\theta)+H_3r^{\lambda_3-1}f_{rr3}(\theta)\right)^2\Big)(k_m+1)+\\ &+4\left(H_1r^{\lambda_1-1}f_{r\theta1}(\theta)+H_2r^{\lambda_2-1}f_{r\theta2}(\theta)+H_3r^{\lambda_3-1}f_{r\theta3}(\theta)\right)^2\big]\Big\}.\end{aligned} \tag{106}$$

Thus after expanding and some simple rearrangements the equation (106) becomes:

$$\begin{aligned}\Sigma_m &= r\frac{1}{2\mu_m}\Re\Big\{H_1^2r^{2(\lambda_1-1)}\left[2f_{\theta\theta1}f_{rr1}(k_m-1)+f^2_{\theta\theta1}(k_m+1)+f^2_{rr1}(k_m+1)+4f^2_{r\theta1}\right]+\\ &+ H_2^2r^{2(\lambda_2-1)}\left[2f_{\theta\theta2}f_{rr2}(k_m-1)+f^2_{\theta\theta2}(k_m+1)+f^2_{rr2}(k_m+1)+4f^2_{r\theta2}\right]+\\ &+ H_3^2r^{2(\lambda_3-1)}\left[2f_{\theta\theta3}f_{rr3}(k_m-1)+f^2_{\theta\theta3}(k_m+1)+f^2_{rr3}(k_m+1)+4f^2_{r\theta3}\right]+\\ &+ H_1H_2r^{(\lambda_1-1)+(\lambda_2-1)}\\ &\quad[2f_{\theta\theta1}f_{rr2}(k_m-1)+2f_{\theta\theta2}f_{rr1}(k_m-1)+2f_{\theta\theta1}f_{\theta\theta2}(k_m+1)+2f_{rr1}f_{rr2}(k_m+1)+8f_{r\theta1}f_{r\theta2}]+\\ &+ H_1H_3r^{(\lambda_1-1)+(\lambda_3-1)}\\ &\quad[2f_{\theta\theta1}f_{rr3}(k_m-1)+2f_{\theta\theta3}f_{rr1}(k_m-1)+2f_{\theta\theta1}f_{\theta\theta3}(k_m+1)+2f_{rr1}f_{rr3}(k_m+1)+8f_{r\theta1}f_{r\theta3}]+\\ &+ H_2H_3r^{(\lambda_2-1)+(\lambda_3-1)}\\ &\quad[2f_{\theta\theta2}f_{rr3}(k_m-1)+2f_{\theta\theta3}f_{rr2}(k_m-1)+2f_{\theta\theta2}f_{\theta\theta3}(k_m+1)+2f_{rr2}f_{rr3}(k_m+1)+8f_{r\theta2}f_{r\theta3}]\Big\},\end{aligned} \tag{107}$$

where the all the functions f_{ijk} above are functions of angle θ. For the sake of saving available text field, the symbol (θ) is intentionally omitted. We can identify the functions $U_{klm}(\theta)$ as:

$$U_{klm}(\theta) = \begin{cases}2f_{\theta\theta k}(\theta)f_{rrk}(\theta)(k_m-1)+(f^2_{\theta\theta k}(\theta)+f^2_{rrk}(\theta))(k_m+1)+4f^2_{r\theta k}(\theta) & k=l\\ 2(f_{\theta\theta k}(\theta)f_{rrl}(\theta)+f_{\theta\theta l}(\theta)f_{rrk}(\theta))(k_m-1)+2(f_{\theta\theta k}(\theta)f_{\theta\theta l}(\theta)+ & k\neq l\\ \quad+f_{rrk}(\theta)f_{rrl}(\theta))(k_m+1)+8f_{r\theta k}(\theta)f_{r\theta l}(\theta) & \end{cases}.$$

Where the function $U_{klm}(\theta)$ is defined for each material region $m = 1, 2$ of bi-material notch as:

$$U_{klm}(\theta) = \begin{cases} U_{kl1}(\theta) & \gamma_1 < \theta < \gamma_2 \\ U_{kl2}(\theta) & \gamma_2 < \theta < \gamma_3 \end{cases}$$

and for the case of bi-material junction as:

$$U_{klm}(\theta) = \begin{cases} U_{kl1}(\theta) & \gamma_0 < \theta < \gamma_1 \\ U_{kl2}(\theta) & \gamma_1 < \theta < \gamma_2 \end{cases}.$$

The formula (107) after further rearrangement becomes:

$$\begin{aligned} \Sigma_m &= \frac{1}{2\mu_m}\Re\left\{H_1^2 r^{2\lambda_1-1}U_{11}(\theta) + H_2^2 r^{2\lambda_2-1}U_{22}(\theta) + H_3^2 r^{2\lambda_3-1}U_{33}(\theta) + \right. \\ &+ \left. H_1H_2 r^{\lambda_1+\lambda_2-1}U_{12}(\theta) + H_1H_3 r^{\lambda_1+\lambda_3-1}U_{13}(\theta) + H_2H_3 r^{\lambda_2+\lambda_3-1}U_{23}(\theta)\right\}. \end{aligned} \tag{108}$$

The mean value of SEDF is defined in Eq. (69) on p. 57. Thus we substitute the equation (108) above into it, integrate it and finally we get:

$$\begin{aligned} \overline{\Sigma}_m &= \frac{1}{2\mu_m}\Re\left\{H_1^2\frac{d^{2\lambda_1-1}}{2\lambda_1}U_{11}(\theta) + H_1H_2\frac{d^{\lambda_1+\lambda_2-1}}{\lambda_1+\lambda_2}U_{12}(\theta) + H_1H_3\frac{d^{\lambda_1+\lambda_3-1}}{\lambda_1+\lambda_3}U_{13}(\theta) + \right. \\ &+ H_2^2\frac{d^{2\lambda_2-1}}{2\lambda_2}U_{22}(\theta) + H_2H_3\frac{d^{\lambda_2+\lambda_3-1}}{\lambda_2+\lambda_3}U_{23}(\theta) + \\ &+ \left. H_3^2\frac{d^{2\lambda_3-1}}{2\lambda_3}U_{33}(\theta)\right\}. \end{aligned}$$

This expression with consideration of n terms leads to Eq. (71) on p. 57. The extreme of function above is found by substitution of equation above into Eq. (72) on p. 58 and its derivation in dependence of angle θ:

$$\begin{aligned} \left[H_1H_1\frac{d^{\lambda_1+\lambda_1-1}}{\lambda_1+\lambda_1}\frac{\partial U_{11}(\theta)}{\partial\theta} + H_1H_2\frac{d^{\lambda_1+\lambda_2-1}}{\lambda_1+\lambda_2}\frac{\partial U_{12}(\theta)}{\partial\theta} + H_1H_3\frac{d^{\lambda_1+\lambda_3-1}}{\lambda_1+\lambda_3}\frac{\partial U_{13}(\theta)}{\partial\theta} + \right. \\ + H_2H_2\frac{d^{\lambda_2+\lambda_2-1}}{\lambda_2+\lambda_2}\frac{\partial U_{22}(\theta)}{\partial\theta} + H_2H_3\frac{d^{\lambda_2+\lambda_3-1}}{\lambda_2+\lambda_3}\frac{\partial U_{23}(\theta)}{\partial\theta} + \\ \left. + H_3H_3\frac{d^{\lambda_3+\lambda_3-1}}{\lambda_3+\lambda_3}\frac{\partial U_{33}(\theta)}{\partial\theta}\right] &= 0. \end{aligned}$$

With consideration of Γ_k and Γ_l and for n terms we finally obtain the general formula (73) as found in the main text on p. 58. The first derivatives of stress eigenfunctions $f_{ijk}(\theta)$ in terms of complex constants are written:

$$\begin{aligned} \frac{\partial f_{rrkm}(\theta)}{\partial\theta} &= \frac{1}{2}i\left[-I_{km}\lambda_k(\lambda_k-3)(\lambda_k-1)e^{i\theta(\lambda_k-1)} + \bar{L}_{km}\lambda_k(\lambda_k-3)(\lambda_k-1)e^{-i\theta(\lambda_k-1)} - \right. \\ &\left. - M_{km}\lambda_k(\lambda_k+1)e^{i\theta(\lambda_k+1)} + \bar{N}_{km}\lambda_k(\lambda_k+1)e^{-i\theta(\lambda_k+1)}\right], \end{aligned}$$

$$\begin{aligned} \frac{\partial f_{r\theta km}(\theta)}{\partial\theta} &= \frac{1}{2}\left[I_{km}\lambda_k(\lambda_k-1)^2 e^{i\theta(\lambda_k-1)} + \bar{L}_{km}\lambda_k(\lambda_k-1)^2 e^{-i\theta(\lambda_k-1)} + \right. \\ &\left. + M_{km}\lambda_k(\lambda_k+1)e^{i\theta(\lambda_k+1)} + \bar{N}_{km}\lambda_k(\lambda_k+1)e^{-i\theta(\lambda_k+1)}\right], \end{aligned}$$

$$\begin{aligned} \frac{\partial f_{\theta\theta km}(\theta)}{\partial\theta} &= \frac{1}{2}i\left[I_{km}\lambda_k(\lambda_k+1)(\lambda_k-1)e^{i\theta(\lambda_k-1)} - \bar{L}_{km}\lambda_k(\lambda_k+1)(\lambda_k-1)e^{-i\theta(\lambda_k-1)} \right. \\ &\left. + M_{km}\lambda_k(\lambda_k+1)e^{i\theta(\lambda_k+1)} - \bar{N}_{km}\lambda_k(\lambda_k+1)e^{-i\theta(\lambda_k+1)}\right]. \end{aligned}$$

and the second derivatives of stress eigenfunctions $f_{ijk}(\theta)$ are written:

$$\begin{aligned}\frac{\partial^2 f_{rrkm}(\theta)}{\partial\theta^2} &= \frac{1}{2}\Big[I_{km}\lambda_k(\lambda_k-3)(\lambda_k-1)^2 e^{i\theta(\lambda_k-1)} + \bar{L}_{km}\lambda_k(\lambda_k-3)(\lambda_k-1)^2 e^{-i\theta(\lambda_k-1)} + \\ &+ M_{km}\lambda_k(\lambda_k+1)^2 e^{i\theta(\lambda_k+1)} + \bar{N}_{km}\lambda_k(\lambda_k+1)^2 e^{-i\theta(\lambda_k+1)}\Big],\end{aligned}$$

$$\begin{aligned}\frac{\partial^2 f_{r\theta km}(\theta)}{\partial\theta^2} &= \frac{1}{2}i\Big[I_{km}\lambda_k(\lambda_k-1)^3 e^{i\theta(\lambda_k-1)} - \bar{L}_{km}\lambda_k(\lambda_k-1)^3 e^{-i\theta(\lambda_k-1)} + \\ &+ M_{km}\lambda_k(\lambda_k+1)^2 e^{i\theta(\lambda_k+1)} - \bar{N}_{km}\lambda_k(\lambda_k-1)^2 e^{-i\theta(\lambda_k+1)}\Big],\end{aligned}$$

$$\begin{aligned}\frac{\partial^2 f_{\theta\theta km}(\theta)}{\partial\theta^2} &= -\frac{1}{2}\Big[I_{km}\lambda_k(\lambda_k+1)(\lambda_k-1)^2 e^{i\theta(\lambda_k-1)} + \bar{L}_{km}\lambda_k(\lambda_k+1)(\lambda_k-1)^2 e^{-i\theta(\lambda_k-1)} + \\ &+ M_{km}\lambda_k(\lambda_k+1)^2 e^{i\theta(\lambda_k+1)} + \bar{N}_{km}\lambda_k(\lambda_k+1)^2 e^{-i\theta(\lambda_k+1)}\Big].\end{aligned}$$

The function $U_{klm}(\theta)$ for $k=l$ is in terms of complex constants written:

$$\begin{aligned}U_{kkm}(\theta) &= 4\lambda_k^2\Big[k_m\left(I_{km}^2 e^{2i\theta(\lambda_k-1)} + \bar{L}_{km}^2 e^{-2i\theta(\lambda_k-1)}\right) + \\ &+ (\lambda_k-1)\left(\bar{L}_{km}M_{km}e^{2i\theta} + I_{km}\bar{N}_{km}e^{-2i\theta}\right) + \\ &+ \left((\lambda_k-1)^2+2k_m\right)I_{km}\bar{L}_{km} + M_{km}\bar{N}_{km}\Big]\end{aligned}$$

The first derivative of function $U_{klm}(\theta)$ for $k=l$ is in terms of complex constants written

$$\begin{aligned}\frac{\partial U_{klm}(\theta)}{\partial\theta} &= 4\lambda_k^2\Big[k_m\left(2i(\lambda_k-1)I_{km}^2 e^{2i\theta(\lambda_k-1)} - 2i(\lambda_k-1)\bar{L}_{km}^2 e^{-2i\theta(\lambda_k-1)}\right) + \\ &+ (\lambda_k-1)\left(2i\bar{L}_{km}M_{km}e^{2i\theta} - 2iI_{km}\bar{N}_{km}e^{-2i\theta}\right) = \\ &= 8i\lambda_k^2(\lambda_k-1)\Big[k_m\left(I_{km}^2 e^{2i\theta(\lambda_k-1)} - \bar{L}_{km}^2 e^{-2i\theta(\lambda_k-1)}\right) + \\ &+ \bar{L}_{km}M_{km}e^{2i\theta} - I_{km}\bar{N}_{km}e^{-2i\theta}\Big]\end{aligned} \tag{109}$$

and the second derivative of function $U_{klm}(\theta)$ for $k=l$ is:

$$\begin{aligned}\frac{\partial^2 U_{klm}(\theta)}{\partial\theta^2} &= -16\lambda_k^2(\lambda_k-1)\Big[k_m(\lambda_k-1)\left(I_{km}^2 e^{2i\theta(\lambda_k-1)} + \bar{L}_{km}^2 e^{-2i\theta(\lambda_k-1)}\right) + \\ &+ \bar{L}_{km}M_{km}e^{2i\theta} + I_{km}\bar{N}_{km}e^{-2i\theta}\Big]\end{aligned}$$

For $k\neq l$ the function $U_{klm}(\theta)$ is written:

$$\begin{aligned}U_{klm}(\theta) &= 4\lambda_k\lambda_l\Big[(\lambda_k\lambda_l-\lambda_k-\lambda_l+2k_m+1)\left(e^{i\theta(\lambda_k-\lambda_l)}I_{km}L_{lm} + e^{-i\theta(\lambda_k-\lambda_l)}I_{lm}L_{km}\right) + \\ &+ (\lambda_k-1)\left(e^{i\theta(\lambda_k-\lambda_l-2)}I_{km}N_{lm} + e^{-i\theta(\lambda_k-\lambda_l-2)}L_{km}M_{lm}\right) + \\ &+ (\lambda_l-1)\left(e^{i\theta(\lambda_l-\lambda_k-2)}I_{lm}N_{km} + e^{-i\theta(\lambda_l-\lambda_k-2)}L_{lm}M_{km}\right) + \\ &+ 2k_m\left(I_{km}I_{lm}e^{i\theta(\lambda_k+\lambda_l-2)} + e^{-i\theta(\lambda_k+\lambda_l-2)}L_{km}L_{lm}\right) + \\ &+ M_{km}N_{lm}e^{i\theta(\lambda_k-\lambda_l)} + M_{lm}N_{km}e^{-i\theta(\lambda_k-\lambda_l)}\Big]\end{aligned}$$

first derivative of function $U_{klm}(\theta)$ is written

$$\begin{aligned}\frac{\partial U_{klm}(\theta)}{\partial\theta} &= 4i\lambda_k\lambda_l\Big[(\lambda_k-\lambda_l)(\lambda_k\lambda_l-\lambda_k-\lambda_l+2k_m+1)\left(e^{i\theta(\lambda_k-\lambda_l)}I_{km}L_{lm}-e^{-i\theta(\lambda_k-\lambda_l)}I_{lm}L_{km}\right)+\\ &+ (\lambda_k-1)(\lambda_k-\lambda_l-2)\left(e^{i\theta(\lambda_k-\lambda_l-2)}I_{km}N_{lm}-e^{-i\theta(\lambda_k-\lambda_l-2)}L_{km}M_{lm}\right)+\\ &+ (\lambda_l-1)(\lambda_l-\lambda_k-2)\left(e^{i\theta(\lambda_l-\lambda_k-2)}I_{lm}N_{km}-e^{-i\theta(\lambda_l-\lambda_k-2)}L_{lm}M_{km}\right)+\\ &+ 2k_m(\lambda_k+\lambda_l-2)\left(I_{km}I_{lm}e^{i\theta(\lambda_k+\lambda_l-2)}-e^{-i\theta(\lambda_k+\lambda_l-2)}L_{km}L_{lm}\right)+\\ &+ (\lambda_k-\lambda_l)\left(M_{km}N_{lm}e^{i\theta(\lambda_k-\lambda_l)}-M_{lm}N_{km}e^{-i\theta(\lambda_k-\lambda_l)}\right)\Big]\end{aligned}$$

and the second derivative of function $U_{klm}(\theta)$ is:

$$\begin{aligned}\frac{\partial^2 U_{klm}(\theta)}{\partial\theta^2} &= -4\lambda_k\lambda_l\Big[(\lambda_k-\lambda_l)^2(\lambda_k\lambda_l-\lambda_k-\lambda_l+2k_m+1)\left(e^{i\theta(\lambda_k-\lambda_l)}I_{km}L_{lm}+e^{-i\theta(\lambda_k-\lambda_l)}I_{lm}L_{km}\right)+\\ &+ (\lambda_k-1)(\lambda_k-\lambda_l-2)^2\left(e^{i\theta(\lambda_k-\lambda_l-2)}I_{km}N_{lm}+e^{-i\theta(\lambda_k-\lambda_l-2)}L_{km}M_{lm}\right)+\\ &+ (\lambda_l-1)(\lambda_l-\lambda_k-2)^2\left(e^{i\theta(\lambda_l-\lambda_k-2)}I_{lm}N_{km}+e^{-i\theta(\lambda_l-\lambda_k-2)}L_{lm}M_{km}\right)+\\ &+ 2k_m(\lambda_k+\lambda_l-2)^2\left(I_{km}I_{lm}e^{i\theta(\lambda_k+\lambda_l-2)}+e^{-i\theta(\lambda_k+\lambda_l-2)}L_{km}L_{lm}\right)+\\ &+ (\lambda_k-\lambda_l)^2\left(M_{km}N_{lm}e^{i\theta(\lambda_k-\lambda_l)}+M_{lm}N_{km}e^{-i\theta(\lambda_k-\lambda_l)}\right)\Big]\end{aligned}$$

A.4. Basic two-dimensional elasticity equations

Many problems in elasticity may be treated satisfactorily by a two-dimensional (plane) theory of elasticity [63]. By that the stress analysis is considerably simplified. There are two general types of problems involved in this plane analysis, plane stress and plane strain. These two types are defined by setting down certain restrictions and assumptions on the stress and displacement fields. The plane stress is defined to be a stress in which the normal stress σ_{zz} and the shear stresses σ_{xz} and σ_{yz} directed perpendicular to the xy plane are assumed to be zero[9]. This approach is applicable on bodies where one dimension is much smaller than the remaining two, e.g. thin flat planes. The stress tensor is for plane stress problem written:

$$\sigma_{ij} = \begin{bmatrix}\sigma_{xx} & \sigma_{xy} & 0\\ \sigma_{yx} & \sigma_{yy} & 0\\ 0 & 0 & 0\end{bmatrix}$$

and strain tensor:

$$\varepsilon_{ij} = \begin{bmatrix}\varepsilon_{xx} & \varepsilon_{xy} & 0\\ \varepsilon_{yx} & \varepsilon_{yy} & 0\\ 0 & 0 & \varepsilon_{zz}\end{bmatrix}.$$

When we consider the cylindrical coordinate system:

$$\sigma_{ij} = \begin{bmatrix}\sigma_{rr} & \sigma_{r\theta} & 0\\ \sigma_{\theta r} & \sigma_{\theta\theta} & 0\\ 0 & 0 & 0\end{bmatrix}$$

$$\varepsilon_{ij} = \begin{bmatrix}\varepsilon_{rr} & \varepsilon_{r\theta} & 0\\ \varepsilon_{\theta r} & \varepsilon_{\theta\theta} & 0\\ 0 & 0 & \varepsilon_{zz}\end{bmatrix}.$$

To assess safety of engineering structure in terms of yield criterion it is in general required to compute equivalent tensile stress. The von Misses stress for example is defined:

$$\begin{aligned}\sigma_e &= \sqrt{\frac{1}{2}\left[(\sigma_{xx}-\sigma_{yy})^2+(\sigma_{yy}-\sigma_{zz})^2+(\sigma_{zz}-\sigma_{xx})^2\right]+3\left(\sigma_{xy}^2+\sigma_{yz}^2+\sigma_{zx}^2\right)}=\\ &= \sqrt{\sigma_{xx}^2+\sigma_{yy}^2+\sigma_{zz}^2-\sigma_{xx}\sigma_{yy}-\sigma_{yy}\sigma_{zz}-\sigma_{zz}\sigma_{xx}+3\left(\sigma_{xy}^2+\sigma_{yz}^2+\sigma_{zx}^2\right)}\end{aligned}$$

[9] Isotropic material is assumed.

which in cylindrical coordinate system is:

$$\begin{aligned}\sigma_e &= \frac{1}{2}\sqrt{\left(\sigma_{rr}-\sigma_{\theta\theta}\right)^2+\left(\sigma_{\theta\theta}-\sigma_{zz}\right)^2+\left(\sigma_{zz}-\sigma_{rr}\right)^2+3\left(\sigma_{r\theta}^2+\sigma_{\theta z}^2+\sigma_{zr}^2\right)}= \\ &= \sqrt{\sigma_{rr}^2+\sigma_{\theta\theta}^2+\sigma_{zz}^2-\sigma_{rr}\sigma_{\theta\theta}-\sigma_{\theta\theta}\sigma_{zz}-\sigma_{zz}\sigma_{rr}+3\left(\sigma_{r\theta}^2+\sigma_{\theta z}^2+\sigma_{zr}^2\right)}\end{aligned} \tag{110}$$

Since the plane stress case if characterized by $\sigma_{zz}=\sigma_{rz}=\sigma_{\theta z}=0$, the von Misses stress is calculated as:

$$\sigma_e = \sqrt{\sigma_{rr}^2+\sigma_{\theta\theta}^2-\sigma_{rr}\sigma_{\theta\theta}+3\sigma_{r\theta}^2}$$

The plane strain is defined to be a state in which the strain normal to the xy plane ε_{zz} and the shear strains ε_{xz} and ε_{yz} are assumed to be zero. The plane strain approach applies to bodies where one dimension is very large in comparison with the dimension of the structure in other two directions. The stress tensor for plane strain problem is written:

$$\sigma_{ij} = \begin{bmatrix}\sigma_{xx} & \sigma_{xy} & 0\\ \sigma_{xy} & \sigma_{yy} & 0\\ 0 & 0 & \sigma_{zz}\end{bmatrix}$$

and strain tensor is:

$$\varepsilon_{ij} = \begin{bmatrix}\varepsilon_{xx} & \varepsilon_{xy} & 0\\ \varepsilon_{yx} & \varepsilon_{yy} & 0\\ 0 & 0 & 0\end{bmatrix}.$$

In cylindrical coordinate system we write:

$$\sigma_{ij} = \begin{bmatrix}\sigma_{rr} & \sigma_{r\theta} & 0\\ \sigma_{\theta r} & \sigma_{\theta\theta} & 0\\ 0 & 0 & \sigma_{zz}\end{bmatrix}$$

$$\varepsilon_{ij} = \begin{bmatrix}\varepsilon_{rr} & \varepsilon_{r\theta} & 0\\ \varepsilon_{\theta r} & \varepsilon_{\theta\theta} & 0\\ 0 & 0 & 0\end{bmatrix}.$$

Considering stress-strain relation (4) on p. 9:

$$\varepsilon_{zz} = \frac{1}{E}\left[\sigma_{zz}-\nu\left(\sigma_{rr}+\sigma_{\theta\theta}\right)\right]$$

The stress component σ_{zz} can be calculated as:

$$\sigma_{zz} = \nu\left(\sigma_{rr}+\sigma_{\theta\theta}\right)$$

Therefore by substitution in Eq. (110) the von Misses stress is:

$$\begin{aligned}\sigma_e &= \sqrt{\sigma_{rr}^2+\sigma_{\theta\theta}^2+\nu^2\left(\sigma_{rr}+\sigma_{\theta\theta}\right)^2-\sigma_{rr}\sigma_{\theta\theta}-\sigma_{\theta\theta}\nu\left(\sigma_{rr}+\sigma_{\theta\theta}\right)-\nu\left(\sigma_{rr}+\sigma_{\theta\theta}\right)\sigma_{rr}+3\sigma_{r\theta}^2}= \\ &= \sqrt{\sigma_{rr}^2\left(1-\nu+\nu^2\right)+\sigma_{\theta\theta}^2\left(1-\nu+\nu^2\right)-\sigma_{rr}\sigma_{\theta\theta}\left(1+2\nu-2\nu^2\right)+3\sigma_{r\theta}^2}\end{aligned}$$

In terms of eigenfunction, the von Misses stress can be written:

$$\sigma_e = \sum_{k=1}^{n} H_k r^{\lambda_k-1} f_{ek}\left(\theta\right)+\bar{H}_k r^{\bar{\lambda}_k-1}\bar{f}_{ek}\left(\theta\right)=2\Re\left\{\sum_{k=1}^{n} H_k r^{\lambda_k-1} f_{ek}\left(\theta\right)\right\}$$

where the eigenfunction $f_{ek}(\theta)$ for plane stress problem is:

$$f_{ek}\left(\theta\right) = \sqrt{f_{rrk}^2\left(\theta\right)+f_{\theta\theta k}^2\left(\theta\right)-f_{rrk}\left(\theta\right)f_{\theta\theta k}\left(\theta\right)+3f_{r\theta k}^2\left(\theta\right)}$$

and for plane strain problem:

$$f_{ek}\left(\theta\right) = \sqrt{f_{rrk}^2\left(\theta\right)\left(1-\nu+\nu^2\right)+f_{\theta\theta k}^2\left(\theta\right)\left(1-\nu+\nu^2\right)-f_{rrk}\left(\theta\right)f_{\theta\theta k}\left(\theta\right)\left(1+2\nu-2\nu^2\right)+3f_{r\theta k}^2\left(\theta\right)}$$

and the eigenequations $f_{ijk}\left(\theta\right)$ are defined in Eq. (23) on p. 25.

B. Attached scripts

The attachment of the thesis consists of the computer scripts created during the years of the author's research. These files can be with author permission distributed and further used for non-commercial research purposes. The written codes may be divided into two parts: the first part consists of the scripts written in APDL (Ansys Program Design Language) and the second of Python scripts (Python 2.7 run in Spyder 2.3 development environment). The scripts written in APDL can be run in commercial software code ANSYS v13 and newer. By these scripts, users have an access to three point bending specimen models of V-notch, bi-material notch specimen, sharp material inclusion and the model of free edge singularity. The model of outer domain for matched asymptotic expansion calculations and script that maps the load on the crack faces is attached, too. The models are parametric, so geometry, loads and bi-material combinations can be widely varied. The outputs of these models are text files which contains parameters about the models, nodal displacements and deflections field.

Next group of scripts was written in Python script using python libraries such as Numpy and Scipy. The Python scripts load the FE data and do the analytical part. Individual scripts calculate the eigenvalues, construct the eigenvectors and create the eigenfunctions. Another script performs the overdeterministic method or calculates the Psi-integral to obtain generalized stress intensity factors. Next it plots the stress or displacement distribution. All the data in tables throughout the dissertation and almost all the pictures were created by Python scripts.

C. Other author's contributions and activities

Published journal papers

- O. Krepl, J. Klusák, Crack onset assessment near the sharp material inclusion tip by means of modified maximum tangential stress criterion, Frattura ed Integrità Strutturale 42 (2017) 77-84.
- O. Krepl, J. Klusák, The influence of non-singular terms on the precision of stress description near a sharp material inclusion tip, Theoretical and Applied Fracture Mechanics 90, 2017, p. 85-99, ISSN 0167-8442, https://doi.org/10.1016/j.tafmec.2017.03.007 (Q1, IF = 2.659).
- O. Krepl, J. Klusák, Multi-parameter Based Stress Distribution in Vicinity of Sharp Material Inclusion Tip, Solid State Phenomena, 2016, p. 169-173.
- J. Klusák, O. Krepl, T. Profant, Behaviour of a crack in a corner or at a tip of a polygon-like particle, Structural Integrity Procedia 2, 2016, p. 1912-1919.
- O. Krepl, J. Klusák, Reconstruction of a 2D stress field around the tip of a sharp material inclusion, Structural Integrity Procedia 2, 2016, p. 1920-1927.
- O. Krepl, J. Klusák, T. Profant, Analytical-numerical determination of stress distribution around a tip of polygon-like inclusion, Key Engineering Materials 1, 2016, p. 94-98.
- J. Klusák, M. Hrstka, T. Profant, O. Krepl, O. Ševeček, M. Kotoul, The influence of the first non-singular stress terms on crack initiation direction in an orthotropic bi-material plate, Theoretical and Applied Fracture Mechanics 71, 2014, p. 67-75 (Q1, IF = 2.659).

Contributions at international conferences

- ICF 14, Rhodes (contribution: O. Krepl, D. Leguillon, J. Klusák, Assessment of crack onset conditions at a sharp tip of a material inclusion by means of the coupled criterion)
- ICF 14, Rhodes (contribution: O.Krepl, J. Klusák, Multi-parameter criterion for crack initiation at sharp material inclusion tip)
- AM 2017, Brno (contribution: O. Krepl, J. Klusák, Crack onset assessment near the sharp material inclusion tip)
- MSMF8, Brno (contribution: O. Krepl, J. Klusák, Multi-parameter based stress distribution in vicinity of sharp material inclusion tip)
- ECF21, Catania (contribution: O. Krepl, J. Klusák, Reconstruction of 2D stress field around a tip of sharp material inclusion)
- ICSMA 17, Brno (contribution: O. Krepl, J. Klusák, T. Profant, Singular and non-singular stress terms for the failure assessment of bi-material notches)
- 26th Colloquium on Fatigue Mechanisms, Brno (contribution: O. Krepl, J. Klusák, Stress concentration on sharp inclusions)
- The fatigue crack propagation threshold as a design criterion, Poitiers (contribution: O. Krepl, J. Klusák, T. Profant, Determination of fatigue fracture parameters of orthotropic bi-material notches)
- Frontiers in Material and Life Sciences, Brno (poster: Stress distribution and fracture parameters of orthotropic bi-material notches determination)

Research internships

- Université Pierre et Marie Curie in Paris (from 2nd October to 1st December 2016) at the Institut Jean Le Rond d'Alembert under Professor Dominique Leguillon's supervision.

Contributions at student conferences

- PhD Retreat II, Telč (contribution: Singular stress field near the sharp material inclusion tip and crack onset assessment)
- School of mechanics / Škola pružnosti a pevnosti, Hrubá voda (contribution: On the stress concentration)

Teaching experience

- Strength of Materials I (seminars) / Pružnost pevnost I (cvičení)

Vysoké učení technické v Brně

Středoevropský technologický institut VUT

Prohlášení o shodě listinné a elektronické formy dizertační práce

Jméno a příjmení studenta: Ing. Ondřej Krepl

Student ID: 115741

Studijní obor: Pokročilé materiály

Název práce: Speciální problémy lomové mechaniky singulárních koncentrátorů napětí v kompozitních materiálech

Akademický rok: 2017/18

Prohlašuji, že elektronická forma odevzdané dizertační práce je shodná s odevzdanou listinnou formou.

V elektronických datových souborech je dále uveden jako příloha soubor *.zip

V Brně dne 2.2.2018

Ing. Ondřej Krepl